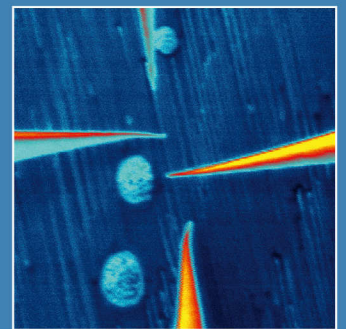
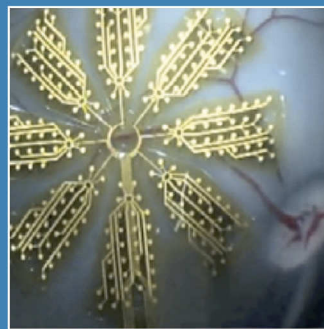
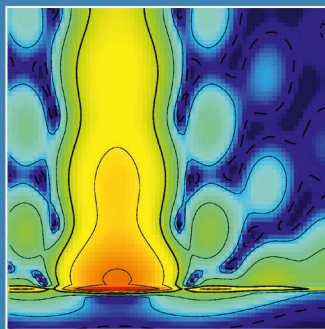
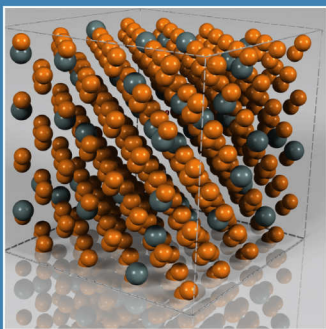


Annual Report 2012



AN INITIATIVE OF

JARA-FIT

**Jülich Aachen Research Alliance for
Fundamentals of Future Information Technology**

Annual Report 2012

**Forschungszentrum Jülich
RWTH Aachen**

Dear Reader,

It was in 1965 when Gordon Moore, co-founder of Intel, realized that the number of components in integrated circuits (ICs) had doubled every year since the invention of the IC in 1958. Moore was optimistic that this increase would continue for at least ten more years. It is amazing to see that 'Moore's law' still describes the trend in the semiconductor industry after 55 years. This increase in performance has important consequences for all of us. Information technology is pervading all areas of our life. It has assumed a key function in areas as varied as communication, industrial production, transport, energy and environmental technology, health, and last but not least entertainment. When we now enjoy inexpensive electronic toys they use more computation power than was available for the first landing of Apollo 11 on the moon in 1969. Since the industrial revolution no other technology has accomplished such a pronounced growth. Yet we all know that exponential growth cannot continue forever. In the next decade, the development of IT systems will be dominated by two major trends - a continuation of the exponential increase in performance and efficiency ("Moore's law") by further down-scaling, new materials, and novel device concepts - and additional functionalities ("More than Moore") by the emergence of advanced concepts in, e.g., sensors and wireless transmission. Beyond this, new concepts of quantum information processes seem close ahead and are likely to bring new innovations in the field of future information technology.

JARA-FIT is one of the drivers of this development and looks back to an exciting year. In June 2012 RWTH Aachen and JARA were successful within the excellence initiative. RWTH Aachen's plan to promote top level research by becoming an Integrated Interdisciplinary University of Technology was selected once again by the German Science Council and will be funded until 2017. RWTH plans to further sharpen its internationally visible scientific profile in close collaboration with the Jülich research center. Within JARA-FIT we are committed to further strengthen the close cooperation between Jülich and Aachen by creating joint institutes for Quantum Computing and GreenIT, which will bring the strategic planning in research, teaching and infrastructure to new levels. JARA-FIT and its researchers were successful in other areas as well. Several colleagues from Jülich and Aachen including Christoph Stampfer and Markus Morgenstern are part of the European Flagship Graphene, which plans to utilize the remarkable properties of this exciting material in novel applications. Rafal Dunin-Borkowski won an ERC Advanced Grant to develop techniques based on electron microscopy to image magnetic field with almost atomic resolution. Paul Körgeler was awarded an ERC Starting Grant to tailor Magnetic Molecules for Spintronic Devices. Furthermore a virtual institute for Topological Insulators was founded within JARA-FIT. These novel materials attract the interest of several scientists, who are also active within a priority program of the German Science Foundation. We were also pleased to be able to share the exciting science with our international colleagues at the Nature Conference on the Frontiers in Electronic Materials, which was held in the Eurogress in Aachen and organized by JARA-FIT and the Nature Publishing Group.

By now nanoelectronics is not only describing the research activities of more than 40 colleagues in JARA-FIT. Nanoelectronics is also becoming more visible in our teaching activities. New courses are developed and a master with specialization in nanoelectronics is now awarded by RWTH Aachen. To further strengthen the field, an IFF-Spring School for Quantum Information Processing was organized by David DiVincenzo.

While we are reluctant to apply Moore's Law to the development of JARA-FIT and predict its future, we are happy to look back at 5 years of continued growth and interaction within JARA-FIT.

Matthias Wuttig
Scientific Director JARA-FIT

Detlev Grützmacher
Scientific Director JARA-FIT

Contents

JARA-FIT in Headlines	4
General Information	13
JARA-FIT Members	15
JARA-FIT Institutes	17
Selected Research Reports	27
Strained Si nanowire complementary tunnel field-effect transistors for low power inverter circuits	29
Lattice Dynamics of Nanocrystalline Silicon for Thermoelectric Application: Effects of Impurities	31
Electronically non-alloyed state of a statistical single atomic layer semiconductor alloy	33
Integrated Silicon Photonics for Optical Communications and Biosensing	35
Synthesis of GeSn Semiconductors for Optoelectronic Applications	37
Growth and vertical integration of (Ga,In)N nanostructures for future single photon emitters	39
Bulk electronic structure of the dilute magnetic semiconductor $\text{Ga}_{1-x}\text{Mn}_x\text{As}$ through hard X-ray angle-resolved photoemission	41
Controllable Supercurrent and Inter-ferece Effect in Nb/InAs-nanowire/Nb Hybrid Devices	43
Scanning tunneling microscopy with InAs nanowire tips	45
Monitoring structural influences on quantum transport in InAs nanowires	47
High-Fidelity Single-Qubit Gates for Two-Electron Spin Qubits in GaAs	49
Electric field-driven coherent spin reorientation of spin packets in InGaAs	51
Noise Analysis of Qubits Implemented in Triple Quantum Dot Systems in a Davies Master Equation Approach	53
Efficiency and Power of a Quantum Dot Energy Conversion Device	55
Readout of carbon nanotube vibrations by intrinsic spin-phonon resonance	57
Multi-wavelength polar-dielectric superlens and graphene superlens	59
Strong correlations on topological insulator surfaces and the breakdown of the bulk- boundary correspondence	61
Higgs transition in quantum spin ice $\text{Yb}_2\text{Ti}_2\text{O}_7$	63
Antiferromagnetism in the Hubbard Model on the Bernal-stacked Bilayer	65
Spin relaxation in metals and thin metallic films	67
Ultrafast magnetization enhancement in metallic multilayers driven by super-diffusive spin currents	69
Quenched Slonczewski-windmill in spin-torque vortex oscillators	71
Topological solitons driven by Landau-Lifshitz-Slonczewski equations	73
Theoretical probing of inelastic spin-excitations in adatoms on surfaces	75
Electrical Transport through Single Nanoparticles and Nanoparticle Arrays	77
Dissecting a Multifunctional Organic-Metal Bond by Molecular Manipulation	79
Orbital tomography for highly symmetric adsorbate systems	81

Surface ‘click’ of DNA followed by directed metallization allows construction of contactable conducting nanostructures	83
Single-crystal neutron-diffraction study of the biomolecule guanidine 151 years after its first synthesis.....	85
Patterned Gold Nanoparticles with Tunable Surface Properties	87
A Very Large Micro Electrode Array for Recording and Stimulation of Retinal Ganglion Cells.....	89
All Diamond Microelectrode Arrays Produced by a Non-Lapidary Method to Detect Cell Action Potentials.....	91
Theory and Simulation of Cortical Networks.....	93
Chemical Surface Modeling of GeTe, an Archetypical Functional Material.....	95
<i>In situ</i> transmission electron microscopy study of the crystallization of bits in $\text{Ag}_4\text{In}_3\text{Sb}_{67}\text{Te}_{26}$	97
Resonating valence bond states in the PEPS formalism.....	99
Disorder-driven Metal-insulator Transitions in Crystalline Phase-change Materials.....	101
Iron-Pnictides: strong Coulomb correlations via Hund’s coupling	103
Multiferroicity from charge ordering? a case study	105
Insulating Ground State of an Interface with Polar Discontinuity: $\text{DyScO}_3/\text{SrTiO}_3$	107
Analysis of polarization and lattice strains at the Interface of ferroelectric heterostructures on atomic scale by Cs-corrected scanning transmission electron microscopy (STEM).....	109
<i>In-situ</i> Structural Investigations of Non-stoichiometric HfO_{2-x} Films Using QEXAFS.....	111
Pulsed laser ablation of complex oxides: the role of congruent ablation and preferential scattering for the film stoichiometry	113
Heavily Donor-Doped Optically Translucent BaTiO_3 -Ceramics through Defect Chemical Engineering	115
Structural Characterization of Resistively Switching Thin SrTiO_3 Films by Grazing Incidence Small Angle X-ray Scattering.....	117
Chemical insights into electroforming of resistive switching manganate heterostructures	119
Simulation of Multilevel Switching in Electrochemical Memory Cells	121
Area-Delay Metric Optimization for Hybrid RS/CMOS Memories based on Passive Nanoelectronic Crossbars	123
Nanobatteries inside Redox-Based Memristive Elements.....	125
Atomic Manipulation of Electrochemical Interfaces for Resistive Switching.....	127
Versatile scanning tunneling microscopy with 120 ps time resolution.....	129
High-sensitivity SQUIDs with dispersive readout for scanning microscopy.....	131
Detection of Liquids based on Reflectance Measurements with High- T_c Superconducting Sensors.....	133
High- T_c quantum interferometers for magnetoencephalography.....	135
Ultra-Compact Multi-Tip Scanning Tunneling Microscope.....	137
Investigations of EUV conversion efficiency of luminophores	139
Publications	141

JARA-FIT in Headlines

RWTH Aachen and JARA successful in the German Excellence Initiative



For the second time in a row, RWTH Aachen University has succeeded in the Excellence Initiative by the German federal and state governments. On Friday, 15 June 2012, the Joint Commission of the DFG and the German Council of Science and Humanities had decided which projects would be funded in the second phase of the Excellence Initiative. The RWTH Aachen was successful in all of the three funding lines of the Excellence Initiative. In particular, its new Institutional Strategy, titled "RWTH 2020: Meeting Global Challenges. The Integrated Interdisciplinary University of Technology," was confirmed by the authorization committee. RWTH wants to invest the funding

amount of approx. 60 million € for the Institutional Strategy II into "excellent" activities. Four measures were defined within this scope:

Measure 1 - Internationally Recognized Scientific Profile

RWTH wants to advance its internationally recognized scientific profile by leveraging the strength of its core competencies in the engineering and natural sciences. Moreover, decisive steps will be taken to integrate the humanities, economics and medicine in order to tackle problems of great scientific, technological and societal relevance. To this end, RWTH will further strengthen the natural sciences and systematically promote interdisciplinary research.

Measure 2 - JARA: Focusing Competences – Shaping the Future

The Jülich Aachen Research Alliance (JARA) between RWTH Aachen and Forschungszentrum Jülich will continue the strategic cooperation that serves as a role model for uniting program and discipline-based research in Germany. JARA will expand in dedicated fields by means of joint strategic planning of research, teaching and infrastructure development (JARA Institutes).

Measure 3 - Place to Be

Additionally, RWTH Aachen is implementing mechanisms to attract the world's best and brightest researchers and students, thus creating an exceptional environment for learning, expanding and disseminating fundamental knowledge.

Measure 4 - Corporate Governance and Structures

The second funding phase introduces novel mechanisms of collaboration, competition, and administration. By establishing cross-faculty profile areas, interdisciplinary research concerning relevant issues of the future will be considerably strengthened.

JARA-FIT partner in the **GRAPHENE FLAGSHIP** Project: A new material takes off



Graphene, the first truly two-dimensional material, is considered one of the most promising materials for future IT applications. This is mainly due to the unique material's properties: it is almost as hard and durable as diamond, but can be stretched like rubber. It outperforms copper as a conductor of heat and silicon as a conductor of electricity. It is virtually invisible, as it is composed of a single-layer of carbon atoms. It is chemically resilient, impermeable to most substances, and based on carbon, a readily available material. By now, graphene can be produced in large quantities, and possible applications are beginning to be developed: the material may be used as an "electronic ink" to produce electronic circuits, or provide the basis for foldable cell phone displays or lighter, enhanced tennis rackets. Planned are new ultra-fast transistors, superfast optocouplers, as well as new concepts for quickly rechargeable batteries, the sequencing of DNA strands, and even water desalination facilities.

The EU-supported FET Flagship program "Graphene," which is expected to receive funding in the amount of one billion Euros over a ten-year period, seeks to help turn several of these envisioned applications into reality. Now 74 institutions from academia and industry from 17 European nations have joined forces to establish international working groups for various research projects.

In the first funding phase, RWTH Aachen University as a partner receives 1.44 percent of the funding sum, that is about 1.034 million Euros. AMO GmbH, which has close ties to the RWTH, specializes in

micro and opto electronics and receives 0.88 million Euros. This makes Aachen the largest partner of the research consortium in Germany.

In the large-scale project, Markus Morgenstern will thoroughly investigate graphene and its defects at the atomic scale. Christoph Stampfer and Bernd Beschoten will investigate the possibility of using graphene for the transport of magnetic information in a spintronics paradigm, which promises a more energy-efficient information processing than conventional technologies. Renato Negra from the Electrical Engineering Department seeks to develop graphene applications in high-frequency electronics, to open up utilization in the fields of communication technology, imaging, medical engineering, and sensor technology.

JARA-FIT scientist Rafal Dunin-Borkowski received ER-C advanced grant from the European Research Council

Rafal Dunin-Borkowski, director of the Ernst Ruska-Centre for Microscopy and Spectroscopy with Electrons and director at the Peter Grünberg Institute of the Forschungszentrum Jülich, has been awarded an Advanced Grant by the European Research Council (ERC). He received funding worth 2.5 million € over a period of five years for his project "Imaging Magnetism in Nanostructures using Electron Holography" (IMAGINE). He wants to use the funds for the development of electron microscopy methods which allow the mapping of magnetic fields in the interior of materials at almost atomic resolution. Fundamental research in the field of nanomagnetism stands to benefit from the success of this project as well as application-oriented research. The objective of the project is to increase the spatial resolution of electron holography for the imaging of magnetic fields in crystalline materials to better than half a nanometre - which is approximately a factor of ten compared to current capabilities.



JARA-FIT scientist Paul Kögerler received ER-C starting grant from the European Research Council

The chemist Paul Kögerler, University Professor of Inorganic Chemistry at the RWTH Aachen University and visiting scientist at the Forschungszentrum Jülich, has received a Starting Grant from the European Research Council. The Starting Grant is given to top-level early-career scientists in order to offer them the opportunity to conduct fundamental research and establish or consolidate their own research team. Paul Kögerler succeeded in the competitive two-stage selection process and has received funding in the amount of approx. 1.5 million Euros over a period of five years.

In his project on "Synthetic Expansion of Magnetic Molecules Into Spintronic Devices" (MOLSPINTRON), he sets out to tackle one of central difficulties in molecular spin electronics: the precise contacting of the particle. To do so he plans to utilize highly stable magnetic metal oxide nanomolecules, at whose surfaces the contacts can be made synthetically, i.e. with atomic precision, using both conductive and nonconductive interfaces.



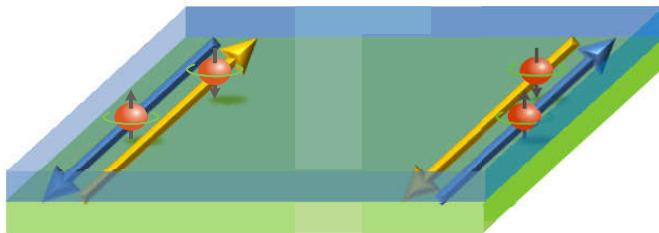
JARA-FIT is active on Topological Insulators

In September 2012 a **Virtual Institute for Topological Insulators** (VITI) went into action. VITI is funded by the Helmholtz Association and brings together the Jülich key competencies in the field of topological insulators with those of RWTH Aachen University and Würzburg University. The Shanghai Institute of Microsystem and Information Technology, Chinese Academy of Science, participates as an international partner.

The research conducted at VITI focuses on a new class of material recently discovered, so called topological insulators. In topological insulators the bulk of the material is insulating, while the edge or the surface is conducting. The scattering of charge carriers is basically forbidden, because of the very specific properties of the electronic states, i.e. the band structure. As a consequence, the electric conductivity is expected to be largely enhanced. This makes this new material system very promising for future high-speed, low power consumption electronic devices. In addition, topological insulators are also very attractive to address fundamental questions in quantum physics.

Topological insulators can be subdivided into two classes: Three-dimensional and two-dimensional systems. The former exhibits a two-dimensional metallic surface with a three-dimensional bulk insulator,

while the latter two-dimensional system consists of conductive edge channels with an insulating two-dimensional area.



In 2-dimensional topological insulators based on layer systems the electrons flow at the edge. The magnetic property of the electrons, the spin determines the direction of the propagation. VITI will mainly focus on the three-dimensional counterpart, where the whole surface is conductive.

VITI will mainly focus on three-dimensional topological insulators, i.e. Bi_2Te_3 or Be_2Se_3 . The relatively large energy band gaps make these materials particularly interesting for room temperature applications.

In the Virtual Institute different experimental groups from Jülich, Aachen, Würzburg, and Shanghai are collaborating closely in the field of material development, characterization and electron transport. The experimental work is supplemented by theory groups in Jülich, Würzburg, and Shanghai, which contribute to each of the experimental areas. Within VITI high quality layers of Bi- and Hg-based topological insulators are produced by means of chemical vapor deposition, molecular beam epitaxy or alternatively by exfoliation of single crystals. The electronic surface states are studied by means of spectroscopy and transport measurements. Finally, the applicability of topological insulators for quantum electronic and spin electronic devices is assessed. Information about VITI activities can be obtained from the VITI webpage: www.vi-ti.de, or by contacting the speaker: Thomas Schäpers, Forschungszentrum Jülich.

In 2012, the German Science Foundation also set up a **priority programme on topological insulators** (SPP 1666, speaker: Oliver Rader, HZB Berlin) with the aim to improve existing topological insulator materials, to investigate the basic properties and develop device structures as well as to find new materials and devise novel concepts. JARA-FIT were successful in receiving approval for 5 projects, namely

Spin and charge transport in Bi-based topological insulators (Bernd Beschoten and Christoph Stampfer, RWTH Aachen University)

First principles studies of electronic and transport properties of one-dimensional edge states of nano-structured topological insulators. (Gustav Bihlmayer, Yuriy Mokrousov, and Daniel Wortmann, Forschungszentrum Jülich)

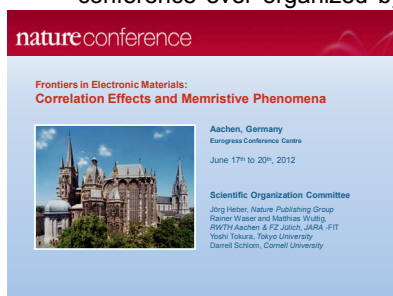
Spin scattering of topologically protected electrons at defects (Phivos Mavropoulos and Stefan Blügel, Forschungszentrum Jülich)

Optimizing interfaces between topological insulators and superconductors: Towards a local detection of Majorana fermions (Markus Morgenstern and Marcus Liebmann, RWTH Aachen University)

Molecular-beam epitaxy of three-dimensional topological insulators (Gregor Mussler, Detlev Grützmacher, Forschungszentrum Jülich)

JARA-FIT organised Nature Conference on the Frontiers in Electronic Materials

From June 17 to 20th 2012, a Nature Conference on the Frontiers in Electronic Materials was held in the Eurogress in Aachen, organized by JARA and the Nature Publishing Group. It was the first Nature conference ever organized by a German university and the first on this topic. The initiative to organize



such conference originated in the preparation phase of the SFB 917 "Resistively Switching Chalcogenides for Future Electronics". Rainer Waser and Matthias Wuttig felt that such an event in 2012 would provide an excellent platform to present the first wave of results of the SFB 917, and to put them into a wider perspective. In fact, the extension of the Nature Conference's title, "Correlation Effects and Memristive Phenomena" promised to cover the most unusual and fascinating electronic phenomena that have emerged in recent years. These phenomena typically occur in oxides and higher chalcogenides and represent the hottest topics in solid-state research today. They comprise of strong electron correlation, multiferroicity, spintronic effects,

topologically protected electron states, as well as unexpected effects at complex heterointerfaces. And they include superionic conduction and artificial photosynthesis, as well as resistive switching and memristive phenomena, based on nanoscale phase change and nanoionic redox processes. The organizers (who were Joerg Heber, Yoshi Tokura, Darrell Schlom, besides the initiators Rainer Waser and Matthias Wuttig) brought together leaders in these interdisciplinary fields to discuss breakthroughs and challenges in fundamental research as well as prospects for future applications. The conference attracted more than 500 participants from 25 countries of the world as well as numerous companies and organizations for display booths in the exhibition hall.

Following the format of the Nature Conferences, the emphasis was placed on the invited keynote talks. There were fundamental talks, for instance, about the new opportunities of atomically resolved electron spectroscopy by David Muller (Cornell Univ.) and about the often overlooked, decisive role of lattice defects by Joachim Maier (MPI Stuttgart). The focal area of memristive devices and systems aimed at the challenge of the ever increasing energy demand of the information technology in modern societies, and at concepts which hold the promise of reducing the energy consumption of non-volatile memories by two to three orders of magnitude (compared to Flash devices). As speakers such as Konstantin Likharev (Stony Brook), Masakazu



Aono (MANA, Tsukuba), U-In Chung (Samsung Electronics), Stanley Williams (HP labs), and Stephen Elliot (Univ. Cambridge) pointed out, these concepts indeed may open the door to completely new, energy-efficient computational concepts – for example, based on neuromorphic computer architectures. In the area of multiferroic phenomena discussed by Nicola Spaldin (ETH Zürich), Jim Scott (Univ. Cambridge), and Ramamoorthy Ramesh (Berkeley) manifold details on the coupled ferroelectric and ferromagnetic ordering emerged from recent studies. In the field of electron correlation effects, novel experimental and theoretical methods significantly broadened the understanding as explained, for instance, by Bernhard



Keimer (MPI Stuttgart), Elbio Dagotto (Univ. Tennessee), and Hidenori Takagi (Univ. Tokyo). Ionic liquid gating of oxide field effect devices have been exploited by Masashi Kawasaki (Univ. Tokyo and RIKEN), Peter Littlewood (Argonne Nat. Lab.), and Stuart Parkin in order to tune the near-interface carrier densities over an unusual large range. And the 2-D electron transport at oxide heterointerfaces such as $\text{LaAlO}_3/\text{SrTiO}_3$ attracted a sustained field of interest as shown in the talks by, for example, of Jochen

Mannhart (MPI Stuttgart), Guus Rijnders (Univ. Twente), Susanne Stemmer (UCSB), and Harold Hwang (Stanford Univ.).

In order to provide a format between these keynote talks and the poster sessions, so-called nanosessions were created where the audience split into approximately a dozen of small groups to listen to brief oral presentations in front of a corresponding set of posters. Discussion leaders for the nanosessions were selected from the abstract submissions prior to the conference. Whilst being tiny events on their own allowing for stimulating, intimate discussions among scientists interested in the details of the topics, the nanosession were kept open physically, creating a relaxed atmosphere and high flexibility for participants to be attracted by the numerous activities.



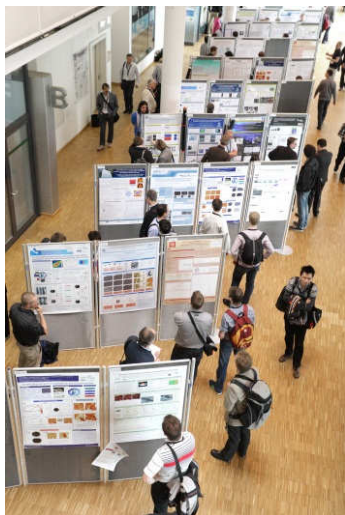
The social programme of the Nature Conference included a guided tour of the Imperial Cathedral with the Palatine Chapel of Charlemagne which is ranked by UNESCO among the World Heritage Sites and an organ concert in the Cathedral, prior to the conference dinner in the Coronation Hall of the medieval town hall of Aachen.

European Workshop on Metalorganic Vapour Phase Epitaxy in Aachen

The 15th European Workshop on Metalorganic Vapour Phase Epitaxy (EWMOVPE XV) returned after 26 years to its birthplace in Aachen and was held at the Technology Centre in Aachen from June 2nd to 5th 2013. Hosts of the workshop were the research alliance JARA (Jülich Aachen Research Alliance), the Peter Grünberg Institute 9 (Forschungszentrum Jülich) and the research group on GaN Device Technology (GaN-BET) at RWTH Aachen University. Traditionally the workshop is a meeting opportunity for the European scientific community involved in MOVPE – physicists, chemists, material science specialists and engineers from universities, research centres and from industry. Student participation is strongly encouraged in this workshop. A best student contribution award is granted.

The current workshop was organized by JARA-FIT scientists Hilde Hardtdegen (Forschungszentrum Jülich) and Andrei Vescan (RWTH Aachen University).





Eight international speakers were invited to give overview talks on special challenges and future applications for MOVPE growth and characterization. All topics relevant to modern MOVPE were addressed, ranging from surface science to device development, from basic growth mechanisms to production issues. Ingrid Koslow (UCSB, USA) explained the relevance of strain relaxation in semipolar nitrides for LEDs and Carol Thompson (Argonne National Labs, USA) discussed in situ X-ray studies during growth to study metastable materials. Colin Humphreys (University of Cambridge, UK) and Jong Min Kim (University of Oxford, UK) reported on GaN LED growth on low cost large Si substrates and on diverse substrates such as glass, respectively. Stuart Irvine (OpTIC Technium, Glyndwr University, UK) presented the past, present and future challenges of MOCVD for solar cells. Massimo Longo (CNR-IMM, Unità di Agrate Brianza, Italy) discussed the deposition of phase change materials and nanostructures produced by MOCVD for non volatile memory applications. Kimberley Dick Thelander (University of Lund, Sweden) and Kirsten Moselund (IBM Research GmbH, Switzerland) reported on III-V nanowire growth and nanowire heterostructure devices for low power electronics, respectively. According to the format of the workshop all 92 contributed papers were poster presentations allowing lively

and stimulating discussions during the four sessions. The technical programme was accompanied by an industrial exhibition comprising 18 companies. The title of the best student contribution was awarded to Andreas Winden from the Peter Grünberg Institute 9 (Forschungszentrum Jülich) for his paper "MOVPE of site-controlled pyramidal (Ga,In)N hetero-nanostructures for future single photon emitters" and to Mikhail Chubarov (Linköping University, Sweden) for his paper "Chemical vapor deposition of epitaxial rhombohedral boron nitride in the presence of small amounts of silicon". The prestigious workshop attracted close to 200 participants from 20 countries and helped promote the scientific exchange in Europe and beyond.

44. IFF Spring School: Quantum Information Processing in Jülich



From the 25 February to 8 March 2013, Jülich hosted the IFF Spring School for the 44th time in its long history. Under the scientific direction of David DiVincenzo, the annual intensive course organized by members of the former Institute for Solid State Research (known as the "IFF") was this year based on both fundamental and current issues in quantum information processing.

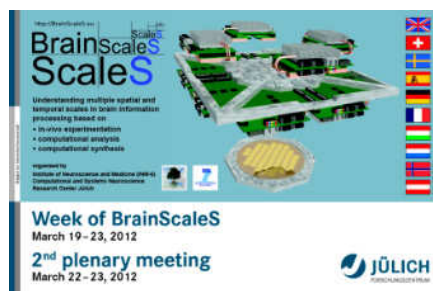
Quantum information processing is an interdisciplinary area that has attracted growing interest over the past 20 years. It describes the type of information processing and data transmission which is not based on the laws of classical physics, but rather on quantum mechanics. This could enable new functionalities to emerge; for instance, quantum cryptography could make it possible to reliably transmit securely encoded messages, and the development of so-called quantum computers could significantly speed up the undertaking of certain types of computational processes when compared with conventional computers. To this end, instead of using classical bits, data must be encoded in the form of quantum bits (known as "qubits", units of quantum information), such as the polarization of a single atom, ion, electron or photon, for example. Not only can they represent the classical binary data of zero and one, but also any amount of information in between. Additionally they can communicate with each other. In this way, many computational steps can be carried out at the same time, instead of strictly in sequence. It was the goal of the Spring School 2013 to provide both a comprehensive introduction to the basics of Quantum Information Processing as well as detailed insights into topics such as solid state qubits, informatics and qubits, and contemporary qubits.



A total of 275 undergraduates, Ph.D. students and young scientists travelled to Jülich to learn from and exchange ideas with some of the most internationally-renowned speakers from leading institutes and organizations in this area of research, such as Harvard University, MIT Lincoln Laboratory, the IBM Research Center Yorktown Heights, the HRL Laboratories in Malibu and many other universities and institutions. Apart from the excellent lectures and seminars, participants were also offered an interesting programme of extra-curricular events, including guided tours of a selection of Jülich laboratories, a visit to one of the largest surface mines in Germany, a guided tour of the city of Cologne, and of course invitations to the Welcome and Farewell dinners organized as part of the School's activities at the campus lakeside restaurant. This year, the IFF Spring School kindly received support from the DAAD (German Academic Exchange Service), making it possible for several students from Egypt to take part in the School.

Annual Week of BrainScaleS organised by JARA scientists

From March 19 to 23th 2012, the Institute of Neuroscience and Medicine - 6: Computational and Systems Neuroscience hosted the annual "Week of BrainScaleS" conference with 100 international participants on Jülich campus. BrainScaleS is an EU-funded Integrated Project centered around the development of neuromorphic hardware. BrainScaleS is based on the previous EU FACETS project and laid the foundations for the upcoming EU Flagship "Human Brain project HBP". The project advances three technology platforms: conventional supercomputing, dedicated digital massively-parallel hardware (SpiNNaker) and analogue VLSI technology. The role of the institute is the determination of constraints by the analysis of experimental data and the development of brain-scale models, the development of simulation technology for supercomputers, and the creation of interfaces and benchmarks for the neuromorphic hardware.



UMBRELLA SYMPOSIUM with Israel Institute of Technology

The 27th UMBRELLA symposium for the development of joint cooperation ideas was held at the Jülich Research Centre on 25 to 27 February 2013. The symposium entitled "Nanoscale Physics and Chemistry as Drivers for Future Technological Developments" was organised by the ER-C and gave participants the opportunity to attend about thirty presentations by researchers from the Israel Institute of

Technology, RWTH Aachen University, and Forschungszentrum Jülich. The symposium also provided a forum for the discussion of plans for collaborative research projects funded by the UMBRELLA cooperation.

Sessions on topical issues of classical solid state research and on topics from the fields of energy and information technology focused on the characterisation and spectroscopy of interfaces and lattice imperfections in solids at atomic resolution, microscopy and spectroscopy of soft matter, self aggregating systems, correlated phenomena in solid state research, nanomaterials for energy research, nanoelectronics and future information technology, quantum information and computation.

JARA-FIT scientists founded Spin-Off Company

The spin-off company mProbes offers scanning probe microscopy solutions of highest performance. The products are based on the KoalaDrive[®] nanopositioner technology which was invented at the research center Jülich and makes scanning probe microscopy design ultra-compact and stable. Scanning probe microscopy solutions from mProbes allow integrating scanning probe microscopy to existing surface analysis or deposition systems and provide operation at low temperatures or high magnetic fields.



A specialty of mProbes is the multi-tip scanning probe microscopy which allows expanding the capacity of scanning probe microscopy from imaging towards electrical measurements at the nanoscale. The spin-off company mProbes GmbH (www.mprobes.com) was launched in 2012 by three JARA-FIT scientists and moved meanwhile to rooms in the Research Center Jülich and the Technologiezentrum Jülich.

Young JARA-FIT scientist won Einstein Slam

Knowledge transfer in another way: explain a scientific topic in a few minutes to a wide audience in the most entertaining and easily comprehensible way possible – that is the aim of participants in the so-called “Science Slams”. Based on the model of poetry recital competitions found in literary circles and known as “Poetry Slams”, scientists are judged by the audience who evaluates the scientific content, ease of comprehension and the entertainment value of short presentations given by the largely young competitors. On 19 September 2012 at the “Einstein Slam”, part of the 2012’s science festival “Highlights from Physics” held in Göttingen, Robert Frielinghaus, a PhD student at the Peter Grünberg Institute of the Forschungszentrum Jülich was able to impress his listeners with his lecture. In less than ten minutes, he explained to an enthusiastic audience how current flows through microscopic nanostructures with the help of beer bottles and elevators, with humorous borrowings from Loriot. The audience selected him as the winner, and in addition, he was presented with a “Golden Albert” trophy, a palm-size bust of the famous physicist, the competition’s namesake.

Young JARA-FIT surface physicist was honoured

Dr. Giuseppe Mercurio of the Peter Grünberg Institute – Functional Nanostructures at Surfaces, who recently graduated at the RWTH Aachen University, has been awarded the prestigious Max Auwärter Prize for his dissertation. The Max Auwärter Award for students and young researchers is offered bi-annually by the Max Auwärter Foundation in Balzers, Principality of Liechtenstein. It is open to university and research institution based scientists up to 35 years of age who have published significant work in the fields of surface physics, surface chemistry, or organic and inorganic thin films. The Prize was granted at the Annual Meeting 2012 of the Austrian Physical Society held in Graz. The award includes a certificate and a prize of 10.000 €. The subject of his PhD research was the interaction of organic molecules with metal surfaces. He performed experiments at the European Synchrotron Radiation Facility (ESRF) in Grenoble by means of the Normal Incidence X-ray Standing Wave (NIXSW) technique. Giuseppe Mercurio also received the 2013 Excellence Prize of the Forschungszentrum Jülich, including prize money of € 5,000, for his outstanding contribution to surface physics.

New appointments

Experimental Nanophysicist Christoph Stampfer

Christoph Stampfer was appointed head of the II. Institute of Physics A at the Faculty of Mathematics, Computer Science and Natural Sciences at the RWTH Aachen University in April 2013. He studied physics and electrical engineering at Technical University Vienna, Austria and received his PhD degree from the Department of Mechanical and Process Engineering at ETH Zurich. After a Postdoc stay at the Laboratory of Solid State Physics at the ETH Zurich he became JARA-FIT junior professor at the RWTH Aachen and the Forschungszentrum Jülich. Christoph Stampfer is working in the field of carbon-based quantum electronics.



EUV specialist Larissa Juschkina



Larissa Juschkina was appointed a professorship for Experimental Physics of Extreme Ultraviolet at the RWTH Aachen University in 2012. She received her diploma degree in plasma physics from the Novosibirsk State University, Russia and her Ph.D. from the Ruhr-University Bochum, Germany. She worked as the R&D head at AIXUV GmbH on the development of EUV sources and systems for metrology. From 2006 to 2010 she was the EUV Technology group leader at the RWTH Aachen University, Chair for Technology of Optical Systems. In 2011 she joined the Plasma Spectroscopy Group at the University College Dublin and was working on the investigation of short wavelength radiation from laser produced plasmas with an emphasis on atomic processes in highly ionized ions. Her scientific interests and activities are concentrated on plasma based short-wavelength radiation sources and their applications, spectroscopy of highly ionized plasmas, EUV metrology and systems, surface and thin film characterization by spectroscopic reflectometry, EUV microscopy and lithography. She has received a Helmholtz Professorship to set up the collaboration with the Forschungszentrum Jülich.

General Information

JARA-FIT Members

- Prof. Dr. St. Appelt, Lehrstuhl für Technische und Makromolekulare Chemie,
Lehr- und Forschungsgebiet Niederfeld-NMR (Methoden der NMR), RWTH Aachen
Zentralinstitut für Elektronik, Forschungszentrum Jülich
- Prof. Dr. H. Bluhm, II. Physikalisches Institut C, RWTH Aachen
- Prof. Dr. S. Blügel, Peter Grünberg Institut – Quanten-Theorie der Materialien, Forschungszentrum Jülich
Institute for Advanced Simulation, Forschungszentrum Jülich
- Prof. Dr. T. Brückel, Peter Grünberg Institut – Streumethoden, Forschungszentrum Jülich
Jülich Centre for Neutron Science, Forschungszentrum Jülich
- Prof. Dr. A. Böker, Makromolekulare Materialien und Oberflächen, DWI an der RWTH Aachen
- Prof. Dr. D. P. DiVincenzo, Institut für Quanteninformation, RWTH Aachen
Peter Grünberg Institut – Theoretische Nanoelektronik, Forschungszentrum Jülich
Institute for Advanced Simulation, Forschungszentrum Jülich
- Prof. Dr. R. Dronskowski, Lehrstuhl für Festkörper- und Quantenchemie und Institut für Anorganische Chemie,
RWTH Aachen
- Prof. Dr. R. Dunin-Borkowski, Peter Grünberg Institut – Mikrostrukturforschung, Forschungszentrum Jülich
Ernst Ruska-Centre für Mikroskopie und Spektroskopie mit Elektronen
- Prof. Dr. D. Grützmacher, Peter Grünberg Institut – Halbleiter-Nanoelektronik, Forschungszentrum Jülich
- Prof. Dr. S. Grün, Institut für Neurowissenschaften und Medizin, Computational and Systems Neuroscience
Forschungszentrum Jülich
- Prof. Dr. C. Honerkamp, Institut für Theoretische Festkörperphysik, RWTH Aachen
- Prof. Dr. L. Juschkin, Lehr- und Forschungsgebiet Experimentalphysik des Extrem-Ultravioletts, RWTH Aachen
- Prof. Dr. P. Kögerler, Institut für Anorganische Chemie (Molekularer Magnetismus), RWTH Aachen
Peter Grünberg Institut – Elektronische Eigenschaften, Forschungszentrum Jülich
- Prof. Dr. U. Klemradt, II. Physikalisches Institut B, RWTH Aachen
- Prof. Dr. J. Knoch, Institut für Halbleitertechnik, RWTH Aachen
- Prof. Dr. P. Loosen, Lehrstuhl für Technologie Optischer Systeme, RWTH Aachen
Fraunhofer-Institut für Lasertechnik, Aachen
- Prof. Dr. S. Mantl, Peter Grünberg Institut – Halbleiter-Nanoelektronik, Forschungszentrum Jülich
- Prof. Dr. M. Martin, Institut für Physikalische Chemie, RWTH Aachen
- Prof. Dr. J. Mayer, Gemeinschaftslabor für Elektronenmikroskopie, RWTH Aachen
Ernst Ruska-Centre für Mikroskopie und Spektroskopie mit Elektronen
- Prof. Dr. R. Mazzarello, Institut für Theoretische Festkörperphysik, RWTH Aachen
- Prof. Dr. V. Meden, Institut für Theorie der Statistischen Physik, RWTH Aachen
- Prof. Dr. Chr. Melcher, Lehrstuhl I für Mathematik, RWTH Aachen
- Prof. Dr. W. Mokwa, Institut für Werkstoffe der Elektrotechnik 1 – Mikrostrukturintegration, RWTH Aachen
- Prof. Dr. M. Morgenstern, II. Physikalisches Institut B, RWTH Aachen
- Prof. Dr. T. Noll, Lehrstuhl für Allgemeine Elektrotechnik und Datenverarbeitungssysteme, RWTH Aachen

- Prof. Dr. A. Offenhäusser, Peter Grünberg Institut – Bioelektronik, Forschungszentrum Jülich
Institute of Complex Systems, Forschungszentrum Jülich
- Prof. Dr. E. Pavarini, Peter Grünberg Institut & Institut for Advanced Simulation, Forschungszentrum Jülich
- Prof. Dr. R. Poprawe Fraunhofer-Institut für Lasertechnik, Aachen
- Prof. Dr. G. Roth, Institut für Kristallographie, RWTH Aachen
- Prof. Dr. H. Schoeller, Institut für Theorie der Statistischen Physik, RWTH Aachen
- Prof. Dr. U. Simon, Institut für Anorganische Chemie, RWTH Aachen
- Prof. Dr. J. Splettstößer, Institut für Theorie der Statistischen Physik, RWTH Aachen
- Prof. Dr. C. Stampfer, II. Physikalisches Institut A, RWTH Aachen
Peter Grünberg Institut – Halbleiter-Nanoelektronik, Forschungszentrum Jülich
- Prof. Dr. C. M. Schneider, Peter Grünberg Institut – Elektronische Eigenschaften, Forschungszentrum Jülich
- Prof. Dr. T. Taubner, I. Physikalisches Institut A, RWTH Aachen
- Prof. Dr. S. Tautz, Peter Grünberg Institut – Funktionale Nanostrukturen an Oberflächen,
Forschungszentrum Jülich
- Prof. Dr. B.M. Terhal, Institut für Quanteninformation, RWTH Aachen
- Prof. Dr. A. Vescan, Lehr- und Forschungsgebiet GaN-Bauelementtechnologie, RWTH Aachen
- Prof. Dr. R. Waser, Institut für Werkstoffe der Elektrotechnik 2, RWTH Aachen
Peter Grünberg Institut – Elektronische Materialien, Forschungszentrum Jülich
- Prof. Dr. M. Wegewijs, Peter Grünberg Institut – Theoretische Nanoelektronik, Forschungszentrum Jülich
- Prof. Dr. S. Wessel, Institut für Theoretische Festkörperphysik, RWTH Aachen
- Prof. Dr. J. Witzens, Lehr- und Forschungsgebiet Integrierte Photonik, RWTH Aachen
- Prof. Dr. M. Wuttig, I. Physikalisches Institut A, RWTH Aachen

JARA-FIT Institutes

Systeme der Elektronik (ZEA-2), Forschungszentrum Jülich, Institut für Technische und Makromolekulare Chemie (ITMC), RWTH Aachen

St. Appelt

Our research revolves around spin order generation, the manipulation, measurement and transfer of spin order by combining Hyperpolarization technology with Nuclear Magnetic Resonance (NMR) spectroscopy. Starting from states with high spin orders, like nuclear singlet states or highly premagnetized (hyperpolarized) spin systems, we investigate the field dependency of the complexity, and thus information content, of corresponding NMR spectra in very low magnetic fields. Our research includes chemical synthesis as a means for substrate generation and optimization of spin order transfer, the development and construction of new hardware for mobile NMR spectroscopy as well as the investigation of the underlying quantum mechanical principles of coupled spins in low magnetic fields.

Peter Grünberg Institut / Institut for Advanced Simulation – Quanten-Theorie der Materialien, Forschungszentrum Jülich

S. Blügel

The analysis and computation of electronic properties of solid-state systems relevant for basic science and practical applications in collaboration with experimentalists is the hallmark of our research. An important asset of our institute is the competence in developing conceptual and computational methods (density functional theory and beyond, wave-packet propagation, diagrammatic techniques). Emphasis is on the investigation of complex magnetism, magnetism in reduced dimensions, oxide interfaces and heterostructures, topological insulators, graphene, organic molecules in contact with metallic and insulating substrates, spin- and spin-orbit-dependent electronic transport phenomena, collective excitations and quasi-particles. A second research theme is nano-scale tribology, friction, adhesion, plastic deformation. Computational materials science research is established by combining first-principles results with macroscopic methods (molecular dynamics, Monte Carlo).

II. Physikalisches Institut (IIC), RWTH Aachen

H. Bluhm

The research group is aiming to realize highly coherent two-level quantum systems in semiconductor quantum dots for quantum information processing. The group studies the physics governing these devices and pushes forward their technological development. Crucial techniques for high-speed control and measurement will be further improved, and multi-qubit systems will be designed, fabricated, and tested. In addition, the group is pursuing scanning SQUID microscopy at ultra-low temperatures for magnetic imaging and ultra-sensitive magnetic measurements on mesoscopic structures.

Lehrstuhl für Makromolekulare Materialien und Oberflächen, DWI an der RWTH Aachen

A. Böker

The chair of Macromolecular Materials and Surfaces is part of the DWI an der RWTH Aachen. The DWI is an independent research institute affiliated to RWTH Aachen University focused on polymer / soft matter materials development with the mission of novel and active properties. Under the heading "Science for Innovation" we aim at a tailor-made surface functionality of soft materials, especially fibers, films, membranes, textiles, and biomaterials. Beyond knowledge-oriented, basic approaches, work at DWI is dedicated to the translation and implementation of this knowledge into application-oriented concepts for functional films and surfaces, antimicrobial polymers and surfaces, encapsulation and release, functional membranes, and biomedical devices. The major research topics at the chair of Macromolecular Materials and Surfaces include bioconjugate polymer materials, nanoparticle composites and guided self-assembly.

Peter Grünberg Institut / Jülich Centre for Neutron Science - Streumethoden, Forschungszentrum Jülich

Th. Brückel

At the Institute of Scattering Methods, we focus on the investigation of structural and magnetic order, fluctuations and excitations in complex or nanostructured magnetic systems and highly correlated electron

systems. Our research is directed at obtaining a microscopic atomic understanding based on fundamental interaction mechanisms. The aim is to relate this microscopic information to macroscopic physical properties. To achieve this ambitious goal, we employ the most advanced synchrotron X-ray and neutron scattering methods and place great emphasis on the complementary use of these two probes. Some of our efforts are devoted to dedicated sample preparation and characterization from thin films and multilayers via nano-patterned structures to single crystals for a wide range of materials from metals to oxides.

Peter Grünberg Institut / Institut for Advanced Simulation – Theoretische Nanoelektronik, Forschungszentrum Jülich

D. P. DiVincenzo, group leaders E. Pavarini, M. Wegewijs

The behavior of interacting electrons in nano-scale structures is a primary focus. The Kondo effect, involving the interaction of an isolated spin impurity with conduction electrons, or the formation and transport of high-spin complexes forming spin quadrupoles, are particular areas of expertise. Novel computational techniques permit accurate calculations with thousands of atoms, and in complex multi-functional perovskites. Correlated electrons also form the basis of the physical creation of qubits, and the coherence and dynamics of such qubits, and multiqubit systems, is being investigated.

Institute for Quantum Information, RWTH Aachen

D. P. DiVincenzo, group leaders B. M. Terhal, F. Hassler, and N. Schuch

The institute has a broad agenda of topics in the theory of quantum information. New principles for the implementation of quantum computation in noisy systems, particularly Fermionic many-body systems. This includes particularly the investigation of Majorana qubits realized in semiconductor nanowires. Protocols for fault tolerance in quantum computation are investigated. New applications of the theory of quantum entanglement for efficient classical simulations are developed. Detailed modeling of hardware for superconducting qubits and circuit-quantum electrodynamic structures is underway, in close collaboration with experiment.

Lehrstuhl für Festkörper- und Quantenchemie und Institut für Anorganische Chemie, RWTH Aachen

R. Dronskowski

The institute is specialized in the fields of synthetic and quantum-theoretical solid-state chemistry, bordering with materials science, solid-state and theoretical physics, crystallography, as well as quantum and computational chemistry. In detail, we synthesize novel, sometimes extremely sensitive, compounds and elucidate their compositions and crystal structures by means of X-ray and neutron diffractive techniques. The characterization of their physical properties, that is electronic transport and magnetism, also plays a very important role.

We regularly perform solid-state quantum-chemical calculations from first principles to yield the electronic (band) structures and, in particular, to extract the important chemical bonding information needed to thoroughly understand the interplay between chemistry and physics. Syntheses are theory-driven and experiments challenge theories.

Peter Grünberg Institut – Mikrostrukturforschung, Forschungszentrum Jülich & Ernst Ruska-Centrum für Mikroskopie und Spektroskopie mit Elektronen

R. Dunin-Borkowski

The institute works on topical fields in solid-state physics. Strategically two directions are followed. Firstly, to make key contributions to the development and application of ultra-high resolution transmission electron microscopy, in particular to aberration-corrected electron optics for subangstrom structural and spectroscopic resolution. Secondly, to produce a number of selected material systems and to study their physical properties. Examples are high-temperature superconductors and the novel complex metallic alloys. The former provide the basis of our work on SQUID sensors and on ac-Josephson effect based Hilbert spectroscopy for the THz range. The head of the institute is co-director of the Ernst Ruska-Centre for Microscopy and Spectroscopy with Electrons.

Institute of Neuroscience and Medicine - Computational and Systems Neuroscience & Institute for Advanced Simulations - Theoretical Neuroscience, Forschungszentrum Jülich

S. Grün together with M. Diesmann and A. Morrison

Progress in the understanding of complex systems like the brain can only be achieved by integrating models on many different scales. The institute for Computational and Systems Neuroscience analyses massively-parallel electrophysiological data in their relation to behavior, maintains a network of experimental partner laboratories, and develops corresponding statistical tools. On this basis the INM-6 develops multi-scale models of the brain, combining data-driven development of brain theory with the bottom-up approach of directly simulated structured networks, and the top down approach, mapping functional models of higher brain function to spiking dynamics. Substantial resources are devoted to the development of the required simulation technology. Close collaborations with partner laboratories in neuromorphic computing ensure that novel algorithms rapidly enter those devices and neurobiologically realistic benchmarks are evaluated.

Peter Grünberg Institut – Halbleiter-Nanoelektronik, Forschungszentrum Jülich

D. Grützmacher

The institute's research activities are based on its competence in semiconductor heterostructure and nanostructure research, both in fundamental and device physics as well as in material and process development. They address three major fields. (1) Si-CMOS technology: novel materials and new device concepts are used to drive CMOS to its limits. (2) III-V and III-nitride semiconductors: high frequency devices are developed up to and into the terahertz range. (3) Nanostructures for quantum electronics: devices based on the tunneling effect and ferromagnetic/semiconductor hybrid structures are investigated, the latter particularly in view of spintronic applications.

Institut für Theoretische Festkörperphysik, RWTH Aachen

C. Honerkamp, R. Mazzarello, M. Schmidt, S. Wessel

The research groups in this institute study many-particle interactions in solids, ranging from quantum effects in magnetic systems over electron correlation effects leading to unconventional superconductivity and magnetism to the dynamics of structural phase transitions. Recent work has focused on interaction effects in graphene systems, topological insulators, pnictide high-temperature superconductors and chalcogenide phase-change materials. The powerful theoretical methods employed and developed here comprise quantum Monte Carlo techniques, the functional renormalization group, density-functional theory and molecular dynamics.

Lehr- und Forschungsgebiet Experimentalphysik des Extrem-Ultravioletts, RWTH Aachen

L. Juschkin

The research in the field of extreme ultraviolet (EUV) radiation is a major contribution for nanoelectronics and future developments in information technology. At the Chair for Experimental Physics of EUV different aspects related to the EUV radiation are investigated ranging from generation and characterization of EUV, to wave propagation and light-matter interaction as well as developing new methods and applications. In combination of EUV interference lithography and the self-organized growth of nanostructures novel materials are prepared, and their properties are analyzed. Moreover, in cooperation with the Fraunhofer Institute for Laser Technology in Aachen different concepts of EUV sources are investigated. On the application side, a series of measurement procedures for which the specific features of EUV radiation can be used, for example, the EUV microscopy and spectroscopic reflectometry, are investigated.

II. Physikalisches Institut (IIB) – Röntgenstreuung und Phasenumwandlungen, RWTH Aachen

U. Klemradt

Our research is centered at the investigation of nanoscale structures and fluctuations, with focus on nanoparticles, polymer-based nanocomposites and ferroic materials. Of particular interest are phase transitions in smart materials like shape memory alloys. The main experimental tools are X-ray scattering and acoustic emission spectroscopy. We use both laboratory tubes and synchrotron facilities for X-ray

experiments and operate a 6-circle diffractometer at HASYLAB (DESY, Hamburg), which is especially suited to the analysis of thin films. Core techniques are small angle X-ray scattering (SAXS), grazing incidence scattering (GISAXS and reflectometry), and photon correlation spectroscopy using coherent X-rays (XPCS).

Institut für Halbleitertechnik, RWTH Aachen

J. Knoch

The institute carries out research on semiconductor technology and device with a special focus on low power and energy harvesting technologies with the long-term vision of energy autonomous systems. To be specific, we work on nanoelectronics transistor devices based on Si- and III-V nanowires as well as on carbon nanotubes and graphene particularly aiming at a realization of so-called steep slope switches that enable a significant reduction of the power consumption of highly integrated circuits. In addition, the institute has broad experience in the science and engineering of Si wafer-based solar cells and also performs research on Si-based third generation photovoltaic cells. A combination of our know-how in micro- and nanotechnology with the solar cell technology is used to investigate and realize novel concepts for energy harvesting and storage based e.g. on efficient direct solar water splitting.

Institut für Anorganische Chemie – Molekularer Magnetismus, RWTH Aachen & Peter Grünberg Institut – Elektronische Eigenschaften (Molekularer Magnetismus), Forschungszentrum Jülich

P. Kögerler

The Molecular Magnetism Group focuses on the chemistry and fundamental physics of discrete and networked magnetically functionalized inorganic molecules. Based on its experience with the control and understanding of magnetic characteristics of purely molecular origin, the group synthesizes magnetic materials based on transition metal clusters that exhibit a complex interplay of charge transport and static/dynamic magnetic properties such as phase transitions, hysteresis, or quantum tunneling. To functionally combine magnetic state switching and charge transport in systems for FIT spintronic devices, the molecule-surface interface is addressed, in particular employing surface structure-directed coupling reactions to molecular aggregates, single-stranded molecular conductors, or 2D networks.

Lehrstuhl für Technologie Optischer Systeme, RWTH Aachen (RWTH-TOS) & Fraunhofer-Institut für Lasertechnik, Aachen

P. Loosen

Extreme ultraviolet radiation (XUV, 1-50 nm, or EUV at 13.5 nm) enables new optical, analytical and manufacturing technologies because of its characteristic interaction with matter, its short wavelength and recent progress on light sources and optical components (e.g. EUV lithography). XUV tools are already deployed by the semiconductor industry, which significantly pushes the further development of XUV technology. Future applications which will support scientific progress in a variety of fields such as nanoelectronics or biotechnology are also within the scope of our research. Activities include structuring on a nanometer scale using interference lithography, XUV microscopy for imaging of dynamic processes or at-wavelength inspection of multilayer mask-blanks for hidden defects, and characterization of thin film coated surfaces using grazing-incidence reflectometry.

Institut für Physikalische Chemie (IPC), RWTH Aachen

M. Martin

The institute's research activities are based on its competence in the physical chemistry of solids with a special emphasis on defects and diffusion in inorganic solids, in particular oxides. Within JARA-FIT two major fields are addressed. (1) Ionic transport: transport of oxygen ions in the bulk, across and along grain boundaries and in space charge zones is investigated by means of secondary ion mass spectrometry (SIMS). (2) Electronic transport: amorphous and highly non-stoichiometric oxides are investigated concerning correlations between structure, electrical conductivity, and electronic structure. Insulator-metal transitions are studied with a view to applications in data storage.

GFE – Gemeinschaftslabor für Elektronenmikroskopie & Ernst Ruska-Centrum für Mikroskopie und Spektroskopie mit Elektronen

J. Mayer

GFE is a central facility of RWTH Aachen University and has state-of-the-art equipment in the fields of transmission electron microscopy, scanning electron microscopy, electron microprobe analysis, focused ion beam instruments and atomic force microscopy. GFE provides services for a large number of institutes from RWTH Aachen University and a broad range of industrial companies. In the field of information technology, GFE participates in research projects on nonvolatile memories and on nanoscale CMOS devices. The head of the GFE is co-director of the Ernst Ruska-Centre for Microscopy and Spectroscopy with Electrons and coordinates the RWTH user activities and contribution to the Centre.

Institut für Theorie der Statistischen Physik, RWTH Aachen

V. Meden, H. Schoeller, J. Splettstösser, M. Wegewijs

The members of the institute are investigating the spectral and transport properties of low-dimensional quantum systems in contact with heat and particle reservoirs. The research focuses on the development of many-body methods for strongly correlated mesoscopic systems in nonequilibrium (quantum field theory and renormalization group in nonequilibrium) as well as on the application to experimentally realizable physical systems like semiconductor quantum dots, quantum wires (e.g. carbon nanotubes), and molecular systems.

Lehrstuhl I für Mathematik, RWTH Aachen

Ch. Melcher

The research at our institute has a focus on nonlinear partial differential equations from mathematical physics and materials science. We are particularly interested in the emergence and dynamics of patterns and topological solitons in models from micromagnetics and Ginzburg-Landau theory. Using tools from functional and multiscale analysis, our aim is to capture the qualitative behavior of solutions to such complex theories and, if possible, to identify simpler models, whose behavior is easier to understand or simulate.

Institute of Materials in Electrical Engineering I, RWTH Aachen

W. Mokwa

The institute's research activities are focused on the development of micro systems for medical and life science applications. Main activities lie on coupling of biological systems to technical systems, development of "intelligent" implants and prostheses and micro fluidic systems for biotechnology and medical diagnostics. For the development of these systems silicon and thin film technologies, silicon micromechanics, micro electroplating, soft lithography as well as sophisticated packaging technologies are used in a clean room of about 600 m².

II. Physikalisches Institut (IIB) – Rastersondenmethoden, RWTH Aachen

M. Morgenstern

The research group develops scanning probe methods working in particular at low temperatures down to 0.3 K and in high magnetic fields up to 14 T in order to investigate the electronic structure of interacting electron systems and systems relevant for nanoelectronic applications. Thereby, we exploit the advantage of mapping the electronic structure down to the atomic scale at an energy resolution down to 0.1 meV, but also use the scanning probes for the excitation of the systems under study. Current topics of interest are graphene flakes and monolayers, quantum Hall physics in III-V-materials, confined wave functions in quantum dots, artificial spin chains, nanomagnetic systems, and phase change materials.

Chair of Electrical Engineering and Computer Systems, RWTH Aachen

T. Noll

The research group is working on developing semiconductor-based architectural strategies for high-throughput digital signal processing, circuit concepts, and design methodologies, with a focus on energy-efficient circuits. The group wants to contribute to the development of highly-integrated, massively-parallel architectures based on nano-electronic device concepts. Emphasis is placed on the issue of reliability and fault-tolerant design.

Peter Grünberg Institut / Institute of Complex Systems – Bioelektronik, Forschungszentrum Jülich

A. Offenhäusser

Our research aims for the application of micro- and nanoelectronics to brain and life sciences. Research activities focus on two main topics: electromagnetic sensing and bioelectronic hybrid systems. This requires a better understanding of the interactions between biological systems and electronic substrates and the development of new technologies, resulting in new concepts of the interconnection of biological matter to electronic probes, and novel approaches to study cellular functions at the micro- and nanoscale. Here, we aim at a better understanding of the physiological behavior and mechanisms of neuronal information processing and new tools for diagnostics and imaging.

Institute of Crystallography, RWTH Aachen

G. Roth

The institute's research profile covers the topics synthesis, structure and properties of novel materials. The synthetic activities include the preparation of new or crystal-chemically modified compounds with interesting properties in bulk poly- or single-crystalline form. Crystal and magnetic structures are studied by powder and single crystal X-ray as well as neutron diffraction methods (outstation at FRM-II/Garching) with special emphasis on complex, defect dominated systems such as partially disordered, incommensurately modulated structures and composite crystals. Among the materials recently studied are superconductors (modulated CaAlSi), fullerenes (C70 high pressure polymer), spin-chain-compounds (vanadates and cuprates) and pyroxene-type multiferroics.

II. Physikalisches Institut (IIA), RWTH Aachen

C. Stampfer

Our research activities are focused on (i) carbon-based quantum electronics, (ii) semiconductor-based spin-electronics, and on (iii) topological insulators. For instance, we focus on studying electronic and mechanical properties of carbon and Bi₂Se₃-based systems that have critical dimensions on the nanometer scale. Such structures approach the atomic scale and the ultimate limit of solid state miniaturization. In particular we investigate systems based on nanostructured graphene (a monoatomic sheet of graphite) and carbon nanotubes. Current interests include (i) developing advanced processing technologies for fabricating novel nanodevices, (ii) understanding new and interesting transport phenomena that arise in these devices, and (iii) learning how to control and detect the charge, spin and mechanical degrees of freedom in these systems. Potential applications include ultra-fast electronics, new spin-based nanoelectronic device concepts and applied quantum technology.

Peter Grünberg Institut – Elektronische Eigenschaften, Forschungszentrum Jülich

C. M. Schneider

The institute is engaged in the study of electronic and magnetic phenomena in novel materials and is one of the birthplaces of magnetoelectronics. Present research concentrates on the fundamental aspects, properties, and control of spin-transfer processes. The activities cover several facets, e.g., the development of new magnetic materials or the engineering of interfaces to improve the spin injection efficiency. Further important research fields comprise nanomagnetism and nanospintronics, which may form a bridge to quantum information processing. To this end new techniques and procedures are being established. Spintronics is also firmly linked to the condensed matter program, providing access to and knowledge about new material classes for use in the spintronics activities of the present program.

Institut für Anorganische Chemie (IAC), RWTH Aachen

U. Simon

Our research is devoted to functional metal and metal oxide nanostructures. One focus is the wet chemical tailoring and the characterization of ligand stabilized metal nanoparticles of different geometries, i.e. nanospheres, nanorods and hollow nanospheres, as well as distinct nanoparticle assemblies. On the one hand these nanostructures are investigated with respect to applications as molecular probes, e.g. in photoacoustic imaging, or as actuators in biomedicine. On the other hand the utilization as fundamental building blocks in nanoelectronic devices is surveyed. Molecules exhibiting distinct functionalities, e.g. anisotropic conductance, or molecules allowing self-organization, e.g. DNA, leading to precisely

controllable nanoparticle superstructures are applied. Our characterization involves conventional techniques as IR, NMR, UV-vis, DLS as well as local probe measuring techniques, and investigations on the properties in biological environments.

A further topic deals with the wet chemical synthesis of metal oxide and higher chalcogenide nanostructures, which are applicable as sensor materials, new electrode materials for batteries or as resistive switching elements. In the latter context chemically-based bottom-up approaches for the fabrication of resistively switching nanostructures are explored and aim at the understanding of the switching and its structural consequences of the resistive switching process by using individual nanoparticles as model systems. Furthermore, self-assembly and surface patterning techniques are applied to produce long range order of nanoparticles on solid supports.

Peter Grünberg Institut – Funktionale Nanostrukturen an Oberflächen, Forschungszentrum Jülich

S. Tautz

Our research tackles fundamental issues in the quest towards functional nanostructures at surfaces, with a particular emphasis on nanoelectronics. Since our focus is placed on molecular materials, an important aspect of our work covers the structural investigations and spectroscopy of complex molecular adsorbates on metal, semiconductor and insulator surfaces. Based on these interface studies, the growth of thin films and nanostructures is investigated. Here, our work is directed towards hybrid materials, comprising both organic and inorganic components. Charge transport being the most important function in the context of nanoelectronics, transport experiments on single molecules and nanostructures round off our activities. It is a specific asset of our institute that we combine well-established surface techniques with the development of new experimental methods.

Lehr- und Forschungsgebiet GaN-Bauelementtechnologie, RWTH Aachen

A. Vescan

The research activities of the GaN Device group are focused on the area of group-III nitride device and technology development. The activities include investigation and development of practical technological building blocks for electronic devices, but also address fundamental device issues and limitations. Currently, particular interest is given to high-frequency and high-power device applications, where scaling issues as well as robustness aspects are being investigated. Novel gate dielectric materials are being pursued and their interface properties to GaN are being investigated. Also, alternative heterostructure device concepts are being developed, aimed at enhanced linearity in high-frequency devices as well improved switching behavior in the high-power regime.

Institut für Werkstoffe der Elektrotechnik 2, RWTH Aachen & Peter Grünberg Institut - Elektronische Materialien, Forschungszentrum Jülich

R. Waser

We focus on the physics and chemistry of electronic oxides and organic molecules, which are promising for potential memory, logic, and sensor functions. Our research aims at a fundamental understanding of nanoelectronic functions based on ferroelectricity, piezoelectricity, space charge effects, and electrochemical redox processes and at the elucidation of their potential for future device application. For this purpose, our institute provides a broad spectrum of facilities ranging from dedicated material synthesis, atomically controlled film deposition methods, molecular self-assembly routes, and integration technologies, to the characterization of processes, structures, and electronic properties with atomic resolution.

Integrated Photonics Laboratory, RWTH Aachen

J. Witzens

The realization of photonic components and systems in Silicon allows to realizing complex integrated optical systems at the chip scale. The integrated photonics laboratory is working on the development of Silicon Photonics devices and systems with activities ranging from core device development, system integration, as well as integration with analog circuitry.

I. Physikalisches Institut (IA), RWTH Aachen

M. Wuttig

The institute's research activities are focused on the development of novel materials for advanced optoelectronic applications. In particular, materials for optical and electronic data storage have been developed in the last few years. For this class of materials we developed design rules and an atomistic understanding of essential material properties. This work has enabled novel functionalities of phase change materials in applications as non-volatile memories. Organic materials are a second focus, where we work on routes to tailor material properties for optoelectronic applications ranging from displays, to solar cells and electronic devices.

Helmholtz Nano Facility

The Helmholtz Nanoelectronic Facility (HNF) at the Forschungszentrum Jülich forms the central technological platform for nanoelectronics with an emphasis on “green microchips/computing” in the Helmholtz Association. It comprises a network of facilities, processes and systems for research, production and characterization of nano and atomic structures for information technology with high strategic importance for the Key Technologies research field and JARA. The HNF facilitates broad access to these technologies for universities, research institutions, industry and the direct transfer of knowledge to society.



Facts and figures

Timetable: Sept. 2013 in operation

Processes for:

- Si/CMOS
- III/V
- Biohybrids
- Oxides, etc.
- Masks

Substrate Dimension:

0.5 mm x 0.5 mm up to 8" wafer

Equipment:

Cleaning

Wafer cleaner
Wet benches

Thin Film Manufacturing

Pfeiffer PLS 500
Pfeiffer PLS 570
Oerlikon SDS LLS EVO II
Centrotherm LPCVD E1200
Sentech PECVD
Oxford PECVD

Patterning:

Electron-Beam Writer Vistec EBPG 5000plus
Nanoimprinter Nanonex NX-2000
Spincoaters
Wetbenches
Oxford AMR System
2 Oxford Plasmalab 100 Cluster Tools
2 Oxford Plasmalab 100
Sentech PECVD
Oxford PECVD
TePla Gigabatch 300
AET Addax furnaces for Si/Ge or III/V
Steag 2800 RTP furnace
Tempress Oxidation Furnace (3 tubes)
Centrotherm Oxidation Furnaces
Süss Mask Aligners
FEI Helios FIB
Wet Benches

Implanter:

Axcelis Optima HDx
Axcelis 8250

Characterization

Dektak Profilometer
Ellipsometers
FEI SEM
Zeiss SEMs
SIS AFM
Automatic Resistivity Probe Veeco AP-150
Microscopes

See: www.hnf.fz-juelich.de

Selected Research Reports

Strained Si nanowire complementary tunnel field-effect transistors for low power inverter circuits

L. Knoll¹, Q. T. Zhao¹, A. Nichau¹, S. Trellenkamp¹, S. Richter¹, A. Schäfer¹, D. Esseni², L. Selmi², K. K. Bourdelle³, and S. Mantl

¹ Peter Grünberg Institut-9, Forschungszentrum Jülich, Germany

² University of Udine, Italy

³ SOITEC, France

Inverters based on uniaxially tensile strained Si nanowire (NW) tunneling field-effect transistors (TFETs) were fabricated. Tilted dopant ion implantation using the gate as a shadow mask allows self-aligned formation of p-i-n TFETs. Steep junctions formed by dopant segregation at low temperatures improve the band-to-band tunneling probability, resulting in high on-currents of n- and p-TFETs of $> 10 \mu\text{A}/\mu\text{m}$ at $V_{\text{DS}} = 0.5 \text{ V}$. The subthreshold slope for n-channel TFETs reaches a minimum value of $30 \text{ mV}/\text{dec}$, and is $< 60 \text{ mV}/\text{dec}$ over one order of magnitude of drain current. The first strained Si NW complementary TFET inverters show sharp transitions and fairly high static gain even at very low $V_{\text{DD}} = 0.2 \text{ V}$, demonstrating the great potential of TFETs for ultralow power electronics.

The switching behavior of metal-oxide-semiconductor field effect transistors (MOSFETs) is primarily determined by the injection mechanism of the carriers from source to the channel. The thermal emission based injection principally limits the inverse subthreshold slope (SS) to $60 \text{ mV}/\text{dec}$ at room temperature. Thus, the threshold voltage cannot be lowered without increasing the off-current (I_{off}) and the minimum drain voltage (V_{DD}) is limited. Band-to-band tunneling field-effect transistors (TFETs) are very attractive for ultralow power applications because of their potential for overcoming the $60 \text{ mV}/\text{dec}$ limit of the inverse subthreshold slope (SS) in conventional MOSFETs at 300 K [1]. For achieving high tunneling currents, new materials and novel device structures have to be implemented. Semiconductor materials with lower band-gap E_g , as well as high-k dielectrics, are needed. Tensile strained Si (sSi) which has a smaller E_g than Si improves the tunneling currents. Nanowire (NW) structures with multi-gates are preferred for TFETs since they provide improved electrostatics, and thus higher tunneling currents. Another critical technology step is the formation of optimized tunneling junctions in order to achieve a steep dopant profile. Implantation and rapid thermal annealing broadens the doped junctions and decreases the tunneling currents drastically. Due to these limitations, no complementary TFETs (C-TFETs) and hence no inverters have been

reported with Si technology. In this work we experimentally demonstrate a novel and simple method to make tunneling junctions by dopant segregation (DS) in sSi nanowire TFETs. With this technique we have fabricated C-TFETs with higher on-currents and better SS.

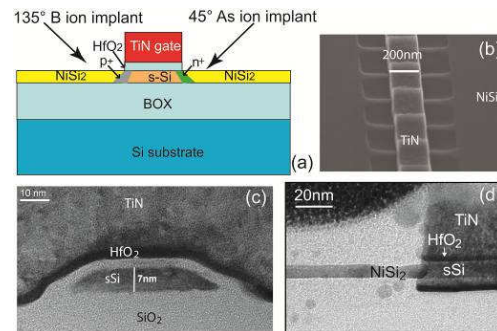


FIG. 1: (a) Schematic of sSi NW TFET fabricated using tilted B+ and As+ ion implantation into epitaxial NiSi₂ S/D contacts. Highly doped n+ and p+ pockets at the silicide edges are formed with IIS at low temperature. (b) SEM image of the NW array TFET; (c) XTEM image of single sSi nanowire with the gate stack. (d) XTEM cross section along the NW, indicating a perfectly aligned NiSi₂ contact to the channel.

Strained Si on insulator (sSOI) wafers with a biaxial strain of 0.8 % were used as substrate. After patterning the sSOI layer into NW arrays, the strain across the NW relaxes, while the strain along the NW remains. The elastic relaxation process yields to NWs with an uniaxial tensile strain along the wires. The gate stack consists of 3 nm HfO₂ layer and a 50 nm thick TiN metal gate. Epitaxial NiSi₂ contacts at source/drain (S/D) were formed by silicidation of a very thin Ni layer ($< 3 \text{ nm}$) on sSi at 700°C [2]. As a novel step, the S/D doped junctions were formed without additional implantation mask. The gate stack is used as a shadow mask for the tilted ($45^\circ/135^\circ$) As⁺ and B⁺ ion implants into the silicide (IIS), as illustrated in Fig.1(a). This allows the formation of perfectly self-aligned n⁺- and p⁺-pockets at the edges of NiSi₂ S/D after a low temperature annealing (450°C) by dopant segregation. The implantations were carried out at energies of 1 keV for B⁺ and at 5 keV for As⁺, both with a dose of $2 \times 10^{15} / \text{cm}^2$. Fig.1 (b) shows a scanning electron microscopy (SEM) image of a section of the final

sSi NW array TFET. The cross section transmission electron microscopy (XTEM) image of Fig.1 (c) reveals a trapezoidal shape of the sSi NW with a thickness of only 7 nm and a base width of 45 nm. An XTEM image (Fig.1 (d)) prepared by focused ion beam cutting along the NW demonstrates the uniformity and perfect gate alignment of the silicide without encroachment into the sSi channel after completed processing

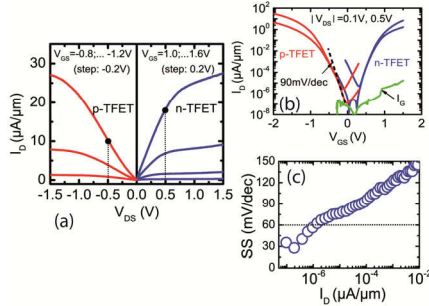


FIG. 2: (a) I_D - V_{DS} characteristics of NW array p- and n-TFETs showing high on-currents; (b) I_D - V_{GS} characteristics of sSi NW array C-TFETs, providing a minimum SS of 30 mV/dec for the n-FET. The ID-range SS < 60 mV/dec extends over one order of magnitude of I_D (c)

Fig.2(a) shows the output characteristics of the sSi NW C-TFETs. Comparatively, high on-currents of $I_{ON} = 10.3 \mu\text{A}/\mu\text{m}$ ($V_{GS} = -1.2$ V, $V_{DS} = -0.5$ V) for the p-TFET and $I_{ON} = 18.3 \mu\text{A}/\mu\text{m}$ ($V_{GS} = 1.6$ V, $V_{DS} = 0.5$ V) for the n-TFET were obtained, distinctly higher than for most reported Si TFETs. Obviously the great improvement stems from the IIS junctions. It is also remarkable to mention that the n-TFET shows a linear I-V on-set and good saturation at $V_{DS} > 0.5$ V, while S-shaped characteristics, as typical for TFETs with non-optimized junctions, were observed for the p-FET. Fig.2(b) shows the transfer curves of C-TFETs measured at 300K. As expected for homo-junction TFETs, ambipolar characteristics are observed. The n-TFET shows a much steeper SS than the p-TFET, reaching a minimum SS ~ 30 mV/dec with an SS < 60 mV/dec range over more than one order of magnitude of I_D , as displayed in Fig. 2(c). The gate leakage currents I_G for the NW n-TFET are much smaller than I_D as shown in Fig.2(b), demonstrating that the very small SS is not caused by the gate leakage current. The p-TFET shows only a minimum SS of 90 mV/dec with a slight kink in the I_D - V_{GS} characteristics, indicating trap assisted tunneling (TAT). The quality of the tunneling junction formed by IIS depends on the diffusion, activation and segregation of dopants, as well as defects remaining in the tunneling region. In the case of the As+ implanted junctions defects obviously remain after annealing at 450°C due to the heavy ion mass, leading to TAT with high tunneling currents but poorer SS. Obviously the B+ implanted tunneling junctions are of significant better quality. A comparison, with the InGaAs homo-junction TFETs reported by Intel reveals similar SS and I_{DS} at very low $V_{DS} = 0.3$ V for the NW n-TFET of this work [3]. Remarkably, the I_{ON}/I_{OFF} ratio of the strained Si NW TFETs is significantly larger, presumably due to the larger

band gap and the NW architecture. The applied C-TFET fabrication process and the improved performance for sSi NW n- and p-TFETs, allows the realization of inverters. The corresponding voltage transfer characteristics (VTC) of the first TFET inverter is shown in Fig.3 (a) at different V_{DD} . A sharp transition with wide noise margin was observed even at a V_{DD} as low as 0.2 V. However, the nominal output voltage V_{OUT} shows a degradation, indicated by $V_{OUT} < V_{DD}$ at small input voltage V_{IN} and $V_{OUT} > 0$ V at high V_{IN} . This degradation is caused by the ambipolar behavior of the C-TFETs, which will be addressed in more detail later. The corresponding inverter gains $\Delta V_{OUT}/\Delta V_{IN}$ at various V_{DD} are displayed in the inset of Fig.3(a). A high gain of 57 was obtained at $V_{DD} = 1.2$ V. Most remarkable, even at $V_{DD} = 0.2$ V a gain of ≈ 3 is still achieved, indicating the potential of TFETs for low power applications.

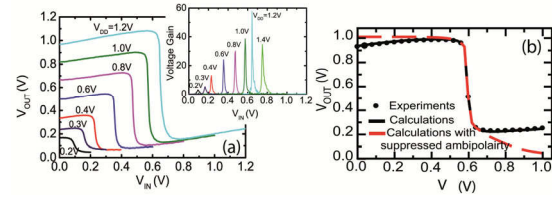


FIG. 3: VTC (a) and voltage gain (inset) for NW TFET inverters, functioning at $V_{DD} = 0.2$ V. (b) Experimental and calculated VTC for NW TFET at $V_{DD} = 1$ V. The calculation confirms that the nominal value of the high V_{OUT} recovers to $V_{DD} = 1$ V and the low V_{OUT} approaches to 0 V as the ambipolarities in both the n- and p-type transistors are removed.

We calculated the VTC of the inverter by adapting currents for both the n- and p-TFETs from the measured I_D - V_D data. Fig.3(b) shows, as expected, that the calculated VTC matches perfectly the measured VTC at $V_{DD} = 1.0$ V. The degradation of the high nominal output voltage ($V_{OUT} < V_{DD}$ at $V_{IN} < 0.5$ V) is found to be mainly due to the strong ambipolarity of the n-TFET, while the low nominal V_{OUT} which does not reach 0 V is caused by the ambipolarity of the p-TFET. To confirm the analysis, we calculated the VTC with suppressed ambipolarity of both, the n- and p-TFETs, by flattening the measured I_D - V_{GS} characteristics at the minimum I_D in the off-states. As can be seen the high nominal output voltage recovers to $V_{OUT} = V_{DD} = 1.0$ V, and $V_{OUT} = 0$ V at high V_{IN} . The slow decrease of V_{OUT} to 0 V in the calculated curve with suppressed ambipolarities is caused by the higher measured minimum currents of p-TFET at larger V_{DD} . Future TFET inverters can be significantly improved i.e. by reducing the ambipolarity with low dose drain implantation and improved n^+ -junctions. Replacing As by P ion implantation lowers implantation defects while maintaining high interface impurity concentrations at low T.

[1] A.M. Ionescu, H. Riel, Nature 479 (7373), 329-337, 2011.

[2] L. Knoll, Q.T. Zhao, S. Habicht, C. Urban, B. Ghyselen and S. Mantl, IEEE Electron Device Lett.31, 350-352, 2010.

[3] G. Dewey et al. IEDM Tech. Dig., 785-788, 2011.

Lattice Dynamics of Nanocrystalline Silicon for Thermoelectric Application: Effects of Impurities

T. Claudio Weber^{1,2} and R. P. Hermann^{1,2}

¹ Jülich Centre for Neutron Science-2 and Peter Grünberg Institut-4, Forschungszentrum Jülich, Germany

² Faculty of Science, University of Liège, Belgium

Silicon nanoparticles produced from the gas phase by microwave reaction have been compacted by current and pressure assisted sintering. The local atomic order in the obtained pellets has been investigated by pair distribution function analysis of high energy synchrotron radiation diffraction and their lattice dynamics was determined by means of ultrasound spectroscopy, heat capacity, and inelastic neutron scattering measurements [1]. Structural and chemical analysis reveals 10 to 15% of amorphous SiO₂ impurities located at the grain boundaries. The consequences of the nanostructuration and of the presence of these SiO₂ impurities are both a reduction in speed of sound and the existence of additional vibrational modes at low energy, i.e. a so called Boson peak. A large decrease in thermal conductivity is observed but also a significant decrease in the electronic transport properties. Overall the thermoelectric figure of merit is enhanced only by a factor of three compared to bulk silicon.

Silicon is potentially a very attractive material for thermoelectric energy recovery from waste heat, as it presents an excellent thermoelectric power factor when doped with boron or phosphorus. Silicon is an abundant and inexpensive element, environmentally friendly and not toxic, unlike many other thermoelectric materials that are lead or tellurium based. As it is passivated with a thin and stable oxide layer in air, bulk oxidation is avoided up to 1000 °C. However, silicon has a very large lattice thermal conductivity, which is a direct result of a very small unit cell and the stiff tetrahedral covalent bonds. This large thermal conductivity negates the excellent power factor and prevents the use of Si as a thermoelectric material. Thus, mechanisms that can lower the lattice thermal conductivity are highly sought after. One such mechanism is alloying with Ge, which results in excellent thermoelectric properties, but is a rather costly approach. Alternatively nanocomposite materials can be used in order to fulfill the guiding principle for good thermoelectric “phonon glass, electron crystal” [2]. A drastic reduction in lattice thermal conductivity can be achieved, but the prepared nanopowders present a large specific surface that implies an extreme sensitivity to oxidation and water uptake during processing.

Silicon nanoparticles were prepared from silane by collaborators at the University of Duisburg-Essen by a plasma-assisted gas phase process inside a microwave reactor [3]. By variation of the microwave power, the plasma gases, and the silane concentration, spherically shaped crystalline particles with 22 and 30 nm diameter were obtained. Addition of phosphine to the precursor gas yields n-type doping by phosphorus [4]. The compaction of the nanoparticles to dense pellets by current and pressure assisted sintering was carried with large heating and cooling rates of 100 °C/min and at 1050 °C with 3 min hold time. In this study, no special care was taken to prevent samples from contamination with oxygen, and our structural and lattice dynamics investigation was aimed at understanding the consequence of this bottom up nanostructuration on the lattice dynamics, including the effect of possible impurity phases.

Microstructural analysis of the pellets was carried out by electron microscopy, x-ray diffraction, and pair distribution function (PDF) analysis of high energy synchrotron radiation diffraction. Firstly, this analysis reveals that the nanostructures are mostly retained in the pellets with moderate coarsening to 30 and 40 nm grain size for the 22 and 30 nm precursors, respectively. Secondly, the SiO₂ impurities observed by electron microscopy, can be quantified to ~10 and 15 mass-% by modeling the pair distribution function. Note that direct analysis of the diffraction pattern does not reveal the amorphous SiO₂ impurities but that the short range correlation peaks are observed in the PDF pattern, see Fig. 1.

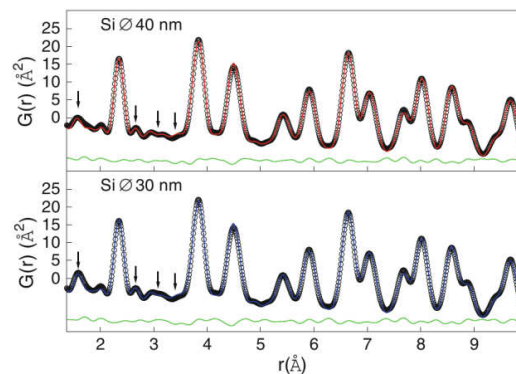


FIG. 1: PDF analysis. The large peaks and arrows indicate the inter atomic distances in Si and SiO₂, respectively [1]. (JCNS MUCAT 6IDD @ APS, Argonne).

In first approximation, the thermal conductivity of a material is expressed by the product of speed of sound, specific heat, and phonon mean free path. We have determined the speed of sound in the nanocomposite pellets by means of resonant ultrasound spectroscopy, which reveals a decrease by about 10% with respect to the bulk, a decrease that can be essentially attributed to a 20% softening in the shear modulus, which we attribute to the grain boundaries.

Further insight in the microscopic lattice dynamics has been obtained by inelastic neutron scattering, see Fig. 2. Overall, the density of phonon states (DPS) in the nanocomposites resembles that of the bulk polycrystalline material. Notable differences are observed at higher energies, above the ~ 65 meV phonon cutoff of Si, where essentially rocking modes of H at Si dangling bonds, at ~ 80 meV, and H-Si-H bending modes, at ~ 110 meV, are observed. We can thus infer that upon processing water uptake has taken place and that this water was partly decomposed. The excess modes at ~ 30 meV are attributed to amorphous SiO_2 . Below 20 meV, an excess contribution, mostly visible in the reduced DPS, see inset to Fig. 2, is observed, a contribution that can be attributed to the Boson peak in amorphous SiO_2 , e.g. an excess of vibrational modes typical for glasses with soft transversal phonon branches. The inelastic neutron scattering data thus also unambiguously reveal the presence of amorphous SiO_2 impurities in the nanocomposites.

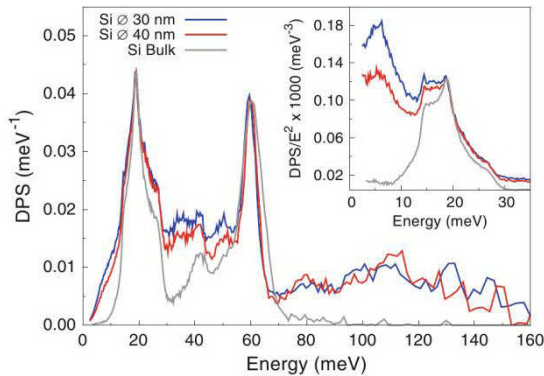


FIG. 2: Density of phonon states of Si nanocomposites and bulk material. Inset: reduced density of states, $g(E)/E^2$ [1]. (IN6 @ ILL, Grenoble)

Measurements of the specific heat of the pellets provides further insights in the composition and lattice dynamics. Below 1 K, the specific heat is linear, which is seen as a proportionality to T^{-2} in the log-log C_p/T^3 representation, see Fig. 3. This linear contribution indicates that in this degenerate semiconductor heavily doped with 1 atom-%, phosphorus, charge carriers do not freeze out even at the lowest temperatures. As compared to bulk Si, a specific heat excess correlated with the excess vibrational modes from inelastic neutron scattering is observed between 1 and 40 K. By using a simple linear combination model of the Si and amorphous SiO_2 specific heat, a quantitative analysis can be carried out, which reveals ~ 11 and ~ 19 mass-% of SiO_2 in agreement with the PDF.

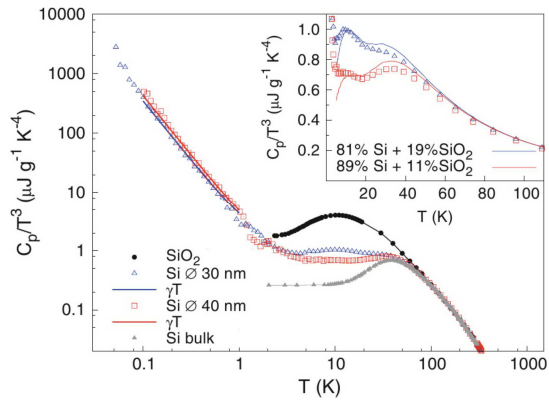


FIG. 3: Heat capacity of nanocomposite Si compared with SiO_2 and bulk Si. The linear, γT , electronic contribution is observed below 1 K. Inset: linear combination model of the specific heat with Si + SiO_2 [1].

At room temperature, the thermal conductivity measured for the 30 and 40 nm grain size pellets is ~ 15 and 25 W/m/K, i.e. substantially lower than 65 W/m/K for heavily doped polycrystalline Si. This reduction can be partly attributed to the reduced speed of sound, but must mostly be related to a reduction in the phonon mean free path. Overall, the materials studied herein are however not suitable for thermoelectric application, as the presence of the observed SiO_2 impurities also hampers the electronic transport properties and reduce the thermoelectric figure of merit. In a follow up study soon to be reported, it was shown that inert conditions during the processing stage can circumvent this problem and yield excellent properties.

We are grateful to the co-authors of the principal publication [1] for the shared work and interesting collaboration. We acknowledge the Institute Laue-Langevin (ILL, Grenoble, France) and the Advanced Photon Source (APS) at Argonne National Laboratory for provision of neutron and synchrotron radiation beam time at IN-6 and 6-ID-D, respectively. The DFG Priority Program SPP-1386 "Nanostrukturierte Thermoelektrika" and the Helmholtz Gemeinschaft Deutscher Forschungszentren young investigator group grant "Lattice dynamics in emerging functional materials" VH NG-407 are gratefully acknowledged.

- [1] T. Claudio, G. Schierning, R. Theissmann, H. Wiggers, H. Schober, M. Marek Koza, and R. P. Hermann, Effects of impurities on the lattice dynamics of nanocrystalline silicon for thermoelectric application, *J. Mater. Sci.* 48, 2836–2845 (2013). Article selected as April finalist for the 2013 Cahn Prize.
- [2] S. Bux, R. Blair, P. Gogna, H. Lee, G. Chen, M. Dresselhaus, R. Kaner, J.-P. Fleurial, *Adv. Funct. Mater.* 19, 2445 (2009).
- [3] J. Knipping, H. Wiggers, B. Rellinghaus, P. Roth, D. Konjhozic, C. Meier, *J. Nanosci. Nanotechnol.* 4, 1039 (2004).
- [4] A. Stegner, R. Pereira, K. Klein, H. Wiggers, M. Brandt, M. Stutzmann, *Physica B* 401–402, 541 (2007).

Electronically non-alloyed state of a statistical single atomic layer semiconductor alloy

Ph. Ebert¹, S. Landrock¹, Y. Jiang¹, K.H. Wu³, E.G. Wang², and R. E. Dunin-Borkowski¹

¹ Peter Grünberg Institut-5, Forschungszentrum Jülich, Germany

² International Center for Quantum Materials, Peking University, Beijing 100871, China

³ Institute of Physics, Chinese Academy of Sciences, Beijing 100080, China

Using atomically and momentum resolved scanning tunneling microscopy and spectroscopy we demonstrate that a two-dimensional (2D) $\sqrt{3}\times\sqrt{3}$ semiconducting Ga-Si single atomic alloy layer exhibits an electronic structure with atomic localization and which is different at Si and Ga sites. No indication of a formation of a new alloy band structure is present, as if no alloying happened.

Alloying semiconductor compounds attracted wide attention, since the materials properties of the resulting semiconductor alloy can be continuously tuned by varying the composition. Hence one can engineer semiconductor materials with, e.g., intentionally designed band gaps, lattice constants, and/or optical properties. This approach has a large technical and economical interest, as it is the basis for defining the wavelength of most optoelectronic devices. For such applications it is crucial that the newly formed semiconductor alloy has spatially homogeneous properties, i.e., the original properties of the individual alloyed compounds merge into the desired new properties. This is generally assumed to be the case for most three-dimensional compound semiconductor alloys [1].

With the ever shrinking dimensions of semiconductor devices, the alloy layers are becoming increasingly thinner. Ultimately only monolayer thin alloy layers may be needed and then the concept of a homogenous alloy band structure, different from that of its alloyed compounds, needs to be reassessed. The sparse experiments suggest that the electronic structure of a single monolayer semiconductor alloy can be tailored by just mixing different atoms [2], whereas calculations yield a decoupling of the electronic states of the different atoms [3]. However, atom selective measurements are lacking thus far. Hence, the central question is if a 2D semiconducting alloy would always exhibit a merged new band structure in analogy to three-dimensional semiconductor alloys, or if locally the different band structures of the constituent semiconductor compounds of the alloy persist.

We present a 2D single atomic layer Ga-Si $\sqrt{3}\times\sqrt{3}$ semiconductor alloy on Si(111) substrates as model system. Using atomically and momentum resolved STM and STS, we demonstrate that the electronic structure is atomically localized and different at Si and Ga atoms. No intermixing and

formation of new alloy related electronic properties are observed, as if no alloying happened. This unmixed state is discussed in terms of the particular bonding structure of the two-dimensional alloy layer [4].

Figure 1a-f shows a series of atomically-resolved STM images acquired at different bias voltages of a $\sqrt{3}\times\sqrt{3}$ Ga_{0.8}Si_{0.2} single alloy layer on a Si(111) substrate. Fig. 1g shows the atomic structure. Each maximum corresponds to one Ga or Si adatom forming the single atomic alloy layer. The maxima with a brighter contrast in Fig. 1a-d (red circles), arise from Si atoms.

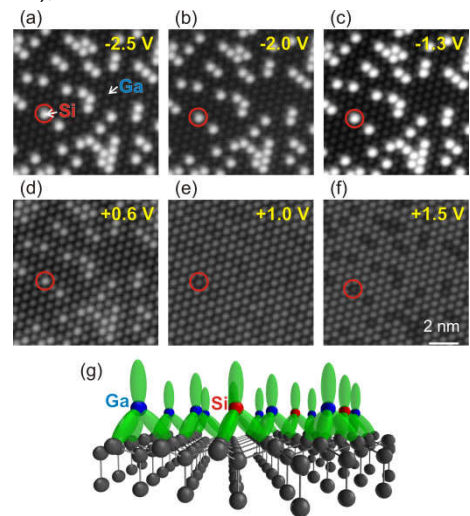


FIG. 1: (a)-(f) High-resolution STM images of a $\sqrt{3}\times\sqrt{3}$ Ga-Si alloy layer on Si (111) obtained at different voltages. Si atoms exhibit pronounced contrast changes with voltage (example marked by red circles). (g) Schematic of the single atomic layer alloy structure with the dangling and back bond states indicated by green ellipsoids. The substrate atoms are shown in grey.

Figure 2 shows the local differential conductivity dI/dV measured above different atoms as indicated in the inset. The black spectrum measured above Ga atoms furthest away from Si atoms (Ga_{N2}) exhibits a band gap of ≈ 1.2 eV. At Si atoms two highly localized orbital states appear at -0.9 and $+0.45$ V (δ_1 and δ_2), which decay almost completely within one lattice constants. These states correspond to the three back-bond states towards the Si substrate and the p_z -dangling bond above the Si atom (see Fig. 1g), respectively.

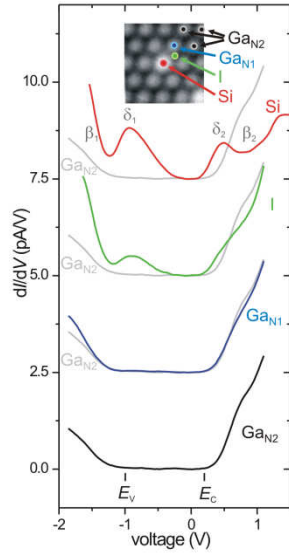


FIG. 2: Local differential conductivity dI/dV measured directly above Si atoms and above different spots with increasing lateral distance from the Si atom (I, GaN1, GaN2, indicated in the inset). The black spectrum measured above Ga atoms furthest away from the Si atom (GaN2) exhibits a band gap of 1.2 eV between the valence (EV) and conduction band edges (EC). With decreasing distance, two localized states appear (δ_1 , δ_2), which decay almost within one lattice constant from a Si atom.

The dI/dV spectra above different atoms are not directly comparable since the Si adatoms stick out of the Ga plane [4]. This changes the tip-sample separation z . Hence, we turn to the decay into the vacuum of $dI/dV \sim e^{-2\kappa z}$ with $\kappa = 2(2m_0 E_B / \hbar^2 + |k_{\parallel}|^2)^{0.5}$, E_B tunnel barrier, and k_{\parallel} parallel wave vector of the tunneling electrons [5]. The red and blue symbols in Fig. 4a represent the inverse decay length κ measured at Si and Ga sites, respectively. The black dashed curve is κ calculated assuming tunneling at the Γ point only ($k_{\parallel} = 0$). The values of κ at Ga atoms are close to the calculated dashed line above +1 V, around -1.2 V, and -2 V. Thus, at these energies the tunneling electrons have no momentum and originate from or tunnel into states at the Γ point. At other energies the larger κ values indicate tunneling with non-zero k_{\parallel} . The changes of κ agree well with the $\sqrt{3} \times \sqrt{3}$ Ga and projected Si(111) band structures (Fig. 4b and c), respectively. At negative voltages, the first states from which electrons can tunnel into the tip, are at E_V of the Si substrate at -1 eV. These states are at the Γ point, which is reflected by the small measured κ . At -1.3 V electrons tunnel from the valence band states of the $\sqrt{3} \times \sqrt{3}$ Ga layer at the edge of the Brillouin zone, resulting in large κ values. With increasing negative voltage κ and k_{\parallel} decrease again in agreement with the valence band dispersion of the $\sqrt{3} \times \sqrt{3}$ Ga layer (Fig. 4b). At positive voltages, an analogous behavior occurs.

The inverse decay lengths measured above $\sqrt{3} \times \sqrt{3}$ Si and Ga atom sites exhibit striking similarities. The overall shapes (peaks, decays etc.) are essentially the same. The main difference is the shift of the Si curve into the band gap. The similarity indicates a similar, but atomically localized, dispersion relation at Si and Ga sites.

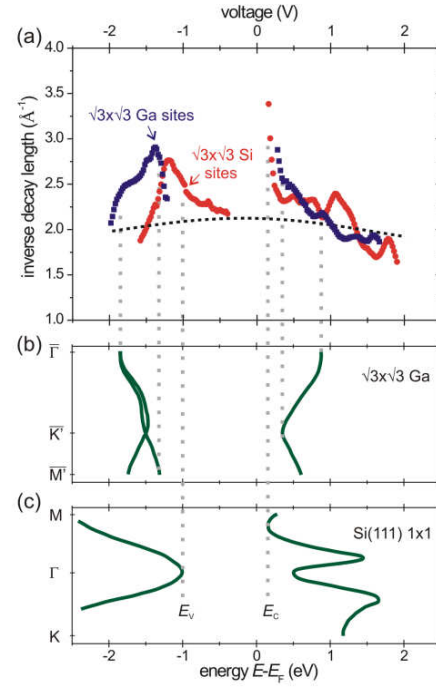


FIG. 3: (a) Inverse decay lengths κ as a function of the voltage [4]. Red and blue symbols show the values measured above Si and Ga atoms, respectively. Note the shift of the red data points towards the band gap from both sides. The black dashed curve shows the calculated inverse decay length assuming tunneling at the Γ point ($k_{\parallel} = 0$). (b) Band structure of a pure $\sqrt{3} \times \sqrt{3}$ Ga overlayer on Si(111) [7]. (c) Projected Si(111) bulk band structure [8].

Atomically and momentum resolved STM and STS show that a 2D single atomic $\sqrt{3} \times \sqrt{3}$ Ga-Si semiconductor alloy layer has an atomic localization of the electronic structure, which is different at Si and Ga sites. No electronic intermixing and formation of new alloy-related electronic features is found. This is in sharp contrast to the thus far observed merging of the constituents' electronic properties into a new alloy band structure in 3D semiconductor alloys. The observed locality of the electronic structure can be explained by the particular bonding structure arising from the two-dimensionality. The Ga and Si adatoms are only bound to Si substrate atoms through 3 back bonds (Fig. 1g). No bonds exist within the $\sqrt{3} \times \sqrt{3}$ Ga-Si alloy layer. Without such intra-alloy layer bonds each alloy atom is an individual entity, whose electronic properties is governed by the bonding to the substrate. Hence, no alloy band structure develops.

- [1] L. Ivanova, et al., Phys. Rev. B 82, 161201 (2010).
- [2] C. D. Teodoro, et al., J. Phys.: Condens. Matter 16, 3507 (2004).
- [3] G. Profeta, et al., Phys. Rev. B 66, 081303 (2002).
- [4] Ph. Ebert, et al., Nano Letters 12, 5845 (2012).
- [5] J. Tersoff, D. R. Hamann, Phys. Rev. B 31, 805 (1985).
- [6] R. M. Feenstra, et al., Surf. Sci. 181, 295 (1987).
- [7] J. M. Nicholls, et al., Phys. Rev. B 35, 4137 (1987).
- [8] M. Schlüter, M. L. Cohen, Phys. Rev. B 17, 716 (1978).

Integrated Silicon Photonics for Optical Communications and Biosensing

J. Hauck, F. Merget, M. P. Nezhad, J. Richter, S. Romero-García, M. S. Sharif Azadeh, B. Shen, and J. Witzens

Lehr und Forschungsgebiet für Integrierte Photonik, RWTH Aachen University, Germany

Steady progress during half a century of development in silicon integrated circuits has resulted in fabrication techniques that allow the large scale fabrication of billions of transistors in a single chip and their miniaturization to deep submicron dimensions. The realization of photonic components and systems in silicon allows leveraging these extraordinary fabrication capabilities to realize complex integrated optical systems at the chip scale. High refractive index contrasts allow drastic miniaturization of optical devices and densely integrated systems; silicon technology results in low cost fabrication with the possibility to directly interface with electronics at the chip level. The primary application fields of Silicon Photonics are DataCom, i.e., the realization of low cost optical transceivers for High Performance Computing and Data Centers, Biosensing and Instrumentation. In this paper we report on two recent results of our lab: a silicon nitride based back-end photonic technology compatible with fluorescent sensing at visible wavelengths, that can be used to produce consumables for biosensing applications, as well as high performance silicon modulators for optical communications at near infrared wavelengths.

Silicon Nitride Back-End of Chip Technology for Biosensing Application: Silicon nitride (SiN) and silicon dioxide (SiO₂) are materials commonly used in the back-end of CMOS processes. This material system also satisfies the requirements for large-scale fabrication of integrated photonic biosensors. Its transparency in the visible domain is an important characteristic for several classes of biomolecular assays [1], such as fluorescence biosensors. The deposition of ultrathin layers of silicon nitride material enables the fabrication of waveguides that are especially attractive for evanescent field biosensors, where a large fraction of the guided light interacts with the top cladding: an aqueous solution with the substance to be sensed. We have addressed by design and experimental validation three important challenges of the technology [2-4]: First, we have experimentally demonstrated thin SiN waveguides (100 nm thick) that exhibit very low losses and allow tight bending for dense integration. We have measured propagation losses below 0.6 dB/cm and insertion losses below 0.05 dB per 90° bends with radii as small as 35 μm . These waveguides are the core of the biosensor and exhibit a good performance in an aqueous environment with

fluorescence dyes (fig. 1). Second, we have designed and fabricated multimode interference couplers (MMI) for the light distribution network inside the chip. These structures have shown very high performance in terms of coupling efficiency (higher than 95%), low imbalance between output ports (less than 10%) and good fabrication tolerances (fig. 1).

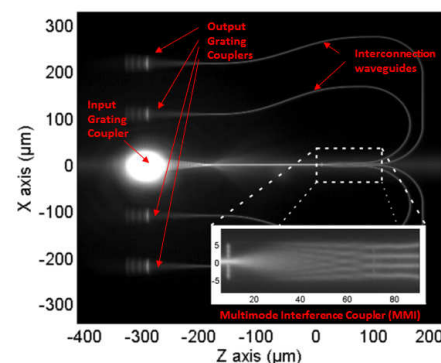


FIG. 1: Fluorescence image of an MMI splitter connected to an optical input port (center) and to 4 output ports. The inset shows the imaged interference pattern inside the MMI.

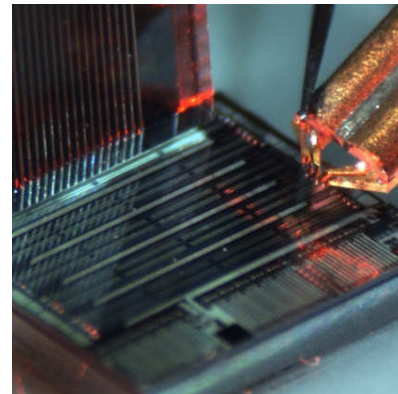


FIG. 2: Silicon Photonics chip with MZI modulators optically connected to a fiber array (left) and electrically connected to an RF probe tip (right).

Finally, we have developed laser to chip couplers, so-called grating couplers, that are compatible with spatial and angular alignment tolerance of free-space optics in instrument grade opto-mechanics. Grating couplers enable dense integration since light can be coupled anywhere onto the chip, as well as wafer testing since wafers do not need to be diced prior to testing (fig. 2).

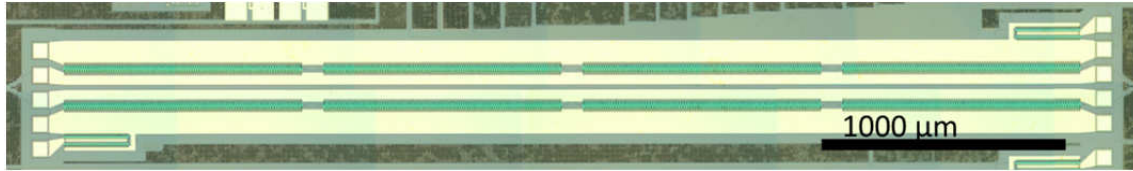


FIG. 3: Mach-Zehnder Modulator with advanced transmission-line design.

However, the fabrication of efficient and compact grating couplers in the SiN/SiO₂ material system represents a great challenge as compared to more mature silicon based devices, due to the reduced index contrast ($\Delta n = 0.5$) and the reduced thickness of the core layer required for evanescent sensing. We have been able to tailor the coupled beam profiles by means of a properly placed CMOS compatible metal reflector leveraging optical feedback (please refer to the references for details).

High-Speed, Low-Voltage Silicon Modulators:

The need for higher bandwidth, increased reach and lower power consumption in modern datacenters is an important driver for novel optical technologies. One of the key components of such optical interconnects is the electro-optical modulator. 25 Gb/s single channel data rates will be the industrial mainstream for the medium term. Particular emphasis in research & development has been placed in reducing power consumption and drive voltages. Direct interfacing of integrated optics with standard low voltage A/D and D/A converters is an important goal, both as a cost saving measure as well as to facilitate software defined optics and the resulting design flexibility. To date, modulators based on free-carrier dispersion in reverse biased pn-diodes have proven to be the most reliable devices in silicon based technology and have been recently commercialized. The modulation bandwidth and thus the achievable data rates of such modulators are limited by losses of the electrical transmission lines resulting from ohmic losses in the connected optical waveguides [5-6]. We have investigated two architectural improvements of the transmission line designs eliminating cross-talk between adjacent modulator arms and reducing ohmic losses, thus significantly increasing the modulation bandwidth [6]. A microscope image of the modulator is shown in fig. 3. The modulator is based on a 4 mm long Mach-Zehnder Interferometer (MZI) architecture. Here, the light at the input of the modulator is split into two arms. Both arms incorporate a high-speed phase shifter. At the output of the modulator the light from the two arms interferes in a second coupling element. If the phase difference between the two arms is 0 or π the light will respectively interfere constructively or destructively, resulting in the light being transmitted or extinguished at the output of the interferometer according to the data stream.

Figure 4 shows the electro-optical transmission characteristic as a function of RF frequency. The optical cutoff frequency of 22 GHz, i.e., the frequency at which the optical modulation

amplitude (OMA) is reduced by a factor two, is amply sufficient to generate a 25 Gb/s signal. The required drive signal of 4V can be further reduced by sacrificing some optical signal strength or by implementing a longer modulator at the expense of additional optical insertion losses.

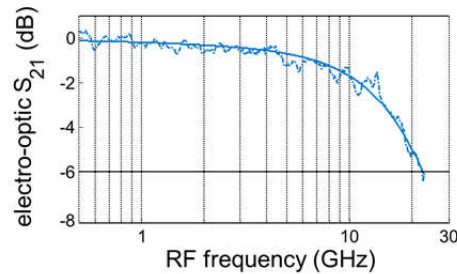


FIG. 4: Electro-optic transmission characteristic of our optical modulators.

Outlook: We are currently working on further reduction of drive voltage and optical losses of Silicon Photonics modulators as part of the BMBF funded SASER project. In the ERC project Frontiers of Integrated Silicon Nanophotonics in Telecommunications (FISNT) we are working on adding additional functionality, such as ultra-high quality factor resonators and parametric light generation, to monolithically integrated Silicon Photonics systems, as well as to develop optical interfaces enabling fully automatized, machine vision guided assembly of Silicon Photonics subsystems.

- [1] J. Witzens, M. Hochberg, "Optical detection of target molecule induced aggregation of nanoparticles by means of high-Q resonators", *Opt. Express* 19, 7034-7061 (2011).
- [2] S. Romero-García, F. Merget, F. C. Zhong, H. Finkelstein, J. Witzens, "Silicon nitride back-analog optics for biosensor applications" (invited), *proceedings of the SPIE* (2013).
- [3] S. Romero-García et al., "Visible wavelength silicon nitride focusing grating coupler with AlCu/TiN reflector," *Opt. Lett.* 38, 2521-2523 (2013).
- [4] S. Romero-García et al., "Silicon nitride CMOS-compatible platform for integrated photonics applications at visible wavelengths", *Opt. Express* 21, 14037-14046 (2013).
- [5] J. Witzens, T. Baehr-Jones, M. Hochberg, "Design of transmission line driven slot waveguide Mach-Zehnder interferometers and application to analog optical links", *Opt. Express* 18, 16902-16928 (2010).
- [6] F. Merget, M. S. Sharif Azadeh, B. Shen, M. P. Nezhad, J. Hauck, and J. Witzens, "Silicon Photonics Plasma-Modulators with Advanced Transmission Line Design", in review.

Synthesis of GeSn Semiconductors for Optoelectronic Applications

S. Wirths, A. T. Tiedemann, B. Holländer, P. Bernardy, T. Stoica, G. Mussler, D. Grützmacher, S. Mantl, and D. Buca

Peter Grünberg Institut-9, Forschungszentrum Jülich, Germany

Ge based compounds of high quality offer a significant potential for the development of near infrared photonics and lasers. In this regard, GeSn alloys attracted lot research interest since for Sn concentrations above 9at.% the transition from an indirect to direct band-gap semiconductor is predicted. Special precursors, like Ge_2H_6 and SnCl_4 exhibiting low growth activation energies, are essential for the epitaxial growth of GeSn crystals with 10 at.% Sn at temperatures as low as 375°C. Pseudomorphic GeSn layers were achieved by growing relaxed Ge buffer layers first in order to reduce the lattice mismatch compared to Si. All GeSn crystals exhibit high single crystal quality and ion channeling measurements indicate Sn substitutionality above 90%.

A complete photonic integrated circuit on Si relies on the development of appropriate direct band-gap group IV semiconductors. Recently, theory and experiments indicated that the indirect semiconductor Ge can be band-engineered to a direct-gap material either by applying sufficient tensile strain or by alloying with Sn [1]. It has been predicted that a direct band-gap can be achieved in unstrained $\text{Ge}_{0.91}\text{Sn}_{0.09}$ binaries or in biaxial strained Ge grown on $\text{Ge}_{0.9}\text{Sn}_{0.1}$ buffer layers [2]. For such high Sn concentrations the conduction band minimum shifts from the L valley to the Γ valley forming a direct band gap at the center of the Brillouin zone, i.e. the Γ -point. However, synthesizing GeSn alloys with reasonable high Sn concentrations and high crystal quality is very challenging mainly due to the very low solid solubility of Sn (<1%) in Ge and the large lattice mismatch of 15 % between α -Sn and Ge demanding non-equilibrium growth conditions.

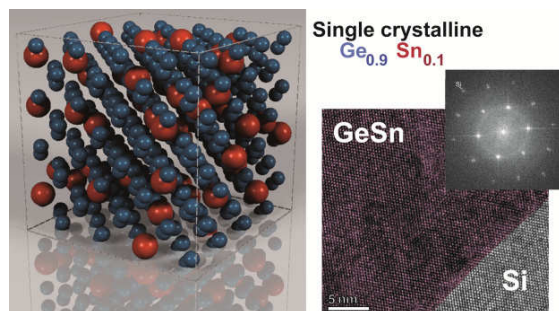


FIG. 1: (Left) sketch of a $\text{Ge}_{0.9}\text{Sn}_{0.1}$ crystal lattice. (Right) TEM micrograph of a 92 nm $\text{Ge}_{0.935}\text{Sn}_{0.065}$ layer grown on Si(100) and the corresponding FFT.

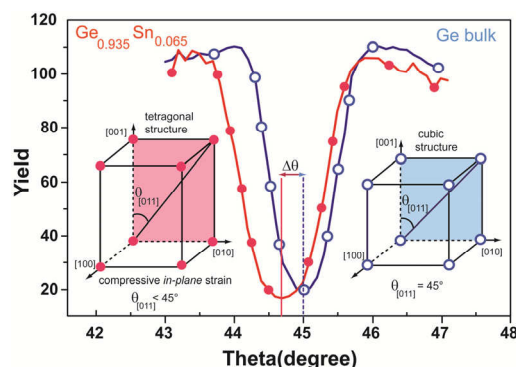


FIG. 2: Angular channeling scan through the [011] direction of a partially relaxed 90 nm $\text{Ge}_{0.935}\text{Sn}_{0.065}$ layer on Si(100) grown at 400°C and a bulk Ge crystal. The tetragonal and cubic crystals of GeSn and Ge, respectively are presented to indicate the ion scans directions and planes.

For our growth studies, we employed an industry compatible metal cold-wall Reduced Pressure AIXTRON TRICENT® reactor with a showerhead technology for 200 mm wafers. The Ge virtual substrates (VS) and GeSn layers were grown on Si(100) wafers. The thin Ge epitaxial layers were grown using Ge_2H_6 while SnCl_4 was added to the growth chamber for the GeSn epitaxy, which warrants reasonable growth rates at growth temperatures as low as 375°C [3].

All GeSn layers grown on Si(100) at 375°C and 400°C evidence a very homogeneous distribution of the Sn atoms with concentrations between 10.6 at.% and 6.5at.%, respectively measured by Rutherford Backscattering Spectrometry (RBS). Monocrystalline epitaxial growth with sharp interfaces is achieved as indicated in Fig. 1.

We performed ion channeling angular yield measurements of the Sn backscattering signal with a high-precision goniometer using 1.4 MeV He^+ ions at a scattering angle of 170°. For (001) samples, angular scans through the [001] sample normal and the [011] direction along the (100) plane were performed. Figure 2 shows the ion channeling angular yield scan of the Sn backscattering signal for a 92 nm $\text{Ge}_{0.935}\text{Sn}_{0.065}$ layer. The position of the minimum represents the absolute angle $\theta_{[011]}$ between the [001] sample normal and the inclined [011] direction. For cubic lattices like unstrained Si or fully relaxed GeSn, the angle between [001] and [011], for instance, has a value of 45°. Compressive tetragonal strains in GeSn/Si lead to smaller angles ($45^\circ - |\Delta\theta_{[011]}|$)

with $|\Delta\theta_{[011]}| < |\Delta\theta_{ps}|$ where $\Delta\theta_{ps}$ denotes the maximum angular shift realized by the pseudomorphic GeSn layer. The sign of the shift is

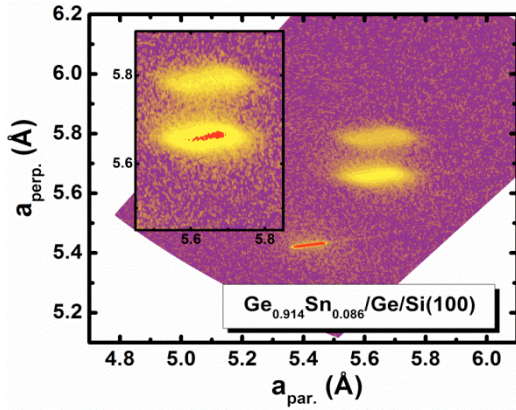


FIG. 3: XRD-RSM around the (224) reflection of a lattice-matched 50 nm $\text{Ge}_{0.914}\text{Sn}_{0.086}$ crystal grown on Ge VS. The inset presents the GeSn and Ge diffraction spots for a better comparison.

negative for compressive strained layers and positive for tensile strained crystals. For symmetric (isotropic) biaxial relaxation, the amount of tetragonal strain and the degree of relaxation are related to the angular shift as: $\varepsilon_T = -2 \cdot \Delta\theta_{[011]}$ and $R = 1 - \Delta\theta_{[110]}/\Delta\theta_{ps}$. The measured angular shift of $\Delta\theta_{[011]} = -0.26^\circ$ corresponds to a residual tetragonal strain of 0.97% in the GeSn layer compared to the strain of 9.4% expected for full pseudomorphic growth on a Si substrate. This amounts to a degree of relaxation of about 90%. We note at this point that the misfit between Si and GeSn layers is larger than for most other semiconductor systems. Relaxation values between 85% and 92% are obtained for all GeSn layers directly grown on Si.

As mentioned in the introduction, relaxed GeSn crystals are suitable to establish CMOS and photonic integration via tensile strained Ge. In order to allow optical gain, high crystalline quality of GeSn alloys is crucial. The use of a Ge virtual substrate reduces the lattice mismatch of GeSn with regard to Si which should substantially improve the GeSn crystal quality. Prior to GeSn growth, thin Ge virtual substrates with thicknesses of about 200 nm were deposited using Ge_2H_6 at 425°C growth temperature. Minimum channeling yield values of 9% obtained for all GeSn layers are identical to the minimum yield of the Ge virtual buffer, suggesting that the virtual substrate quality is limiting the GeSn crystal quality. The coherent growth is demonstrated for a $\text{Ge}_{0.914}\text{Sn}_{0.086}$ single crystalline layer on Ge VS by RSM presented in Fig. 3. The Ge VS is partially relaxed (97%) in this case and the GeSn crystal is pseudomorphically grown with the same in-plane lattice constant as the Ge VS, see inset of Fig. 3. The increase of the out-of-plane lattice constant with respect to unstrained GeSn is in agreement with the elasticity theory, assuming the same elastic constants of GeSn and Ge. The high crystal quality is proven by the TEM micrograph in Fig. 4 for 30 nm $\text{Ge}_{0.92}\text{Sn}_{0.08}$ layer.

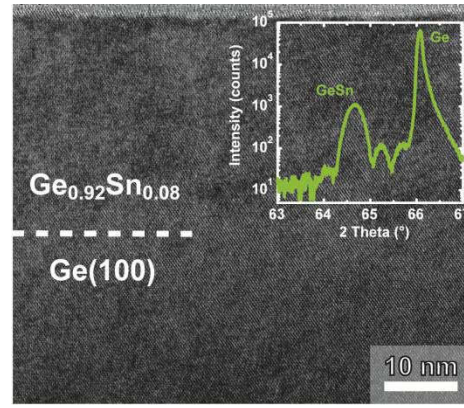


FIG. 4: TEM image of 30 nm $\text{Ge}_{0.92}\text{Sn}_{0.08}$ layer grown on Ge VS. The inset presents the corresponding XRD rocking curve. These measurements prove pseudomorphic GeSn growth.

Complementary XRD 2θ scans (inset in Fig 4) show thickness fringes around the GeSn peak which demonstrates pseudomorphical growth of high quality layers with sharp interfaces. XRD-RSM measurements exhibit identical in-plane lattice constants for the GeSn layers compared to the Ge VS accounting for fully strained layers.

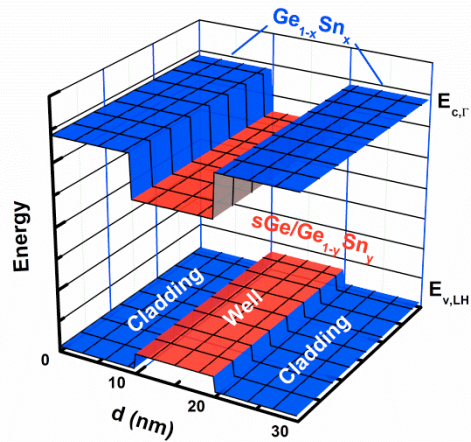


FIG. 5: Proposed band structure for a strained Ge and GeSn based LASER concept.

The ability to grow different GeSn/Ge heterostructures and the high quality of our GeSn layers enable the design and realization of GeSn based lasers as shown in Fig. 5 using the theoretically direct band-gap tensile strained GeSn as laser active medium and GeSn layers as integrated resonators.

- [1] P. Moontragoon, Z. Ikonić, P. Harrison, Semiconductor Science and Technology 22, 742–748 (2007).
- [2] S. Wirths, A.T. Tiedemann, Z. Ikonic, P. Harrison, B. Holländer, T. Stoica, G. Mussler, M. Myronov, D. Buca and S. Mantl, submitted for publication.
- [3] S. Wirths, D. Buca, G. Mussler, A.T. Tiedemann, B. Holländer, P. Bernardy, T. Stoica, D. Grützacher and S. Mantl, ECS Journal of Solid State Science and Technology, 2(5) N99-N102 (2013)

Growth and vertical integration of (Ga,In)N nanostructures for future single photon emitters

A. Winden, M. Mikulics, D. Grützmacher, and H. Hardtdegen

Peter Grünberg Institute-9, Forschungszentrum Jülich, Germany

Crucial technological steps are realized for future room temperature operation of III-nitride single photon sources (SPS). In this respect both the growth technology of positioned single InN nanopillars capped by Mg-doped GaN and the device concept technology for singularly addressable nanostructures is presented.

Light emitting diode structures with (GaIn)N based quantum dots as active material are expected to be extremely suitable for room temperature single photon emission in the telecommunication wavelength range, due to their appropriate band gap range and their large electronic band offsets in small nanostructures promoting quantization and strong carrier confinement. Secure and fast data transfer requires compact, electrically driven sources. They should exhibit efficient and narrowband emission, their integration into a circuit should allow for the controlled emission of single photons upon electrical excitation.

Up to now, neither material deposition technology nor circuitry fulfilled the requirements. Singular addressability and narrowband emission of the sources called for exact position and size control of low-density GaInN based quantum dots which the standard self-assembly fabrication method

could not meet [1]. The growth method of selective area metalorganic vapour phase epitaxy (SA-MOVPE) together with the integration of the SPS into a layout suitable for high frequency operation addresses the basic conditions for the envisaged application and will be dealt with in this report. A number of challenges were addressed. Among others, SA-MOVPE of the InN nanostructures with a large separation distance, optimal nanostructure size with respect to efficient narrowband emission and wavelength, a p-doped GaN cap on InN nanostructures and the provision of Ohmic contacts to the n- and p-doped GaN materials with sufficient contact transparency and without degradation of the structure's basic optical characteristics.

Initially, Si-doped GaN/sapphire templates were masked with 50 nm thick SiO₂ layer which was patterned with a hexagonal array of apertures exhibiting an inter-hole distance of 3 μ m and apertures down to 20 nm. Growth was carried out at 400 mbar using nitrogen (N₂) as the carrier gas, trimethylindium (TMIn) and triethylgallium (TEGa) as the group III sources, ammonia (NH₃) as the group V source and dicyclopentadienyl-magnesium (Cp₂Mg) as the p-dopant precursor. The optical properties were characterized by

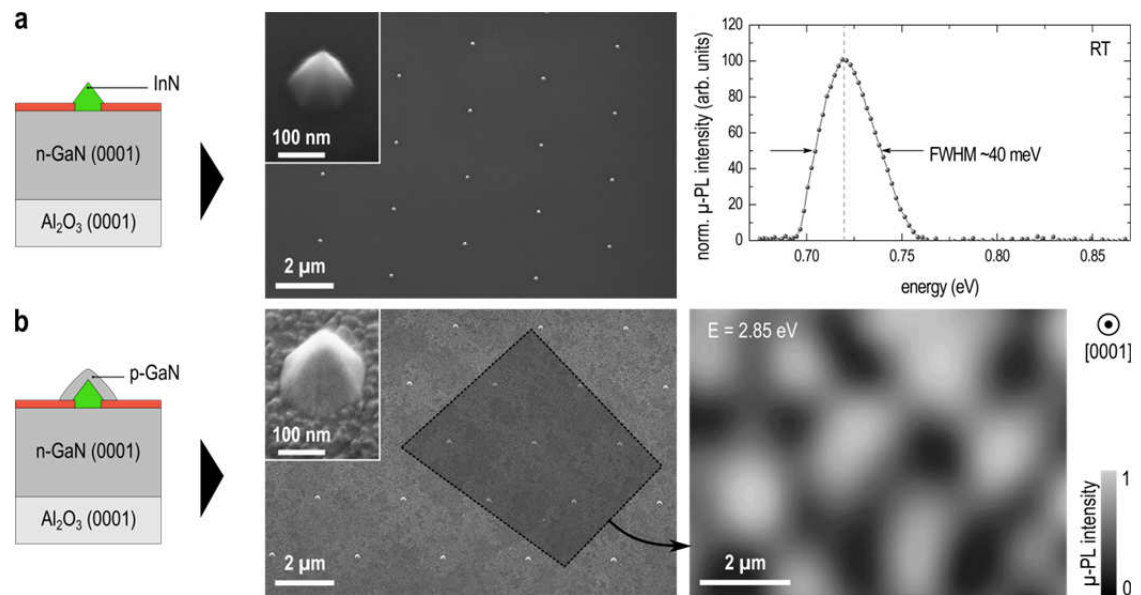


FIG. 1: (a) Selective area growth of InN nanopillars and μ -PL spectrum of single InN nanostructure emitting in the telecommunication wavelength. (b) InN nanopillars covered with p-GaN and μ -PL mapping at ~ 2.85 eV correlating to the DA transition of GaN:Mg.

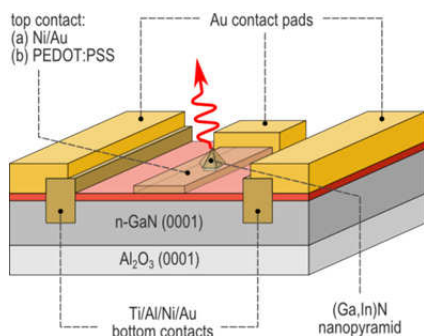


FIG. 2: Scheme of the integration technology of a single p-GaN/InN/n-GaN nanopyramid. After selective nanostructure growth recessed Ohmic bottom contacts were processed by various lithography, dry etching and annealing steps. A thin semi-transparent metallic film of Ni/Au and p-conductive polymer PEDOT:PSS, respectively, was used for the top contact.

micro-photoluminescence (μ -PL) studies at room temperature. Two different 10 nm thick top contact materials – Ni/Au and the intrinsically conductive polymer PEDOT:PSS – were employed. Their suitability as a top contact was studied by determining their resistance and their contact properties and using IV curve and DC dark current measurements, respectively. Additionally transmission/absorption experiments were carried out with both contacting layers (Ni/Au and PEDOT:PSS) at the 1550 nm wavelength to be used for future operation.

It was found that a narrow growth temperature window around 650°C and a group V/group III precursor molar flow ratio of 4.4×10^4 lead to the selective growth of pyramidal shaped InN nanostructures [2]. The emission energy of single nanopyrramids increases with the structure size and can be tuned to the desired emission wavelength by appropriately varying growth time and aperture size [2]. It was also observed that the full width at half maximum (FWHM) and the peak intensity of the emission diminishes as the nanopyramid's size is reduced. Narrow band edge emission is recorded at ~ 0.72 eV for the smallest fully developed nanopyrramids [cf. Fig. 1(a)].

A less stable gallium source was chosen for the deposition of GaN at the same temperature as for InN nanopyramid growth. This temperature is 350°C lower than for standard GaN growth and ensures that InN does not decompose. The approximately 10 nm thick p-doped GaN layer was grown without any interruption on the fully developed InN nanopyrramids [cf. Fig. 1(b)]. Micro-PL was recorded at the energy at which the donor acceptor pair emission band is to be expected for Mg as the acceptor. The studies reveal that its intensity follows the hexagonal pattern of the positioned nanostructures. Only these sites emit PL at this energy indicating successful p-doping of the GaN cap.

A schematic of the vertical integration technology of a single p-GaN/InN/n-GaN nanostructure is presented in Fig. 2. The dielectric growth mask serves as a natural isolation between top- and bottom contacts and insulates the individual SPSs.

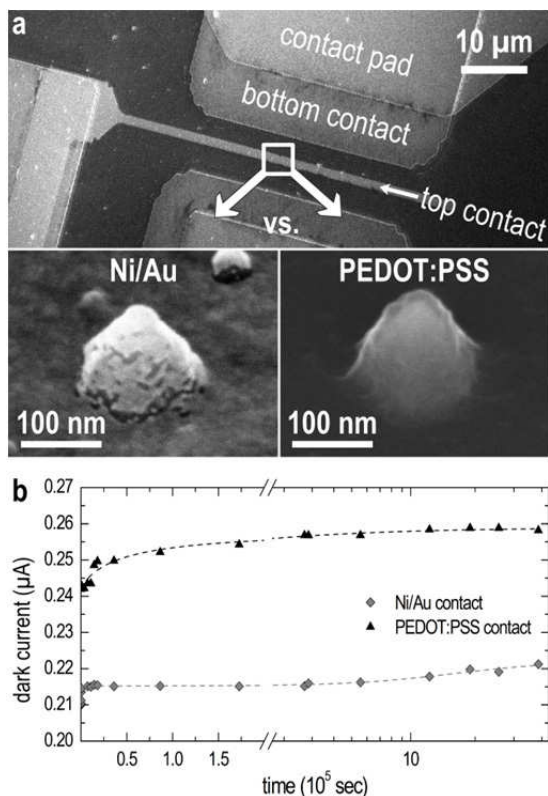


FIG. 3: (a) Integration of single p-GaN/InN nanopyrramids into a device layout tested for HF operation [3]. Here, the top contact materials, 10 nm Ni/Au and 10 nm PEDOT:PSS were compared. (b) Test of both contact materials by DC dark current measurements using quasi-operation mode under 5V bias voltage for 1000 hours. The lines are guides to the eye.

After device technology optimization, the contact resistance of the top contact was found to be as low as $6.9 \times 10^{-6} \text{ cm}^2$. A light transmittance of about 72% and 89% was measured at 1550 nm for the metallic and conductive polymer contacts, respectively. No evidence for degradation or current collapse for both materials was found using a quasi-operation mode under 5V reverse bias for 1000h [cf. Fig. 3]. Due to gentle processing, the optical properties did not deteriorate during the integration.

Our results demonstrate that all ingredients are now accessible towards room temperature operating, electrically driven InN based SPS emitting within the telecommunication wavelength range.

This work was financially supported by the German Ministry of Education and Research (BMBF) within the projects QPENS and EPHQUAM.

- [1] K. Sebold, J. Kalden, H. Lohmeyer, J. Gutowski, Phys. Status Solidi B 248, 1777 (2011).
- [2] A. Winden, M. Mikulics, T. Stoica, M. von der Ahe, G. Mussler, A. Haab, D. Grützmacher, J. Cryst. Growth 370, 336 (2013).
- [3] M. Mikulics, P. Kordoš, D. Gregušová, R. Adam, M. Kočan, S. Wu, J. Zhang, R. Sobolewski, D. Grützmacher, M. Marso, IEEE Photonics Technol. Lett. 23, 1189 (2011).

Bulk electronic structure of the dilute magnetic semiconductor $\text{Ga}_{1-x}\text{Mn}_x\text{As}$ through hard X-ray angle-resolved photoemission

L. Plucinski¹, J. Minar², A. X. Gray^{3,4}, S. Ueda⁵, P. R. Stone^{4,7}, Y. Yamashita⁵, J. Fujii⁸, J. Braun², G. Panaccione⁸, H. Ebert², O. D. Dubon^{4,7}, K. Kobayashi⁵, C. S. Fadley^{3,4}, and C. M. Schneider^{1,6}

¹ Peter Grünberg Institut-6, Forschungszentrum Jülich, Germany

² Department of Chemistry, Ludwig Maximilian University München, Germany

³ Department of Physics, University of California Davis, Davis, CA 95616, USA

⁴ Materials Sciences Division, Lawrence Berkeley National Laboratory, Berkeley, CA 94720, USA

⁵ NIMS Beamline Station at SPring-8, Nat. Inst. for Mat. Science, Hyogo 679-5148, Japan

⁶ Fakultät für Physik, University of Duisburg-Essen, Germany

⁷ Dept. of Mat. Science and Engineering, Univ. of California Berkeley, Berkeley, California 94720, USA

⁸ Istituto Officina dei Materiali IOM-CNR, 34149 Trieste, Italy

A detailed understanding of the origin of the magnetism in dilute magnetic semiconductors is crucial to their development for applications. Using hard x-ray angle-resolved photoemission (HARPES) at 3.2 keV, we investigate the bulk electronic structure of the prototypical dilute magnetic semiconductor $\text{Ga}_{0.97}\text{Mn}_{0.03}\text{As}$, and the reference undoped GaAs. The data are compared to theory based on the coherent potential approximation and fully relativistic one-step-model photoemission calculations including matrix-element effects. Distinct differences are found between angle-resolved, as well as angle-integrated, valence spectra of $\text{Ga}_{0.97}\text{Mn}_{0.03}\text{As}$ and GaAs, and these are in good agreement with theory. Direct observation of Mn-induced states between the GaAs valence-band maximum and the Fermi level, centered about 400 meV below this level, as well as changes throughout the full valence-level energy range, indicates that ferromagnetism in $\text{Ga}_{1-x}\text{Mn}_x\text{As}$ must be considered to arise from both p-d exchange and double exchange, thus providing a more unifying picture of this controversial material.

Spintronic technology, in which data is processed on the basis of electron spin rather than charge, promises to revolutionize the computing industry with smaller, faster and more energy efficient data storage and processing. Materials drawing a lot of attention for spintronic applications are dilute magnetic semiconductors - normal semiconductors to which a small amount of magnetic atoms is added to make them ferromagnetic. Understanding the source of ferromagnetism in dilute magnetic semiconductors has been a major road-block impeding their further development and use in spintronics. Now a

significant step to removing this road-block has been taken [1].

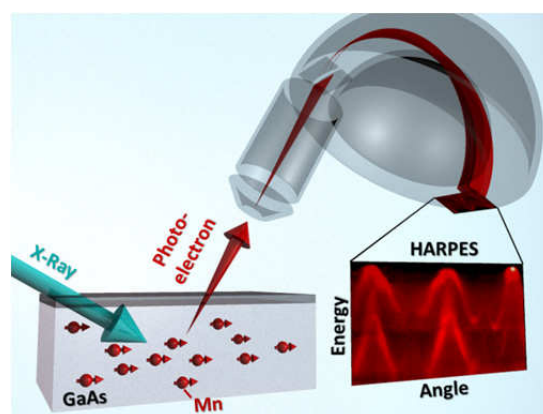


FIG. 1: With the HARPES technique, a beam of hard x-rays flashed on a sample causes photoelectrons from within the bulk to be emitted. Measuring the kinetic energy of these photoelectrons and the angles at which they are ejected reveals much about the sample's electronic structure. Here the Mn atoms in GaMnAs are shown to be aligned ferromagnetically, with all their atomic magnets pointing the same way.

ARPES is the most powerful tool to study the valence band electronic structure of solid, giving direct access to the k-resolved electronic bands in the direction parallel to the measured surface. In the widely used vacuum ultraviolet and soft x-ray regions ($h\nu = 10\text{-}1000\text{ eV}$) [2, 3] photoemission is surface sensitive due to the electron mean free path of 5-10 Å. This surface sensitivity is advantageous in case one is interested in surface-relates features, however, it commonly disturbs the interpretation of the bulk related properties such as the magnitude of the fundamental gap or the shape of three-dimensional Fermi surface. The

only certain way to increase the electron mean free path, and in turn increase the bulk sensitivity, is to increase kinetic energy of the valence band electrons by increasing the photon energy.

The recent advent of new high-energy third-generation synchrotron facilities and the development of new high-energy electron analyzers makes it possible to attempt such novel angle-resolved experiments extending deep into the hard x-ray regime. The overall energy resolutions (down to 50 meV), as well as the angular resolutions of these newly-developed facilities (down to 0.2-0.3°) in principle make it possible to perform meaningful studies of dispersive energy bands up to e.g. 3-6 keV excitation energies [4]. A key advantage of such energies lies in increasing the inelastic mean-free path of the electrons by a factor of about 10-20, thereby markedly enhancing the bulk sensitivity of the measurement, and also permitting it to study, in some cases, deeply buried layers.

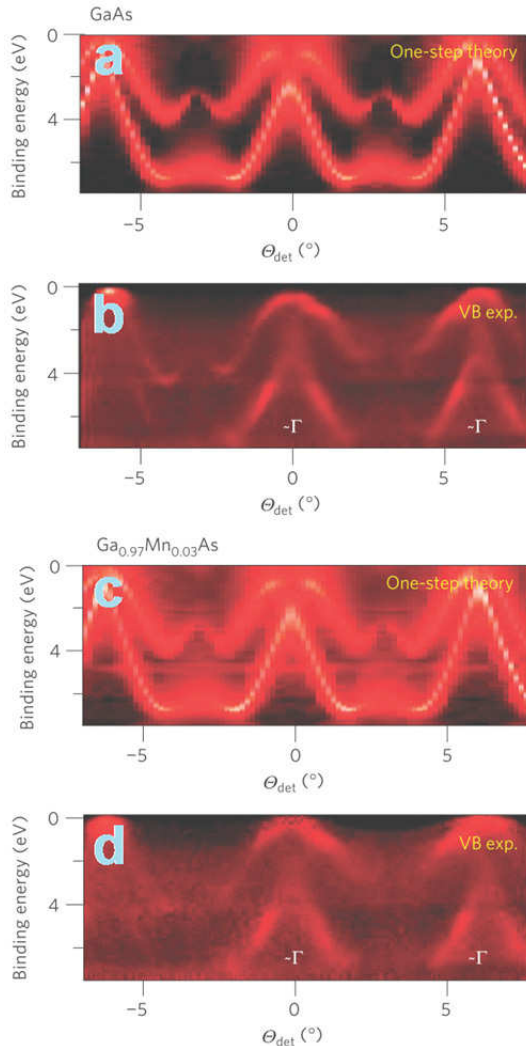


FIG. 2: HARPES measurements and one-step theory for bulk GaAs and $\text{Ga}_{0.97}\text{Mn}_{0.03}\text{As}$ at $h\nu=3.2\text{keV}$. **a,c**, Results of one-step HARPES calculations for GaAs (**a**) and $\text{Ga}_{0.97}\text{Mn}_{0.03}\text{As}$ (**c**). **b,d**, Experimental HARPES data obtained for GaAs (**b**) and $\text{Ga}_{0.97}\text{Mn}_{0.03}\text{As}$ (**d**). In **b** and **d**, the approximate positions of the repeated Γ points are indicated.

We have used HARPES to study the differences between the bulk electronic structures of a parent semiconductor GaAs and a dilute ferromagnetic semiconductor derived from it, $\text{Ga}_{1-x}\text{Mn}_x\text{As}$ with $x = 0.03$ [1]. Clear differences between the electronic structures of GaAs and $\text{Ga}_{0.97}\text{Mn}_{0.03}\text{As}$ were observed, including smearing of the sharp band features, changes throughout the entire valence-band manifold, and the appearance of extra intensity at the VBM that extends up to the Fermi level. These changes are furthermore in excellent agreement with one-step photoemission theory. A further analysis of angle-resolved data near the VBM indicates additional states induced by Mn over roughly 0 - 0.4 eV binding energy. Finally, element- and orbital-projected DOS calculations are consistent with theory in showing significant Mn contributions over the 0 - 4 eV binding energy, and particularly near E_F . Our results thus strongly favour a model of $\text{Ga}_{1-x}\text{Mn}_x\text{As}$ in which there is no gap between the Mn-induced impurity band and the GaAs valence bands, with this band being centred about 400 meV below and weakly overlapping the Fermi level, and by implication suggest that the magnetism originates from the coexistence of the two different mechanisms discussed in previous papers – double exchange and p-d exchange, as recently suggested on the basis of theory.

- [1] A. X. Gray, J. Minar, S. Ueda, P.R. Stone, Y. Yamashita, J. Fuji, J. Braun, L. Plucinski, C.M. Schneider, G. Panaccione, H. Ebert, O. D. Dubon, K. Kobayashi, and C.S. Fadley: Bulk Electronic Structure of the Dilute Magnetic Semiconductor $\text{Ga}_{(1-x)}\text{Mn}_x\text{As}$ via Hard X-Ray Angle-Resolved Photoemission, *Nature Materials* 11, 957 (2012).
- [2] L. Plucinski, J. Minar, B.C. Sell, J. Braun, H. Ebert, C.M. Schneider, and C.S. Fadley: "Band mapping in higher-energy x-ray photoemission: Phonon effects and comparison to one-step theory; *Phys. Rev. B* 78, 035108 (2008).
- [3] C. Papp, L. Plucinski, J. Minar, J. Braun, H. Ebert, and C.S. Fadley: Band mapping in x-ray photoelectron spectroscopy: an experimental and theoretical study of W(110) with 1.25 keV excitation, *Phys. Rev. B* 85, 045433 (2011)
- [4] A. X Gray, C. Papp, S. Ueda, B. Balke, Y. Yamashita, L. Plucinski, J. Minar, J. Braun, E. R. Ylvisaker, C. M. Schneider, W. E. Pickett, H. Ebert, K. Kobayashi, and C. S. Fadley: Probing Bulk Electronic Structure with Hard-X-Ray Angle-Resolved Photoemission: W and GaAs, *Nature Materials* 10, 759 (2011).

Controllable Supercurrent and Interference Effect in Nb/InAs-nanowire/Nb Hybrid Devices

H. Y. Günel¹, H. Hardtdegen¹, K. Sladek¹, G. Panaitov², D. Grützmacher¹, and Th. Schäpers¹

¹ Peter Grünberg Institut-9, Forschungszentrum Jülich, Germany

² Peter Grünberg Institut-8, Forschungszentrum Jülich, Germany

We report on the fabrication and measurements of planar mesoscopic Josephson junctions formed by InAs nanowires coupled to superconducting Nb terminals. The controllable doping of the nanowires provides to tune the Josephson properties of the junctions. We have studied the junction characteristics as a function of temperature, gate voltage and magnetic field. For junctions with high doping concentrations in the nanowire, Josephson supercurrent values up to 100 nA are found. Owing to the use of Nb as superconductor, the Josephson coupling persists at temperatures up to 4 K. In all junctions, the critical current monotonously decreased with the magnetic field as opposed to the standard Fraunhofer pattern. For the low-doped nanowire junctions, a full control of the supercurrent has been achieved by means of gate voltage. Furthermore, we have demonstrated, for the first time, a quasiparticle interference effect in the semiconducting nanowires by defining two well-defined superconductor/normal metal (or semiconductor) (SN) interfaces.

One of the common goals in superconductor/semiconductor hybrid devices is to fabricate Schottky barrier free contacts at the interface of the two materials. The natural formation of an electron accumulation layer on InAs surfaces prohibits the formation of a Schottky barrier. Therefore, this material became the most preferred one for semiconducting weak links in Josephson junctions. This unique property of InAs in combination with the bottom-up growth approach of nanowires enabled us to study the superconducting proximity effect in mesoscopic regime. On the other hand, owing to the higher critical temperature ($T_c \sim 9\text{K}$) and magnetic field ($B_c \sim 3\text{T}$) of the superconducting Nb compared to the conventional superconductor counterparts can offers the possibility to operate the junction at wide spectrum of the coupling regimes.

The InAs-nanowires were grown by selective area metal-organic vapor phase epitaxy without using catalyst material. For n-type doping Si was incorporated during growth. The grown wires have typically diameters of 100nm and a lengths of 2-3 μm , cf. upper panel of Fig. 1(a). Detailed

information about doping, crystal structure and normal state electrical characterization of the nanowires can be found elsewhere [1].

In order to contact the nanowires standard electron beam lithography was employed. The 100 nm thick Nb layer was deposited via magnetron sputtering after cleaning/etching nanowires by Ar milling. We have used Ar milling both to clean the surface of the nanowire – to achieve a high contact transparency by covering the nanowire (see Fig.1 (a), lower left) – and also to completely remove the nanowire in the contact area by etching – in order to contact the superconductor only at both ends of the remaining part of the nanowire (see inset Fig. 2).

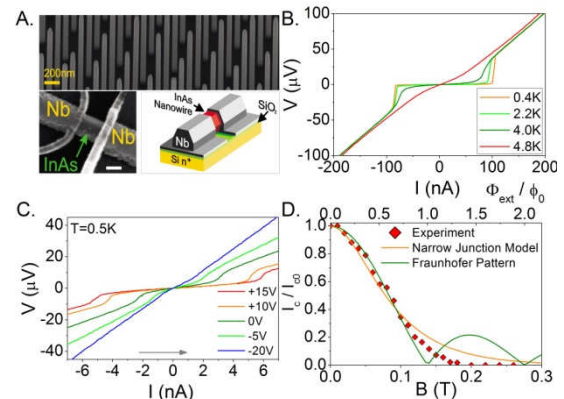


FIG. 1: A. Scanning electron micrograph of the as grown nanowires with doping factor 500 (upper figure), a representative scanning electron micrograph of Nb contacted sample (lower left), schematic illustration of the junction layout (lower right). B. IV-characteristics of a highly doped device at various temperatures. C. Gate voltage dependent IV-characteristics of the junction with the low doped nanowire at 0.5 K, the arrow indicate the current bias sweep direction. D. Zero field normalized critical current I_0/I_{c0} versus magnetic field B for a highly doped sample. The solid orange line represents the calculation according to the theoretical model [3]. The solid green line represents the calculated Fraunhofer patterns with corresponding junction area (upper x-axis).

Controllable Supercurrent: In Fig. 1(b) [2], the current-voltage (IV) characteristics at various temperatures between 0.4 and 4.8 K are shown for a sample with a highly doped nanowire. At temperatures $T \leq 4\text{ K}$ and small bias, a clear supercurrent is observed in the junction. As the

bias current exceeds a certain value I_c , the Josephson junction switches from the superconducting to the normal state. The critical current I_c measured at 0.4 K for the highly doped sample is about 100 nA. With increasing the temperature I_c is reduced. At $T > 4.5$ K, the supercurrent is suppressed completely.

The control of the doping concentration in the nanowires provides us to tune the supercurrent by the electric field. For such a low doped nanowires a full control of the supercurrent was achieved. In Fig. 1(c) [2] the I - V -characteristics at 0.5 K are plotted for back-gate voltages between -20 V and $+15$ V. At zero gate voltage, the measured I_c is about 2.8 nA, which is considerably smaller than the I_c of the junctions with the highly doped nanowires. The lower I_c is due to the fact that lower doped nanowires have smaller carrier concentration thus larger normal state resistance.

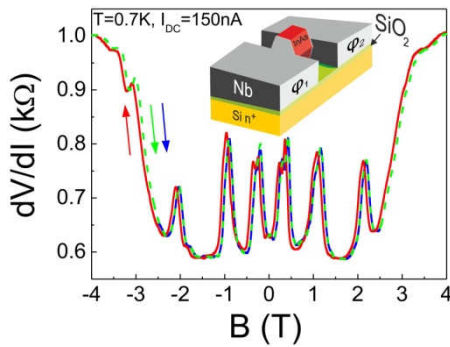


FIG. 2: A. Differential resistance dV/dI against magnetic field for a temperature of 0.7 K, two measurements (dashed green and continuous blue curves) are for the forward magnetic field sweep direction and one (red curve) for the reverse sweep direction, the constant bias current $I_{dc} = 150$ nA is applied in addition to $I_{exc} = 10$ nA excitation current, inset figure shows the schematic representation of the etched junction.

Owing to the large critical field of Nb, a Josephson supercurrent is maintained up to relatively large magnetic fields. The magnetic field was applied perpendicular to the substrate. Unlike Fraunhofer diffraction patterns in wide junctions, we have observed a monotonous decrease of the critical current I_c with magnetic field B , see Fig. 1(d) [2]. The monotonous decrease of I_c with increasing B can be explained within the framework of a recently developed theoretical model for the proximity effect in diffusive narrow-width junctions [3]. There, it is shown that for junctions with a width comparable to or smaller than the magnetic length $\xi_B = \sqrt{\Phi_0/B}$, with Φ_0 the magnetic flux quantum, the magnetic field acts as a pair-breaking factor that suppresses monotonously the proximity-induced superconductivity in the wire and the critical current. As shown in Fig. 1(d) (orange curve), the theoretical calculation based on Ref. [3] for a representative highly doped sample is in a good agreement with the experimental values.

Interference Effect: Usually SNS Josephson junctions are referred to as a circuit analogue of an optical Fabry-Pérot resonator. Due to phase-conjugated Andreev particles (electrons and

holes), the SN interfaces play a role of “mirrors” which can be “moved” back and forth by changing the phase difference between two superconducting electrodes. This leads to Fabry-Pérot interference patterns. The normal metal (N) or semiconductor in between two superconducting electrodes plays the role of a resonator. Here, we have demonstrated for the first time a nanowire-based quasiparticle interferometer. One of the most important prerequisites to form an interferometer is well defined SN interfaces. As schematically shown in Fig. 2 (inset), a highly doped nanowire section underneath the superconducting electrodes is etched so that the electrodes are touching only both ends of the nanowire. Eventually, the phase-conjugated electron-hole quasiparticles form standing waves within two well defined SN boundaries. In the Andreev reflection process the phase of quasiparticles is shifted by the superconducting phase at the NS interface. The constructive or destructive interference of quasiparticles can be created by changing the macroscopic phase of the superconducting electrodes. Here, we have controlled the phase of the electrodes by applying a perpendicular magnetic field. The measurement result of the resonance peaks are shown in Fig. 2. The measurements are performed by a standard lock-in technique with a 10 nA excitation current in addition to a 150 nA constant dc current which is slightly larger than the junction critical current. The corresponding voltage drop at this bias regime is around 0.08 mV which is considerably smaller than the superconducting energy gap $\Delta = 1$ meV. Therefore, the junction can be considered as in quasistatic state in which the phase of the superconducting electrodes does not evolve with time [4]. At this bias regime three consecutive measurements have been performed in order to confirm the reproducibility of the measurement. Two measurements are performed for forward magnetic field sweep direction (blue and dashed green curves) and one measurement for the reverse magnetic field sweep direction (red curve). The resonance peaks are only appeared when the electrodes are in the superconducting state. When the magnetic field exceeds the critical field of the superconducting Nb ($B_c \sim 3$ T) the junction switches to the normal state in which the resonance conditions are destroyed.

- [1] S. Wirths, K. Weis, A. Winden, K. Sladek, C. Volk, S. Alagha, T. E. Weirich, M. von der Ahe, H. Hardtdegen, H. Lüth, N. Demarina, D. Grützmacher, and Th. Schäpers. J. of Appl. Phys., 110, 2011.
- [2] H. Y. Günel, I. E. Batov, H. Hardtdegen, K. Sladek, A. Winden, K. Weis, G. Panaitov, D. Grützmacher, and Th. Schäpers. J. of Appl. Phys., 112, 2012.
- [3] J. C. Cuevas and F. S. Bergeret. Phys. Rev. Lett., 99, 2007.
- [4] G. Bastian, E. O. Göbel, A. B. Zorin, H. Schulze, J. Niemeyer, T. Weimann, M. R. Bennett, and K. E. Singer. Phys. Rev. Lett., 81, 1998.

Scanning tunneling microscopy with InAs nanowire tips

K. Flöhr¹, K. Sladek², H. Y. Günel², M. I. Lepsa², H. Hardtdegen², M. Liebmann¹, Th. Schäpers², and M. Morgenstern¹

¹ II. Physikalisches Institut B, RWTH Aachen University, Germany

² Peter Grünberg Institut-9, Forschungszentrum Jülich, Germany

Indium arsenide nanowires grown by selective-area vapor phase epitaxy are used as tips for scanning tunneling microscopy (STM). The STM tips are realized by positioning the wires manually on the corner of a double cleaved gallium arsenide wafer with sub- μm precision and contacting them lithographically, which is fully compatible with further integrated circuitry on the GaAs wafer. STM images show a z -noise of 2 pm and a lateral stability of, at least, 0.5 nm on a Au(111) surface. $I(z)$ -spectroscopy reveals an exponential decay indicating tunneling through vacuum. Subsequent electron microscopy images of the tip demonstrate that the wires are barely modified during the STM imaging.

Scanning tunneling microscopy (STM) is the most advanced tool to probe the local density of states, excitations including dynamics as well as fingerprints of correlations down to the atomic scale. However, since the tip is typically metallic, all long-range correlations are effectively screened. Using materials with a charge density lower than a metallic tunneling tip (e.g. doped semiconductors) would partially resolve this problem and, in addition, might open the possibility of integrated circuitry directly at the tip. One appealing possibility is to use the well-developed epitaxially grown semiconductor nanowires [1].

However, several challenges have to be overcome to reach this goal. Especially the preconditions of the same quality in mechanical stability, electrical characteristics and the possibility of atomic resolution as conventional metallic tips have to be achieved. To this end, we show that single InAs nanowires, known for their conducting surfaces without Schottky barriers[2], are suitable for STM tips. For the fabrication of our STM tips, we use InAs nanowires which are grown epitaxially by catalyst-free selective area metal organic vapor phase epitaxy [3,4]. The nanowires are n-doped ($n \approx 2 \times 10^{18} \text{ cm}^{-3}$, $\mu \approx 500 \text{ cm}^2 \text{ Vs}$) as determined by four-terminal transport measurements, have diameters of approximately 120 nm and are about 3 μm long. As a support for the InAs nanowires we use a semi-insulating GaAs(100) wafer, which is glued to a stainless steel block to mount the tip either on a standard STM tip holder or in a protective frame for better handling. To prepare the InAs nanowire STM tips, we developed a technique described in detail elsewhere [5,6].

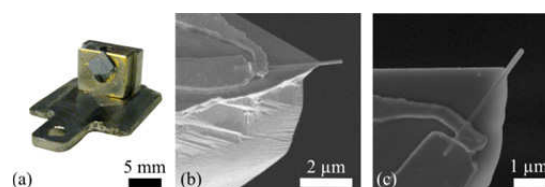


FIG. 1: (a) GaAs support with contacted InAs tip mounted on the STM tip holder. (b) SEM image (75°-tilted view) of the STM tip before approaching a Au(111) sample. The small overhang of the GaAs support corner provides a tolerance of about 2.5° in angular adjustment accuracy of the nanowire with respect to the probed surface, still guaranteeing a protruding nanowire during the tip approach. (c) SEM image (top view) of the same nanowire after use as a STM tip on a Au(111) surface.

For STM measurements, the support block with the processed InAs tip is mounted on the tip holder of a home-built room temperature STM system operating in ultrahigh vacuum (10^{-8} Pa). Using the geometry shown in Fig. 1(b), we estimate that the InAs nanowire will reach the surface of the sample first, as long as it is oriented perpendicular to the surface within a deviation of less than 2.5° . In order to remove the oxide barrier at the end of the nanowire, Ar sputtering (ion energy: 0.3 keV) has to be applied in-situ before approaching the tip to the sample. Indeed, we did not achieve stable imaging without this sputtering step. The wires are firstly ion bombarded under two opposite angles of $\pm 45^\circ$ to the axial direction, for 30 min each, and afterwards at 0° for about 60 min. SEM pictures, recorded directly after sputtering, show an abrasion of less than 10 nm in diameter and length of the wire.

STM images are recorded on a Au(111) crystal prepared by several cycles of ion bombardment (600 eV Ar) and annealing (450°C). To approach the tip to the Au surface, we use a sample bias of +1V, safely avoiding tunneling into the band gap of the nanowire (tunnel current: 10 pA). Figure 2(a) shows an STM image of a single atomic step of the Au(111) surface. The well-known herringbone reconstruction is visible on both terraces. The STM image represents the raw data except that it has been flattened using a plane fit. The quality of the STM data is clearly seen in the line scan of Fig. 2(b) revealing a height difference between the two terraces of $(224 \pm 26) \text{ pm}$, as determined using histograms of the z values on both terraces. This is in good agreement with the known value of 235 pm. The width of the step obtained by averaging a few line scans is $(0.6 \pm 0.1) \text{ nm}$, which

can be regarded as an upper limit of the lateral resolution. In particular, it excludes that the nanowire oscillates laterally by an amplitude of more than 0.5 nm. This is an important finding, rather difficult to achieve, e.g., for carbon nanotube tips [7]. Forward and backward line scans exhibit a relative lateral shift of about (0.53 ± 0.07) nm, which is nearly identical to the shift observed by using PtIr tips, (0.65 ± 0.26) nm. The difference is probably due to a remaining creep of the piezo scanner. This excludes, in addition, a strong bending of the nanowire at the step edge or during the scanning process.

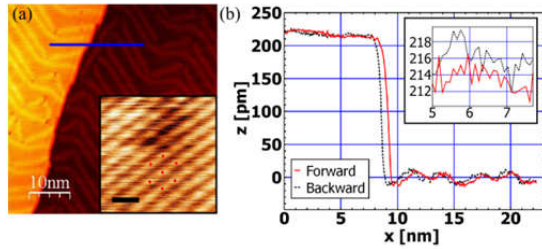


FIG. 2: (a) STM topography of Au(111) (sample bias: $U = +1V$, $I = 50$ pA). Inset: STM images exhibiting atomic resolution ($U = +1V$, $I = 10$ pA) with red dots marking the atoms. The scale bar is 5 Å. (b) Line scan along the blue line in (a). Full red curve: forward scan, dashed black curve: backward scan. The relative shift of the step edge is 0.6 nm. Inset: zoom into the range from 5 nm to 8 nm.

The noise level in z-direction is determined as the standard deviation from the mean value of several line scans recorded on the flat areas of the surface, i.e., in between the reconstruction lines [see inset of Fig. 2(b)]. It is $\sigma_z = 2.2$ pm at a remaining current noise of $\sigma_I = 1.7$ pA for a current of $I = 50$ pA. For a room temperature STM system, this excellent value points again to the high mechanical stability of the nanowire tip. Atomic resolution on the Au(111) surface has been occasionally observed. One example is shown in the inset of Fig. 2(a). The structure did not change by rotating the scan direction and varying the scan speed excluding that it is a measurement artifact. However, the atomic distance is about 5-10 % less than the known distance of Au(111), probably due to thermal drift. The apparent line structure of the atoms might be related to a tilted p -orbital at the end of the imaging nanowire.

$I(z)$ -spectroscopy results are shown in Fig. 3(a) revealing an exponential decay of the current with tip-sample separation, as expected for tunneling. The decay constant of $\kappa = 6.17 \times 10^9 \text{ m}^{-1}$ is nearly identical to the one observed for W tips on InAs(110) [8], but slightly reduced with respect to metals probably due to surface band bending effects on the InAs surface. This implies a favorable low charge density at the tip surface. The dI/dU curve shown in Fig. 3(b) is recorded using a lock-in amplifier. It exhibits a reduced dI/dU signal within about 300 meV around the Fermi level as expected from the InAs band gap. Importantly, it strongly deviates from spectra expected on GaAs [9] (band gap: 1.42 eV) additionally evidencing that the InAs nanowire and not the GaAs support is used for STM imaging.

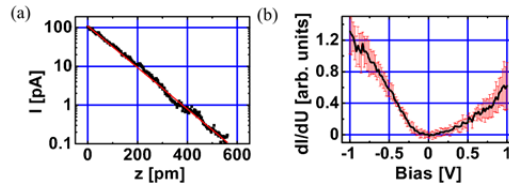


FIG. 3: (a) $I(z)$ curve averaged over 5 spectra recorded with the InAs tip (black squares) at different positions of the Au(111); stabilization at $U = 1V$, $I = 100$ pA; an exponential fit $e^{-\kappa z}$ with $\kappa = 6.17 \times 10^9 \text{ m}^{-1}$ (red line) is shown for comparison. (b) $dI/dU(U)$ curve averaged from 10 spectra; stabilization at $I = 100$ pA, $U = 1V$.

In summary, we have fabricated InAs nanowire tips for STM measurements exhibiting a RMS z-noise level of only 2 pm and a lateral resolution better than 0.5 nm. $I(z)$ -spectroscopy reveals the tunneling characteristics of the tip and subsequent electron microscopy images show its stability during coarse approach and removal from the substrate. All these results show the good quality of STM imaging with a semiconducting nanowire in comparison to well-prepared metallic tips at room temperature in ultrahigh vacuum. The InAs tips are placed and lithographically contacted on a GaAs wafer opening the possibility for integrated circuitry directly at the tip.

We thank Mike Pezzotta and Florian Muckel for technical assistance and acknowledge financial support by the excellence initiative of the German federal government.

- [1] M. Law, J. Goldberger, and P. Yang, *Ann. Rev. Mat. Res.* 34, 83 (2004).
- [2] V. Y. Aristov, G. LeLay, P. Soukiasian, K. Hricovini, J. E. Bonnet, J. Oswald, and O. Olsson, *Europhys. Lett.* 26, 359 (1994).
- [3] K. Sladek, A. Winden, S. Wirths, K. Weis, C. Blömers, O. Gül, T. Grap, S. Lenk, M. von der Ahe, T. E. Weirich, H. Hardtdegen, M. I. Lepsa, A. Lysov, Z.-A. Li, W. Prost, F.-J. Tegude, H. Lüth, Th. Schäpers, and D. Grützmacher, *Phys. Status Solidi C* 9, 230 (2012).
- [4] M. Akabori, K. Sladek, H. Hardtdegen, Th. Schäpers, and D. Grützmacher, *J. Cryst. Growth* 311, 3813 (2009).
- [5] K. Flöhr, M. Liebmann, K. Sladek, H. Y. Günel, R. Frielinghaus, F. Haas, C. Meyer, H. Hardtdegen, Th. Schäpers, D. Grützmacher, and M. Morgenstern, *Rev. Sci. Instr.* 82, 113705 (2011).
- [6] K. Flöhr, K. Sladek, H. Y. Günel, M. I. Lepsa, H. Hardtdegen, M. Liebmann, Th. Schäpers, and M. Morgenstern, *Appl. Phys. Lett.* 101, 243101 (2012).
- [7] H. Dai, J. Hafner, A. Rinzler, D. Colbert, and R. Smalley, *Nature* 384, 147 (1996).
- [8] M. Morgenstern, D. Haude, V. Gudmundsson, C. Wittneven, R. Dombrowski, C. Steinebach, and R. Wiesendanger, *J. Electr. Spectr. Rel. Phen.* 109, 127 (2000).
- [9] R. M. Feenstra and J. Stroscio, *J. Vac. Sci. Technol. B* 5, 923 (1987).

Monitoring structural influences on quantum transport in InAs nanowires

Robert Frielinghaus,¹ Kilian Flöhr,² Kamil Sladek,³ Thomas E. Weirich,⁴ Stefan Trellenkamp,⁵ Hilde Hardtdegen,³ Thomas Schäpers,^{2,3} Claus M. Schneider,¹ and Carola Meyer¹

¹ Peter Grünberg Institut-6, Forschungszentrum Jülich, Germany

² II. Physikalisches Institut, RWTH Aachen University, Germany

³ Peter Grünberg Institut-9, Forschungszentrum Jülich, Germany

⁴ Central Facility for Electron Microscopy GFE, RWTH Aachen University, Germany

⁵ Peter Grünberg Institut-8/PT, Forschungszentrum Jülich, Germany

A sample design that allows for quantum transport and transmission electron microscopy (TEM) on individual suspended nanostructures is used to investigate moderately *n*-type doped InAs nanowires (NWs). The nanowires were grown by metalorganic vapor phase epitaxy. Universal conductance fluctuations in the nanowires are investigated at temperatures down to 0.35 K. These fluctuations show two different temperature dependences. The very same nanowire segments investigated in transport are subsequently analyzed by TEM revealing crystal phase mixing. However, we find no correspondence between the atomic structure of the wires and the temperature dependences of the conductance fluctuations.

Self-assembled semiconductor nanowires (NWs) like InAs NWs receive a considerable interest as possible candidates for future nanoelectronic devices as well as for model systems for the study of various fundamental quantum effects [1,2]. However, there are two factors inherent in the device geometry that greatly influence standard transport experiments and result in an experimental fingerprint for each NW. First, the high aspect ratio and enhanced surface conduction lead to an increased sensitivity to the environment. Second, a usually unknown defect distribution individual for each nanowire is used to explain many quantum interference effects and transport phenomena [2,3].

In our work, we use a sample design where individual InAs nanowires [3] are suspended across holes in a Si_3N_4 transmission electron microscopy (TEM) membrane [4,5,6]. The NWs are subsequently contacted and universal conductance fluctuations (UCFs) are measured at cryogenic temperatures [7]. We find highly reproducible fluctuation patterns and clear temperature dependences as we do not have any substrate influence in our suspended geometry. Two distinct temperature dependences of the phase coherence length are observed in a set of four wires. We correlate these transport data with the atomic structure of the NWs obtained in a successive TEM measurement on the very same wire section.

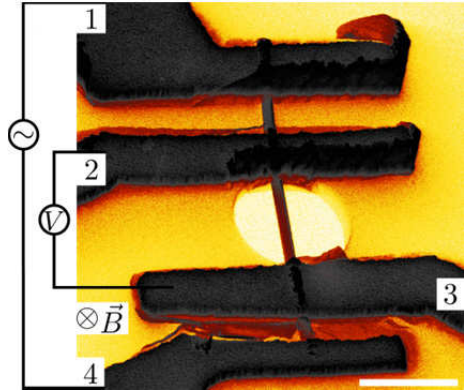


Fig. 1 Scanning electron micrograph of wire A with a schematics of the configuration used in the transport measurements. Scale bar is 1 μm . The color scale of the secondary electron yield is inverted for clarity.

Four as-grown NWs were mechanically removed from the growth substrate with an In needle and selectively placed across holes of a TEM membrane [5]. Individual Ti/Au contacts were defined by electron beam lithography. A typical device is given in Fig. 1 [6]. Transport measurements were performed in a He-3 cryostat with a standard lock-in technique and TEM images were acquired in an FEI Tecnai F20 at 200 kV acceleration voltage.

The magnetoconductance fluctuates as a function of the magnetic field at low temperatures as shown in Fig. 2(a). This variation in magnetoconductance can be attributed to UCFs. The fluctuation patterns reproduce themselves with exponentially decreasing amplitude upon increasing the temperature. This can be explained with the phase-coherence length l_ϕ being shorter than the contact separation for $T > 1$ K. It can be determined from the correlation field B_c , defined as the half-width at half maximum of the autocorrelation function. It is

$$l_\phi = \gamma \Phi_0 / (dB_c).$$

Here, $\Phi_0 = h/e$ denotes the magnetic flux quantum, d the wire diameter and γ is a proportionality

constant determined from the saturation at low temperatures and the contact separation [2,7].

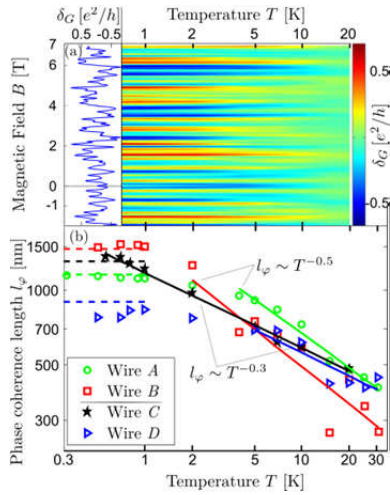


Fig. 2: (a) UCF pattern δG of wire A as a function of magnetic field and temperature. The curve on the left side shows the conductance fluctuations at 0.35 K. (b) Phase-coherence length vs temperature determined from the correlation field. The solid lines are the fitted exponential temperature dependences. The dashed horizontal lines indicate the contact separation length.

We observe two distinct dephasing rates of l_ϕ upon increasing the temperature as shown in Fig. 2 (b). We obtain $l_\phi \sim T^{-0.5}$ for wires A and B while l_ϕ in wires C and D decays with $T^{-0.3}$.

The origin of the different temperature dependences is unclear at this point. We can neglect all detrimental substrate effects due to the suspended geometry of our samples. Thus, this origin can only lie within the structure of the wires themselves. The devices show no difference on the length scales accessible in scanning electron microscopy. Thus, we take advantage of our sample design and use TEM to investigate if the atomic structure of the wires has an influence on the UCFs and on the different dephasing rates of l_ϕ .

Here, we present a direct mapping of the crystal phases along the current flow (see right part of Fig. 3 (a)) and correlate the phase mixing with the transport data of the very same wire. We evaluate the typical wurtzite segment length and, therefore, the potential fluctuation periodicity in Fig. 3 (b). All distributions exhibit an average segment length of 3 nm and a similar profile. Thus, the fluctuations in the crystal phase cannot account for the distinct transport behaviours.

We thus have to account the transport property variations to differences that we cannot extract from the TEM measurements. Two candidates are the local dopant and atomic defect distribution and thermal strain.

In summary, we have investigated freely suspended InAs nanowires with a sample design that offers two major advantages to standard

transport experiments. First, with the suspended geometry, no substrate interaction can affect the low-temperature transport experiments. Second, it

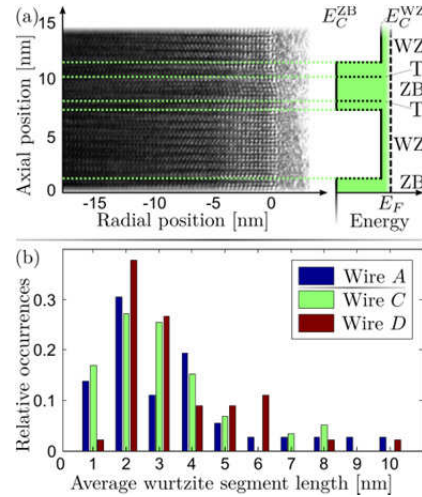


Fig. 3: (a) Example high-resolution TEM image of wire A along with a schematics of the conduction band profile E_C of the wurtzite (WZ) and zinc blende (ZB) crystal phases with twinning planes (T). E_F marks the Fermi energy. (b) Distribution of the axial WZ segment lengths of the investigated NWs.

is possible to subsequently measure the crystal structure of the very same nanowires by transmission electron microscopy and to thus correlate transport and crystalline properties. The NWs show very clear universal conductance fluctuations unperturbed by any substrate influence at cryogenic temperatures. We could extract, i.e., the phase coherence length that showed significantly different temperature dependences from these UCFs. All nanowires exhibit crystal phase mixing between zinc blende and wurtzite structure in the TEM measurements. This phase mixing cannot account for the different transport properties, since the NWs show no systematic differences.

- [1] Y. Li, F. Qian, J. Xiang, C. M. Lieber, *Mater. Today* **9**, 18 (2006).
- [2] C. Blömers, M.I. Lepsa, M. Luysberg, D. Grützmacher, H. Lüth, T. Schäpers, *Nano Lett.* **11**, 3550 (2011).
- [3] S. Wirths, K. Weis, A. Winden, K. Sladek, C. Volk, S. Alagha, T.E. Weirich, M. von der Ahe, H. Hardtdegen, H. Lüth, N. Demarina, D. Grützmacher, T. Schäpers, *J. Appl. Phys.* **110**, 053709 (2011).
- [4] R. Frielinghaus, K. Flöhr, K. Sladek, T.E. Weirich, S. Trellenkamp, H. Hardtdegen, T. Schäpers, C.M. Schneider, C. Meyer, *APL* **101**, 062104 (2012).
- [5] K. Flöhr, M. Liebmann, K. Sladek, H. Y. Günel, R. Frielinghaus, F. Haas, C. Meyer, H. Hardtdegen, T. Schäpers, D. Grützmacher, M. Morgenstern, *Rev. Sci. Instrum.* **82**, 113705 (2011).
- [6] R. Frielinghaus, K. Goß, S. Trellenkamp, L. Houben, C. M. Schneider, C. Meyer, *pssb* **248**, 2660 (2011).
- [7] C. W. J. Beenakker and H. van Houten, *Phys. Rev. B* **37**, 6544 (1988).

High-Fidelity Single-Qubit Gates for Two-Electron Spin Qubits in GaAs

P. Cerfontaine¹, T. Botzem¹, K. Khodjasteh², L. Viola², D. DiVincenzo^{3,4}, and H. Bluhm¹

¹ II Institute of Physics C, RWTH Aachen University, Germany

² II. Department of Physics and Astronomy, Dartmouth College, New Hampshire, USA

³ Institute for Quantum Information, RWTH Aachen University, Germany

⁴ Department of Theoretical Nanoelectronics, PGI, Forschungszentrum Jülich, Germany

High fidelity gate operations for manipulating individual and multiple qubits in the presence of decoherence are a prerequisite for fault-tolerant quantum information processing. The control methods used in earlier experiments on semiconductor two-electron spin qubits are based on unrealistic approximations, which preclude reaching the required fidelities. An attractive remedy is to use control pulses found in numerical simulations. Calibrating these control pulses on the experiment requires a self-consistent approach. Starting with inaccurate control pulses we numerically show that elimination of individual systematic gate errors is possible by applying a modification of the bootstrap protocol proposed in [1]. Furthermore, we show that more complex control pulses which are insensitive to slow charge noise and fluctuations of the nuclear hyperfine field exist [2].

Spins in semiconductors are attractive solid state qubits because of their potential for scale-up using well established processing techniques. Furthermore, their generally weak coupling to other degrees of freedom allows these spins to retain their quantum state for relatively long times. Electron spins in GaAs quantum dots are amongst the most advanced and promising types of spin qubits. All aspects of single qubit operation (e.g. initialization and coherence time measurements, single shot readout and universal control) have been demonstrated experimentally for logical qubits encoded in two electron spins, the so-called S- T_0 qubit (Fig. 1). This qubit allows for all-electrical control by applying voltage pulses that change the potential difference between the two dots, $\epsilon(t)$. This detuning affects the singlet-triplet energy splitting $J(\epsilon(t))$ resulting from the exchange interaction of the two electrons (Fig. 2). Devising gate operations corresponds to finding suitable voltage pulses for $\epsilon(t)$. The effective qubit Hamiltonian is given by

$$H = \frac{\Delta B_z}{2} \sigma_x + \frac{J(\epsilon)}{2} \sigma_z,$$

where $\Delta B_z = (B_{\text{nuc,L}} - B_{\text{nuc,R}})/2$ is the magnetic field difference between the two dots. Our earlier work [3] has shown that this field gradient can be set to a fixed value by dynamically induced nuclear polarization. Because of constraints on J , the need

for fast gates, and nonlinear coupling, standard Rabi control is not applicable.

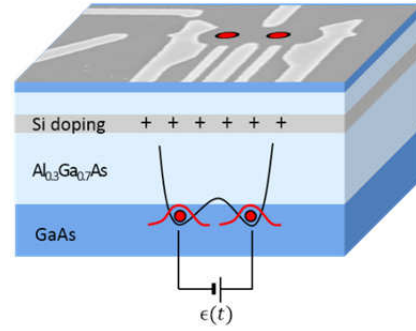


Fig. 1 Typical GaAs double quantum dot. The qubit is manipulated via fast voltage pulses on the gates (light gray), which are biased to capture two electrons (red) in the two-dimensional electron gas. Only the S- T_0 subspace of the two-electron wave function is used for computation.

Earlier experiments relied on the notion that $J(\epsilon)$ can be switched instantaneously and can be varied over a wide range. These assumptions are not fulfilled to the degree required for high fidelity control. Hence, we use numerical search procedures to determine a control profile for $J(\epsilon)$, using a realistic model of the qubit and taking important experimental constraints into account.

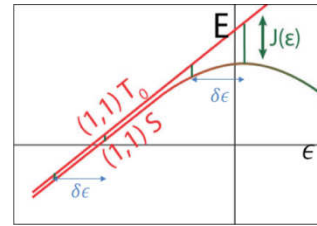


Fig. 2 Energy diagram of the S- T_0 qubit as a function of the detuning ϵ . Fluctuations $\delta\epsilon$ in ϵ , for example from charge noise, have a bigger impact on the singlet-triplet splitting $J(\epsilon)$ when operating at larger ϵ .

As a first step, we find control pulses that implement $\pi/2$ -gates around two orthogonal axes. A pulse consists of a sequence of ϵ values and a constant ΔB_z . We model finite rise times in our hardware and make sure we start at and return to a predefined baseline at the beginning and end of the pulse sequence. This insures that concatenation of pulse sequences does not lead to additional systematic errors. Furthermore, we

avoid excursions to noise sensitive regions at large J by trying to keep ϵ as low as possible (Fig.2).

Thus, we solve the optimization problem

$$\min_{\epsilon_i, \Delta B_z} \sum_{i=1}^n J(\epsilon_i)^2 \tau \text{ s.t. } U_{\text{tot}}(\epsilon_i, \Delta B_z) = U_{\text{tar}},$$

where U_{tot} is the time evolution operator of the current iteration step's set of parameters, U_{tar} is the desired time evolution operator, τ the duration of one ϵ -segment and the summation goes over all segments. The solutions generally resemble the positive half-waves of Rabi-like oscillations, where the non-sinusoidal shape corrects imperfections from non-rectangular pulse shaping (Fig. 3). Using the noise spectrum measured in [4], we conduct Monte Carlo simulations to calculate the average fidelity of this gate to about $\langle F \rangle \approx 99\%$, which is confirmed by analytical calculations following [5].

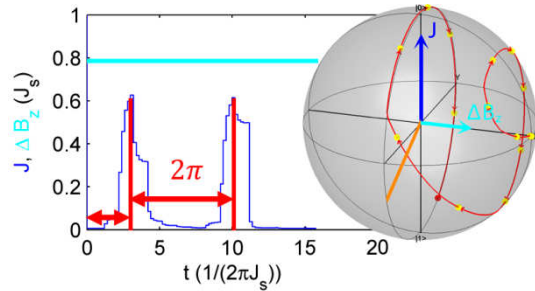


Fig. 3 Pulse sequence for a $\pi/2$ -pulse around the orange colored axis in the Bloch sphere representation. The initial state is on the ΔB_z -axis, the final state is shown in red.

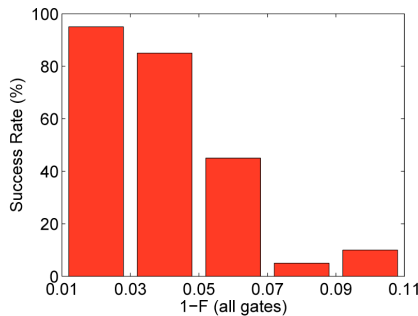


Fig. 4 Convergence of the bootstrap algorithm depends on the initial infidelities of the single qubit gates. Only unitary infidelities have been used.

One problem when experimentally implementing these (or other) gates is that the qubit control is imperfectly calibrated, leading to systematic errors if directly transferring simulation results to the experiment. Our solution to this problem is to fine tune the pulses based on their measured performance.

To this end, we modify the bootstrap protocol proposed in [1] to eliminate systematic errors of a set of two orthogonal $\pi/2$ gates, each represented by a control pulse as in Fig. 3. Our bootstrap protocol works by concatenating these gates in six different ways, applying each of the resulting gate sequences to an initial state on an axis orthogonal to both $\pi/2$ gates, and then reading out along this axis afterwards. For ideal gates, the resulting six element signal vector is zero and it grows linearly with systematic errors. Wrapping it in an iterative

optimization algorithm we are thus able to tune the gate set self consistently. Since this method is also insensitive to decoherence in first order, we only consider systematic errors in the following convergence analysis. Introducing systematic errors to the perfect gates found in the previous numerical optimization, we see that our method converges for initial infidelities as high as 11% (Fig. 4), allowing elimination of systematic errors to a high degree. We are currently adapting the method in order to achieve good convergence when realistic measurement noise is taken into account.

The infidelity in the gates from the initial numerical optimization is only due to noise in the control variables since the target gates are realized perfectly in our noiseless simulations. In order to further improve the fidelities in the presence of noise, we add the condition to the numerical optimization that the first derivatives of the resulting unitary time evolution operator with respect to the control variables should vanish. These dynamically corrected gates (DCGs) are similar to dynamical decoupling sequences like Hahn echo or CPMG. We thus find pulse sequences (Fig. 5) which are not only free from systematic errors, but also to lowest order decoupled from slow fluctuations in ϵ and ΔB_z [2]. This decoupling will hopefully lead to a higher fidelity gate than the sequence in Fig. 3.

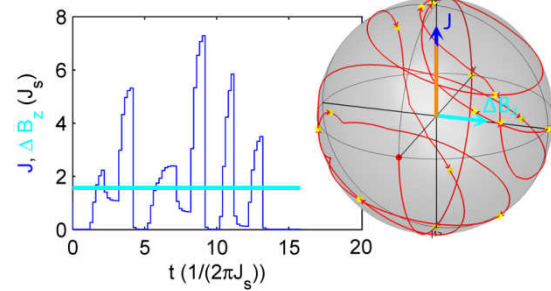


Fig. 5 Pulse sequence and state trajectory of a dynamically corrected $\pi/2$ -gate around the z-axis.

In conclusion, we have shown that high fidelity single qubit gates exist even in the presence of noise and experimental imperfections. Furthermore, we have presented a method to self consistently eliminate systematic errors from such sequences. Dynamically corrected sequences dealing with slow noise exist and were found in numerical simulations.

Future work will include implementation of these methods on the experiment and finding a way to eliminate systematic errors from the DCGs while keeping their decoupling properties.

This work was supported by IARAP; U.S. ARO, U.S. NSF and the Alfred Krupp von Bohlen und Halbach – Foundation.

- [1] Dobrovitski et al., *PRL* **105** (2010)
- [2] Khodjasteh et al., *PRA* **86** (2012)
- [3] Bluhm et al., *PRL* **105** (2010)
- [4] Dial et al., *PRL* **110** (2013)
- [5] Green et al., arXiv:1110.6686 (2012)

Electric field-driven coherent spin reorientation of spin packets in InGaAs

S. Kühlen¹, K. Schmalbuch¹, M. Hagedorn¹, P. Schlammes¹, M. Patt¹, M. Lepsa², G. Güntherodt¹, and B. Beschoten¹

¹ II. Institute of Physics, RWTH Aachen University, Germany

² Peter Grünberg Institut (PGI-9), Forschungszentrum Jülich, Germany

Full electric-field control of spin orientations is one of the key tasks in semiconductor spintronics. We demonstrate that electric-field pulses can be utilized for phase-coherent $\pm\pi$ spin rotation of optically generated electron spin packets in InGaAs epilayers detected by time-resolved Faraday rotation. Through spin-orbit interaction, the electric-field pulses act as local magnetic field pulses. By the temporal control of the local magnetic field pulses, we can turn on and off electron spin precession and thereby rotate the spin direction into arbitrary orientations in a two-dimensional plane.

In recent years, a new pathway towards spintronics without ferromagnets has evolved, which allows us to generate and to manipulate spins by electric fields E only [1]. In ordinary nonmagnetic semiconductors, dc E fields can generate spins by two complementary effects, the spin Hall effect [2] and the so-called current induced spin polarization (CISP) [3]. Both result from the spin-orbit (SO) coupling. Although the microscopic origin of CISP is not fully understood in most systems electron spins get oriented along the effective internal magnetic field B_{int} , which can be tuned by the E field strength through SO coupling. The control of B_{int} is of fundamental importance for spin manipulation.

We report on time-resolved electrical spin manipulation experiments of electron spins in InGaAs. Coherent spin packets are optically generated by circularly polarized laser pump pulses. Their initial spin direction is manipulated by E field pulses, which act as effective local magnetic field pulses (LMFP) due to SO coupling. Using time-resolved Faraday rotation (TRFR), we probe the Larmor precession of spin packets induced by the SO field pulse. By changing the pulse width and polarity, we are able to rotate the spins into arbitrary directions within a two-dimensional plane [4]. In addition to spin precession, the E field pulses also yield a lateral drift of the spin packet over several μm . As sign reversal of the pulses will reverse both spin precession and drift direction, we are able to explore spin echo of the spin packet in the diffusive spin transport regime.

Our studies were performed on a 500 nm thick $\text{In}_{0.07}\text{Ga}_{0.93}\text{As}$ epilayer grown on semi-insulating (100) GaAs by molecular beam epitaxy. The room temperature carrier density was set to

$n \sim 3 \times 10^{16} \text{ cm}^{-3}$ by Si doping to allow for long spin dephasing times at low temperatures. By chemical wet etching a 140 μm wide and 680 μm long transport channel was patterned and contacted with standard Au/Ge/Ni electrodes. For spin manipulation experiments, the electric field was applied along the $[01\bar{1}]$ crystal axis (or x axis) as shown in Fig. 1(a). For our samples, this configuration yields the strongest CISP with internal magnetic fields pointing along the $[011]$ or y axis. The device is embedded in a coplanar wave guide and connected to microwave probes. Coherent electron spin ensembles are generated along the z direction by circularly polarized picosecond laser pump pulses and detected by TRFR in polar geometry. The E field will be used for time-resolved spin manipulation.

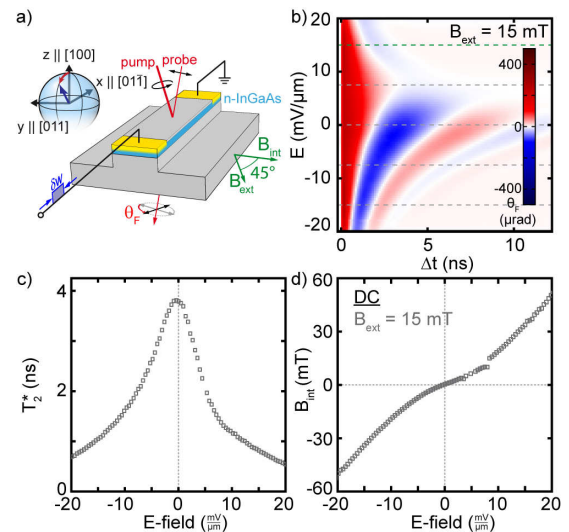


FIG. 1: (a) Schematic setup: dc or pulsed E fields are applied along the $[01\bar{1}]$ direction of an n -InGaAs transport channel. Optically generated spins are probed by static and TRFR in polar geometry. (b) TRFR after optical spin orientation in InGaAs ($T = 30 \text{ K}$). Electron drift in an E field induces B_{int} , which results in spin precession about $B_{\text{tot}} = B_{\text{int}} + B_{\text{ext}}$ ($B_{\text{ext}} = 15 \text{ mT}$), (c) T_2^* vs E and (d) B_{int} vs E .

We first explore the influence of dc E fields on the coherent spin ensemble in Fig. 1(b) at $B_{\text{ext}} = 15 \text{ mT}$. From this experiment it is obvious that SO induced electron spin precession can be triggered by electrical means. Spin precession is accelerated for $E < 0 \text{ mV}/\mu\text{m}$ while it is slowed down for $0 < E < 7.5 \text{ mV}/\mu\text{m}$. This dependence

proves the reversal of the B_{int} direction upon sign reversal of E .

All TRFR data can be described by an exponentially damped cosine function

$$\Theta_F = \Theta_0 \exp\left(-\frac{\Delta t}{T_2^*}\right) \cos(\omega_L \Delta t + \delta)$$

with amplitude Θ_0 , pump-probe delay Δt , Larmor frequency ω_L and phase δ . This way we can determine the spin dephasing time T_2^* and B_{int} , which are plotted vs E in Figs. 1(c) and (d), respectively. We note a strong decrease of T_2^* , which limits the observable spin coherence.

We now want to manipulate the phase of the optically generated coherent spin packet. Here, we use E field pulses both to initialize and to stop spin precession at $B_{\text{ext}} = 0$ mT. When the E field pulse reaches the optically generated spin packet, it will create a LMFP for the duration of the pulse. This LMFP will trigger spin precession in the xz plane [see Fig. 1(a)]. The precession frequency depends on the E field strength, while the total precession time is given by the pulse width δw . In Fig. 2(a), we show a sequence of TRFR measurements of optically generated coherent spin packets, which are manipulated by E field pulses of $E = 7$ mV/ μm and various pulse widths ranging from 0 to 8 ns. As expected, we observe spin precession for long pulses of 8 ns (black curve). For shorter pulse widths, Θ_F always follows this spin precession curve during the field pulse. However, spin precession abruptly stops after the pulse has been turned off with elapsed δw . This is seen by a simple exponential decay thereafter, which is observed for all pulse widths. The minimum in Θ_F at 3.7 ns shows that the LMFP of 4 ns operates as π pulse [blue curve B in Fig. 2(a)], which rotates the spins by 180° from the $+z$ into the $-z$ direction. The difference between a decaying signal after a 4 ns pulse and further precession (i.e., for 6 and 8 ns pulses) is clearly visible.

As seen in Fig. 1(d), reversing the E field polarity will reverse B_{int} , which results in a reversal of the spin precession direction. When using a bipolar pulse sequence, which consists of two subsequent pulses with opposite polarity and equal width and magnitude, we expect spin reorientation of the spin packet to its original direction at the end. The red curve A in Fig. 2(a) shows spin manipulation by a bipolar pulse sequence with the same magnitude (4.8 V) and total width (4 ns) as the blue curve B for spin manipulation by a unipolar pulse. During the first 2 ns, both unipolar and bipolar pulses rotate the spin packet by $\pi/2$ into the sample plane. While spin precession for the unipolar pulse will continue to π rotation, spin precession is reversed during the subsequent 2 ns for bipolar pulses, which function as $-\pi/2$ pulses. Remarkably, at 4 ns the value $|\Theta_F|$ is larger for the bipolar pulse than for the unipolar pulse but less than the value obtained for free decay of the

ensemble (see dashed black curve for $\delta w = 0$). As Θ_F is a direct measure of the net spin moment, its increase indicates partial spin rephasing.

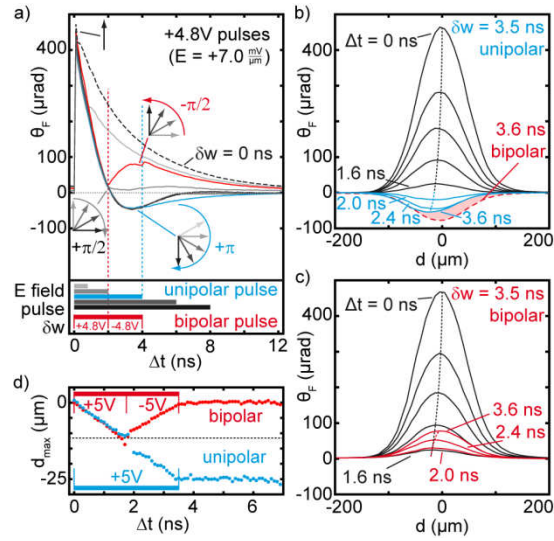


FIG. 2: (a) TRFR of optically created spin packets, which precess at $B_{\text{ext}}=0$ during E field pulses of different width δw . Spatiotemporal evolution of spin packet after spin manipulation by (b) unipolar and (c) bipolar pulse. The temporal spacing is 0.4 ns. The final spin distribution at 3.6 ns in (c) has been reversed and added as a dashed line in (b). (d) Drift of spin packet after manipulation with unipolar (blue) and bipolar (red) pulses of equal pulse width and magnitude.

To exclude that the different amplitudes result from the E field-induced drift of the spin packet away from the probe laser spot, we show a series of spatiotemporal profiles of the spin packet in Figs. 2(b) and 2(c) after unipolar and bipolar spin manipulation, respectively. The data have been taken by scanning the probe relative to the pump beam along the E field direction. While the spin packet drifts continuously to the left for unipolar pulses, it reverses the drift direction after 2 ns for bipolar pulses and returns to its original position thereafter [see also Fig. 2(d)]. To better compare the final spin distributions at 3.6 ns for both manipulation schemes, we added the respective curve from Fig. 2(c) with reversed sign as a red dashed line in Fig. 2(b). Despite their small difference in peak positions, the dashed red curve has an overall larger magnitude showing that drift effects are too small to account for the difference in amplitudes and that the observed effect is indeed caused by rephasing.

Work was supported by JARA-FIT, and by DFG through FOR 912.

- [1] D.D. Awschalom and N. Samarth, *Physics* **2**, 50 (2009).
- [2] Y. K. Kato *et al.*, *Science* **306**, 1910 (2004).
- [3] Y. K. Kato *et al.*, *Phys. Rev. Lett.* **93**, 176601 (2004).
- [4] S. Kuhlen *et al.*, *Phys. Rev. Lett.* **109**, 146603 (2012).

Noise Analysis of Qubits Implemented in Triple Quantum Dot Systems in a Davies Master Equation Approach

Sebastian Mehl and David P. DiVincenzo

Peter Grünberg Institut and Institute for Advanced Simulation, Forschungszentrum Jülich, Germany

We analyze the influence of noise for qubits implemented using triple quantum dot spin system. We give a detailed description of the physical realization and develop error models for the dominant external noise sources. We use a Davies master equation approach to describe their influence on the qubit.

For universal quantum computation the singlet-triplet qubit requires, in addition to intra-dot exchange interaction, a magnetic field gradient between the two quantum dots. It was natural to ask if a different coding of the qubit would enable universal computation with the exchange interaction alone; this is realized if the qubit is embodied by the states of three singly occupied quantum dots. The exchange coupling of at least two of the three dot pairs should be controllable. Laird et al. and Gaudreau et al. have now shown this universal exchange control experimentally of the three-electron states in a trio of quantum dots.

Model: The effective Hamiltonian H describing the triple quantum dot contains the exchange interaction between two neighboring quantum dot pairs. Additionally, an out of plane magnetic field is added. Our notations follow Laird et al.:

$$H = \frac{J_{12}}{4} (\sigma_1 \cdot \sigma_2 - 1) + \frac{J_{23}}{4} (\sigma_2 \cdot \sigma_3 - 1) - \frac{E_z}{2} \sum_{i=1,2,3} \sigma_z^i$$

J_{12} (J_{23}) represents the Heisenberg exchange interaction between two neighboring dots. It can be changed by applying an electric bias on the outer dots.

The coupling parameters J_{12} and J_{23} can be derived from a three site Hubbard Hamiltonian describing the quantum dot layout in 1:

$$H_{\text{Hubbard}} = \sum_{\alpha,s} \varepsilon_{\alpha} n_{\alpha,s} + \sum_{\alpha} U_{\alpha} n_{\alpha,\uparrow} n_{\alpha,\downarrow} + t \sum_{\langle \alpha, \beta \rangle, s} (a_{\alpha,s}^{\dagger} a_{\beta,s} + h.c.) \quad (1)$$

ε_{α} is the single particle energy, U_{α} the coulomb repulsion and t the tunnel coupling between neighboring quantum dots. For simplicity we take only tunneling into account for the left (right) quantum dot with the center dot ($(1,2)$ and $(2,3)$).

Additionally, we assume these tunnel couplings to be equal. When going from H_{Hubbard} to H , we take

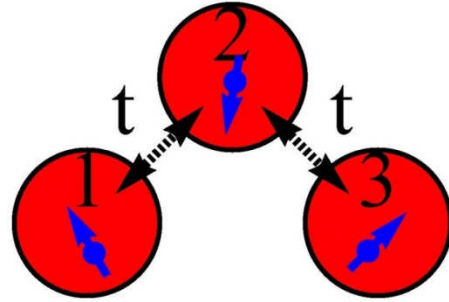


Fig. 1: Layout of the triple quantum dot setup: Each quantum dot is occupied with one electron. Neighboring dot pairs are tunnel coupled with the coupling strength t . An external electric bias is used to occupy either the left (dot 1) or the right (dot 3) quantum dot with two electrons.

into account single occupation of all three qubits $((1,1,1)$ -configuration) and use an electric bias to go to a double occupied left (right) dot $((2,0,1)$ and $((1,0,2)$ -configuration). For the double occupied states, we consider only the orbital ground state. One arrives at the exchange parameters:

$$J_{12} = \frac{\varepsilon_- - \varepsilon}{2} + \sqrt{\left(\frac{\varepsilon_- - \varepsilon}{2}\right)^2 + 2t^2} \quad (2)$$

$$J_{23} = \frac{\varepsilon - \varepsilon_+}{2} + \sqrt{\left(\frac{\varepsilon - \varepsilon_+}{2}\right)^2 + 2t^2} \quad (3)$$

For our later use we construct a subsystem and a subspace qubit inside the 8-dimensional Hilbert space spanned by the eigenstates of the triple dot Hamiltonian (1). The basis states of the subspace qubit define the computational subspace:

$\text{span}\{\Delta_{\frac{1}{2}}, \Delta'_{\frac{1}{2}}\}$. We identify the state $\Delta_{\frac{1}{2}}$ as logical "1", $\Delta'_{\frac{1}{2}}$ as logical "0". For the subsystem qubit we

use the larger subspace $\text{span}\{\Delta_{\frac{1}{2}}, \Delta'_{\frac{1}{2}}, \Delta_{-\frac{1}{2}}, \Delta'_{-\frac{1}{2}}\}$ as the computational subspace. We identify both states $\Delta_{\frac{1}{2}}$ and $\Delta_{-\frac{1}{2}}$ as logical "1" (represented by the quantum number $l=1$). The $l=0$ states are identified as logical "0". For the subsystem qubit the S_z -population does not matter. In the Nakajima-Zwanzig approach, we fix this population to a constant value.

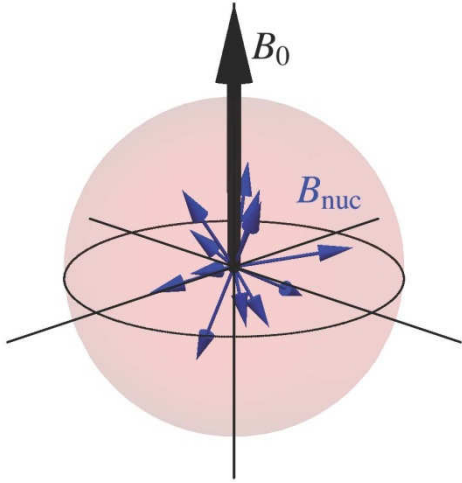


Fig. 2: Semiclassical picture used for the time evolution of a single electron spin in a distribution of hyperfine configurations. For every experiment the hyperfine field acts like a static magnetic field, which is randomly varying between every run of the experiment.

The thermal distribution over the Zeeman-split eigenstates will be a reasonable choice:

$$\rho_0^{s_z} = e^{-\frac{E_z \sigma_z}{T_K}} / \text{Tr} \left[e^{-\frac{E_z \sigma_z}{T_K}} \right]. \quad (4)$$

The eigenstates of the Hamiltonian H are:

$$Q_{\frac{3}{2}} = |\uparrow\uparrow\uparrow\rangle \quad (5)$$

$$Q_{\frac{1}{2}} = \frac{1}{\sqrt{3}} (|\uparrow\uparrow\downarrow\rangle + |\uparrow\downarrow\uparrow\rangle + |\downarrow\uparrow\uparrow\rangle) \quad (6)$$

$$\Delta_{\frac{1}{2}} = \frac{(J_{12} - J_{23} + \Omega)|\uparrow\uparrow\downarrow\rangle + (J_{23} - \Omega)|\uparrow\downarrow\uparrow\rangle - J_{12}|\downarrow\uparrow\uparrow\rangle}{\sqrt{4\Omega^2 + 2\Omega(J_{12} - 2J_{23})}} \quad (7)$$

$$\Delta'_{\frac{1}{2}} = \frac{(-J_{12} + J_{23} + \Omega)|\uparrow\uparrow\downarrow\rangle - (J_{23} + \Omega)|\uparrow\downarrow\uparrow\rangle + J_{12}|\downarrow\uparrow\uparrow\rangle}{\sqrt{4\Omega^2 + 2\Omega(2J_{23} - J_{12})}} \quad (8)$$

where $\Omega = \sqrt{J_{12}^2 + J_{23}^2 - J_{12}J_{23}}$. For later analysis we introduce the notation $W_{\frac{1}{2}}$, indicating the $s_z = \frac{1}{2}$ subspace ($W \in \{Q, \Delta, \Delta'\}$). All remaining eigenstates can be obtained by flipping all three spins, to obtain from the states $Q_{\frac{3}{2}}$ and $W_{\frac{1}{2}}$ the corresponding states $Q_{\frac{1}{2}}$ and $W_{\frac{1}{2}}$.

The eigenenergies of H are:

$$E_{Q_k} = -k \cdot E_z, k \in \left\{ \pm \frac{3}{2}, \pm \frac{1}{2} \right\} \quad (9)$$

$$E_{\Delta_{\pm \frac{1}{2}}} = -\frac{1}{2}(J_{12} + J_{23} - \Omega) \mp \frac{E_z}{2} \quad (10)$$

$$E_{\Delta'_{\pm \frac{1}{2}}} = -\frac{1}{2}(J_{12} + J_{23} + \Omega) \mp \frac{E_z}{2} \quad (11)$$

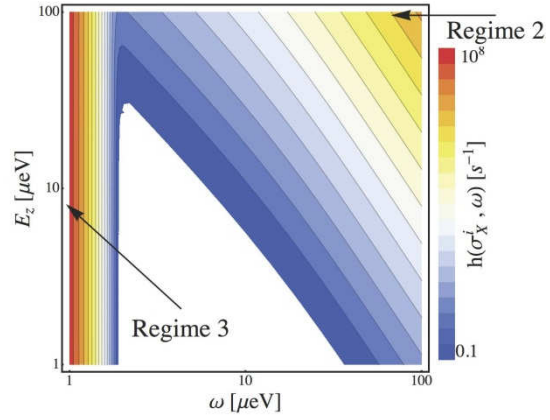


Fig. 3: Density plot of the transition rates for local spin relaxation $h(\sigma_x, \omega)$ as a function of the energy difference ω and the external magnetic field E_z . The influence of hyperfine interaction (Regime 2) and phonon interaction (Regime 3) can be separated due to the different parameter ranges when the effects are dominant. The hyperfine mechanism is independent of E_z .

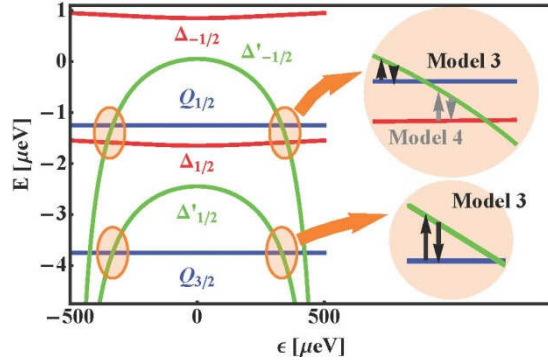


Fig. 4: Transition diagram for subsystem qubit when hyperfine interactions generate local spin flips. Large error rates are observed only at the region of level crossings. They can be described by leakage transitions to a quadruplet state or internal transitions between two states of the subsystem qubit.

The energy diagram is sketched in Fig. 4. For the upcoming analysis we introduce three quantum numbers (I, S, s_z) , which fully characterize the eigenstates. S describes the total spin of the eigenstates. It has the value $3/2$ for all Q_k -states and $1/2$ for the remaining ones. The s_z -quantum number labels the spin projection in z -direction. It has values $\pm 3/2$ and $\pm 1/2$. Furthermore we introduce a third formal quantum number I . It distinguishes the $\Delta_k (I=1)$ and $\Delta'_k (I=0)$.

For more details see [1]

[1] S. Mehl and D. P. DiVincenzo, Phys. Rev. B, in press.

Efficiency and Power of a Quantum Dot Energy Conversion Device

D.M. Kennes, D. Schuricht, and V. Meden

Institut für Theorie der Statistischen Physik, RWTH Aachen University, Germany

We study linear response and nonequilibrium steady-state thermoelectric transport through a single-level quantum dot tunnel coupled to two reservoirs held at different temperatures. A fermion occupying the dot interacts with those in the reservoirs by a short-ranged two-particle interaction. For parameters for which particles flow against a bias voltage from the hot to the cold reservoir this setup acts as an energy-conversion device with which electrical energy is gained out of waste heat. We investigate how correlations affect its efficiency and output power. In linear response the changes in the thermoelectric properties can be traced back to the interaction induced renormalization of the dots resonance line shape. In particular, small to intermediate repulsive interactions reduce the maximum efficiency. In nonequilibrium the situation is more complex and we identify a parameter regime in which for a fixed lower bound of the output power the efficiency increases.

Quantum dots (QDs) are considered as high-potential solid-state energy conversion devices to gain electrical energy out of waste heat [1]. In a minimal setup electrons from a hot right reservoir (at temperature T_R) are transported via a weakly coupled QD to a cold left one (at T_L) against a bias voltage $V = \mu_L - \mu_R \geq 0$ (elementary charge $e = 1$). Here μ_α denotes the chemical potential of reservoir $\alpha=L,R$. Within linear response, that is for small temperature differences and small bias voltages, one aims at a high efficiency η of energy conversion. It is defined as $\eta = P / |I_c|$, with the output power $P = V |I_c|$ and the charge/heat currents I_{ch} . As a measure of η in QD setups one often uses the so-called figure of merit ZT [1]; the larger ZT the closer η comes to its upper bound, the Carnot efficiency η_C . The electronic contribution to the figure of merit is inversely proportional to the Lorenz number. Under the assumption of scattering processes which on the scale $T_R \approx T_L \approx T$ only weakly depend on energy the Wiedemann-Franz law states that the latter is a material independent number. This in turn limits the electronic ZT in bulk materials which obey this law. In QDs due to the strong energy dependence of the transmission close to transport resonances the Wiedemann-Franz law does not apply as long as the temperature is larger than the resonance width Γ . Therefore, in transport through dots with sharp resonances a large figure of merit and thus a high efficiency can be realized [1,2]. Equivalently, QDs can be used as efficient solid-

state systems for cooling of nanoelectronic devices [3].

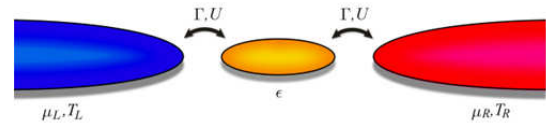


FIG. 1: The interacting resonant level model considered here constitutes a prototype model of a charge fluctuating quantum dots. Electrons in the left or right reservoir can tunnel to the central site (via a hybridization Γ). Electrons on the central site interact with electrons at the tip of the reservoir via a Coulomb interaction U . The central site has onsite energy ϵ which can be tuned by a voltage to an external gate.

Due to the confinement of electrons in QDs to meso- or nanoscopic regions the local Coulomb interaction becomes a relevant energy scale. This two-particle interaction strongly alters the line shape of resonances and thus the thermoelectric properties [2]. For example, the Kondo effect, resulting from correlated spin fluctuations, leads to a very sharp many-body resonance of width much smaller than the noninteracting Γ . This has crucial consequences for the thermoelectric transport [4]. Even in the absence of the Kondo effect correlated charge fluctuations affect the line width as was worked out in detail for the interacting resonant level model (IRLM), which will be considered here (see Fig.1). For weak to intermediate local Coulomb repulsions the interaction renormalized width Γ_{eff} is increased compared to the noninteracting one Γ , while for strong repulsive interactions as well as attractive ones $\Gamma_{\text{eff}} < \Gamma$. Effectively attractive interactions might be realized in molecular QDs with strong local electron-phonon coupling [5].

For vanishing interaction one can derive explicit expressions for the charge and heat current

$$I_c(\epsilon) = \frac{\Gamma}{2\pi} \text{Im} \left[\Psi \left(0, \frac{1}{2} + \frac{i}{2\pi T_R} [\epsilon - \mu_R - i\Gamma] \right) - \Psi \left(0, \frac{1}{2} + \frac{i}{2\pi T_L} [\epsilon - \mu_L - i\Gamma] \right) \right]$$

$$I_h(\epsilon) = (\epsilon - \mu_R) I_c(\epsilon) - \frac{\Gamma}{\pi} \oint d\epsilon' \frac{I_c(\epsilon')}{\epsilon - \epsilon'}.$$

Here $\Psi(0,x)$ is the Digamma function. For finite interaction we use the functional renormalization group approach to treat the full-fledged

nonequilibrium steady state of the IRLM [6] at weak interactions.

Linear response: In linear response one aims at the maximum efficiency achievable by varying ε and V at fixed temperature difference $|\Delta T|=|T_L-T_R| \ll \Gamma$. For this case one succeeds in making analytic predictions by substituting [7]

$$\Gamma_{\text{eff}} = \Gamma \left(\frac{2\Gamma}{D} \right)^{-2U},$$

for Γ in the charge and heat current formulae with D being the reservoirs' bandwidth. The results of the maximum efficiency for different temperatures are shown in the top panel of Fig. 2. The analytical data (lines) are very close to the full numerical solution (symbols) of the approximate functional renormalization group flow equations [6,7]. For attractive interactions the efficiency is considerably increased, while it is decreased for repulsive ones.

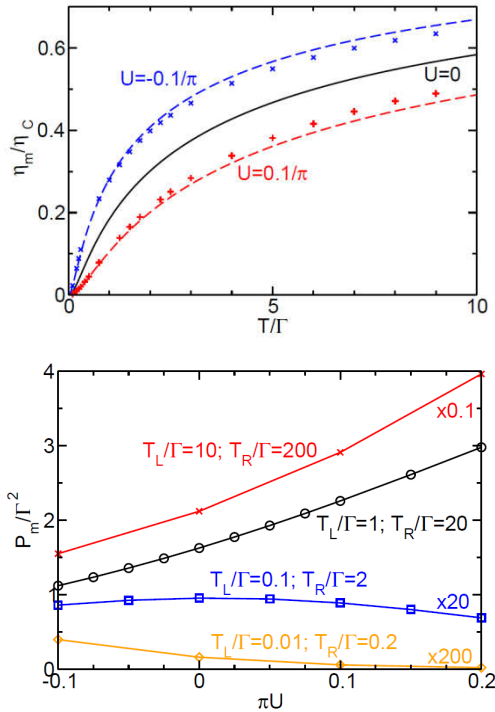


FIG. 2: Top: Linear response maximum efficiency for different temperatures. Lines are the analytical results, while symbols are the full numerical solution. For repulsive interactions the efficiency can be increased considerably. Bottom: Maximum power for different interaction strengths. Lines are guides to the eyes only. The data are scaled by the factors given in the figure to enhance the visibility of the features.

Far from equilibrium: For the far from equilibrium case we first aim at the maximum power output of the device (by again varying ε and V). We find that the emerging picture is much richer than in the linear response case [7]. Depending on the temperature difference the two-particle interaction enhances or suppresses the power output as shown in the bottom panel of Fig. 2. Increasing the interaction leads to a monotonic decrease in the efficiency for any temperature difference just as for the case of linear response.

We finally investigate a situation in which even a weak repulsive interaction can lead to an increase of the efficiency. Let us assume that our "heat engine" has to produce at least a certain minimal output power. This might e.g. be a sensible requirement if we are interested in charging a battery. For appropriate temperatures $T_{L/R}$ the maximum power increases with U (see Fig. 2) and one can hope to overcome the decrease of the efficiency. For fixed $T_{L/R}$ we proceed as follows: as our lower bound of the power P_{bound} we take the maximum power at $U=0$. This is a convenient choice to reduce the number of parameters. Varying ε and V we then search for the largest efficiency $\eta_>$ at fixed $U>0$ with $P>P_{\text{bound}}$. For, e.g., $T_L=1$ and $T_R=20$ and under the above requirement one can increase the efficiency by a few percent by turning on a small repulsive interaction as shown in Fig. 3.

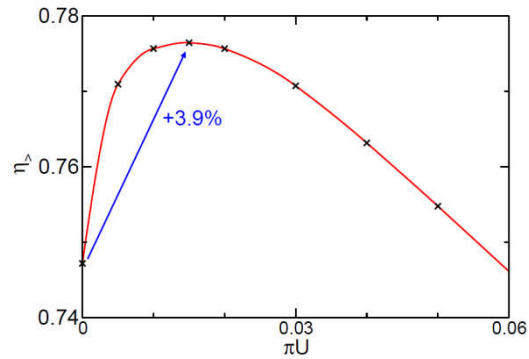


FIG. 3: Under the assumption that our 'heat engine' has to produce at least a certain minimal output power a weak repulsive interaction can lead to an increase of the efficiency. The lower bound P_{bound} is chosen as the maximum power at $U=0$. The temperatures are $T_L=1$ and $T_R=20$.

This work was supported by the DFG via FOR 723 (DK and VM) as well as the Emmy-Noether program (DS). We thank S. Andergassen for useful discussions.

- [1] G.D. Mahan, and J.O. Sofo, Proc. Natl. Acad. Sci., USA, 93, 7436 (1996).
- [2] P. Murphy, S. Mukerjee, and J. Moore, J., Phys. Rev., B, 78, 161406(R) (2008).
- [3] F. Giazotto, T.T. Heikkilä, A. Luukanen, A.M. Savin, and J.P. Pekola, Rev. Mod. Phys., 78, 217 (2006).
- [4] T.A. Costi, and V. Zlatić, Phys. Rev. B, 81, 23512 (2010).
- [5] S. Andergassen, T.A. Costi, and V. Zlatić, Phys. Rev. B, 84, 241107(R) (2011).
- [6] D.M. Kennes, and V. Meden, Phys. Rev. B, 87, 075130 (2013).
- [7] D.M. Kennes, D. Schuricht, and V. Meden, Europhys. Lett. 102, 57003 (2013)

Readout of carbon nanotube vibrations by intrinsic spin-phonon resonance

C. Ohm¹, C. Stampfer^{2,3}, J. Splettstoesser¹, and M. R. Wegewijs^{1,4}

¹ Institute for Theory of Statistical Physics, RWTH Aachen University, Germany

² Peter Grünberg Institut-9, Forschungszentrum Jülich, Germany

³ II. Physikalisches Institut B, RWTH Aachen University, Germany

⁴ Peter Grünberg Institut-2, Forschungszentrum Jülich, Germany

We propose a scheme for spin-based detection of the bending motion of a suspended carbon-nanotube using the curvature-induced spin-orbit interaction. We show that the resulting effective spin-phonon coupling can be used to down-convert the high-frequency vibration-modulated spin-orbit interaction to spin-flip processes at a much lower frequency. This vibration-induced spin-resonance can be controlled with an axial magnetic field and can be read out using a Pauli spin blockade scheme.

Carbon nanotubes (CNTs) are an ideal playground for realizing both spintronic nanodevices and high-frequency nano-electromechanical systems with high-Q resonators. Their development into quantum electromechanical systems however crucially relies on advanced schemes for their readout. Here, we propose a new scheme of *built-in, spin-based motion detection*, which allows for a sensitive readout of ultra-high frequencies and tiny vibration amplitudes. To utilize the cross talk of spin and vibrations via spin-orbit (SO) interaction for the readout of the vibration frequency and amplitude, one needs a selective sensitivity to spin-flip processes. This is provided by the well established technique of Pauli spin blockade spectroscopy, sensitive even to nuclear and impurity spins in nanotube quantum dots. A complementary work [1] has explored this spin-phonon coupling in the quantum limit.

We consider a CNT, *clamped* between a source, a central gate and a drain electrode, as in Fig. 1 (a). Only one part of the CNT is suspended while the other is fixed on the substrate. By electrostatic gating, two quantum dots are defined in the nanotube - one on the suspended part and one on the fixed part.

Spin-phonon coupling in nanotubes: We first focus on the suspended, vibrating part of the nanotube. In the presence of a high magnetic field, it constitutes a well-defined two-level spin system (TLS) with an effective spin-phonon coupling due to the interplay between SO interaction and flexural vibrations of the nanotube. The ground state multiplet of a CNT quantum dot formed by a strong confinement potential is nearly fourfold degenerate, and described by the product states $|S\tau\rangle$ of spin ($S \in \{\uparrow, \downarrow\}$) and isospin ($\tau \in \{K, K'\}$). For deflections with curvature radii much larger than

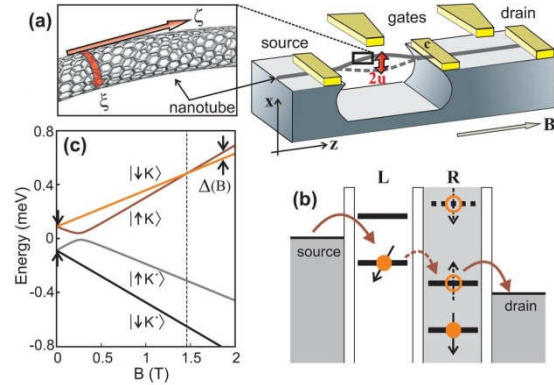


FIG 1: (a) Setup with a partly suspended, vibrating CNT. (b) Pauli spin blockade diagram: interdot tunneling is suppressed when an electron entering the left dot creates a triplet state with the electron trapped in the right (triplet with two electrons on the right dot involves a high orbital excitation, dashed level). Vibrations of the left dot can lift this blockade by rotating the spin through spin-phonon coupling, creating a singlet state which allows interdot tunneling to proceed through the ground state orbital. (c) Spectrum of a CNT, Eq. (1), as function of the magnetic field B applied along the unbent CNT.

the quantum dot length the quantum dot Hamiltonian for this subspace reads as [2]:

$$\hat{H}_d = -\Delta_{so} \mathbf{e}_z \cdot \hat{\mathbf{S}} \otimes \hat{\tau}_3 - \frac{1}{2} \Delta_{KK'} \hat{\tau}_1 + \mu_s \mathbf{B} \cdot \hat{\mathbf{S}} + \mu_{orb} \mathbf{B} \cdot \mathbf{e}_z \hat{\tau}_3. \quad (1)$$

where $\hat{\tau}_1, \hat{\tau}_3$ are Pauli operators acting on the valley (K, K') space. Here the curvature enhanced spin-orbit coupling, Δ_{so} , leads to a spin polarization along the nanotube axis \mathbf{e}_z in Fig. 1(a). Various types of disorder break the symmetry of the honeycomb lattice and lead to an inter-valley scattering term $\Delta_{KK'}$. Additionally, the external magnetic field, $\mathbf{B} = B\mathbf{e}_z$, applied along the axis of the unbent CNT, gives rise to an orbital and spin ($\hat{\mathbf{S}}$) Zeeman effect through μ_s and μ_{orb} . At high fields the spectrum in Fig. 1(c) splits into two sectors with fixed isospin and we concentrate on the TLS defined in the isospin K sector. The spin-phonon coupling arises when treating the vibrations as instantaneous deflections of the CNT. The displacement of a point on the nanotube is given by the vector $\mathbf{u}(z, t)$ in Fig. 1(a). For deflections small relative to the nanotube length the time-dependent tangent vector of the vibrating CNT – written as function of z , with the coordinate

z along the axis of the unbent nanotube – reads $\mathbf{e}_z \approx \mathbf{e}_z + \frac{d}{dz} \mathbf{u}(z, t)$. The quantum dot located on the vibrating part of the CNT is then described by \hat{H}_d plus the effective spin-phonon Hamiltonian $\hat{H}_{s-ph} = \lambda \cos(\alpha t) \hat{S}_x \otimes \hat{\tau}_{3s}$. The coupling constant depends on the vibrational amplitude as well as on the spin-orbit coupling strength: $\lambda = \Delta_{so} \frac{du_x}{dz}$.

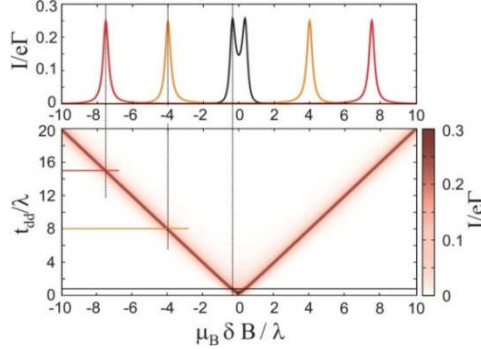


FIG. 2: Charge current as function of the magnetic field detuning $\delta B = B - B_{res}$ from the resonant value ($\Delta(B_{res}) = \hbar\omega$) and the inter-dot tunneling t_{dd} , both in units of λ .

For high magnetic fields $B \approx B_{cross}$ (cf. Fig. 1(b)) the isospin decouples from the real spin states and we can project onto the isospin- K sector, obtaining a standard electron spin resonance (ESR) situation:

$$\hat{H}_{ESR} = \Delta \hat{S}_z + \lambda \cos(\alpha t) \hat{S}_x \quad (2)$$

where \hat{S}_x , \hat{S}_z are the electron spin 1/2 operators. The energy splitting Δ of the TLS, indicated in Fig. 1(a), is clearly tunable with the magnetic field.

Down-mixing the high-frequency spin-orbit field: The flexural mode of the vibrating CNT of interest is supposed to have a high frequency $f = \omega/(2\pi) \approx 2 \text{ GHz} \sim 8.3 \text{ } \mu\text{eV}$. Importantly, when tuning Δ to match the frequency ω in order to affect the spin states via the spin-phonon coupling, the coupling is relatively small, $\lambda \ll \Delta$, giving a narrow spin-resonance of width $\sim \lambda$. There, the transverse component of the spin performs a Larmor precession with a high-frequency $\Delta \sim \omega$, whereas the z component oscillates at the Rabi-

frequency $\Omega_R = \hbar^{-1}[(\Delta - \hbar\omega)^2 + (\frac{\lambda}{2})^2]^{\frac{1}{2}}$ and the time-dependent spin-flip probability is $W_{\uparrow\downarrow}(t) \propto \sin(\Omega_R t / 2)$.

At resonance, $\Delta \sim \omega$, the down-conversion of the original driving frequency is maximal, $\omega/\Omega_R \sim 2\hbar\omega/\lambda \approx 1700$ for typical CNT parameters. One can thus detect high-frequency vibrations by using the spin-phonon resonance effect.

Readout using Pauli spin blockade: One can detect the vibration directly by measuring the charge current in a double dot setup in the spin-are coupled with interdot tunnel amplitude t_{dd} , controlled by the center gate voltage, and by blockade regime, as shown in Fig. 1(b). The dots Coulomb charging effects. Only the left dot

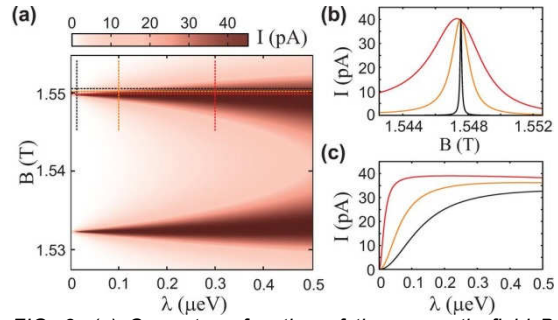


FIG. 3: (a) Current as function of the magnetic field B and the coupling λ and vertical and horizontal cuts in (b) and (c).

due to spin-phonon coupling. In the high magnetic field regime, we can focus on those energy levels of the left and right quantum dot, $\alpha \in \{L, R\}$ differing only by the spin degree of freedom, $s \in \{\uparrow, \downarrow\}$, that we denote by $\varepsilon_{\alpha s}$. We tune the double dot into the spin-blockade regime by gating the right dot such that it is always occupied by an electron with $s = \downarrow$, see Fig. 1(b). As soon as an electron with spin $s = \downarrow$ enters the left dot, transport is blocked, until a transition between triplet and singlet states occurs due to the time-dependent spin-orbit field induced by the vibrations. In Fig. 2 the calculated low-temperature leakage-current ($V_{bias}, \Delta \gg k_B T$) exhibits two sharp resonances as function of the two experimentally tunable parameters, B and t_{dd} (tunable through the central gate): when $\Delta \approx \hbar\omega \pm t_{dd}$, the magnetic field tunes the vibration into resonance with the spin, making the spin-flip rate maximal. For typical CNT parameters and $t_{dd} = 1.0 \text{ } \mu\text{eV}$, $\Gamma = 1 \text{ GHz}$, the maximal leakage current is on the order of 40 pA . The vibrational frequency can be determined – independent of t_{dd} – from $\hbar\omega = \frac{1}{2}[\Delta(B_1) + \Delta(B_2)]$ and the required value of Δ_{so} can be obtained independently by measuring the spectrum in Fig. 1(c). For $\Delta_{KK'} \ll |\Delta_{so} \pm 2\mu_{orb} B|$ this simplifies to $\hbar\omega \approx \frac{1}{2}\mu_s(B_1 + B_2) - \Delta_{so}$ and Δ_{so} can be read off directly at $B = 0$ in Fig. 1(c). Note, that for the readout one has to measure the absolute field strength. The variable δB , used in Fig. 2 for clarity, is not a measurable quantity, because the value of B_{res} is unknown. As shown in Fig. 3(a), the readout depends strongly on the coupling constant λ and through this on the deflection amplitude, $\frac{du_x}{dz} = \lambda / \Delta_{so}$. In Fig. 3(c), we show the sensitivity of

the near-to resonant current to the vibration amplitude which is tunable with the magnetic field. Thus amplitude readout is possible, as well. Our scheme is estimated to be even able to resolve ground state fluctuations when a magnetic field resolution in the regime of mT is available. In addition, the presented detection scheme might be also very interesting for highly sensitive nanotube resonator-based mass and strain sensing.

- [1] A. Pályi et. al., Phys. Rev. Lett. 108, 206811 (2012)
- [2] Flensberg and C. M. Marcus, Phys. Rev. B 81, 195418 (2010)
- [3] C. Ohm et. al., Appl. Phys. Lett. 100, 143103 (2012)

Multi-wavelength polar-dielectric superlens and graphene superlens

P. Li and T. Taubner

I. Institute of physics (IA), RWTH Aachen University, Germany

A superlens is a very promising device to overcome the diffraction limit and resolve subwavelength features. However, the practical application of the superlens is limited by its narrow bandwidth. For dispersive materials, this condition limits operation to a very small wavelength range for each material system. In order to overcome this bandwidth limitation of superlenses, we propose two new designs based on layered materials: a multi-wavelength superlens using different polar dielectrics and a frequency-tunable graphene superlens.

A so-called superlens (SL) is capable of imaging the samples at subwavelength resolution by using a thin slab of a material with negative permittivity [1]. In principle, due to the small effective wavelength of surface modes at the interfaces between the negative-permittivity layer and positive-permittivity host, the SL can be seen as a practical version of perfect lens allowing for non-diffraction-limited imaging and sensing. However, a practical limitation in the SL is the narrow bandwidth. Although the surface resonance contributes a lot to the ultrahigh resolution of the SL, it also constrains that the SL can only work in the frequency range close to the resonance [2], which limits superlenses in spectroscopic applications.

In order to overcome this limitation, we present two possibilities based on layered materials. The first idea is a multi-wavelength SL [3] with layered phonon-resonant dielectrics. This proposed scheme is based on the fact that increasing the number of phonon resonant dielectrics in a multilayered system can provide additional degrees of freedom for superlensing at multiple wavelengths. In other words, a subwavelength image can be achieved at many different wavelengths by only one single lens. Considering the abundance of polar dielectrics, the wavelength range of our lens can cover from IR to THz frequencies by choosing suitable materials.

Generally, the superlensing effect requires a matching condition $\epsilon_{\text{lens}}(\lambda) = -|\epsilon_{\text{host}}(\lambda)|$, where ϵ_{host} is the permittivity of the host medium interfacing the lens [1]. For dispersive materials, this condition limits operation to a small wavelength range for each material system. For example, the condition is met at a wavelength of around 365 nm for silver-polymer combination [4], and 11 μm [2] for SiC-SiO₂ case. Our design is based on a multilayer (ML) superlensing theory. The superlensing condition $\epsilon_{\text{lens}}(\lambda) = -|\epsilon_{\text{host}}(\lambda)|$ can be fulfilled in two cases: (1) $\epsilon_1 > 0$, $\epsilon_2 < 0$ and (2) $\epsilon_1 < 0$, $\epsilon_2 > 0$. Polar

dielectric layers, such as SiC, indium phosphide (InP), indium antimonide (InSb), can provide additional degrees of freedom for achieving superlensing at different wavelengths. As shown in Fig.1, dielectric permittivities of polar dielectrics are negative in the so-called *reststrahlen* band between the transverse and longitudinal optical-phonon frequencies. When the wavelength is out of the *reststrahlen* band, their permittivities become positive.

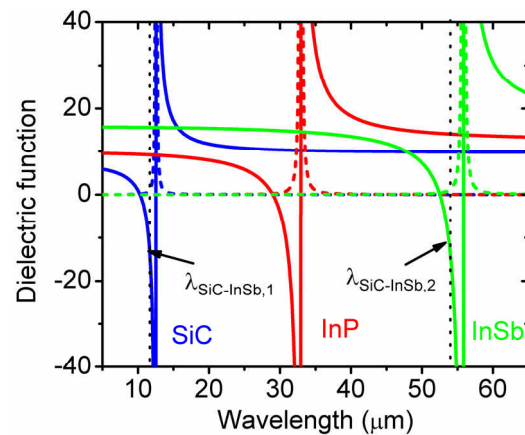


FIG. 1: Real parts (solid lines) and imaginary parts (dashed lines) of dielectric permittivities of SiC, InP and InSb. Black dotted lines indicate the matched wavelengths of SiC-InSb system

Exploiting different phonon resonances of multiple polar dielectrics can easily provide a possibility of superlensing simultaneously at multiple wavelengths. It is clearly seen in Fig.1 that the superlensing conditions for a SiC-InSb system are matched at two distinct wavelengths: $\text{Re}[\epsilon_{\text{InSb}}] = -\text{Re}[\epsilon_{\text{SiC}}] = 15.6$ at $\lambda_1 = 11.7 \mu\text{m}$, and $\text{Re}[\epsilon_{\text{InSb}}] = -\text{Re}[\epsilon_{\text{SiC}}] = -9.9$ at $\lambda_2 = 53.7 \mu\text{m}$. Moreover, respective absorption of the two materials is small at these matching wavelengths, which will significantly improve the resolution of our SL. Our further numerical simulations also confirm that a subwavelength sized Au slit can be well resolved by a SiC-InSb SL at these two different wavelengths (see ref.3).

The second idea is to design a frequency-tunable “graphene superlens” (GL) [5]. This novel graphene-based device enables the enhancement of evanescent waves for near-field subwavelength imaging. Due to the non-resonant enhancement provided by the graphene sheets, this graphene lens yields new promising properties including broad intrinsic bandwidth and low sensitivity to loss, together with a still good subwavelength resolution of around $\lambda/7$ for a bilayer case and over

$\lambda/10$ for the multilayered configuration. Most importantly, due to the large frequency-tunability via the dynamical tuning of chemical potentials μ_c , our proposed graphene lens can act as an ultrabroadband sub-diffraction-limited imaging device to in principle cover the nearly whole range from mid-IR to THz frequencies.

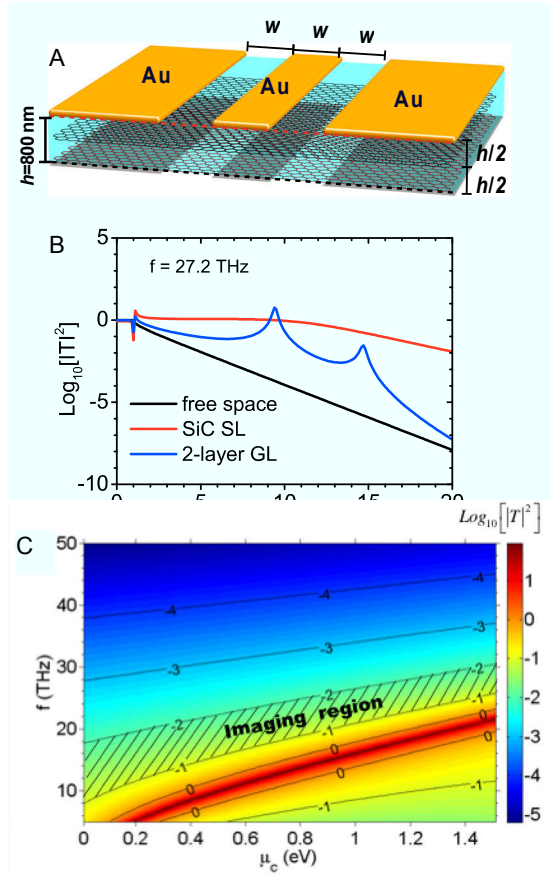


FIG. 2: A. Sketch of a 2-layered GL under the Au double slit. B. Comparison of the OTF for the SiC superlens, 2-layer GL and the case in free space. C. The broadband frequency-tunability in a GL.

In order to show this important effect, we start with a bilayer GL as illustrated in Figure 2A, where two GSs are embedded in a host dielectric medium with a permittivity of $\epsilon_h=3$. The total thickness of the GL is $h=800$ nm. To better show this performance, we compare optical transfer functions (the transmittance of high- k_x components) of the double-layer GL, the SiC-SL and the case of free space at the same frequency $f=27.2$ THz (≈ 11 μm , the resonance of the SiC-SL) in Figure 2B. It is clearly seen that in free space the transmittance of subwavelength components decays very fast. On the other hand, in the SiC-SL the transmittance for all evanescent waves is uniformly amplified due to the resonant nature of surface modes at the matching SiC-SiO₂ interface, leading to nearly perfect imaging in the near field. Interestingly, the bilayer GL is an intermediate case between the SL and the case of free space. This near-field enhancement leads to the subwavelength imaging in our graphene lens.

The biggest advantage of using graphene for subwavelength imaging is the frequency tunability. In Figure 2C, we show the contour plot of the transmittance as a function of the chemical potential μ_c and frequency f . In principle, the imaging frequency range (marked with oblique lines) of the GL can be continuously tuned from mid-IR to THz frequencies when we decrease the chemical potential from 1.5 eV to 0.1 eV. For example, the frequency corresponding to $|T|=0.3$ (for $k_x=7k_0$) will shift from 27.2 THz to 13 THz when we change the μ_c from 1.5 eV to 0.2 eV. And for a reasonable doping level $\mu_c \leq 1.2$ eV, as seen from Figure 3b, the operating frequencies of our 2-layered GL are covering the range from 28 THz (maximum covered frequency at $\mu_c=1.2$ eV) to 8 THz (minimum covered frequency at $\mu_c=0.1$ eV). With this large tunability of imaging frequencies, our bilayer GL can definitely act as an ultra-broadband subdiffractive imaging system at IR and THz regimes.

Besides these presented exciting results, the GL concept further offers other bright prospects: for example, a possibility is to roll the planar GL into a cylindrical shape, which may provide a tunable magnifying lens for far-field imaging at IR and THz frequencies. Moreover, since graphene is two-dimensional (2D) conducting sheet, our concept of using conducting sheets for subwavelength imaging can also be generalized to that of a "conducting sheet lens" (CSL) and easily transferred to other conventional systems like 2D electron gases (2DEG), opening up various exciting ways to achieve broadband subwavelength imaging with semiconductor heterostructures.

This work was supported by the Excellence Initiative, the Ministry of Innovation of North Rhine-Westphalia, the DFG under the SFB 917.

- [1] J. B. Pendry, Phys. Rev. Lett. 85, 3966 (2000)..
- [2] T. Taubner, D. Korobkin, Y. Urzhumov, G. Shvets and R. Hillenbrand, Science 313, 1595 (2006).
- [3] P. Li and T. Taubner, Opt. Express 20, 11787 (2012).
- [4] N. Fang, H. Lee, C. Sun and X. Zhang, Science 308, 534 (2005).
- [5] P. Li and T. Taubner, ACS Nano 6, 10107 (2012)

Strong correlations on topological insulator surfaces and the breakdown of the bulk- boundary correspondence

Manuel J. Schmidt

Institut für Theoretische Festkörperphysik, RWTH Aachen University, Germany

There is a widespread belief that the topological classification of the bulk of an insulator gives information about the presence or absence of gapless surface states: if the bulk topological index is non-trivial, surface states are guaranteed. This relation is known to solid-state physicists as the bulk-boundary correspondence. In the present work a simple scenario is studied which shows that this bulk-boundary correspondence does not hold if electron-electron interactions are involved. In special cases this breakdown occurs even for arbitrarily weak interactions.

The topological classification of insulating band structures started in the early 1980s with the work of Thouless, Kohmoto, Nightingale, and Nijs about the geometric origin of the quantum Hall effect [1]. They calculated a certain integer number (the TKNN integer) from a bulk band structure of a time-reversal symmetry broken two-dimensional electron gas (2DEG), and were able to show that this integer number is proportional to the Hall conductance. Thus, the Hall conductance must be quantized. On the other hand, the quantum Hall effect is known to be tightly connected to one-dimensional edge states in that each edge state contributes one quantum of conductance. Thus, the TKNN integer, calculated from a bulk 2DEG, i.e., with periodic boundary conditions, counts the number of edge states, a relation which is known as bulk-boundary correspondence (BBC). This is remarkable in at least two respects: (1) although, the TKNN integer is usually calculated with periodic boundary conditions, it makes predictions about arbitrary geometries. (2) Knowing the TKNN integer of the bulk region of a 2DEG, one needs not care about the (possibly complicated) details of its boundaries; the edge properties are enforced by the bulk topology. These two aspects are certainly related, but they emphasize the theoretical and experimental advantages of topological classifications, respectively. (1) tells a theorist that he may perform his calculations in a simple bulk system in which crystal momentum is a good quantum number, and yet make predictions about very complicated geometries with all kinds and shapes of edges. On the other hand, (2) tells the experimentalist that once he has carefully designed the bulk of his system, he gets the edge physics for free – this is why the quantum Hall effect gives rise to such a perfect quantized conductance.

With the advent of topological insulators (TIs) the variety of materials with non-trivial topology was

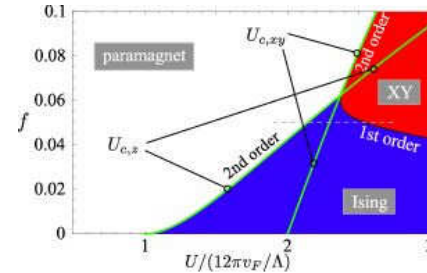


Fig.1: Phase diagram of the normal Dirac cone, i.e., $g_3 = g_5 = 0$. There exists a paramagnetic phase for small interaction and polarized phases for larger interactions. In the Ising phase with an easy axis anisotropy the mean-field theory may be expected to be applicable far from the phase transitions. In the XY phase with an easy-plane anisotropy the mean-field treatment is expected to break down.

greatly increased [2]. Even the dimensionality of a TI may vary. However, since TIs are time-reversal invariant, the traditional topological invariant of TKNN is always trivial there and the topological classification is based on other invariants. Again, these invariants may be calculated in the bulk, and, as long as the system under consideration is effectively non-interacting, there is a BBC for TIs, enforcing the presence of gapless boundary states in case of a non-trivial bulk. Recently, the topological classification of TIs has been generalized to include electron-electron interactions [3]. In particular, it was shown that

$$n = \frac{\pi}{6} \int \frac{d^4 k}{(2\pi)^4} \text{Tr} \varepsilon^{\mu\nu\rho\sigma} \quad (1)$$

$$\times [G \partial_\mu G^{-1} G \partial_\nu G^{-1} G \partial_\rho G^{-1} G \partial_\sigma G^{-1} G \partial_\sigma G^{-1} G \partial_\mu G^{-1}]$$

is an integer. Here, G is the full Green's function (including interactions). In the non-interacting limit $G \rightarrow G_0$ and n is identical to the ordinary non-interacting topological index. In both cases, i.e., with and without interactions, a bulk insulator with $n=0$ ($n=1$) is called topologically trivial (nontrivial). It is not clear, however, in how far the BBC holds in the presence of electronic interactions. I will now give a simple argument that the BBC may indeed be violated in three-dimensional TIs.

The argument starts with noting that in the limit of vanishing interactions the generalized invariant n

reduces to the non-interacting one for which the BBC holds, and that n is invariant under infinitesimal changes of the interacting model Hamiltonian. Thus, as long as there are no interactions, a surface with one single Dirac cone must be the boundary of a topologically nontrivial insulator with $n = 1$. Now we adiabatically switch on the electron-electron interactions (the strength of which is quantified by a Hubbard U), but make sure that it is still weak compared to the typical energy scales of the bulk (quantified by the band gap Δ). For sufficiently small U/Δ one will thus find $n = 1$ also from the generalized formula Eq. (1). Thus, if it can be shown that the single surface Dirac cone acquires a gap for arbitrarily small U/Δ , the interacting BBC is violated. In the remainder of this paper this will be done on the basis of a generalized interacting effective model for one surface Dirac cone.

The non-interacting Dirac cone dispersion is modeled by

$$H_0 = (v_F + g_3 \mathbf{k}^2 + g_5 \mathbf{k}^4 + \dots)(k_x s_x + k_y s_y), \quad (2)$$

where v_F is the ordinary Fermi velocity, $\mathbf{k} = (k_x, k_y)$ is the surface momentum, and s_μ are Pauli matrices. The usual Dirac cone with linear spectrum is recovered by setting $g_3 = g_5 = 0$. However, there is nothing about the bulk topological classification that restricts the choice the higher order momentum terms (as long as they are odd in \mathbf{k}).

The electron-electron interaction is modeled in a Hubbard-type fashion. However, it is important to note that one single Dirac cone cannot be described with a two-dimensional real-space model. Thus, we formulate also the interaction in momentum space

$$H_1 = \frac{U}{L^2} \sum_{\mathbf{k}, \mathbf{k}', \mathbf{q}} \Gamma(\mathbf{k}, \mathbf{k}', \mathbf{q}) c_{\mathbf{k}+\mathbf{q}\uparrow}^\dagger c_{\mathbf{k}\uparrow} c_{\mathbf{k}'-\mathbf{q}\downarrow}^\dagger c_{\mathbf{k}'\downarrow}, \quad (3)$$

where $a_{\mathbf{k},\sigma}$ annihilates surface state electron with momentum \mathbf{k} and spin σ . In the original two-dimensional Hubbard model $\Gamma(\mathbf{k}, \mathbf{k}', \mathbf{q}) = 1$. For surface state electrons, however, $\Gamma(\mathbf{k}, \mathbf{k}', \mathbf{q})$ is governed by the transverse wave function shapes of the edge states, which delocalize into the bulk as the edge states leave the bulk energy gap. Thus, $\Gamma(\mathbf{k}, \mathbf{k}', \mathbf{q}) \rightarrow 0$ if one of the fermion momenta $|\mathbf{k}+\mathbf{q}|$, $|\mathbf{k}|$, $|\mathbf{k}'-\mathbf{q}|$, $|\mathbf{k}'|$ hits a certain ultraviolet cutoff Λ , which is on the order of the momentum at which the edge states leave the band gap.

We perform an $SU(2)$ -invariant mean-field decoupling of the Hubbard Hamiltonian (3), which leads to an expression $E_{\text{tot}}(\mathbf{m})$ for the total energy in dependence of the magnetization vector \mathbf{m} . Minimization of $E_{\text{tot}}(\mathbf{m})$ w.r.t. \mathbf{m} gives rise to the phase diagram.

We start with the conventional Dirac cone, i.e., $g_3 = g_5 = 0$ and $v_F \neq 0$. The remaining parameters are the filling f relative to half-filling (Fermi-level at the Dirac point) and U/v_F . Figure 1 shows the corresponding phase diagram. At half-filling there exists a polarized Ising phase for $U > 12\pi v_F \Lambda$. In

this phase the surface spectrum acquires a gap right at the Dirac point. If one could show that for such an interaction strength the bulk topological number is still nontrivial, this would already be a demonstration of the BBC breakdown. However, since the bulk band gap $\Delta \sim v_F \Lambda$, the required $U \sim 12\pi \Delta$ for driving the Ising phase transition in the $g_3 = g_5 = 0$ case is also large from a bulk perspective.

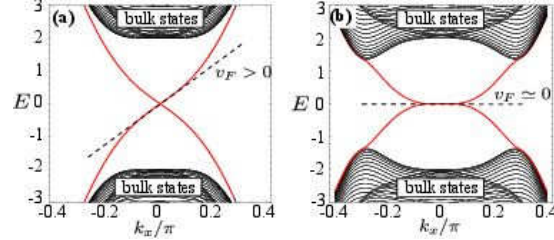


Fig. 2: Tuning the surface state Fermi velocity without changing the bulk gap. The band structure is calculated from a three-dimensional tight-binding model for TIs.

In order to reduce the critical interaction strength one may use the freedom of adding higher order momentum terms in the Dirac cone dispersion to decrease v_F while the bulk gap $\Delta \sim v_F \Lambda + g_3 \Lambda^3$ remains large. This may be done directly in the effective model [Eq. (2)], but may also be seen in a more elaborate 3D lattice model for a TI. In Fig. 2 one can see the surface state dispersion together with the bulk states in case of large $v_F \sim \Delta \Lambda$ (a) and vanishing v_F (b). In both cases the bulk energy gap is of the same order of magnitude.

Finally, we show that in the limit $v_F \rightarrow 0$ with constant Δ the critical U vanishes. An explicit formula for the critical $U_c(v_F)$ may be given (see Ref. mypaper), but is very lengthy. An approximation for $v_F 0.1 \Delta / \Lambda$ reads

$$U_c \cong \frac{8\sqrt{v_F g_3}}{1 - v_F / g_3 \Lambda^2 + \sqrt{v_F / g_3 \Lambda^2} \log(v_F / g_3 \Lambda^2)} \quad (4)$$

and shows that U_c indeed vanishes for $v_F \rightarrow 0$. This means that an arbitrary small U is in principle sufficient to remove the gapless surface states, if their non-interacting spectrum is tuned appropriately. However, as argued above, arbitrarily small U are not sufficient to change the bulk topological index from non-trivial to trivial. Thus, the BBC is violated in a weakly interacting topological insulator if the surface state dispersion is tuned such that the linear terms are suppressed, while the cubic terms keep the bulk gap open.

- [1] D. J. Thouless, M. Kohmoto, M. P. Nightingale, and M. den Nijs, Phys. Rev. Lett. 49, 405-408 (1982).
- [2] M. König et al., Science 318, 766 (2007); C. L. Kane and E. J. Mele, Phys. Rev. Lett. 95, 226801 (2005); X.-L. Qi, T. L. Hughes, and S.-C. Zhang, Phys. Rev. B 78, 195424 (2008).
- [3] Z. Wang, X.-L. Qi, and S.-C. Zhang, Phys. Rev. Lett. 105, 256803 (2010).
- [4] M. J. Schmidt, Phys. Rev. B 86, 161110(R) (2012).

Higgs transition in quantum spin ice $\text{Yb}_2\text{Ti}_2\text{O}_7$

Y. Su¹, L.J. Chang², and S. Onoda³

¹ Jülich Centre for Neutron Science, Forschungszentrum Jülich, Germany

² Department of Physics, National Cheng Kung University, Taiwan

³ Condensed Matter Theory Laboratory, RIKEN, Japan

In classical spin ice, magnetic monopoles emerge as classical defects and interact via the magnetic Coulomb law. In the quantum version of spin ice where quantum fluctuation dominates, these magnetic charges are carried by fractionalized bosonic quasi-particle spinons, which can undergo a Bose-Einstein condensation through a first-order transition via the Higgs mechanism. Evidence on such an exotic phase transition has indeed been obtained in a polarized neutron scattering experiment carried out on a high quality single-crystal sample $\text{Yb}_2\text{Ti}_2\text{O}_7$ at the diffuse scattering spectrometer DNS that is operated by JCNS at FRM II. The results are explained on the basis of a quantum spin ice model, whose high-temperature phase is effectively described as a magnetic Coulomb liquid, whereas the ground state is a nearly collinear ferromagnet, which can be regarded as a Higgs condensate of fractionized quasi-particles hosting dissipationless monopole current of spins.

Magnetic monopoles can be regarded as the magnetic version of a charged particle like electrons

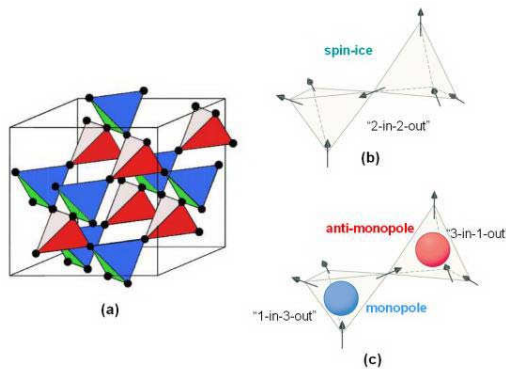


FIG. 1: (a) Lattice structure of $\text{Yb}_2\text{Ti}_2\text{O}_7$ where the spins reside at the corners of the adjacent tetrahedral. (b) The spins at the corners of a tetrahedron can point either inwards or outwards. In each tetrahedron, there are two spins inwards and two outwards, similar to the arrangement of the water molecules in a water ice crystal. This “ice rule” permits various degenerate ground states with a “2-in and 2-out” configuration. (c) Excitations and geometric deviations can cause magnetic defects (“3-in and 1-out” or “1-in and 3-out”) which lead to the emergence of north or south poles on the inside and which reproduce across the lattice structure, which means that the centre of the tetrahedron can be seen as a magnetic monopole.

and protons. They carry an isolated magnetic pole, either the North or the South poles. Normally magnets come in the form of dipoles, with both North and South poles appearing in pairs. Recent neutron scattering [1-2] and magneticity experiments have identified the low-temperature state of the dipolar spin ice pyrochlore compounds $\text{Ho}_2\text{Ti}_2\text{O}_7$ and $\text{Dy}_2\text{Ti}_2\text{O}_7$ as a classical magnetic Coulomb phase, which hosts the emergent magnetic monopoles obeying the magnetic Coulomb law. This classical Coulomb phase is characterized by dipolar spin correlations with power-law decay. In this class of spin ice materials, four electron spins residing at the corners of a tetrahedron will be compromised to a spin configuration of “2-in and 2-out” toward to the center of the tetrahedron, i.e. obeying the “ice rule” as in the water ice crystal (as schematically shown in Fig. 1). When a spin is excited and reverse its direction, emergent magnetic monopoles can be created as a classic defect that interacts with each other via the magnetic Coulomb law.

However, in the quantum version of spin ice, where spins can rotate away from the strict “in” and “out” spin configuration as imposed by local single-ion anisotropy, magnetic monopoles may appear as fractionalized pseudospin-1/2 bosonic quasi-particle spinons. Thus, these systems provide a unique playground to study the intriguing quantum dynamics of monopolar spinons. It has recently been suggested that pyrochlore $\text{Yb}_2\text{Ti}_2\text{O}_7$ can be a prototypical system described by an effective pseudospin-1/2 quantum spin ice model owing to its Kramers doublet ground state and a high-lying first excited state. Furthermore, the exact nature of the intriguing phase transition at ~ 0.21 K in this compound as indicated in earlier specific heat, Mössbauer and μSR etc. experiments has yet to be established.

We have recently performed polarized neutron scattering experiments on single crystal $\text{Yb}_2\text{Ti}_2\text{O}_7$ at the high-flux polarized diffuse neutron scattering spectrometer DNS at FRM II [3]. A $^3\text{He}/^4\text{He}$ dilution refrigerator was used for the measurements in the temperature range 0.02-1 K. A neutron wavelength of 4.74 \AA was chosen in the experiments. The [1–10] direction of the crystals was aligned perpendicular to the horizontal scattering plane so that the (h, h, l) reciprocal plane can be mapped out by rotating the sample step by step. The neutron polarization at the sample position was aligned along the [1–10], perpendicular to the (h, h, l) plane,

allowing us to probe the scattering intensities in the spin-flip (SF) and the non-SF (NSF) channels as well as for the sum of these two channels. The magnetic diffuse scattering pattern in the (h, h, l) reciprocal plane measured at 0.3 K is shown in Fig. 2 (a). A broad intensity from (000) through (111) to (222) is identified in the sum (Fig. 2a, right), as previously reported in unpolarized neutron scattering experiments. This feature is dominant in the NSF channel (Fig. 2a, middle). The [111]-rod scattering is accompanied by a branch from (111) to (220) in the SF channel (Fig. 2a, left), and by another from (222) towards (004) in the NSF channel (Fig. 2a, middle). The anisotropic nature of the spin correlations is clearly seen around (111) in the SF channel (Fig. 2a, left), suggesting a remnant of the pinch-point singularity as a signature of an unusual finite-temperature paramagnetic phase, which in practice can be described as a classical magnetic Coulomb liquid. The experimental observations have been well reproduced in our theoretical calculation based on an effective pseudospin-1/2 quantum spin ice model (as shown in Fig. 2 (b)). These results thus strongly support the scenario that the high-temperature phase of $\text{Yb}_2\text{Ti}_2\text{O}_7$ is a classical magnetic Coulomb liquid, which hosts the pinch-point features and monopolar spinons that are deconfined with finite excitation energy.

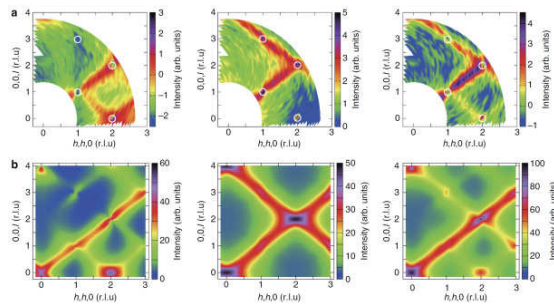


FIG. 2: (a) Experimentally observed profiles for the spin-flip (SF) (left), non spin-flip (NSF) (middle) and total (right) magnetic diffuse neutron scattering cross-sections in the (h, h, l) plane above T_C at $T = 0.3$ K. (b) Theoretically calculated magnetic profiles via RPA for the SF (left), NSF (middle) and total (right) magnetic diffuse neutron scattering cross-sections [3].

Below $T_C \approx 0.21$ K we observe that the rod-like diffuse scattering along the [111] directions and the pinch-point features are suddenly suppressed, and the incident polarized neutron beam is completely depolarized. This is ascribed to the formation of macroscopic ferromagnetic domains. The first-order nature of the phase transition is revealed via the observation of a thermal hysteresis around T_C (as shown in Fig. 3 (a)). It is possible that the magnetic scattering intensity along the diffusive [111]-rod is removed to form the magnetic Bragg peaks below T_C . Well above T_C the flipping ratio (the ratio of the NSF to SF cross-sections) at (111) gradually decreases on cooling and then falls more rapidly to unity around T_C (Fig. 3 (a)). This indicates that the incident neutron spins are already partially depolarized in the high-temperature phase because of short-range ferromagnetic correlations, and are fully

depolarized well below T_C , pointing to the emergence of macroscopic ferromagnetic domains. In fact, a nearly collinear ferromagnetic structure consistent with previous non-polarized neutron scattering experiments on the same single crystal is also identified theoretically using an effective pseudospin-1/2 quantum spin ice model on a microscopic basis.

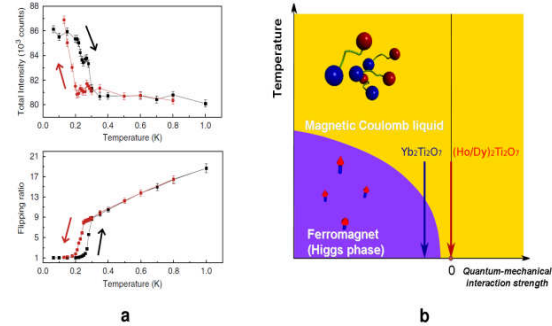


FIG. 3: (a) Top: the sum of the SF and the NSF (111) Bragg peak intensities versus temperature showing a hysteresis with temperature. The sum increases by almost 6% below T_C in agreement with the previous measurements. Bottom: the flipping ratio of the scattered (111) Bragg peak as a function of temperature. This ratio falls off steeply to unity below T_C with a clear hysteresis. The data were collected by first warming and then cooling. This sequence is indicated by the arrows. (b) A schematic phase diagram as a function of temperature and the quantum-mechanical interaction strength of $\text{Yb}_2\text{Ti}_2\text{O}_7$ [3].

From the viewpoint of gauge theory, the high-temperature phase of $\text{Yb}_2\text{Ti}_2\text{O}_7$ is effectively described as a Coulomb phase, where bosonic fractionalized quasi-particles spinons that carry magnetic monopole charges are deconfined without a static non-uniform proliferation of monopole charges and host fluctuating $U(1)$ gauge fields responsible for the analogous ‘quantum electrodynamics’. These magnetic monopolar spinons can undergo a Bose-Einstein condensation to form the classical ferromagnetic moment (as schematically shown in Fig. 3 (b)). This pins the global $U(1)$ phase of the spinon fields, and breaks the nontrivial emergent $U(1)$ gauge structure. This condensation of matter (spinon) fields coupled to gauge fields occurs through the Higgs mechanism. Thus, the ferromagnetic state can be viewed as a Higgs phase of magnetic monopoles.

The discovery of the Higgs phase of magnetic monopoles in quantum spin ice not only will motivate scientists to investigate many fascinating physical properties of this exotic state of matter, but also may open up a new direction in spintronics that aims at efficient controls of spins for technological applications.

- [1] T. Fennell, *et al.*, Science **326**, 415 (2009).
- [2] L.J. Chang, Y. Su, Y.J. Kao, Y.Z. Chou, R. Mittal, H. Schneider, Th. Brueckel, G. Balakrishnan, and M. R. Lees, Phys. Rev. B **82**, 172403 (2010).
- [3] L.J. Chang, S. Onoda, Y. Su, Y.J. Kao, K.D. Tsuei, Y. Yasui, K. Kakurai and M.R. Lees, Nature Communications **3**, 992 (2012).

Antiferromagnetism in the Hubbard Model on the Bernal-stacked Bilayer

T. C. Lang^{1,2}, Z. Y. Meng³, M. M. Scherer¹, S. Uebelacker¹, F. F. Assaad⁴, A. Muramatsu⁵, and S. Wessel¹

¹ Institut für Theoretische Festkörperphysik, RWTH Aachen University, Germany

² Department of Physics, Boston University, USA

³ Center for Computation and Technology, Louisiana State University, USA

⁴ Institute for Theoretical Physics and Astrophysics, University of Würzburg, Germany

⁵ Institut für Theoretische Physik III, University of Stuttgart, Germany

Based on a combined analysis from ground state projective quantum Monte Carlo (QMC) simulations and functional renormalization group (fRG) calculations, we examine interaction induced electronic instabilities of the Hubbard model on the half-filled honeycomb bilayer with Bernal stacking, relevant for bilayer graphene (BLG). Our results exhibit an antiferromagnetic instability towards a state that spontaneously breaks sublattice and spin rotational symmetry, once local Coulomb repulsions are introduced to the free system. The magnetization profile reveals an inhomogeneous participation of the spin moments within the ordered ground state, with the enhanced formation of moments along the threefold coordinated lattice sites. This layered antiferromagnetic state is found to be robust with respect to enhanced interlayer couplings as well as extended Coulomb interactions.

Recent experimental studies suggest the formation of a symmetry broken state in (BLG), but its actual nature remains ambiguous and is at the moment a highly debated topic [1]. In the absence of external perturbations, due to the finite density of states at the Fermi level in the free band limit, the electronic Coulomb interaction is expected to trigger a genuine electronic instability and drive BLG into a correlated ground state. Possible candidate states that have been proposed include an (layered) antiferromagnetic state, several topological states such as quantum anomalous Hall, quantum spin Hall or quantum valley Hall states, all of which exhibit a finite bulk gap, as well as a gapless nematic state. While most recent experiments identified a finite excitation gap of a few meV emerging in bilayer graphene, at low temperatures other transport data has been interpreted towards the formation of a gapless, possibly nematic state. Within the currently inconclusive experimental situation, an AF state is considered a probable ground state among the (gapfull) candidates and thus worth a more detailed examination. We explore the nature of this possible ground state by taking screened Coulomb interactions into account within a tight-binding approach for BLG via a local Hubbard model description of the carbon π -electrons. In particular, since the neutrality point relates to half-filling in the Hubbard model, we take

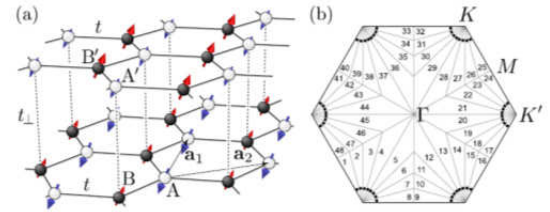


FIG. 1: (a) Bernal stacking of the honeycomb bilayer with intra- (inter)layer hopping t (t_{\perp}) between the sublattices A, B and A', B' (A', B). Within the sublattices an equal number of sites have a coordination number $z = 3$ or 4. (b) Patching scheme of the Brillouin zone employed in the fRG calculations on BLG.

the opportunity to explore possible electronic instabilities using unbiased QMC methods. We performed QMC simulations on finite systems of linear extent L for L up to 12 with periodic boundary conditions. In the following, we consider the Hamiltonian $H = H_0 + H_{\text{int}}$, with the local interaction term $H_{\text{int}} = U \sum_i n_{i,\uparrow} n_{i,\downarrow}$. Furthermore, H_0 denotes the free tight-binding model containing both intralayer nearest neighbor hopping t as well as interlayer hopping t_{\perp} , as illustrated in Fig. 1(a). We employed the fRG patching of the Brillouin zone shown in Fig. 1(b), to obtain accurate estimates for the critical energy scale Λ_c where an electronic instability emerges during the fRG flow. Up to an order of magnitude, Λ_c can serve as an estimate for the single particle gap. For a broad range of pure Hubbard interactions U , we observe a flow to strong coupling with the signature of an AF instability. The AF instability is also robust with respect to variations of the band structure, in particular the interlayer coupling. Our main findings thus result from analyzing this local Hubbard limit, where we can efficiently employ QMC. We fix $t_{\perp} = t$; this choice allows us to reliably study electronic instabilities, due to the well pronounced quadratic band touching at the Fermi level. From a fit of the imaginary-time displaced QMC Green's function, the single-particle gap Δ_{sp} can be extracted. In Fig. 2, we present our results for the single particle gap obtained from QMC and a mean field theory (MFT) alongside the fRG critical scale as a function of U/t . The extrapolation to the thermodynamic limit (TDL) using a second order polynomial yields a continuous onset.

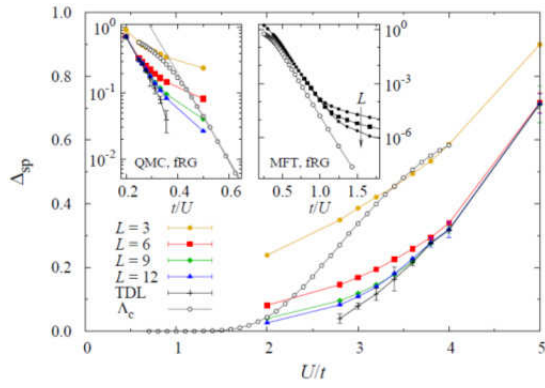


FIG. 2: Single particle gap from QMC simulations for different system sizes and the finite size extrapolation to the TDL, along with the fRG critical scale as a function of U/t . The inset on the left shows the same data vs. t/U in a semilog scale, exhibiting an exponential onset of the gap in the large t/U range. The inset on the right shows the fRG data along with MFT results.

Finite size extrapolation of the available data points deceptively suggests a finite critical value of U for the transition from the semimetal to the Mott insulator. This can be attributed to pronounced finite size effects at low energies. The fRG critical scale for the same parameters indeed reproduces such a continuously increasing associated single particle gap for all finite values of U . The fRG data show an exponential gap in the large t/U regime (left inset). Accordingly, the extrapolated QMC data follow the same behavior. One can readily see that larger lattices are needed in order to clearly identify this exponential onset at smaller values of U/t . The same effect is observed already within the MFT approach (right inset): increasingly larger system sizes allow us to identify the exponential opening of the single particle gap $\Delta_{sp} \propto \exp(-\alpha t/U)$. From our fRG data, we can extract the exponent $\alpha \approx 16$, which is close to the Hartree-Fock value of $9\pi^2 t^2/2t_\perp$. Deviations from this exponential behavior emerge beyond an intermediate coupling strength of $U/t \approx 2$, and relate to the onset of the strongly correlated regime. Note that within this model, the energy gap for realistic values of the Hubbard $U \approx 3t$ are rather large, $\Delta_{sp} \approx 0.07t \approx 200$ meV. To quantify the AF order within QMC simulations, we measure the overall staggered structure factor, from which we obtain the mean staggered magnetization m per lattice site. We also consider restricted order parameters m_z for sites with coordination numbers $z = 3$ and 4 . While m steadily increases with $U > 0$ as does the single particle gap, we observe pronounced differences in the two sublattice magnetizations, which arise due to the presence of inequivalent sites in the lattice structure [cf. Fig. 3(a)-(b)]. In particular, we find that sites with the *higher* coordination $z = 4$ (filled symbols) exhibit a *lower* ordered moment, at odds with the usual intuition that high coordination favors more robust Néel order. An increase of z on one sublattice will generically make the ordering more robust everywhere, although not uniformly so for all sublattices. This hierarchy of magnetic moments can indeed be also inferred directly from the fRG

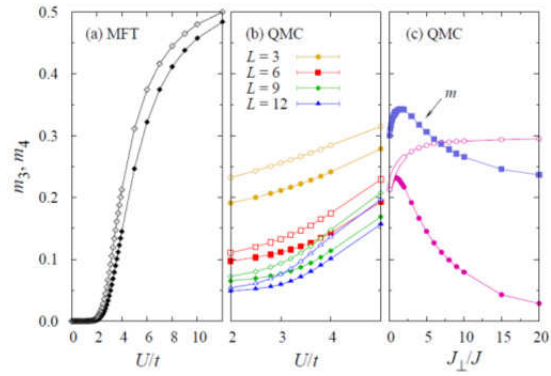


FIG. 3: The sublattice magnetization vs. U/t for sites with coordination number $z = 3$ (open symbols) and $z = 4$ (filled symbols) from (a) MFT in the TDL, (b) QMC simulations for different system sizes, and (c) in the Heisenberg limit vs. the interlayer AF exchange coupling J_\perp/J . The data in (c) result from stochastic series expansion QMC simulations, after extrapolation to the TDL; also shown in (c) is the staggered magnetization m .

calculations over a wider range of nonlocal interactions, by comparing the relative strengths of the effective interactions on the different sites of a unit cell. Similar effects of an enhanced magnetic order near low-coordinated sites have previously been observed in localized quantum spin models on other inhomogeneous lattice structures. In the current case, the joint bonds on sites with coordinated number $z = 4$ interconnect the two layers [cf. Fig. 1 (a)]. With increasing U and t_\perp , the moments along these bonds hybridize between the layers and tend to form spin singlets, suppressing the participation in the long range AF order on these sites. In Fig. 3(c), we consider the staggered magnetizations in the large- U limit, wherein the model becomes a spin only Heisenberg model, with an intralayer exchange coupling $J = 4t^2/U$ and an interlayer coupling $J_\perp = 4t_\perp^2/U$. All three order parameters exhibit an initial increase upon increasing J_\perp/J . Furthermore, while m_3 saturates for large J_\perp/J , m and m_4 scale to zero in the large J_\perp limit. These results show that for all finite values of J/J_\perp , the system remains antiferromagnetically ordered, but with a suppressed staggered moment on the $z = 4$ sites for large J_\perp/J , due to the tendency towards forming J_\perp -singlets along the interlayer bonds. Further details and additional data from the QMC simulations can be found in our publication [2].

This research was supported in part by the DFG research units FOR 723, 912, and 1162 and the NSF EPSCoR Cooperative Agreement No. EPS-1003897 with additional support from the Louisiana Board of Regents. Furthermore, we acknowledge the JSC Jülich and the HLRS Stuttgart for the allocation of CPU time.

[1] E. McCan and M. Kishino, arXiv: 1205.6953 for a review and further references.

[2] T. C. Lang, Z. Y. Meng, M. M. Scherer, S. Uebelacker, C. Honerkamp, F. F. Assaad, A. Muramatsu, and W. Wessel, Phys. Rev. Lett. 109, 126402 (2012).

Spin relaxation in metals and thin metallic films

P. Mavropoulos, N.H. Long, B. Zimmermann, Y. Mokrousov, and S. Blügel

Peter Grünberg Institut-1 and Institute for Advanced Simulation-1, Forschungszentrum Jülich, Germany

Spin relaxation is the decay of an out-of-equilibrium spin population in a material. Since the electron spin is a carrier of information, the effect of spin relaxation is fundamental to the field of spintronics. Here we predict a new effect, concerning the anisotropy of the spin relaxation time with respect to the angle between the spin polarization axis \hat{s} and the crystallographic axes in inversion-symmetric systems. The anisotropy can reach gigantic values, e.g. 830 % in hcp Hafnium. The effect and its origin are discussed for bulk metals as well as thin films in terms of their electronic structure with focus on near-degenerate states, surface states and spin-orbit coupling (SOC).

In non-magnetic solids with space-inversion symmetry, the Elliott-Yafet mechanism [1,2] for spin relaxation is generally accepted as the most important one. According to the Elliott-Yafet theory, one must take into account that, in the presence of spin-orbit coupling (SOC), the electron eigenstates in a crystal cannot be eigenstates of the spin operator. One finds, instead, states with dominant but not absolute spin-up or spin-down character, denoted as $\Psi_k^+(r)$ or $\Psi_k^-(r)$ respectively, that form a degenerate pair at each k and energy by virtue of the time-reversal and space-inversion invariance. Denoting by S the spin operator and S_z its z -component, the deviation of any of the Ψ_k^\pm from being an eigenstate of S_z is quantified by the dimensionless parameter

$$b_k^2 = \frac{1}{2} \left(\langle \Psi_k | S_z | \Psi_k \rangle - \min \{ \langle \Psi_k | \uparrow \rangle, \langle \Psi_k | \downarrow \rangle \}^2 \right) \in [0, \frac{1}{2}]$$

where $|\uparrow\rangle$ and $|\downarrow\rangle$ denote respectively the up-spin and down-spin eigenstates of S_z . In the limit $b_k^2 = 0$, the state Ψ_k is an eigenstate of S_z ; in the limit $b_k^2 = \frac{1}{2}$ it shows full spin mixing. When SOC is present, the limit $b_k^2 = 0$ cannot occur, but the limit $b_k^2 = \frac{1}{2}$ can be reached for special points in the Brillouin zone (BZ) that are called *spin-flip hot spots* [3] and that can be formed where a band degeneracy is lifted only by spin-orbit coupling. By continuity, the value of b_k^2 in the region of the band structure around the spin-flip hot spots is also high but smaller than $\frac{1}{2}$.

Following Elliott [1] we accept that an excited spin population occupies states of the type Ψ_k^+ which, after scattering off phonons or defects, have a finite probability $P_{k'k}^+$ of a transition to states of the type $\Psi_{k'}^-$. This scattering event from a “+” state to a “−” state represents a spin-flip, because the

former state has a predominantly spin-up character and the latter a predominantly spin-down character. According to the Elliott approximation the spin-relaxation rate $1/T_1 = \sum_{k'k} P_{k'k}^+$ scales proportionally to the integrated parameter $b^2 = \sum_k b_k^2$ that is also called the *Elliott-Yafet parameter* (EYP). The summation over k' and k takes place around the Fermi energy with an appropriate convolution with the Fermi function.

In the above discussion we assumed that the excited population has a polarization along the z axis. However, in an experiment there is the freedom to excite a spin polarization along any axis \hat{s} . This is especially the case in a non-magnetic material, since there are no internal magnetic fields that distinguish a polarization axis. For a theoretical description of this experiment we must form appropriate linear combinations of the type $c_k(\hat{s})\Psi_k^+(r) + d_k(\hat{s})\Psi_k^-(r)$, with $c_k(\hat{s})$ and $d_k(\hat{s})$ coefficients to be calculated in such a way that the linear combination yields a maximal expectation value of the operator $\pm S \cdot \hat{s}$. In this way we obtain a new parameter $b_k^2(\hat{s})$ and a new (integrated) EYP $b^2(\hat{s})$. The latter quantity obeys the crystal point group symmetry, as does the spin-relaxation time $T_1(\hat{s})$, i.e., they are invariant with respect to symmetry rotations of \hat{s} . However, they are not invariant under general rotations. We thus define the anisotropy of the EYP and of T_1 as

$$A[b^2] = \{ \max_{\hat{s}} [b^2] - \min_{\hat{s}} [b^2] \} / \min_{\hat{s}} [b^2] \quad (1)$$

$$A[T_1] = \{ \max_{\hat{s}} [T_1] - \min_{\hat{s}} [T_1] \} / \min_{\hat{s}} [T_1], \quad (2)$$

where the maximum and minimum values are found with respect to rotations of \hat{s} in the whole unit sphere. Eq. (2) (as well as Eq. (1), in the Elliott approximation) expresses the relative change of the spin-relaxation time in an experiment where the excited spin polarization is tried along all possible directions with respect to the crystallographic axes.

It is expected, and found in our calculations, that the global maximum and minimum values should be found for \hat{s} along high-symmetry crystallographic axes. For cubic crystals one should thus compare the [001], [110], and [111] directions, for hcp crystals the c -axis to the directions in the ab -plane, and for thin films the out-of-plane direction to the in-plane direction. We did this for a number of systems and found that the anisotropy can vary between them by five orders of magnitude (from $A=10^{-2}$ in fcc Au to 10^3 in hcp Hf) even though the

investigated systems have comparable spin-orbit coupling strength [4,5,6].

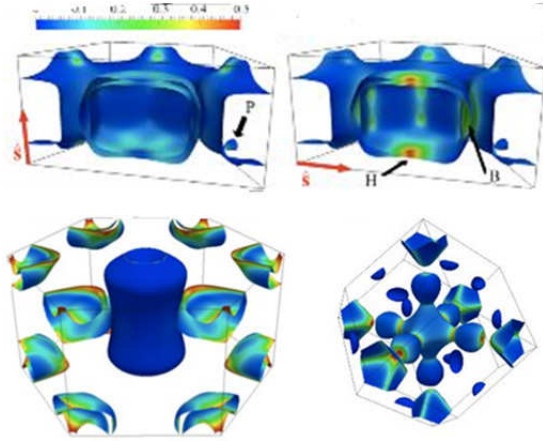


FIG.1: Top: Fermi surface of hcp Os with a colour code showing the distribution of b_k^2 for $\hat{s} \parallel [001]$ (left) and $\hat{s} \parallel [100]$ (right). Bottom: Fermi surface of hcp Hf for $\hat{s} \parallel [001]$ (left) and W for $\hat{s} \parallel [001]$ (right). The “hot spots” and “hot regions” (in red) are strongly suppressed upon varying \hat{s} .

Fig. 1 shows the distribution of b_k^2 on the Fermi surface of Os, Hf and W. In all cases, the spin-flip hot spots and the “hot regions” around them are visible in red colour. In the case of Os it is shown that a change of \hat{s} from the [001] to the [100] direction changes completely the distribution of b_k^2 and thus the integrated b^2 . In particular, a large hot region (indicated by H) appears around the center of the top and bottom sheets, where they are almost degenerate. The situation is analogous to Hf when changing from $\hat{s} \parallel [100]$ to [001]: the red loops on the hexagonal face of the Brillouin zone lose their intensity (not shown here). Also in W we find a strong difference between the [001] and [111] directions of \hat{s} . Overall, this leads to an anisotropy of b^2 with a value of $A=830\%$ for Hf, 59% for Os, and 6% for W. For Au, that has an almost spherical Fermi surface with no hot spots, the anisotropy is less than 0.1% .

From our calculations it becomes clear [4,5] that the largest contribution to the anisotropy comes from the spin hot-spots and from the region around them. In a deeper analysis we have revealed the origin of this strong effect. By separating the spin-flip part $\xi(LS)_{\perp}$ from the spin-conserving part $\xi(LS)_{\parallel}$ in the spin-orbit operator $\xi \mathbf{L} \cdot \mathbf{S} = \xi(LS)_{\perp} + \xi(LS)_{\parallel}$ ($LS)_{\perp}$ (where ξ is the spin-orbit coupling strength) we observe that both $\xi(LS)_{\perp}$ and $\xi(LS)_{\parallel}$ depend on the choice of \hat{s} , even if their sum does not, since it is represented by a scalar product. The parameter b_k^2 depends on the matrix elements of $\xi(LS)_{\perp}$ and through these on \hat{s} . Thus, we focus our discussion on $\xi(LS)_{\perp}$. The contribution of this term depends on m , i.e. the z -component of the orbital angular momentum of the states, since one must have $\Delta m = \pm 1$ in transitions through this term (the transitions are k -conserving between different

bands due to the action of the SOC). At each point on the Fermi surface the Bloch eigenfunctions have a certain resolution in m determined by the directional orbitals, the electron hopping between the neighbor atoms, and the direction of the nearest neighbors. E.g., the resolution in d orbitals will contain $m=0$ if the d_{z^2} state is involved in the hopping along the [001] direction in the crystal. But when we rotate \hat{s} , we effectively rotate the z -axis in which the orbitals are expressed. Then, what was previously a d_{z^2} ($m=0$) state changes to a linear combination of orbitals with different m . Under these circumstances it can be that the condition $\Delta m = \pm 1$ between bands is met in one reference frame and not in another, and as a consequence the matrix elements of $\xi(LS)_{\perp}$ can be present in one frame and vanish in another. From here comes the anisotropy. Additionally, the magnitude of the effect must increase strongly around the hot spots, because there the band structure shows degeneracies or near-degeneracies thus the transitions become largest, as perturbation theory arguments show.

Finally, we comment on our findings in thin films [6]. Here, our investigation is focused on W(001) from where it becomes clear that the surface-states will play an important role in the EYP and its anisotropy: we find $A[b^2]=37\%$ for a 10-layer film, which is larger than the bulk value of 6% . In particular, the combination of the broken translational symmetry at the surface with spin-orbit coupling introduces an additional splitting of surface states that is known as Rashba splitting [7]. A consequence of this splitting is that the direction of spin-polarization of the Bloch eigenfunctions is k -dependent and mostly points in the surface plane. As a result, if the spin population is excited with a direction of \hat{s} perpendicular to the surface plane, it is incompatible with the surface band structure and can only be accommodated by special linear combinations of surface wavefunctions that result in $b_k^2 = 1/2$ for all surface states. The remaining states (bulk-like states) of the film are not affected by the Rashba splitting and behave just as in the case of a bulk metal. The theoretical analysis shows that, qualitatively, the effect of surface states will be not specific to W(001) but general.

- [1] R. J. Elliott, Phys. Rev. , 266 (1954).
- [2] Y. Yafet, in Solid State Physics, edited by F. Seitz and D. Turnbull, Academic, NewYork , 1 (1963).
- [3] J. Fabian and S. Das Sarma, Phys. Rev. Lett. , 5624 (1998).
- [4] B. Zimmermann, P. Mavropoulos, S. Heers, N.H. Long, S. Blügel, and Y. Mokrousov, Phys. Rev. Lett. , 236603 (2012).
- [5] Y. Mokrousov, H. Zhang, F. Freimuth, B. Zimmermann, N. H. Long, J. Weischenberg, I. Souza, P. Mavropoulos, and S. Blügel, J. Phys.: Condens. Matter , 163201 (2013).
- [6] N.H. Long, P. Mavropoulos, B. Zimmermann, S. Heers, D. Bauer, S. Blügel, and Y. Mokrousov, arXiv:1302.0140 (2013)
- [7] S. LaShell, B. A. McDougall and E. Jensen, Phys. Rev. Lett. , 3419 (1996).

Ultrafast magnetization enhancement in metallic multilayers driven by superdiffusive spin currents

Dennis Rudolf¹, Roman Adam¹, Patrik Grychtol^{1,2}, Claus M. Schneider¹, Chan La-O-Vorakiat², Emrah Turgut², Henry C. Kapteyn², Margaret M. Murnane², Marco Battiato³, Pablo Maldonado³, Peter M. Oppeneer³, Justin M. Shaw⁴, Hans T. Nembach⁴, Thomas J. Silva⁴, Stefan Mathias^{2,5}, and Martin Aeschlimann⁵

¹ Peter Grünberg Institut-6, Forschungszentrum Jülich, Germany

² Department of Physics and JILA, University of Colorado and NIST, Boulder, CO, USA

³ Department of Physics and Astronomy, Uppsala University, SE-75120 Uppsala, Sweden

⁴ Electromagnetics Division, National Institute of Standards and Technology, Boulder, CO, USA

⁵ University of Kaiserslautern and Research Center OPTIMAS, 67663 Kaiserslautern, Germany

Uncovering the physical mechanisms that govern ultrafast charge and spin dynamics is crucial for understanding of the fundamental limits of ultrafast spin-based electronics. The first pioneering experiments in 1996 [1] have established that spin-dynamics in magnetic materials can be quenched by femtosecond laser light pulses within a few hundred femtoseconds. However, understanding the details of physical mechanisms governing femtosecond spin-dynamics remains elusive. In our experiments we spatially separated the spin-dynamics using Ni/Ru/Fe magnetic trilayers, where the Ni and Fe layers can be ferro- or antiferromagnetically coupled. By exciting the layers with a laser pulse and probing the magnetization response in Ni and Fe *simultaneously but separately*, we discovered that optically induced demagnetization of the Ni layer transiently *enhances* the magnetization of the buried Fe layer when the two layer magnetizations are initially aligned parallel. Our observations are explained by a laser-generated superdiffusive spin current between the layers [6].

One of the major roadblocks for continued progress in nanoelectronics is energy dissipation caused by the flow of electrical current. Encoding data in electron spin, rather than charge, promises a new route for technology with the potential to dramatically reduce energy requirements. A current grand challenge in this area is to control the static and dynamic behavior of spins and spin ensembles. Spin-dynamics is in-itself of fundamental interest for understanding spin-photon-charge-phonon interactions and their complex interplay on pico- and femtosecond timescales. The potential to rapidly manipulate spins was first demonstrated in a pioneering experiment [1] that observed that the magnetization of Ni can be optically quenched within few hundreds femtoseconds after excitation by an ultrashort laser pulse. Up to date, spin

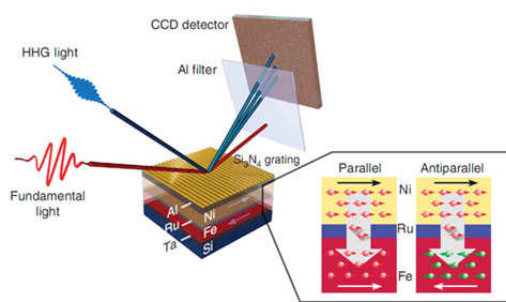


FIG. 1: Experimental setup and the multilayer sample schematics. The magnetization of the Al/Ni/Ru/Fe multilayer samples is probed by laser higher harmonics in the extreme ultraviolet (XUV) spectral range, at the 3p absorption edges of Ni (66 eV) and Fe (52 eV). The Si_3N_4 -grating, patterned on top of the layers, spectrally separates the XUV high harmonic beams that are then detected by an X-ray CCD detector. The pump laser light absorbed in the thin Al and Ni layers results in a spin current (marked by grey arrow in the inset) that travels through the non-magnetic Ru spacer layer into the Fe layer. The magnetization of the Fe layer increases or decreases depending on its orientation relative to Ni. The inset illustrates schematically the relative magnetization of the Ni and Fe layers (thin black and white arrows), the majority spin alignment in the layers (red and green circles) and the flow of the spin current (large grey arrow)

dynamics in a broad range of materials, including alloys [2,3] and magnetic multilayers[4,5] have been explored.

Despite a considerable number of experimental data the microscopic mechanisms behind the ultrafast spin phenomena are not fully understood.

In our work, we studied the spin dynamics in interlayer exchange-coupled Ni/Ru/Fe trilayers (Fig.1). Our experiment show that for the parallel magnetization orientation of the top Ni and the bottom Fe layers the magnetization of Ni is transiently quenched after the laser excitation,

whereas, the Fe magnetization is transiently enhanced [6]. In contrast, in antiparallel magnetization alignment we observed the transient demagnetization of both layers. We attribute our

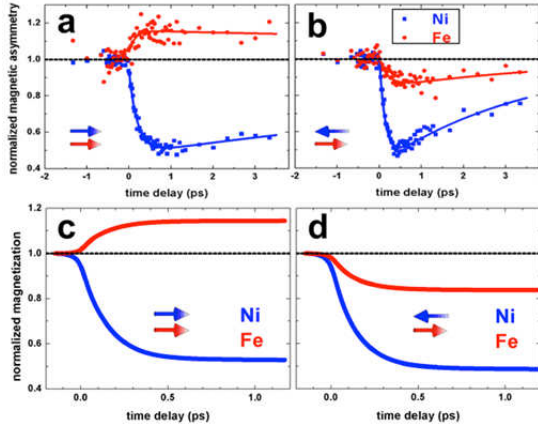


FIG. 2: Experimentally measured (a,b) and calculated (c,d) time- and layer-resolved magnetization. The time-resolved magnetization of the Ni and Fe layers in the Ni(5 nm)/Ru(1.5 nm)/Fe(4 nm) trilayer for the parallel (a) and antiparallel (b) magnetization alignment. The data have been extracted by integrating the magnetic asymmetry signal over the 3p absorption edges of Ni and Fe, respectively, and normalizing to the magnetic asymmetry values before the time zero (black broken line). The magnetic asymmetry at the Fe 3p absorption edge anomalously increases for the parallel (a), and decreases for antiparallel magnetization orientation of Ni and Fe layers (b). In our model, laser-induced ultrafast demagnetization of the Ni layer (blue curves in c and d) generates superdiffusive spin currents that increase the Fe magnetization for parallel orientation (red curve in c), while decreasing the Fe magnetization for antiparallel alignment (red curve in d). The strengths and timescales of demagnetization and magnetization agree well with the measured data.

observation to the ultrafast spin transport between the layers [8]. In our experiment, we excited the sample by 25 fs infrared laser pulses and probed the magnetization of Ni and Fe layers by a broadband laser-generated high harmonics comb spanning 20-72 eV covering the 3p absorption edges of Ni (66 eV) and Fe (52 eV). Employing the transversal magneto-optical Kerr effect (T-MOKE) we measured the magnetic asymmetry (A) layer-selectively at the Ni and Fe 3p absorption edges with A being proportional to the magnetization and defined by

$$A = \frac{I_r(H^\uparrow) - I_r(H^\downarrow)}{I_r(H^\uparrow) + I_r(H^\downarrow)},$$

where $I_r(H^\uparrow)$ and $I_r(H^\downarrow)$ denote the intensity of light reflected from the sample for external magnetic field vector $H^{\uparrow,\downarrow}$ pointing up or down perpendicular to the plane of incidence. The harmonics were spectrally separated by a Si_3N_4 optical grating fabricated on the top of the multilayer stack (Fig. 1). Femtosecond dynamics for Ni and Fe layers in both antiparallel and parallel alignments are shown in (Fig.2). We explain these observations by

ultrafast spin transport between the layers based on the asymmetry between the transport properties for majority and minority spins in Ni and Fe. For Ni, the inelastic mean free path for laser-excited majority spins is longer than for the minority ones [8] reaching the Fe layer. Assuming parallel magnetization of Fe and Ni, the Ni majority spins fill the empty majority spin states of Fe, thus transiently increasing the net magnetization of Fe. In the opposite case of antiparallel magnetization alignment, the Ni majority spins fill the empty Fe minority states resulting in demagnetization of the Fe layer. These arguments are supported by the numerical solution based on the superdiffusive spin transport equation [8] for the Ni and Fe layers (Fig. 2c,d). The simulations agree well with the experimental data (Fig. 2a,b) in terms of time scales and strengths of the observed effects. The anomalous enhancement of the Fe magnetization is most prominent at relatively low excitation fluence, below $F \approx 2.0 \text{ mJ/cm}^2$. We find that at higher fluence (see ref [6]), direct optical excitation of the Fe layer becomes the dominant source of demagnetization, exceeding the effect of the superdiffusion. In experiment, by increasing the excitation fluence to $F \approx 2.7 \text{ mJ/cm}^2$, we observe the Fe magnetization to decrease in response to the excitation pulse even when the Ni and Fe magnetizations are parallel. Laser-generated spin currents can possibly find application in moving domain walls, switching magnetic nano-elements on sub-picosecond timescales or in spin-based electronics operating in the Terahertz frequency range.

- [1] Beaupaire, E., Merle, J.-C., Daunois, A. & Bigot, J.Y., *Phys. Rev. Lett.* **76**, 4250-4253 (1996).
- [2] La-O-Vorakiat, C., Turgut, E., Teale, C.A., Kapteyn, H.C., Murnane, M.M., Mathias, S., Aeschlimann, M., Schneider, C.M., Shaw, J., Nembach, H. & Silva, T., *Phys. Rev. X* **2**, 011005 (2012).
- [3] Mathias, S., La-O-Vorakiat, C., Grychtol, P., Granitzka, P., Turgut, E., Shaw, J.M., Adam, R., Nembach, H.T., Siemens, M., Eich, S., Schneider, C. M., Silva, T., Aeschlimann, M., Murnane, M.M. & Kapteyn, H. P. *Natl. Acad. Sci. USA* **109**, 4792–4797 (2012).
- [4] Malinowski, G., Dalla Longa, F., Rietjens, J., Paluskar, P., Huijink, R., Swagten, H. & Koopmans, B., *Nat. Phys.* **4**, 855-858 (2008).
- [5] Melnikov, A., Razdolski, I., Wehling, T.O., Papaioannou, E.T., Roddatis, V., Fumagalli, P., Aktsipetrov, O., Lichtenstein, A.I. & Bovensiepen, U., *Phys. Rev. Lett.* **107**, 076601 (2011).
- [6] Rudolf, D., La-O-Vorakiat, C., Battiato, M., Adam, R., Shaw, J. M., Turgut, E., Maldonado, P., Mathias, S., Grychtol, P., Nembach, H.T., Silva, T.J., Aeschlimann, M., Kapteyn, H.C., Murnane, M.M., Schneider, C.M. & Oppeneer, P.M., *NatComm* **3** 1037 (2012).
- [7] Battiato, M., Carva, K. & Oppeneer, P. M., *Phys. Rev. B* **86**, 024404 (2012).
- [8] Zhukov, V.P., Chulkov, E.V. & Echenique, P.M., *Phys. Rev. B* **73**, 125105 (2006).

Quenched Slonczewski-windmill in spin-torque vortex oscillators

Volker Sluka¹, Attila Kakáy¹, Alina M. Deac², Daniel E. Bürgler¹, Riccardo Hertel³, and Claus M. Schneider¹

¹Peter Grünberg Institut-6, Forschungsgszentrum Jülich, Germany

²Institute of Ion-Beam Physics and Materials Research, Helmholtz-Zentrum Dresden-Rossendorf, Germany

³Institut de Physique et Chimie des Matériaux de Strasbourg, Université de Strasbourg, France

Spin-torque nano-oscillators (STNO) operating based on the interaction between a spin-polarized current and nanomagnets are promising candidates for on-chip microwave sources that would allow greatly advancing today's state of the art telecommunication. We present a combined analytical and numerical study on double-vortex STNOs and describe a mechanism that suppresses the unwanted Slonczewski-windmill modes. These theoretical findings based on the spin-torque-coupled Thiele equations are supported by experimental measurements on Fe/Ag/Fe nanopillars. The results open up a new perspective for building high quality-factor STNOs operating at selectable, well-separated frequency bands.

Spin-torque nano-oscillators (STNO) typically consist of two single-domain ferromagnetic layers separated by a metallic spacer or a tunnel barrier, one with its magnetization fixed (polarizing layer), the other one susceptible to torques (free layer). An electric current traversing the system perpendicular to the layers becomes spin-polarized and exerts torques on the magnetizations [1,2] leading to magnetization dynamics of the free layer. These excitations are typically in the range of a few GHz and can be detected by measuring the time variation of the magnetoresistance.

Here, we investigate STNOs containing two stacked magnetic vortices [3], i.e., a system consisting of two ferromagnetic disks, each in a magnetic vortex state and separated by a metallic, nonmagnetic spacer [see Fig. 1(a)]. Such double-vortex systems have so far rarely been treated in the literature [4]. Depending on the relative chiralities, the vortex pair can be either in a parallel or antiparallel configuration. There is a fundamental difference between our device and typical STNOs (consisting of homogeneously magnetized layers): In our double-vortex system, neither of the two ferromagnets is pinned, one vortex serves as the polarizer for the other and vice versa. Thus, in both layers, magnetization dynamics can be excited by spin-transfer torque. This is a particularly interesting condition, since for the case of two spin-torque coupled macrospins the spin-transfer torque has the tendency to conserve the relative angle of the two moments. A

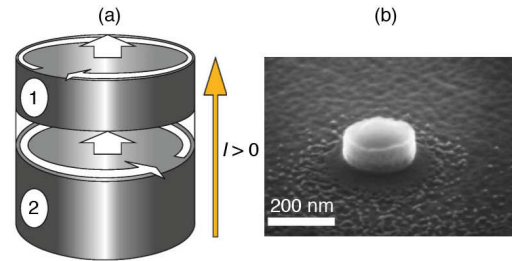


FIG. 1: (a) Sample structure used in the calculations. The sample consists of two ferromagnetic Fe disks (1 and 2), each containing a vortex characterized by its chirality (C_i) and core polarity. The upper disk is 15 nm thick, the lower 25 nm. Both have a diameter of 230 nm. A metallic, nonmagnetic spacer Ag separates the two ferromagnetic layers. The positive technical current direction is shown, corresponding to an electron flow from the top to the bottom layer. (b) Scanning electron micrograph of a nanopillar after ion beam etching used employed in the experiment after applying a top contact.

dynamic state where both macrospins precess while their relative angle remains constant in time is referred to as Slonczewski-windmill. It has been shown [5] that in single-domain-based STNOs, such states can appear if the degree of symmetry between the two layers is sufficiently high.

The dynamics of the magnetic vortex in each disk (assuming rigid vortex structures) is governed by the Thiele equation [6]. The spin-transfer torque induced force in this equation can be decomposed into two contributions; the first term arises from the in-plane magnetization of the polarizer vortex and acts on the core of the other vortex, while the second term is caused by the core of the polarizer vortex and acts on the in-plane magnetization of the vortex in the free layer. We analytically calculated both contributions following a procedure given in Ref. 7 as a function of the core-core separation. The second term is negligible for large core-core separations and is thus not included in our investigation, since we are interested in the high amplitude excitations for large current densities.

The solutions to the coupled Thiele equations for vortices 1 and 2 [see Fig. 1(a)] are obtained numerically. The results can be summarized as follows: For positive currents and equal chiralities, the top vortex gyrates around the disk center on a trajectory of about 50 nm in radius, regardless of the core polarity. The sense of rotation, however,

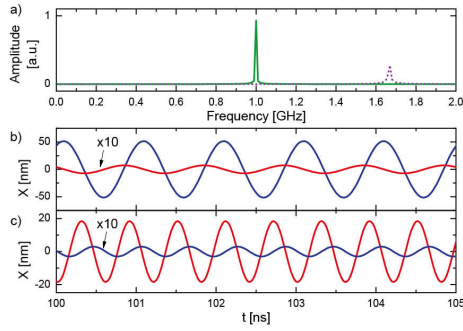


FIG. 2: Vortex dynamics obtained for the case of equal chiralities, represented by the time variation of the respective X coordinates of the vortex cores. (a) For positive and negative current, the system gyrates at 1.0 GHz (green) and 1.67 GHz (purple), respectively. The X coordinate of the vortex cores is shown in the lower panels for the positive (b) and negative (c) currents. The blue lines correspond to the top, the red lines to the bottom vortex. In (b), both cores have positive polarity, while in (c) they are antiparallel with the bottom core pointing down.

is determined by the core polarization. The gyration frequency is 1.0 GHz. The bottom vortex adapts its frequency and sense of gyration according to the top vortex. A dynamic equilibrium develops with a constant phase difference between the vortices even in the case of opposite relative core orientation. This frequency adaption is accompanied by a strong reduction in radius of the bottom core trajectory to less than 1 nm. For negative currents, the vortices switch roles: The bottom vortex gyrates on a large orbit, while the top vortex' trajectory is quenched. In the dynamic equilibrium the phase difference is constant and the gyration frequency is about 1.67 GHz. This frequency corresponds to the eigenfrequency of the bottom vortex, while the sense of rotation is determined by its core polarity (The different eigenfrequencies arise from the different thickness of the two disks). The gyration phase difference between the two vortices depends on the relative core alignment. A strong reduction of the orbit radius or, in other words, a quenching of the windmill modes accompanies the phase shifting. The phase shift always serves to adapt the magnetization dynamics of the polarizer layer to the frequency of the dominantly excited vortex' gyration frequency. Figures 2(b) and (c) depict the X coordinates of the two vortex cores for positive and negative current, respectively. Figure 2(a) displays the resulting spectra, in each case obtained from the dynamics in the dominantly excited disk.

From the coupled Thiele equations it is clear that the solutions for opposite chiralities and positive current polarity are identical to those obtained for equal chiralities with a negative current polarity. For large enough current density $|j|$, the obtained characteristics of the dynamics are the generalization of the criterion found in Ref. 8. In our case, both disks can be polarizing or free layer. For a given combination of chiralities C_1C_2 and applied current polarity, the system responds with a damped and a dominant gyration, the former defining the polarizing and the latter the

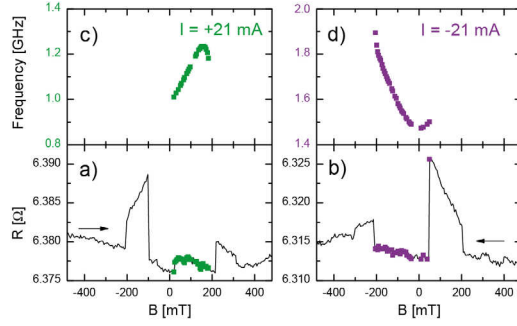


FIG. 3: Experimental resistance vs. field measurements of a Fe(25 nm)/Ag(6 nm)/Fe(15 nm) nanopillar with a diameter of 230 nm for (a) increasing field at +21 mA and (b) decreasing field at -21 mA. The low-resistance region around $B=0$ indicates the existence of the double-vortex state. Simultaneously recorded high-frequency spectra show peaks only in this region (colored symbols). The excitation frequencies for positive and negative current, respectively, are shown in (c) and (d). The frequency ranges are clearly different and well separated for the two current polarities. The ratio of the frequencies at $B=0$ is about 1.46. Taking into account the Oersted field and the magnetostatic field contributions this ratio shifts to a value of 1.54, very close to the ratio of the disk aspect ratios $5/3=1.67$, the value predicted by our model.

free disk. It is the product of current and chiralities that matters. Therefore, for given chiralities, the current polarity determines which disk is dominantly excited. On the other hand, changing the current sign influences the dynamics in the same way as changing one of the chiralities. Therefore we can formulate a generalized jC criterion: for $jC_1C_2>0$ the top and for $jC_1C_2<0$, the bottom disk is excited. These theoretical findings are supported by our experimental data obtained from double-vortex Fe/Ag/Fe STNOs (see Fig. 3). The details of the model and experiment can be found in Ref. 3.

In summary, we have presented a spin-torque-based mechanism that quenches windmill-modes in double-vortex STNOs. The origin is frequency and phase adaption of the gyrotropic motions in the two disks, which results in a strong suppression of the gyration radius in one of the disks. Changing the sign of the product jC_1C_2 interchanges the roles of active and suppressed vortices. In particular, flipping the current sign at a fixed relative chirality combination provides, in agreement with our experimental data, an effective mode selection mechanism, which allows deliberately choosing between separated frequency bands of the oscillator.

- [1] J. C. Slonczewski, *J. Magn. Magn. Mater.* **159**, L1 (1996).
- [2] L. Berger, *Phys. Rev. B* **54**, 9353 (1996).
- [3] V. Sluka et al., *Phys. Rev. B* **86**, 214422 (2012).
- [4] N. Locatelli et al., *Appl. Phys. Lett.* **98**, 062501 (2011).
- [5] Y. B. Bazaliy et al., *J. Nanosci. Nanotechnol.* **8**, 2891 (2008).
- [6] A.A. Thiele, *Phys. Rev. Lett.* **30**, 230 (1973).
- [7] E. Feldtkeller and H. Thomas, *Phys. kondens. Mat.* **4**, 8 (1965).
- [8] A.V. Khvalkovskiy et al., *Appl. Phys. Lett.* **96**, 212507 (2010).

Topological solitons driven by Landau-Lifshitz-Slonzewski equations

Christof Melcher

Dept. of Mathematics, RWTH Aachen University, Germany

Spin polarized currents offer the possibility to manipulate topological solitons, such as magnetic vortices in thin-film elements, and to switch between topologically separated states. Improved theoretical understanding of such singular switching mechanisms is required in order to develop suitable control strategies. Topologically obstructed evolution problems and singularity formation in geometric evolution equations are a well-established and active areas of applied mathematical analysis, and we shall report on new perspectives in the context of Landau-Lifshitz dynamics driven by a spin torque.

Spin-polarized currents interact with local magnetizations via the so-called spin-transfer torque, introduced in 1996 by Slonczewski and Berger. This effect can be used to excite magnetization oscillations or to switch magnetization orientation, and it gave rise to a number of new trends for future storage technologies and spintronic applications. A well-accepted continuum equation for the (normalized) magnetization $\mathbf{m}=\mathbf{m}(x,t)$ in the presence of a spin-polarized current, represented by a spin velocity field $\mathbf{v}=\mathbf{v}(x,t)$ is the following modification of the classical Landau-Lifshitz-Gilbert equation

$$\frac{\partial \mathbf{m}}{\partial t} + \mathbf{v} \cdot \nabla \mathbf{m} = \mathbf{m} \times \left(\alpha \frac{\partial \mathbf{m}}{\partial t} + \beta \mathbf{v} \cdot \nabla \mathbf{m} - \gamma \mathbf{h}_{\text{eff}} \right),$$

proposed by Zhang & Li and Thiaville et al., that we shall call Landau-Lifshitz-Slonzewski equation (LLS), anticipating our later discussion on the relationship with Slonczewski's original model. Here, $\mathbf{h}_{\text{eff}} = -\delta E(\mathbf{m})$ is the effective field given by the functional gradient of micromagnetic energy $E=E(\mathbf{m})$. For an ideally soft ferromagnet occupying a region $\Omega \subset \mathbb{R}^3$, $E=E(\mathbf{m}, \Omega)$ is the sum of exchange and stray-field energy, i.e., after non-dimensionalization,

$$E(\mathbf{m}, \Omega) = d^2 \int_{\Omega} |\nabla \mathbf{m}|^2 + \int_{\mathbb{R}^3} |\nabla \zeta|^2,$$

where d is the exchange length and where the stray-field $\mathbf{h}_{\text{stray}} = -\nabla \zeta$ is determined from \mathbf{m} via Maxwell's equation

$$\nabla \cdot (\mathbf{m} \chi_{\Omega} - \nabla \zeta) = 0 \text{ in } \mathbb{R}^3,$$

making the equation non-local. Observe that LLS is obtained from the original Landau-Lifshitz-Gilbert equation by adding two non-variational terms

$$\mathbf{v} \cdot \nabla \mathbf{m} \quad \text{and} \quad \beta \mathbf{m} \times (\mathbf{v} \cdot \nabla \mathbf{m}),$$

referred to as the adiabatic and non-adiabatic spin-transfer torque, respectively. Discussions on

the origin of non-adiabatic spin-torque components and the size of $\beta > 0$, which is expected to be close to Gilbert damping α and crucial e.g. for an adequate description of current induced domain wall motion, are notable issues not only in the context of modeling. The case $\alpha = \beta$, suggested on thermodynamic grounds, is special. Introducing the particle derivative

$$D_{\mathbf{v}} \mathbf{m} = \frac{\partial \mathbf{m}}{\partial t} + (\mathbf{v} \cdot \nabla) \mathbf{m},$$

LLS exhibits the particularly simple form

$$D_{\mathbf{v}} \mathbf{m} = \mathbf{m} \times (\alpha D_{\mathbf{v}} \mathbf{m} - \mathbf{h}_{\text{eff}}).$$

In particular, it can be obtained from the original Landau-Lifshitz equation by adding a single transport term $(\mathbf{v} \cdot \nabla) \mathbf{m}$

$$D_{\mathbf{v}} \mathbf{m} = -\mathbf{m} \times \mathbf{h}_{\text{eff}} - \alpha \mathbf{m} \times \mathbf{m} \times \mathbf{h}_{\text{eff}}.$$

The transport term in the above version of LLS can be understood as a continuum limit of discrete spin transfer terms. But in order to obtain a non-adiabatic contribution, it clearly matters to which form of the Landau-Lifshitz-Gilbert equation (Gilbert or Landau-Lifshitz form) it is added, or, in other word, how internal damping is expressed.

Relation with Slonczewski's spin torque

The spin-transfer terms (at least the adiabatic one) in LLS are typically interpreted as homogenized versions of Slonczewski's spin transfer model between two homogeneously magnetized layers separated by paramagnetic spacers within a five-layer system. If no additional interaction or damping mechanisms are active, Slonczewski's semi-classical approach has led, in suitable units, to a dynamical system

$$\begin{cases} \dot{S}_1 - J S_1 \times (S_1 \times S_2) = 0 \\ \dot{S}_2 - J S_2 \times (S_1 \times S_2) = 0 \end{cases}$$

in terms of two director fields S_1 and S_2 .

Extending this system to an infinite spin chain of spacing $h \ll 1$, we are led to consider the modified Slonczewski spin torque

$$\tau_k^h(\mathbf{m}) = J \mathbf{m}_k \times \mathbf{m}_k \times \frac{(\mathbf{m}_{k+1} - \mathbf{m}_{k-1})}{2h}.$$

In a discrete-to-continuum limit, when $h \searrow 0$ and $\{\mathbf{m}_k\}_{k \in \mathbb{Z}}$ approximates $\mathbf{m}=\mathbf{m}(x,t)$, we expect

$$\dot{\mathbf{m}}_k - \tau_k^h(\mathbf{m}) \rightarrow \frac{\partial \mathbf{m}}{\partial t} + J \frac{\partial \mathbf{m}}{\partial x}.$$

This can be made rigorous, starting from a three dimensional lattice model, see [1].

Theorem. *The Landau-Lifshitz-Slonczewski equation is the continuum limit of lattice Landau-Lifshitz equations with Slonczewski's spin-transfer torque.*

Singularity formation and changes in topology

A typical phenomenon in the context of LLG dynamics is the spontaneous formation of finite time singularities, i.e., the blow-up of magnetization gradients $\nabla \mathbf{m}$. Such an event is inherently connected with topological changes. In fact, blow-up can be ruled out under a smallness condition on initial configurations \mathbf{m}_0 in terms of integrals of the form

$$\int_{\Omega} |\nabla \mathbf{m}_0|^n dx \quad (n=2,3 \text{ is the space dimension})$$

which provides topological lower bounds. For $n=2$ the integral corresponds to a multiple of the exchange energy. In this case, the possible blow-up scenario is precisely characterized: concentration of exchange energy at certain singular points leads to a quantized energy drop and the formation of one or more magnetic bubbles in certain homotopy classes. More precisely, at singular times $t=t_0$ the energy drops

$$\lim_{t \nearrow t_0} E(\mathbf{m}(t)) = E(\mathbf{m}(t_0)) + 4\pi d^2 |k|$$

for $k \in \mathbb{Z} \setminus \{0\}$ according to a change in the topological \mathbf{S}^2 -degree, measuring the oriented number of covers of \mathbf{S}^2 by the mapping \mathbf{m} ,

$$\lim_{t \nearrow t_0} \deg(\mathbf{m}(t); \mathbf{S}^2) = \deg(\mathbf{m}(t_0); \mathbf{S}^2) + 4\pi k.$$

This is the result of the formation of bubbles in the vicinity of singular points x_j , i.e.

$$\frac{1}{2} |\nabla \mathbf{m}(t)|^2 \rightarrow \frac{1}{2} |\nabla \mathbf{m}(t_0)|^2 + 4\pi \sum_{j=1}^{\ell} |k_j| \delta(x_j)$$

$$\omega(\mathbf{m}(t)) \rightarrow \omega(\mathbf{m}(t_0)) + 4\pi \sum_{j=1}^{\ell} k_j \delta(x_j)$$

for point masses $\delta(x)$ and where $\omega(\mathbf{m})$ is the topological vorticity given by

$$\omega(\mathbf{m}) = \left\langle \mathbf{m}, \frac{\partial \mathbf{m}}{\partial x_1} \times \frac{\partial \mathbf{m}}{\partial x_2} \right\rangle.$$

For the free LLG without external forcing, this phenomenon is part of the relaxation process converging towards a stable configuration. A spin transfer torque offers the possibility to induce bubbling and hence a change in topology starting from stable configurations. An interesting situation is the current induced switching of a magnetic vortex core \mathbf{v}^+ mediated by the nucleation of an vortex-antivortex pair $(\mathbf{v}^-, \mathbf{a}^-)$ of reverse polarization as demonstrated in [2]. A lower bound for the energy barrier for the nucleation process is $\Delta E = 4\pi d^2$. This corresponds to the energy release after the collision and annihilation of the original vortex with the antivortex which together form a bubble $\mathbf{S}^2 = \mathbf{v}^+ \oplus \mathbf{a}^-$. In the above energy balance this corresponds to $k=1$ and a change in topology from $\deg(\mathbf{m}(t); \mathbf{S}^2) = 1/2$ for $t < t_0$ the time of collision to $\deg(\mathbf{m}(t_0); \mathbf{S}^2) = -1/2$.

A crucial step is to investigate optimal conditions on the size and profile of the applied current \mathbf{v}

suitable to overcome the energy barrier, a challenging yet untouched inverse problem of mathematical analysis.

Thiele's equation in the presence of a spin torque

Rescaling space by the exchange length and approximating stray-field interaction by shape anisotropy leads to the following effective energy density for a planar nanomagnet

$$e_{\varepsilon}(\mathbf{m}) = \frac{1}{2} |\nabla \mathbf{m}|^2 + \left(\frac{m_3}{\varepsilon} \right)^2.$$

Complemented by curling boundary conditions, the system accommodates magnetic vortices of core size ε . In the regime $\varepsilon \ll 1$, energy and vorticity concentrate near vortex locations X , i.e., more precisely,

$$e_{\varepsilon}(\mathbf{m}) \sim \pi \log(1/\varepsilon) \delta_X \quad \text{and} \quad \omega(\mathbf{m}) \sim 4\pi q \delta_X.$$

Conversely, in the singular limit $\varepsilon \searrow 0$, vortex trajectories can be retraced by following the dynamics of energy and vorticity concentration, governed by corresponding conservation laws associated with LLS. Such a reduction to a point system is typically possible in the absence of bubbling, i.e., under tight restrictions on initial energies (well-preparedness) and the external energy supply. We proved in [3]:

Theorem. *For well-prepared initial configurations with $\omega(\mathbf{m}_0) \sim 4\pi q \delta(X_0)$ and $\alpha_{\varepsilon} e_{\varepsilon}(\mathbf{m}_0) \sim D \delta(X_0)$ and below a critical current density, we have $\omega(\mathbf{m}(t)) \sim 4\pi q \delta(X(t))$ for $t < T$, where $X = X(t)$ is governed by the modified Thiele equation*

$$G \times (\dot{X} - \mathbf{v}) + D (\dot{X} - \xi \mathbf{v}) + \nabla W(X) = 0$$

with $G = 4\pi q \hat{\mathbf{e}}_3$ and $\xi = \lim_{\varepsilon \rightarrow 0} \beta_{\varepsilon} / \alpha_{\varepsilon}$.

Current research addresses the problem of merging Thiele's description for LLS with the bubbling analysis discussed before, in order to incorporate topological changes. A first step has been achieved in [4] for the the unforced LLG equation with large energy excess, giving rise to a time-dependent gyro-force $G(t) = 4\pi q(t) \hat{\mathbf{e}}_3$ and offering, e.g., the possibility to reverse the sense of gyration upon bubbling.

- [1] Melcher, C., Ptashnyk, M.: Landau-Lifshitz-Slonczewski equations - global weak and classical solutions. *SIAM J. Math. Anal.* (1), 407–429 (2013)
- [2] Liu, Y., Gliga, S., Hertel, R., Schneider, C.M.: Current-induced magnetic vortex core switching in a Permalloy nanodisk *Appl. Phys. Lett.* (11), 112501 (2007)
- [3] Kurzke, M., Melcher, C., Moser, R.: Vortex motion for the Landau-Lifshitz-Gilbert equation with spin-transfer torque, *SIAM J. Math. Anal.* (3), 1099–1121 (2011)
- [4] Kurzke, M., Melcher, C., Moser, R., Sporn, D.: Vortex dynamics in the presence of excess energy for the Landau-Lifshitz-Gilbert equation *Calc. Var. Partial Differential Equations* (2013), to appear

Theoretical probing of inelastic spin-excitations in adatoms on surfaces

S. Lounis¹, A. T. Costa², R. B. Muniz², and D. L. Mills³

¹ Peter Grünberg Institut/Institute for Advanced Simulation, Forschungszentrum Jülich, Germany

² Instituto de Física, Universidade Federal Fluminense, 24210-340 Niterói, Rio de Janeiro, Brazil

³ Department of Physics and Astronomy, University of California Irvine, California, 92697 USA

Within time-dependent density functional theory, combined with the Korringa-Kohn-Rostoker Green function method, we devised a real space method to investigate spin excitations, which are probed nowadays by state of the art inelastic scanning tunnelling spectroscopy. Our scheme enables the description and prediction of the main characteristics of these excitations, i.e. their resonance frequency, their lifetime and their behaviour upon application of external perturbations such as a magnetic field. We illustrate our method with application to 3d adatoms and dimers on several metallic substrates.

Magnetic atoms adsorbed on nonmagnetic substrates have been a topic of active study, both to provide insight into fundamental aspects of magnetism and as possible elements for future information technology. Scanning tunneling spectroscopy (STS) was, for example, utilized for atom-by-atom engineering and magnetometry of tailored nanomagnets [1]. It was also demonstrated, that such an experiment detects magnetic excitations by measuring the changes of the conductance (see e.g. [2,3]). The possibility to excite the substrate leads to an increase of the number of possible final channels for the tunneling electron when the STS bias matches an excitation energy threshold, leading to an abrupt increase of the conductance. Several parameters can affect the properties of these excitations, e.g. (i) the type of substrate, (ii) the details of the hybridization between the electronic states of the adsorbate and those of the substrate, (iii) and the symmetry, shape and size of the adsorbate. Describing such excitations from first-principles is a highly non-trivial task requiring access to dynamical response functions such as the transverse dynamical magnetic susceptibility χ that, in linear response, describes the amplitude of the transverse spin motion produced by an external magnetic field B_{ext} of frequency ω . The imaginary part of χ gives access to the local density of spin-excitations.

We developed a method that allows us to address magnetic excitations using the Korringa-Kohn-Rostoker single particle Green function (KKR-GF) within the framework of time-dependent density functional theory [4]. Our scheme is readily applied to bulk materials, to surfaces with adsorbed films, and it is a real space formalism ideal for diverse small nanostructures. To illustrate our scheme, we explore spin-excitations of 3d adatoms (Cr, Mn, Fe

and Co) on Cu(100), Cu(111) and Ag(111) surfaces.

We solve the following Dyson-like equation:

$$\chi = \chi_0(1 - U\chi_0)^{-1}, \quad (1)$$

where χ_0 , a convolution of Green function integrated over the energy, is the Kohn-Sham susceptibility and χ , the total susceptibility, is exact in principle if the full exchange and correlation kernel U is known. In practice, one often invokes the adiabatic local spin density approximation (ALDA); U can also be viewed as a Stoner parameter, i.e. ratio of the local exchange splitting divided by the magnetic moment, whose value is in the range of $1\text{ eV}/\mu_B$ for 3d transition elements.

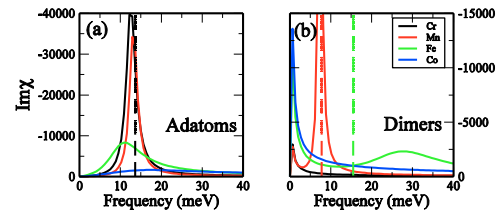


FIG. 1: In (a) the imaginary part of χ is plotted for every adatom when applying an additional magnetic field along the z -direction corresponding to a Larmor frequency of 13.6 meV (dashed line). In (b) are shown $\text{Im}\chi$ calculated for the four dimers. The optical modes, estimated for Mn and Fe from a Heisenberg model, are represented as dashed lines.

In Fig. 1(a), we show our calculations of the resonant response of the local moments for the four adatoms we have investigated on the Cu(001) surface [4]. If one applies an external magnetic field along the initial direction of the magnetic moments, we expect from a Heisenberg model a delta function in the response spectrum located at the Larmor frequency. For the field we have applied, a g value of 2 would provide a resonance at 13.6 meV . As can be seen in Fig. 1(a), instead of delta functions we obtain resonances of different widths, i.e. resonances that are shifted differently from the ideal Larmor frequency depending on the chemical nature of the adatom. Cr and Mn are characterized by sharper resonances compared to Fe and Co, meaning that the former adatoms would be reasonably described by a Heisenberg model where the magnetic exchange interactions are evaluated within an adiabatic approach. The observed damping is induced by Stoner (electron-hole) excitations described by the Kohn-Sham susceptibility χ_0 and is related to the local density of states (LDOS) [3,4], and is thus influenced by

the position of the d levels relative to the Fermi energy. Consequently, the Co and Fe resonances are quite broad, since their minority spin levels intersect the Fermi level, whereas those for Mn and Cr are much sharper since for these adatoms the Fermi level lies between the majority and minority states.

The resonant (Larmor) frequency scales linearly with the applied magnetic field, as does the damping of the resonances for small frequencies, which is the regime of interest for STS. We have shown in a combined theoretical and experimental work [3] that such a behavior holds for an Fe adatom on Cu(111) and on Ag(111) surfaces (see e.g. Fig.2). The g-value on the latter, however, and contrary to the copper substrate, was surprisingly larger than 3, both experimentally and theoretically.

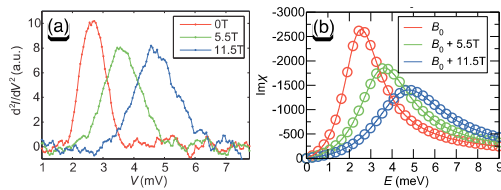


FIG. 2: Fe adatom on Ag(111) surface: The second derivative of the current with respect to the bias voltage measured experimentally by STS (left) and the calculated $\text{Im}\chi$ (right). Increasing the magnitude of an external magnetic field leads to a shift of the resonances to higher energies as well as a linear decrease in their lifetime. Stoner excitations create such a broadening.

Fig.2 shows a nice agreement between theory and experiment, although the theoretical lifetimes are smaller compared to the experimental ones. One would think naively that since Cu and Ag have rather similar electronic properties, their impact on the magnetic response of the adatoms should be qualitatively the same. An important difference, though, between the two surfaces consist in the position of their surface states. For Ag, the bottom of the surface state is much closer to the Fermi energy (~ 60 meV) compared to the one of Cu (~ 500 meV).

A careful theoretical investigation was carried out considering several magnetic 3d adatoms at different locations: (i) on top of the surface, (ii) embedded in the last surface layer, (iii) and embedded in the center of the slab (30 Ag layers) employed to simulate the surface. The closer to the surface, the stronger should be the interaction between the impurity and the surface state. Among all investigated impurities, only the Fe adatom and Mn atom embedded in the surface layer exhibit a large g-value of ~ 3 . Additionally, a strong disturbance of the surface state can be achieved by reducing the thickness of the slab, which modifies the electronic properties of the surface at the Fermi energy and restores the usual g-value of Fe and Mn. This indicates, that the electronic properties of the surface state as well as details of the hybridization to the electronic states of the impurities play a crucial role in the observed g. We could relate this strong g-shift to the behavior of the real part of χ_0 [3].

We have also explored next nearest neighbor dimers of the 3d adatoms deposited on Cu(001) surface [4] starting from a ferromagnetic configuration (Fig.1 b). For the dimer, there are two resonances, a zero frequency acoustical mode, and a high frequency optical mode that is damped by decay into Stoner excitations. The position of the optical mode provides information on the stability of the assumed ground state. For Cr and Co, we find the optical mode at negative frequency, which informs us that the ferromagnetic state is unstable, whereas for Fe and Mn dimer the modes reside at positive frequencies, so ferromagnetism is stable in total accordance with our static DFT ground-state calculations. The adiabatic approximation and a Heisenberg model gives optical mode frequencies (shown as dashed lines in Fig1.b) at -19.7 meV, 15.4 meV, 39.2 meV and -33.1 meV for respectively Cr, Mn, Fe and Co dimers. The same arguments used to describe the response of the single adatoms apply for the optical modes of dimers: compared to the optical resonance of Mn dimer, the one of Fe is substantially broader and more shifted from the mode expected in the adiabatic approximation.

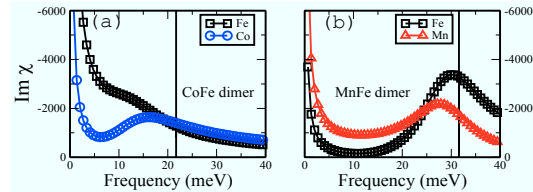


FIG. 3: Mixed dimers on Cu(001) surface: Local $\text{Im}\chi$ are shown in (a) for FeCo dimer and in (b) for MnFe dimer.

In the case of dimers made of different magnetic adatoms, i.e. FeCo dimer and FeMn dimer, we find the optical modes to occur at distinctly different frequencies (Fig. 3). This behavior, also explained from damping via Stoner excitations, is at variance with the Heisenberg description of the excitation spectrum of two well-defined localized spins where the optical mode is predicted to be unique for both adatoms. In the case of the FeMn dimer, the motion of Fe spin is damped far more strongly than that of Mn spin, but during its precession the latter feels the magnetic force of the heavily damped Fe spin which provides more damping on Mn.

Research supported by the HGF-YIG Programme VH-NG-717 (Functional nanoscale structure and probe simulation laboratory-Funsilab).

- [1] L. Zhou, J. Wiebe, S. Lounis, E. Vedmedenko, F. Meier, S. Blügel, P. H. Dederichs, R. Wiesendanger, Nature Physics 6, 187 (2010); A. A. Khajetoorians, J. Wiebe, B. Chilian, S. Lounis, S. Blügel, R. Wiesendanger, Nature Physics 8, 497 (2012).
- [2] A. A. Khajetoorians, S. Lounis, B. Chilian, A. T. Costa, L. Zhou, D. L. Mills, J. Wiebe, R. Wiesendanger, Phys. Rev. Lett. 106, 037205 (2011).
- [3] B. Chilian, A. A. Khajetoorians, S. Lounis, A. T. Costa, D.L. Mills, J. Wiebe, R. Wiesendanger, Phys. Rev. B 84, 212401 (2011).
- [4] S. Lounis, A. T. Costa, R. B. Muniz, D. L. Mills, Phys. Rev. Lett. 105, 187205 (2010); *ibid.* Phys. Rev. B 83, 035109 (2011).

Electrical Transport through Single Nanoparticles and Nanoparticle Arrays

Marcel Manheller¹, Silvia Karthäuser^{1,2}, Rainer Waser¹, Kerstin Blech², and Ulrich Simon²

¹Peter Grünberg Institut-7, Forschungszentrum Jülich, Germany

²Institute of Inorganic Chemistry, RWTH Aachen University, Germany

Electrical transport measurements on 3D arrays as well as on individual particles were performed on biphenylpropanethiol-capped gold nanoparticles with a diameter of 4 nm. The individual nanoparticle measurements exhibit Coulomb blockade behavior at room temperature. Depending on temperature different types of transport mechanisms can be distinguished, such as hopping, superexchange coupling, and tunneling. Furthermore, a discontinuity in the temperature dependent conductance was observed between 200 and 290 K. This discontinuity might be a consequence of a theoretically predicted structural crossover in the particle's morphologies.

Due to their unique electrical properties and their ease of modification ligand stabilized gold nanoparticles (AuNPs) are interesting building blocks for nanoelectronic applications. However, application of such nanoelements requires detailed investigations of the charge transport characteristics in order to understand and control the electrical transport. In this context we have synthesized biphenylpropanethiol (BP3)-capped AuNPs and performed detailed studies on the charge transport through BP3 capped AuNP arrays as well as through individual AuNPs. The particles have been synthesized in a two phase approach.[1] TEM measurements revealed particles with narrow size distribution and a mean metal core diameter of 4.1 ± 0.5 nm (derived from 251 particles).

Temperature dependent conductance measurements on AuNP arrays: Arrays of BP3 capped AuNPs were formed on IDE structures (interdigitated electrode structures) by drop casting a solution of AuNPs in toluene. The electrical transport characteristics were investigated by complex impedance measurements, recorded as a function of frequency (10 mHz – 1 MHz) and temperature ($340 > T/K > 10$) at a constant voltage ($U_{SD} = 100$ mV). The results are depicted in Figure 1. In principle, depending on temperature three different transport regimes can be distinguished. The first and the third regime (Fig. 1, (I) $T_{red} = 300\text{--}340$ K, $E_A = 184$ meV; (III) $T_{blue} = 100\text{--}220$ K, $E_A = 58$ meV), follow a linear dependence according to the Arrhenius relation. For regime (I) a hopping process between nearest neighbors is deduced, while in regime (III) the charge transport is less temperature dependent and resembles features of the granular metal

model or the superexchange model, respectively. However, in the second regime (Fig. 1, II) $T_{yellow} = 230\text{--}290$ K) an atypical discontinuity is observed. An explanation might be a transition in the particle morphologies, which has been proposed from relativistic *ab initio* calculations [2].

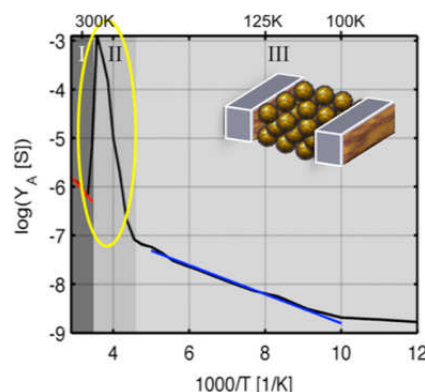


FIG. 1: Temperature-dependent conductance of a BP3-AuNP array plotted according to Arrhenius ($\log Y_A$ vs T^{-1}). The yellow circle marks the discontinuity in the I-V characteristic. Reprinted with permission from Ref. 3. Copyright 2012 American Chemical Society.

Temperature dependent conductance measurements on individual AuNPs: In order to investigate the charge transport on individual BP3-capped AuNPs, tailored nanoelectrode configurations have been prepared by e-beam lithography. A new fabrication route based on an optimized two-layer resist system in combination with an adopted developer system, as well as an elaborated nanoelectrode pattern was developed in order to achieve reproducible nanoelectrode structures comprising sub-5 nm gaps (Fig. 2) [4].

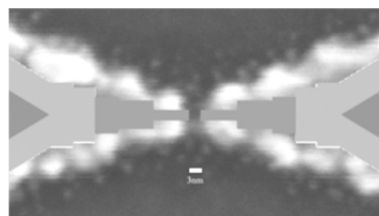


FIG. 2: High resolution SEM of nanoelectrode pairs with electrode separation of 3 ± 1 nm and a fabrication yield of 55% [4].

Immobilization of BP3-AuNPs was performed by dc dielectrophoretic trapping (DC-DEPT). Electrical measurements on the individual nanoparticle-nanogap test-devices were performed in a continuous flow cryostat with

varying temperature (RT– 4 K). It should be noted that the resistances measured for empty nanoelectrode gaps are usually larger than 1 T Ω , while nanoelectrode gaps filled with BP3-AuNPs exhibit resistances smaller than 10 G Ω . The temperature-dependent conductance obtained for the nanoelectrode/BP3-NP–BP3/nanoelectrode device is depicted in Fig. 3.

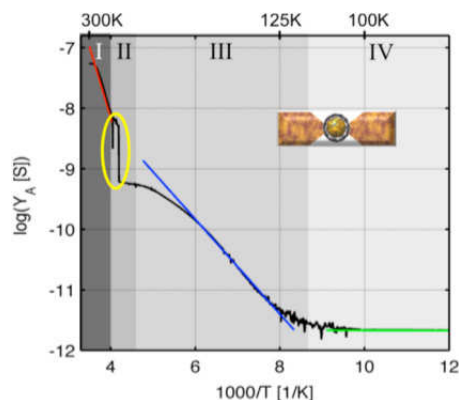


FIG. 3: Temperature-dependent conductance of an individual BP3-AuNP plotted according to Arrhenius ($\log Y_A$ vs T^{-1}). The yellow circle marks the significant singularity in conductance at $T \sim 235$ K. Reprinted with permission from Ref. 3. Copyright 2012 American Chemical Society.

Four different transport regimes can be distinguished clearly and are attributed according to their temperature dependence, to different transport mechanisms. In the highest temperature range (Fig. 3, (I), $T_{\text{red}} = 265\text{--}245$ K) an exponential decrease of the conductivity with decreasing temperature is observed, which is assigned to a thermally activated charge transport reflecting an activated hopping involving molecular moieties. In the lower temperature ranges (Fig. 3, (III), $T_{\text{blue}} = 200\text{--}110$ K and (IV), $T_{\text{green}} < 110$ K) a weaker temperature dependence or no significant temperature dependence are observed, respectively. In the temperature range T_{blue} superexchange coupling or electrical transport according to the granular metal model is considered as underlying charge transport mechanism. The main conduction mechanism in the lowest temperature regime, T_{green} , corresponds to tunneling, either direct or *Fowler–Nordheim* tunneling. Significantly, an analogous discontinuity as observed for the arrays (Fig. 1, (II), $T_{\text{dis}} = 230\text{--}290$ K) can be detected for individual AuNPs (Fig. 3, (II), $T_{\text{dis}} \sim 235$ K). Furthermore, this change of current, in the order of one magnitude, was fully reproducible, so that an accidental geometrical change can be excluded and thus might be referred to a transition in the particle morphologies.

Transport Measurements on a Single AuNP Showing Coulomb Blockade Behavior: Beside temperature dependent conductance measurements, we also performed cyclic I-U measurements of single BP3-AuNPs. Figure 4 depicts the resulting differential conductivity, (dI/dU), obtained from 250 cycles.

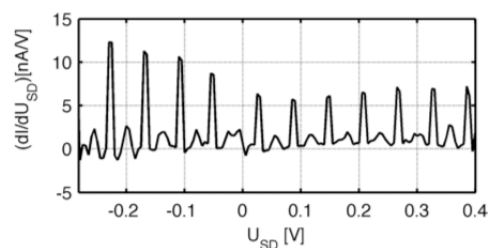


FIG. 4: First derivative of cyclic I-U measurements on a single BP3-NP in a nanogap at RT (averaged over 250 cycles and flattened). Periodic peaks with a distance of $\Delta U_{\text{CB}} = 61$ mV and a height of $\Delta G \approx 8$ nS are detected. Reprinted with permission from Ref. 3. Copyright 2012 American Chemical Society.

Most interestingly, equidistant periodic peaks are measured over a large range of applied voltage, which can be attributed to Coulomb blockade peaks and indicate that the electrical current flows through a single NP only. The peak distances allow the determination of the charging energy ($\Delta U_{\text{CB}} = 4E_C/e$; $E_C = 15$ meV) and the total capacitance of the NP ($E_C = e^2/2C_{\text{tot}}$; $C_{\text{tot}} = 5.2$ aF). However, since $E_C > k_B T = 25$ meV is a necessary requirement for measurements in the “strong” Coulomb blockade regime, it is not surprising that Coulomb blockade peaks appear here only as small modification of the total conductance. Nevertheless, the detection of Coulomb blockade behavior observable on a single-nanoparticle (NP) device at room temperature (RT) was so far only achieved in measurements with STM configurations and on AuNPs with a diameter of $d < 2.0$ nm [5,6].

Summarizing, the temperature dependent electronic transport investigations of BP3-AuNP arrays or individual BP3-AuNP revealed different transport mechanisms, assigned to thermally activated hopping, superexchange coupling, and tunneling. Furthermore, a discontinuity in the temperature dependence of the conductance in both experimental setups was observed, probably arising from a transition in the nanoparticle’s core morphology. Moreover, Coulomb blockade behavior was observed in the single-NP device at room temperature.

This work is supported by the DFG program Si609/9-1 and KA 1819/2-1.

- [1] M. J. Hostettler, et al., *Langmuir* 1998, 14, 17–30.
- [2] A. Barnard, et al., *ACS Nano* 2009, 3, 1431–1436.
- [3] M. Manheller, et al., *J. Phys. Chem. C*, 2012, 116, 20657–20665.
- [4] M. Manheller, et al., *Nanotechnology* 2012 23 (12), 125302 (6pp).
- [5] R. P. Andres, et al., *Science* 1996, 272, 1323–1325.
- [6] U. Zhang, et al., *Nano Lett.* 2003, 3, 305–307.

Dissecting a Multifunctional Organic-Metal Bond by Molecular Manipulation

C. Wagner¹, N. Fournier¹, F. S. Tautz¹, and R. Temirov¹

¹ Peter Grünberg Institut-3, Forschungszentrum Jülich, Germany

Based on single molecule manipulation experiments in a combined STM/FM-AFM (scanning tunneling microscope / frequency modulated atomic force microscope), we quantify the individual binding energy contributions to an organic-metal bond experimentally. The method allows the determination of contributions from, e.g., local chemical bonds, metal-molecule hybridisation and van der Waals interaction, as well as of the total adsorption energy.

The bonding of large organic adsorbates to metal surfaces is subject of an intense research effort. If the molecule has functional groups, one may expect different bonding channels to contribute to the overall bonding of the molecule to the surface. An example for such a multifunctional bond is that of the well-studied model molecule PTCDA to noble metal (111)-surfaces. The PTCDA-metal bond consists of local bonds of the carboxylic oxygen atoms (O_{carb}) to metal atoms, chemisorption of the perylene core due to hybridization of molecular and metal states, and the van der Waals interaction. The theoretical description of such multifunctional bonds is challenging as non-local dispersion is only now being included into density functional theory.

We present an experimental method which allows the partitioning of the overall bonding energy between different bonding channels, and apply it to PTCDA/Au(111) [1]. The approach is based on molecular manipulation in a combined low temperature UHV STM/FM-AFM with a qPlus sensor (Fig. 1). STM is used for high resolution imaging and location of the functional group at which to dock the tip to the molecule, FM-AFM is used to measure the junction stiffness dF_z/dz [1,2] while manipulating the molecule off the surface by tip retraction (z = vertical tip coordinate) [3]. Because the stiffness of the surface-molecule-tip junction is measured throughout the complete removal process, the strength of all interaction potentials constituting the PTCDA-Au(111) bond is probed, albeit in a tangled manner. To disentangle the contributions, we parameterize the bonding channels of the molecule-substrate interaction with generic potentials of sufficient generality, simulate the junction stiffness based on these potentials throughout the manipulation process, and fit the simulated stiffness to the experiment.

After a bond between the tip and one O_{carb} atom is established, the tip is retracted vertically from the surface. Each experiment consists of 10

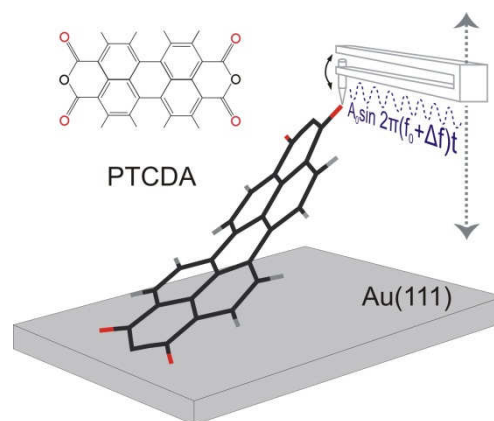


FIG. 1: Scheme of the experimental setup. A single PTCDA molecule on Au(111) is contacted by a tip attached to a qPlus sensor. The oscillating sensor is retracted from and approached to the surface. In this way, the molecule is repeatedly detached from the surface and brought back. Changes in the resonance frequency of the sensor reflect changes in the junction stiffness.

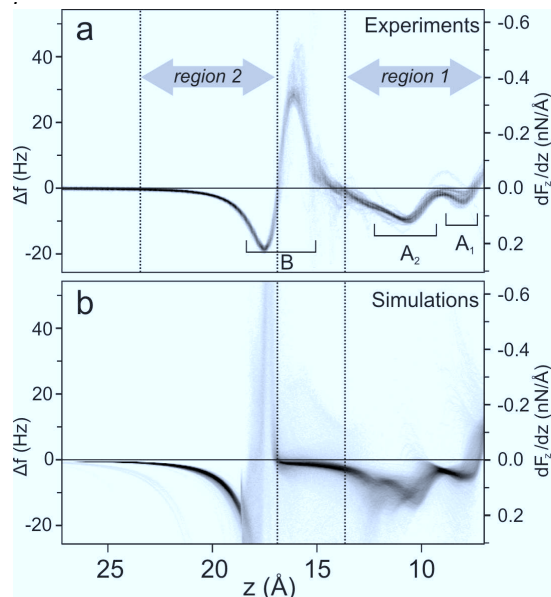


FIG. 2: (a) Histogram of 226 Δf traces acquired during lifting and lowering of PTCDA. All curves have been aligned at feature B. The z -axis is shifted to match the simulated curves in panel b. Dotted lines mark regions 1 and 2 within which the correspondence between experiment and simulation is calculated (reduced χ^2). Distinct features of the histogram are labeled A_1 , A_2 , and B [2]. (b) Histogram of 4166 Δf traces simulated with different parameter sets P .

reproducible retraction-approach cycles during which the molecule-surface bond is always fully broken and $dF_z/dz(z) = -2k_0/f_0 \Delta f(z)$ is recorded [Fig. 2(a)].

We model the PTCDA-metal bond by generic atom-surface potentials that describe local chemical bonds, molecule-metal hybridization, dispersion interaction, and Pauli repulsion. The dispersion interaction is modeled by a C_3z^{-3} potential, the other potentials by exponential functions. The potentials are parameterized by a set P of nine parameters [1]. The internal mechanical properties of the molecule itself are described by a standard molecular-mechanics model. We calculate the force gradient dF_z/dz for 4166 sets P generated by a Monte Carlo approach. A histogram of the simulated $\Delta f(P, z)$ curves is shown in Fig. 2(b). Evidently, our generic potentials simulate the experiment very well. The features A_1 , A_2 , and B are reproduced with remarkable accuracy. The remaining discrepancies between simulation and experiment [1] are accounted for by neglecting the experimental data between 13.7 Å and 16.9 Å when quantifying the correspondence between simulations experiment (reduced χ^2).

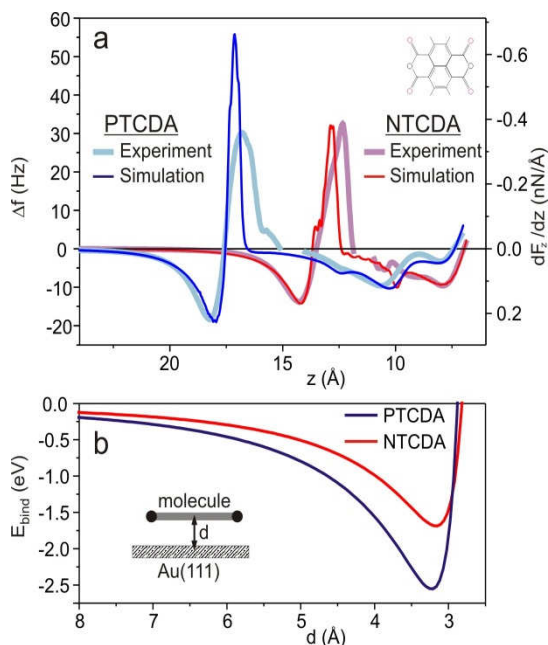


FIG. 3: (a) Comparison between simulated and experimental Δf curve for PTCDA and NTCDA on Au(111). The experimental curves are cut in the region of an instable junction (Fig. 2) and both parts are separately aligned with the simulation. (b) Binding potential as a function of molecule-substrate separation for PTCDA and NTCDA.

The best fit to the experiment is found for a binding energy of 2.5 eV for PTCDA on Au(111). The Δf curve for the respective simulation is shown in Fig. 3(a). We find that the van der Waals attraction is in the range of 100 meV for each C as well as O atom, while neither of the two species has any chemical interactions with the Au(111) surface. This is consistent with *ab-initio* calculations, as well as other spectroscopic methods that suggest pure physisorption of PTCDA on Au(111) [4].

Recent DFT calculations which include dielectric screening within the substrate yield an energy of 2.4 eV, which is close to our experimental result [5].

To validate our method further, we calculate the frequency shift of the smaller NTCDA molecule during lift-off from Au(111). The comparison between simulation and experiment in Fig. 3(a) shows an excellent agreement. Note that this agreement for NTCDA is *not* the result of any fitting, but just a consequence of the universal character of our potentials obtained for PTCDA. The potentials have predictive power for systems which exhibit similar physics.

In conclusion, we have reported the first analysis which allows the quantitative identification of different bonding channels of large organic adsorbates on the basis of experimental data alone. As a result of this analysis, the precise shape of the total binding potential can be determined. As an example, we show the van der Waals-like potential that results if the distance between a flat and fully relaxed PTCDA molecule and the Au(111) surface is varied [Fig. 3 (b)]. The resulting curves can be compared to *ab-initio* calculations. Moreover, the method reported here represents a novel way to measure the adsorption energy of molecular adsorbates on a single-molecule level. Note that this method is also applicable in cases where the determination of the adsorption energy by thermal desorption spectroscopy is impossible because molecules decompose before desorbing. In the present paper, we have carried out the experiments and the corresponding analysis for an adsorbate-substrate combination which exhibits a small lateral corrugation potential, to demonstrate the principle. However, we anticipate that our approach is also applicable to more strongly corrugated substrates, if combined with a customized tip retraction trajectory [2] which minimizes sliding as much as possible.

We gratefully acknowledge T. Lippert, N. Attig, O. Büchner, and W. Homberg (Forschungszentrum Jülich) who have supported us with CPU time on JUDGE. We thank D. Park and J. Mayer from RWTH Aachen for the help with the FIB. R.T. thanks the Helmholtz-Gemeinschaft for financial support for his Young Investigator Research Group.

- [1] C. Wagner, N. Fournier, F. S. Tautz, and R. Temirov, Phys. Rev. Lett. 109, 076102 (2012).
- [2] N. Fournier, C. Wagner, C. Weiss, R. Temirov, and F. S. Tautz, Phys. Rev. B 84, 035435 (2011).
- [3] R. Temirov, A. Lassise, F. B. Anders, and F. S. Tautz, Nanotechnology 19, 065401 (2008).
- [4] J.F. S. Tautz, Prog. Surf. Sci. 82, 479 (2007).
- [5] V. G. Ruiz, W. Liu, E. Zofer, M. Scheffler, and A. Tkatchenko, Phys. Rev. Lett. 108, 146103 (2012).

Orbital tomography for highly symmetric adsorbate systems

Benjamin Stadtmüller¹, Martin Willenbockel¹, Eva M. Reinisch², Thomas Ules², Francois C. Bocquet¹, Sergey Soubatch¹, Peter Puschnig², Georg Koller², Mike G. Ramsey², F. Stefan Tautz¹, and Christian Kumpf¹

¹ Peter Grünberg Institut-3, Forschungszentrum Jülich, Germany

² Institut für Physik, Karl-Franzens-Universität Graz, Austria,

Orbital tomography is a new and very powerful tool to analyze the angular distribution of a photoelectron spectroscopy experiment. It was successfully used for organic adsorbate systems to identify (and consequently deconvolute) the contributions of specific molecular orbitals to the photoemission data. The technique was so far limited to surfaces with low symmetry like fcc(110) oriented surfaces, owing to the small number of rotational domains that occur on such surfaces. In this letter we overcome this limitation and present an orbital tomography study of a 3,4,9,10-perylene-tetracarboxylic-dianhydride (PTCDA) monolayer film adsorbed on Ag(111). Although this system exhibits twelve differently oriented molecules, the angular resolved photoemission data still allow a meaningful analysis of the different local density of states and reveal different electronic structures for symmetrically inequivalent molecules. Our results demonstrate that orbital tomography is not limited to low-symmetry surfaces, a finding which makes a broad field of complex adsorbate systems accessible to this powerful technique.

The alignment of the electronic levels at interfaces between different materials plays a crucial role for the functionality of (organic) electronic devices. In case of metal-organic interfaces, in particular, the lowest unoccupied and highest occupied molecular orbitals (LUMO and HOMO) play an important role in the interaction of molecules across the interface since they, e.g., determine the bonding mechanisms of molecules on surfaces. Direct access to the occupied frontier orbitals can be provided by ultra violet photoelectron spectroscopy (UPS) which allows a very precise determination of the energetic positions of the occupied molecular orbitals as well as the substrate states. However, the assignment of the features in the photoemission spectra to molecular states is not easy, in conventional UPS it is often even impossible without additional knowledge about the system. Charge redistribution at and across the interface can lead to both population and depopulation of the individual molecular levels, even simultaneously within the same molecule. To some extent these limitations can be overcome by angular resolved photoemission spectroscopy (ARPES). The momentum distribution of the photoemission intensity from a specific molecular orbital can be understood in terms of the square of the Fourier

transform of the molecular wave function by approximating the final state as a plane wave. This opens the possibility to identify the molecular orbital from its ARPES signature, an idea which recently has been utilized in the "orbital tomography" technique [1,2]. Also spectral contributions of different molecules in the spectra can be separated. Therefore, this new technique holds great potential for investigating the arrangements of molecules in the unit cell, their orientations with respect to the substrate, and consequently allows to evaluate the complex interplay between intermolecular and molecule-substrate interactions [2].

So far the orbital tomography approach has only been applied to (110)-oriented surfaces of face centered cubic crystals. This is clearly due to the fact that this surface has a low symmetry (p2mm) which allows only few different molecular orientations since most molecules (especially elongated molecules) tend to align along high symmetry directions of the substrate. Adsorbate systems on higher symmetric surfaces, however, were so far considered to be too difficult to be analyzed by orbital tomography. In this work we attack this perceived limitation of the technique by investigating a very popular adsorbate system on the Ag(111) surface having p3m1 symmetry: The monolayer structure of PTCDA on Ag(111). The unit cell contains two inequivalent molecules with distinct azimuthal orientations [3]. Due to three rotational domains, each having one additional mirror domain, we hence have to deal with 12 molecules with different orientations on the surface.

It has been shown that the ARPES intensity emitted by one individual molecular orbital can be calculated from the wave function of the orbital [1,2]. An intensity map of such ARPES data can be obtained from a hemispherical cut through the three dimensional Fourier transform of the molecular orbital wave function at a radius $|k|$ which is determined by the kinetic energy of the electrons in the final state. Fig. 1(a) shows such an ARPES map for the HOMO of one individual PTCDA molecule which is oriented with its long axis in horizontal direction in the Figure. In panel (b) and (c) the two different molecular orientations in the unit cell (0° and 77° with respect to the $[-101]$ substrate directions, see inset) and the occurrence of six rotational and mirror domains according to the symmetry of the surface are considered. For molecule B the misalignment of the molecule with

respect to the high symmetry direction becomes clearly visible: The intensity of the HOMO emission is smeared out to a continuous, modulated ring, see Fig. 1(c).

In Fig. 1(d) a calculated CBE map for the overall emission from the PTCDA herringbone monolayer structure in the HOMO region is shown. The map corresponds to the sum Fig. 1(b) and (c) for molecules A and B and is dominated by the pattern of molecule A. This is due to the coincidence of several peak positions in this map.

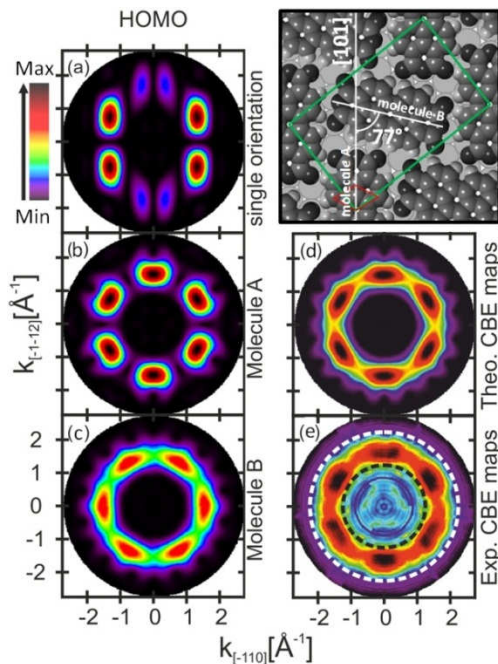


FIG. 1: Constant binding energy maps for the HOMO of PTCDA, calculated by density functional theory (a-d) and measured by ARPES (e). Panel (a) shows the map for a single molecule, in (b) and (c) the $p3m1$ symmetry of the substrate surface and the molecular orientation as shown in the inset are considered. In (d) the calculated map for the complete herringbone structure of is shown, in (e) the corresponding experimental map recorded at $E_B = 1.6$ eV.

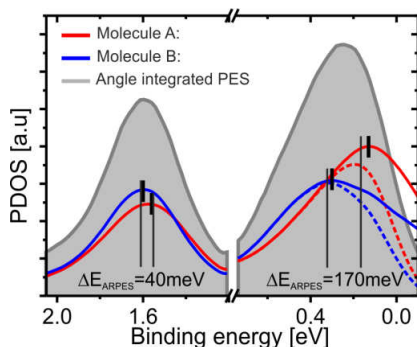


FIG. 2: Orbital projected density of states (PDOS, solid lines) of HOMO and LUMO for both molecules, obtained by orbital tomography. The ARPES data is shown as gray-shaded curves. Dotted lines consider the reduced population close to the Fermi edge. Short thick and long thin markers indicate peak positions obtained from our ARPES data and from STS [3], respectively.

In Fig. 1(e) the map with the corresponding experimental data is shown, obtained from a cut through the ARPES data cube at a binding energy

of 1.6 eV. It matches the calculated map very well. Already at this point we can conclude that the ARPES yield for a molecular adsorbate system with six rotational and mirror domains can be qualitatively understood by the concept of the plane wave approximation for the PES final state.

For a more quantitative analysis of the ARPES data we have used a tomographic approach to deconvolute the measured ARPES intensity and extract the contributions of the orbitals of the two individual molecules to the density of states. The details can be found in the principal publication [4]. The fitting parameters, which can be understood as the (energy resolved) density of states projected onto a molecular orbital (projected density of states, PDOS) [2] are shown in Fig. 2 for both molecules as a function of the binding energy. The measured PES intensity is also shown in gray. The latter is what one would see in a conventional photoemission experiment, and shows no indications for an energy splitting of the orbitals of both molecules, neither for the HOMO nor the LUMO. However, the result of the deconvolution algorithm reveals that molecule B has higher binding energies for both orbitals. While a relatively small difference of 40 meV was found between the HOMO levels of both molecules, the difference between the LUMO peaks is much larger: 170 meV. These differences in the binding energies of the electronic states of molecules A and B stem from the complex interplay between intermolecular and molecule-substrate interactions. Note that our results are in excellent agreement with scanning tunneling spectroscopy data (40 meV for the HOMO, 160 meV for the LUMO, see [3]).

In conclusion, we have achieved orbital-projected densities of states of the HOMO and LUMO resonances of the symmetrically inequivalent molecules in the PTCDA/Ag(111) herringbone monolayer structure. The results are in excellent agreement with STS data. This emphasizes that orbital tomography based on ARPES data, even though it represents an integrating method and hence has pretended disadvantages compared to a local probe technique like scanning tunneling spectroscopy, provides reliable results even for complex surfaces with high symmetry and a correspondingly large number of equivalent domains.

This work was supported by the Austrian Science Fond and the Deutsche Forschungsgemeinschaft.

- [1] P. Puschnig, S. Berkebille, A.J. Fleming, G. Koller, K. Emtsev, T. Seyller, J.D. Riley, C. Ambrosch-Draxl, F.P. Netzer, M.G. Ramsey, *Science* **326**, 702 (2009)
- [2] P. Puschnig, E.-M. Reinisch, T. Ules, G. Koller, S. Soubatch, L. Ostler, L. Romaner, F.S. Tautz, C. Ambrosch-Draxl, M.G. Ramsey, *Phys. Rev. B* **84**, 235427 (2011)
- [3] A. Kraft, R. Temirov, S.K.M. Henze, S. Soubatch, M. Rohlfing, F.S. Tautz, *Phys. Rev. B* **74**, 041402 (2006)
- [4] B. Stadtmüller et al., *EPL (Europhysics Letters)* **100**, 26008 (2012)

Surface ‘click’ of DNA followed by directed metallization allows construction of contactable conducting nanostructures

Jan Timper¹, Katrin Gutmiedl², Christian Wirges², Janine Broda¹, Michael Noyong¹, Joachim Mayer³, Thomas Carell², and Ulrich Simon¹

¹ Institut für Anorganische Chemie, RWTH Aachen University, Germany

² Department Chemie und Biochemie, Ludwig-Maximilians-Universität München, Germany

³ Gemeinschaftslabor für Elektronenmikroskopie, RWTH Aachen University, and Ernst Ruska-Centrum, Forschungszentrum Jülich and RWTH Aachen, Jülich, Germany

A difunctional DNA template was designed with one segment for immobilization on a functionalized substrate by a copper-catalyzed reaction, and a second sequence which is equipped with reductive groups. These groups create silver nucleation centers which act as seeds for the metallization by gold deposition. The diameter of the resulting metallically conductive nanowires can be adjusted.

In the last decade the huge potential of the DNA base pairing for self-assembled nanostructures has been demonstrated in a huge number of publications. Impressive examples include e.g. two- and three-dimensional DNA origami structures. Thus, this highly programmable molecule is of considerable interest for the bottom-up creation of electronic circuitry. However, the intrinsic conductivity of DNA is low. Therefore different protocols have been developed to achieve electronic conductivity, e.g. by continuously coating the DNA templates with metals. These routes mainly rely on the reduction of electrostatically bound metal ions, which serve as counter ions for the negatively charged DNA backbone. In this process, small metal clusters are formed which act as seeds for a subsequent development step, i.e. the reductive deposition of metal from solution. In order to increase the selectivity of the metallization process, specific routes, that rely on bimetallic coating, the photoinduced deposition of silver or the formation of DNA-Pt(II) adducts as precursors to metal deposition, brought progress in this direction.

We recently reported the successful formation of silver/gold bimetallic coatings on artificial DNA templates [1]. Along the templates alkyne labeled sugar molecules were localized in an azide-alkyne-cycloaddition to modified Thymine bases which served as localized reducing agents for Ag⁺ in a Tollens reaction. The resulting Ag⁰ seeds then served as catalytic centers for the reductive gold deposition. Nanowires as small as 10 nm could be obtained.

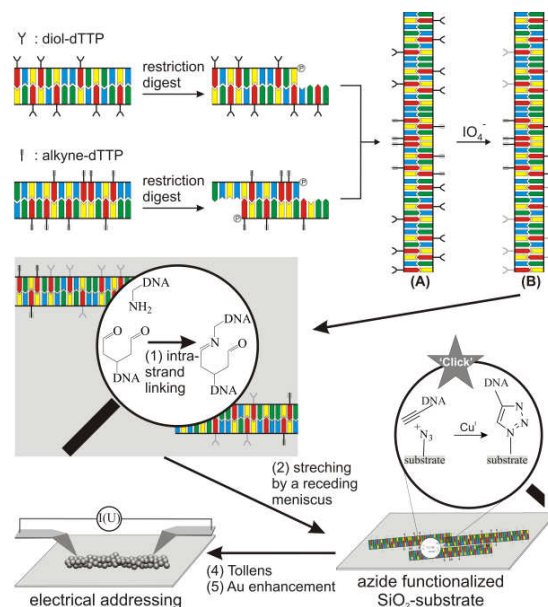


FIG. 1: Schematic of the DNA metallization template by restriction digest followed by ligation of the three PCR-fragments to form alkyne-diol-DNA (aldoDNA, A). Subsequent application of periodate solution resulted in alkyne-di-aldehyde-DNA (aldaDNA, B) enabling the two step metallisation process. The aldaDNA exhibits intermolecular coupling (1) resulting in micrometer long DNA multi-strands after stretching onto an azide functionalized Si-substrate (2). The strands were covalently immobilized by ‘click’-reaction (3) which could be metallised (4, 5) forming electrically addressable nanowires. (dTTP: deoxythymine triphosphate) (Reproduced from Ref. [3]).

We identified the silver seed formation as the crucial step for obtaining a homogeneous gold coating. Hence, diol-containing nucleobases were designed to study the silver nucleation process in more detail [2]. These diol groups could be cleaved into mono- and dialdehyde groups, respectively, leading to a high density of reducing functional groups capable of Ag⁺ reduction which were homogeneously distributed along the DNA double strand. The dialdehyde DNA (daDNA) turned out to be more efficient with respect to Ag

seed density and distribution, and thus may lead to homogeneous metal coating in a subsequent Au development for nanowire formation. Although the approach we developed allows to metallise DNA in a programmed manner, the nanowires obtained are structurally highly delicate or even fragile and suffer from the lack of specific binding affinity to a stabilizing substrate, which is an indispensable prerequisite for future device integration.

In order to overcome these obstacles a novel type of DNA is needed, which, at the same time, is suitable for programmable metallization and for covalent immobilization on technically relevant substrates, e.g. silicon wafers (Figure 1). Furthermore, the DNA should be capable of intermolecular linking, which would allow multistrand formation for enhanced structural integrity. At the same time the capability of integration into programmed DNA assemblies should be retained, enabling the defined surface positioning of complex architectures, by utilization of pre-patterned functionalized surfaces.

Facing these challenges, we designed bi-functional DNA by ligation of an immobilization and a metallization sequence [3]. The immobilization sequence consists of a 300 bp long alkyne functionalized DNA sequence enabling the covalent binding to azide terminated Si-surfaces via the copper catalysed alkyne azide cycloaddition (CuAAC), whereas the 900 bp long metallization sequence uses the diol-nucleobase approach. This approach can serve two purposes at the same time: The formation of Ag seeds as the first step of a two step metallization process and the aldehyde derived interstrand linking analogous to glutaraldehyde crosslinking of proteins. We anticipate that this novel type of DNA fulfils the requirements formulated above, being continuously metallizable up to a length of micrometers.

The metallization process was first optimized on individual strands by immobilization prior to periodate cleavage. This way we obtained after 50 s Ag staining and 10 s Au development structures of only 5 to 9 nm in height in the AFM microscope. This corresponds to an increased height compared to DNA double strands.

Finally, by combining the interstrand linking and the covalent immobilization by applying a stretching technique to the DNA templates on an azide functionalized silicon surface, we obtained micrometer long DNA structures, that could be fixed with Cu(I)-catalyst. These DNA templates could be metallised by applying the procedure described above with a Au development time of 50 s. The structures obtained were stable enough to apply our in situ measuring setup for the assessment of the electrical properties [4]. Figure 2 shows three images taken on a micrometer long and about 80 nm thick nanowire with two measuring tips attached.

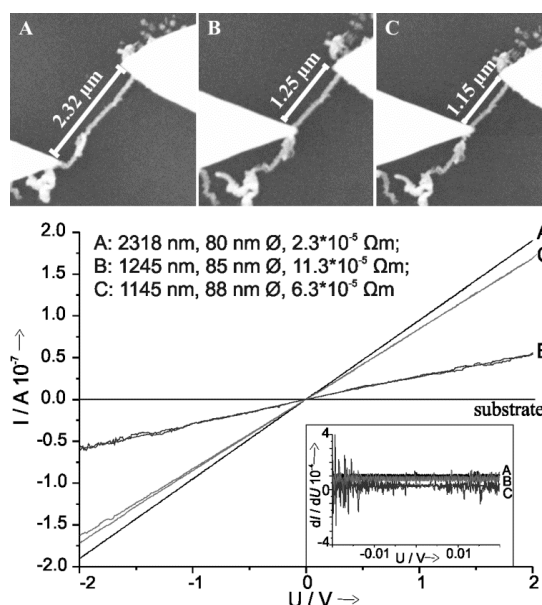


FIG. 2: The SEM pictures show conducting AFM tips in different positions on the metal structures during the contacting process. The resulting $I(U)$ -characteristics were measured in situ and clearly show ohmic behaviour. The inset shows the respective dI/dU -curves, representing constant conductivity values within the noise range. Variations in conductivity can be assigned to the quality of the contacts. The $I(U)$ -characteristics correspond to the different positions of the nanomanipulator tips on the DNA templated Au nanowire. The measurements clearly show linear $I(U)$ -characteristics with no hysteresis. Resistances are independent of the tip-to-tip distances, with the differences resulting from the respective contact quality. (Reproduced from Ref. [3]).

$I(U)$ -characteristics recorded at three different tip-to-tip distances clearly show a linear response over the whole voltage range, reflecting metallic conductivity. The respective conductivities however are far too low for polycrystalline gold, but in good agreement with data obtained for polycrystalline nanowires.

The combined application of the presented metallization and immobilization sequences in complex DNA architectures, e.g. DNA origami, present a promising approach for the construction of DNA templated nanoelectronic circuitry or molecular lithography.

- [1] M. Fischler, U. Simon, H. Nir, Y. Eichen, G. A. Burley, J. Gierlich, P. M. E. Gramlich, Th. Carell, *Small* **2007**, 3, 1049-1055.
- [2] C. T. Wirges, J. Timper, M. Fischler, A. S. Sologubenko, J. Mayer, U. Simon, Th. Carell, *Angew. Chem. Int. Ed.* **2008**, 48, 219-223.
- [3] J. Timper, K. Gutmiedl, C. Wirges, J. Broda, M. Noyong, J. Mayer, T. Carell, U. and Simon, *Angew. Chem. Int. Ed.* **2012**, 51, 7586-7588.
- [4] a) M. Noyong, K. Blech, A. Rosenberger, V. Klocke, U. Simon, *Meas Sci Technol*, **2007**, 18, N84-N89; b) K. Blech, M. Noyong, F. Juillerat, T. Nakayama, H. Hofmann, U. Simon, *J. Nanosci. Nanotechnol.* **2008**, 8, 461-465.

Single-crystal neutron-diffraction study of the biomolecule guanidine 151 years after its first synthesis

P. K. Sawinski¹, M. Meven^{2,3}, U. Englert¹, and R. Dronskowski¹

¹ Institute of Inorganic Chemistry, RWTH Aachen University, Aachen, Germany

² Institute of Crystallography, RWTH Aachen University, Aachen, Germany

³ Jülich Centre for Neutron Science at FRM II, Forschungszentrum Jülich, Outstation at FRM II, Garching, Germany

The biochemically fundamental molecule guanidine crystallizes with a primitive orthorhombic unit cell and two symmetry-independent almost Y-shaped molecules in the asymmetric unit. Because crystallization of guanidine is extremely difficult – very probably due to the compound's extraordinarily large sensitivity towards moisture – the crystal-structure analysis had to wait since the molecule's first synthesis in the late 19th century, namely in the year 1861, until 2009. A single-crystal neutron-diffraction study now carried out using the HEiDi diffractometer at temperatures of 100 and 273 K eventually gives access to precious vibrational and bond-length data needed for a detailed understanding of the molecule on the basis of anisotropic displacement parameters. 151 years after its first synthesis, the structural secrets of guanidine have been uncovered.

The fundamental biomolecule guanidine, CN_3H_5 , may be considered as the imino-derivative ($\text{HN}=\text{C}$ linkage instead of $\text{O}=\text{C}$) of the likewise fundamental biomolecule urea, OCN_2H_4 , which defines the distinction between inorganic and organic chemistry. Although STRECKER synthesized guanidine for the first time in 1861 already, the crystal structure was unknown until the early 21st century, amazingly enough [1]. It is important to note that molecular guanidine which appears as a fragment in a plethora of various biomolecules (for example, in the DNA base guanine or in the biochemical break-down product creatinine), offers a fascinating opportunity for studying hydrogen-bonding phenomena in detail. As a matter of fact, this very compound features a fairly complicated hydrogen-bond network. Based on a preceding single-crystal X-ray diffraction study, we had tentatively identified a set of eight hydrogen bonds using simple donor–acceptor distance criteria [1]. In a next step, the hydrogen-bonding energies had been numerically quantified using GGA-PBE density-functional theory. As a result, bond strengths of up to 33.8 kJ mol^{-1} had been revealed, and one of the eight hydrogen “bonds” turned out as being *repulsive* in nature [2], an energetically unfavorable combination of an imino-nitrogen (donor) and an amino-nitrogen

(acceptor). In what follows, we present the results of a single-crystal neutron-diffraction study of guanidine carried out with the HEiDi instrument. By doing so, highly accurate spatial and anisotropic displacement parameters for all the atoms (C, N, and also H) were derived, a long-sought experimental benchmark for further theoretical studies.

To prepare the neutron-diffraction experiments, a suitable single crystal (72 mm^3) of guanidine was very slowly grown in a Schlenk tube over half a year, carefully sealed and then subjected to structural analysis using the hot-neutron four-circle diffractometer HEiDi at FRM II. At the beginning, selected rocking scans on the very first reflections confirmed the almost perfect quality of the crystal from the presence of Gaussian-like profiles, and there were no signs whatsoever for more than one grain. In order to collect all necessary Bragg data, a full half shell ($\pm h + k \pm l$) was recorded between 7 and 30° in 2Θ . As expected from the earlier X-ray analysis, there were also no violations of systematic extinctions, thereby corroborating the previously known space group *Pbca*. In the next step, another quarter shell ($+h + k \pm l$) was recorded between 30 and 70° . In order to further optimize the data quality and stabilize its subsequent refinement, we also measured another symmetry-equivalent set of the strongest 500 reflections ($l > 2\sigma$) in this 2Θ range with $(-h + k + l)$. In total about 3000 reflections were collected. To understand the influence of temperature, a second data set was obtained at 273 K, only 50 K below the melting temperature of guanidine. In order to measure these “high-temperature” data more rapidly, only those reflections with significant intensities of the measurement at 100 K were collected, summing up to about 2000 reflections [3].

As already known from the prior X-ray study, the guanidine molecule is composed of a central carbon (C) and three nitrogen (N) atoms, forming a Y-shaped C–N backbone which is planar within experimental uncertainties. The small molecule incorporates two chemically different functional groups, namely one imino (NH) and two amino (NH_2) functions. Without knowing anything about the spatial parameters of the H atoms contained in these functional groups, both amino and imino functions are easy to spot by comparing their bond

lengths, that is, from principles of organic freshmen chemistry. The relatively short C–N distance (about 1.30 Å) is assigned to the imino function connected by a double bond, and the longer C–N distances (ca. 1.37 Å) belong to the amino functions which are bonded to the central C atom through single bonds [3].

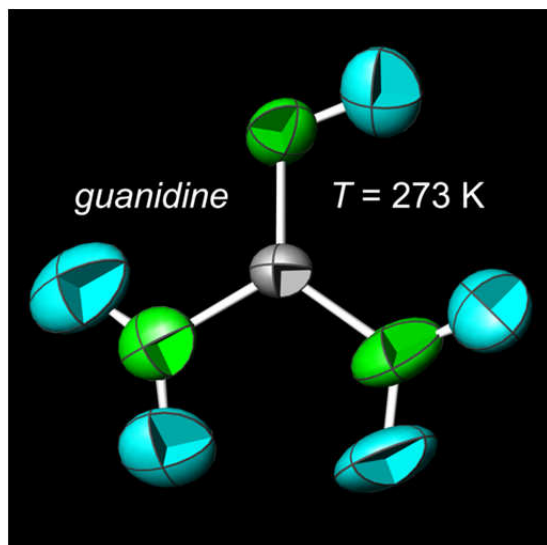


FIG. 1: ORTEP representation (50% probability level) of one of the two symmetry-independent guanidine molecules at 273 K.

Puzzlingly enough, the preceding X-ray study from 2009 revealed that one C–N bond exhibited an unusually strong bond-length shrinkage upon rising the temperature together with a relatively large thermal displacement parameter of one of the involved nitrogen atoms [1]. This rather unphysical phenomenon – regular chemical bonds do *not* shrink when the temperature is raised – served as an alarm sign to check for a rigid-body movement of the entire molecule. Such a rigid-body correction, however, can only be carried out if *all* thermal parameters of *all* the atoms are experimentally available, the basic necessity for this neutron study. Indeed, by applying such a rigid-body analysis based on the carefully refined anisotropic displacement parameters, the aforementioned C–N bond eventually arrives at a typical value of 1.37 Å at 273 K instead of the formerly refined 1.34 Å, a classical X-ray artifact. In conclusion and as already speculated in 2009, the two symmetry-independent guanidine molecules move as rigid entities, and molecule #1 exhibits a larger thermal motion than molecule #2.

We also note that the previously predicted N–H bond lengths as derived from GGA-PBE density-functional theory [2] were impressively verified by this neutron study. As a matter of fact, the leftover errors between theory and experiment turn out as being smaller than 0.03 Å. This comparison underlines the ability of modern quantum-chemical calculations based on the right functionals to correctly model the hydrogen-atom positions without prior information, even in those systems which hold a large number of hydrogen bonds, and it also emphasizes the necessity of having accurate experimental data available.

At this point, one may think of comparing guanidine's crystal structure with those of other ubiquitous molecules such as carbonic acid, OCO_2H_2 , and urea, OCN_2H_4 , once again. Very unfortunately, for carbonic acid such comparison is plainly impossible because of the staggering fact that its crystal structure is still unknown, despite the groundbreaking phase-pure synthesis of the molecule thirteen years ago already. With respect to urea, that particular molecule contains a carbonyl group instead of an imino group found in guanidine, as said at the beginning. Since this carbonyl O atom is a stronger hydrogen-bond acceptor than the imino-N atom, urea's tetragonal crystal structure is heavily affected by hydrogen bonds and, thus, looks very different from the one of guanidine. In particular, the rather short distance $\text{N–H}\cdots\text{O} = 2.07$ Å found at 123 K underlines the hydrogen-bond strength [4]. Due to the high crystal symmetry, the central carbonyl O atom simultaneously accepts four hydrogen bonds, mirrored by the planarity of the urea molecule and point-group symmetry *mm2*. Various models for the rigid-body motion of the urea molecule have been computationally tested in 1984 already, and the best seems to be the one in which the molecule vibrates as a rigid body but with the inclusion of two selected librations for the non-rigid motion of the amino groups [4]. The guanidine case, however, is different.

Coming back to the presently refined crystal structure using neutron data, the large data set of anisotropic displacement parameters for all the hydrogen atoms was eventually analyzed in order to find a simple correlation between these thermal parameters and the theoretically calculated strengths of the corresponding hydrogen bonds, but no such correlation was detected.

Summarizing, single-crystal neutron diffraction experiments performed with the HEiDi instrument at FRM II, Garching, succeeded in deriving a self-consistent set of spatial and anisotropic displacement parameters for crystalline guanidine at two different temperatures. The excellent data quality allowed to computationally model the molecular movement by performing a rigid-body correction, correctly so. Indeed, the data reveal that the two symmetry-independent guanidine molecules undergo libration. The unphysical thermal behavior of a single C–N bond as detected in a preceding single-crystal X-ray study was scrutinized and turned out to go back to that librational movement. We trust that the new data set will serve as a benchmark for further quantum-theoretical studies and may contribute to a deeper understanding of hydrogen bonds in general.

- [1] T. Yamada, X. Liu, U. Englert, H. Yamane, R. Dronskowski, *Chem. Eur. J.*, 15, 5651 (2009).
- [2] V. Hoepfner, V. L. Deringer, R. Dronskowski, *J. Phys. Chem. A*, 116, 4551 (2012).
- [3] P. K. Sawinski, M. Meven, U. Englert, R. Dronskowski, *Cryst. Growth and Des.*, 13, 1730 (2013).
- [4] S. Swaminathan, B. M. Craven *Acta Cryst. B*, 40, 300 (1984)

Patterned Gold Nanoparticles with Tunable Surface Properties

S. Gilles^{1,3}, S. Winter¹, K. E. Michael^{1,*}, S. H. Meffert¹, P. Li¹, K. Greben¹, U. Simon², A. Offenhäusser¹, and D. Mayer¹

¹ Peter Grünberg Institute-8, Forschungszentrum Jülich, Germany

² Institute of Inorganic Chemistry, RWTH Aachen University, Germany

³ Present address: Institute of Inorganic Chemistry, RWTH Aachen University, Germany

* K. E. Michael deceased in January 2011

A modular method to establish nanostructured chemical templates for local deposition of gold nanoparticles is presented. A process comprising nanoimprint lithography, silanization, lift-off, and gold nanoparticle immobilization is used to fabricate particle patterns. The chemical composition of the surface can be modified by in situ adsorption of cell-binding ligands to locally address primary neurons.

Cellular bio-electronic research including neuronal implants, neuronal prostheses, and cell-based biosensors often relies on the alignment of neurons with solid-state devices to achieve precise interfacing with neurons.[1,2] Several biomolecules can be used as guiding cues. It has been recognized that, in particular, positively charged domains assist the adhesion of neurons.[3] Gold nanoparticles (AuNP) have been shown to be appropriate as anchor points for cell guiding molecules.[4]

Herein, we show a modular method to establish a chemical template on a silicon dioxide surface by locally depositing AuNPs, which provides a material contrast to the surrounding SiO₂ surface. This material contrast can later be used to selectively modify predefined areas of the solid surface in situ. To demonstrate the versatility of this approach, we switched the surface properties of the locally addressed AuNPs between attractive and repulsive for neuron adhesion.

Chemical surface patterns of aminoterminated silane (3-aminopropyltriethoxysilane, APTES) were established on oxidized silicon samples (Si/SiO₂) by a process using nanoimprint lithography (NIL), silanization, and lift-off [5]. Surface-bound amino groups can be protonated in neutral and acidic solution, hence exhibiting positive charges. In this way, we created a chemical contrast of positively charged structures surrounded by comparatively negative SiO₂ surface areas (Fig. 1a). In the next step the aminosilane pattern was decorated with citrate-stabilized AuNPs. These particles are chemically inert, have a narrow size distribution, and are commercially accessible. Furthermore, gold provides a high chemical contrast to the surrounding SiO₂ surface with a very well es-

tablished thiol-based surface chemistry. The citrate AuNPs were immobilized via electrostatic attraction on the positively charged chemical structures (Fig. 1b). The citrate ligands were later removed from the particles by oxygen plasma, which resulted in a pattern of "naked" AuNPs (Fig. 1c). In this stage, the overall surface is free of organic molecules and exposes a chemical contrast between Au and SiO₂ areas that can be used to locally apply molecules with desired functional groups via selective adsorption reactions. Following this idea, we established a new ligand shell on the AuNPs that comprised linear molecules with thiol functionality on one end, amino functionality on the other end, and an alkyl/polyethylene glycol (PEG) chain in between, resulting in a positively charged ligand shell (Fig. 1d)

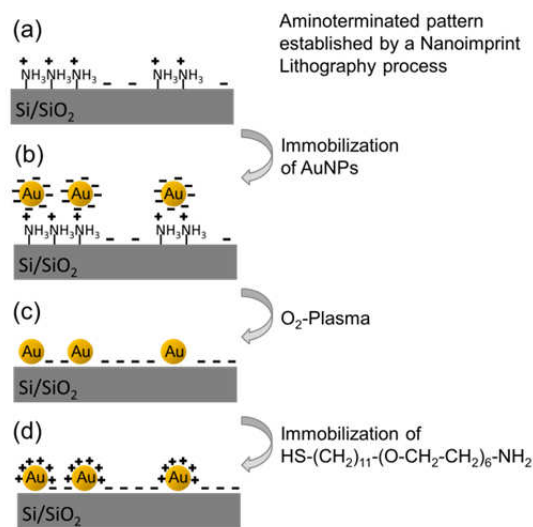


FIG. 1: Schematic representation of the fabrication of nanostructures decorated with AuNPs with tunable surface properties (adapted from [6] with permission of John Wiley & Sons, Inc.).

Rat cortical neurons were cultured on patterned surfaces of APTES, naked AuNPs, and amino PEG AuNPs and their growth characteristics were investigated at day 3 and day 9 in vitro (DIV3 and DIV9) by fluorescence microscopy (after staining to distinguish living cells) and by SEM for higher resolution inspection of neurite growth on nano-

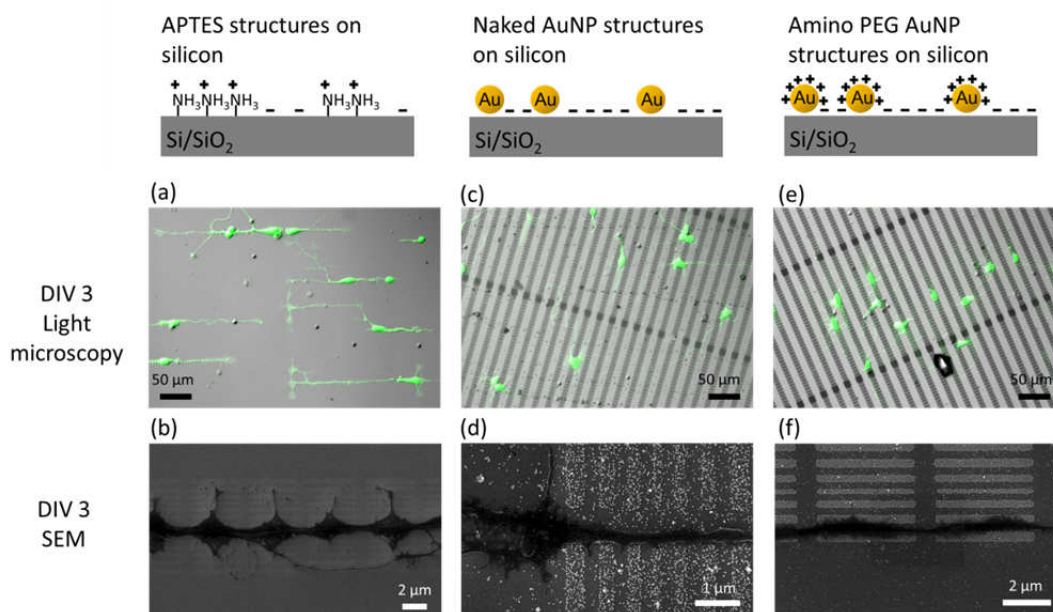


FIG. 2: Neurons cultured on nanostructured surfaces. a) light microscopy image of neurons on APTES structures, b) SEM image of neurons on APTES structures, c) light microscopy image of neurons on naked AuNP structures, d) SEM image of neurons on naked AuNP structures, e) light microscopy image of neurons on amino PEG AuNP structures, f) SEM image of neurons on amino PEG AuNP structures (adapted from [6] with permission of John Wiley & Sons, Inc.)

structured areas (Fig. 2). A culture time of 9 days is especially interesting since synapsis of rat cortical neurons do not evolve before DIV7.

The cultured neurons at DIV3 on APTES structures seemed to grow precisely along the pattern following APTES lines over distances up to several hundred micrometers (Fig. 2a). At DIV9, few cells were found attached on these substrates (not shown). Apparently, most of the neurons detached from the surface after extended time in culture, meaning that APTES structures are minor promising for extended neuron guiding. For naked AuNP substrates, we found that at DIV3 (Fig. 2c) and at DIV9 neurons were primarily attached to particle-free areas. The pure gold surface of the particles was cell-repellent, whereas the pure SiO_2 surface was better suited for attachment. Neurons even grew into particle-free spaces for up to 300 nm, as observable in SEM measurements (Fig. 2d). For amino PEG AuNP samples, the adhesion predilection of neurons was reverted to a preference for particles. Investigations at DIV3 (Fig. 2e,f) and DIV9 showed neurons were attached for both cases and were guided primarily on nanoparticle patterns.

Altogether, our results confirm that surface-bound charges can be used for neurite guiding and patterning of neuronal networks. A chemical or charge contrast can be introduced by generating areas of high local coverage by positively charged amino groups on an otherwise negatively charged background. In such a case, the positive amino groups form the preferential binding sites for neuronal adhesion. Alternatively, negatively charged areas can be used as a support surface if patterns of cell-repulsive agents, such as naked AuNPs, are present. The derived gradient of

neuron affinity to the surfaces discussed is schematically illustrated in Fig. 3.

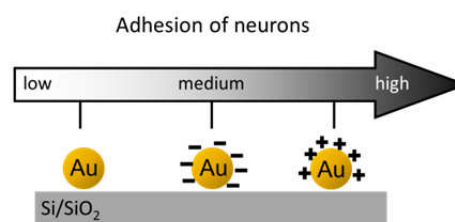


FIG. 3: Graduation of neuron affinity to variably functionalized AuNPs derived from the experimental results (reprinted from [6] with permission of John Wiley & Sons, Inc.).

In summary, we have realized a high-resolution surface modification strategy that allows one to define, just by wet-chemical means, whether neurons should adhere preferentially on predefined submicrometer areas or if the neurons should avoid these parts of the sample surface.

- [1] P. Roach, T. Parker, N. Gadegaard, M. R. Alexander, *Surf. Sci. Rep.*, 65, 145 (2010)
- [2] K. Riehemann, S. W. Schneider, T. A. Luger, B. Godin, M. Ferrari, H. Fuchs, *Angew. Chem. Int. Ed.*, 48, 872 (2009)
- [3] E. Yavin, Z. Yavin, *J. Cell. Biol.*, 62, 540 (1974)
- [4] M. Arnold, M. Schwieder, J. Blümmel, E. A. Cavalcanti-Adam, M. López-García, H. Kessler, B. Geiger, J. P. Spatz, *Soft Matter*, 5, 72 (2009)
- [5] S. Gilles, C. Kaulen, M. Pabst, U. Simon, A. Offenhäusser, D. Mayer, *Nanotechnology*, 22, 295301 (2011)
- [6] S. Gilles, S. Winter, K. E. Michael, S. H. Meffert, P. Li, K. Greben, U. Simon, A. Offenhäusser, D. Mayer, *Small*, 8, 3357 (2012)

A Very Large Micro Electrode Array for Recording and Stimulation of Retinal Ganglion Cells

F. Waschkowski¹, Claudia Brockmann², G. Roessler³, T. Laube², W. Mokwa¹, and P. Walter³

¹ Institute of Materials in Electrical Engineering Chair 1, RWTH Aachen University, Germany

² Department of Ophthalmology, University Hospital Essen, Germany

³ Department of Ophthalmology, University Hospital Aachen, Germany

It has been shown that electrical stimulation of the retina of patients suffering from retina degeneration generates visual perceptions and may be a possible therapy for these patients. Implants which have been developed until now mostly use electrode arrays with sizes of $\sim 10 \text{ mm}^2$. Within this work different approaches for an epiretinal stimulator were developed and tested with an effective stimulation area of approximately 100 mm^2 . The key aspects for the development were a good implantability and a best possible adaption of the implant to the curvature of the eye.

One of the most common diseases accompanied by retina degeneration is *retinitis pigmentosa* (RP). RP is a hereditary disease leading to a successive loss of vision from the peripheral to the central field of view due to a degeneration of the rods and cones, the light sensitive cells of the retina.[1] However about 30% of the neuronal ganglion cells are still intact even after a long period of total blindness. Clinical studies show that by electrical stimulation of these cells patients could have visual perceptions. Based on this discovery arose the idea of a retinal prosthesis as a treatment for those patients.[2][3]

Nowadays most of the developed implants are based either on the subretinal [4] or the epiretinal approach.[5] A subretinal implant is placed between the sclera and the retinal tissue with the electrodes in contact with the backside of the retina, whereas an epiretinal implant is placed inside the eye on the foreside of the retina and in direct contact with the neuronal cells. To keep the trauma low for the patient the electrode arrays are very small, i.e. $\sim 10 \text{ mm}^2$, and are placed on the fovea centralis. Taking the optical properties of the eye into account one can predict that the visual perceptions are concentrated on an area that corresponds to a visual field of around 10° . [6]

The goal for the VLARS-stimulator is an epiretinal prosthesis with an effective stimulation area on the retina of $\sim 100 \text{ mm}^2$. This corresponds to a visual field of about 40° . Together with a decent number of electrodes it would give the patient the possibility of a better orientation in unknown environment.

To find a proper design for the implant one has to consider two important aspects. The first aspect is the implantability. To keep the surgery minimally invasive the necessary incision of the sclera should not exceed a length of 5 mm. That means the electrode array has to be folded during implantation and regain its original shape inside the eye. Additionally the material needs to be elastic so that the implant does not suffer any permanent damage during surgery. Therefore the VLARS implant is fabricated on a polyimide (PI) base structure. PI is a polymer commonly used in biomedical devices because of its excellent bio compatibility and low moisture uptake. Furthermore it complies with the requirements regarding the mechanical properties.

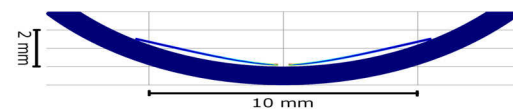


FIG 1: Result of a FEM simulation of a PI foil pressed into a spherical shell.

The second aspect is the curvature of the eyeball. As the implant is fabricated with photolithographic techniques on silicon wafers it has a flat two dimensional structure. When brought in to a spherical shape like the eyeball it needs a stress relieving pattern to prevent it from wrinkling. For a successful stimulation the electrodes on the device must be in contact with the retina over the whole area. We carried out simulations with FE methods to visualize the behavior of a PI foil on a curved surface. As you can see in Figure 1 in the absence of a certain shape the foil leaves a gap of approximately $250 \mu\text{m}$ to the substrate. That is much more than the height of the contact electrodes to be used for the functional devices.

While the implant will be fixated on the retina by retinal tacks one would want to reduce the number of tacks to bring the device in position as they also damage the tissue around the fixation site.

The prototypes are fabricated on silicon wafers (see Figure 2) which are coated with a sacrificial aluminum layer to allow the detachment of the devices in the last process step. The polyimide is

spin coated in two layers on the wafer and structured with photolithographic techniques. The PI2611 used for the devices is soluble in the developer of common photoresists which makes the processing very easy.

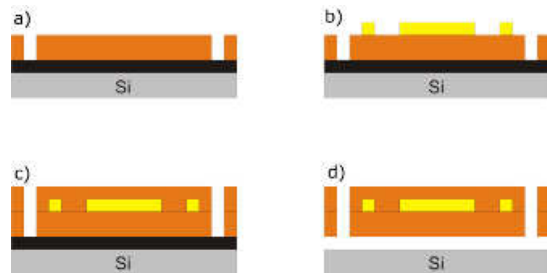


FIG. 2: Fabrication steps of VLARS prototypes: a) first PI layer, b) electroplating of dummy electrodes and conducting paths, c) second PI layer, d) devices are released from the wafer by etching the sacrificial layer (black).

To find a possible positioning for the electrodes gold dummies were created by electroplating between the two PI layers.

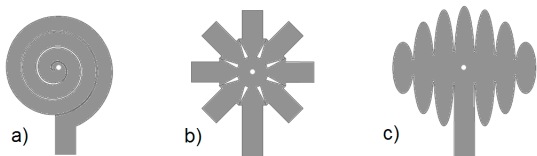


FIG. 3: First ideas for a MEA base structure, a) the spiral design, b) the star pattern, c) the globe shape.

In Figure 3 the first designs of the base structure are presented. All patterns have a central hole for primary fixation and additional fixation sites on the edges in case of the structure lifting up from the tissue. The spiral design (see Figure 3a) should adapt itself well to the curvature of the eye due to its segmented pattern, at the same time it is expected to be easy to handle during surgery as the spiral could be unwound and guided through a very small incision. That expectation is not fulfilled in experiments on porcine cadaver eyes. Inside the eye the structure does not regain its original shape but instead gets entangled, which makes it difficult to get the implant positioned on the retina. After explantation the device shows permanent plastic deformations (see Figure 4).



FIG. 4: A VLARS prototype with spiral design after experiments on porcine cadaver eyes.

The star shape and the globe shape pattern (see Figure 5a and b) behave much better during surgery and are pursued for further development.

There are still a lot of things to address for the functional implants. It was observed that though the adaption to the curvature of the retina is fairly good, the underlying tissue is being dent on the edges of the implant.

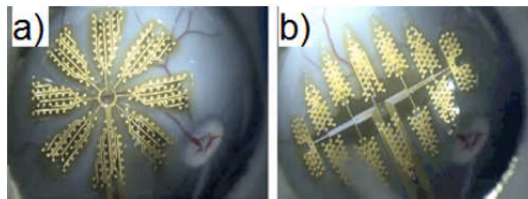


FIG. 5: Early VLARS prototypes with dummy electrodes in star and globe shape on the fundus of porcine cadaver eyes.

To solve that problem one could think of controlling the inherent curvature of the device. The functional devices for in vivo experiments will get an additional coating of Parylene C, a hydrophobic polymer, to reduce the moisture uptake even more. It has been shown that heating Parylene after deposition changes its molecular structure creating mechanical stress. [7] This can be utilized to create pre-curved implants which could also reduce the number of fixation sites needed.

This work was supported by a research grant provided by the Jackstaedt Stiftung.

- [1] D. T. Hartong, et al., "Retinitis pigmentosa," *Lancet*, vol. 368(9549), November 2006, pp. 1795-1809.
- [2] A. Santos, et al., "Preservation of the inner retina in retinitis pigmentosa: A morphometric analysis," *Archives of Ophthalmology*, vol. 115(4), April 1997, pp. 511-515.
- [3] T. Fujikado, et al., "Evaluation of phosphenes elicited by extraocular stimulation in normals and by suprachoroidal-transretinal stimulation in patients with retinitis pigmentosa," *Graefe's Archive for Clinical and Experimental Ophthalmology*, vol. 245(10), March 2007, pp. 1411-1419.
- [4] E. Zrenner, et al., "Visual Sensations Mediated By Subretinal Microelectrode Arrays Implanted into Blind Retinitis Pigmentosa Patients," in *Proc. 13th Annu. Conf. of the IFESS*, Freiburg, 2008.
- [5] G. Roessler, et al., "Implantation and Explantation of a Wireless Epiretinal Retina Implant Device: Observations during the EPIRET3 Prospective Clinical Trial," *Investigative Ophthalmology & Visual Science*, vol. 50(6), April 2009, pp. 3003 - 3008.
- [6] N. Drasdo, et al., "Non-linear projection of the retinal image in a wide-angle schematic eye," *British Journal of Ophthalmology*, vol. 58, 1974, pp. 709.
- [7] S. Dabral, et al., "Stress in Thermally Annealed Parylene Films," *Journal of Electronic Materials*, vol. 21(10), 1992, pp. 989-994.

All Diamond Microelectrode Arrays Produced by a Non-Lapidary Method to Detect Cell Action Potentials

V. Maybeck¹, R. Edgington², A. Bongrain³, J. O. Welch², E. Scorsone³, P. Bergonzo³, R. B. Jackman², and A. Offenhäusser¹

¹ Peter Grünberg Institute-8 and Institute of Complex Systems: Bioelectronics-8, Forschungszentrum Jülich, Germany

² LCN, University College London, Great Britain

³ CEA LIST, Diamond Sensors Laboratory, CEA-Tech, France

A method of patterned nanocrystalline diamond (NCD) growth is presented. Using this method, microelectrode arrays (MEAs) that present only a diamond surface to cultured cells are fabricated. These devices are not significantly different from Au MEAs, but have the higher biocompatibility associated with diamond. Diamond devices were proven capable of detecting cell action potentials (APs) using the cardiomyocyte-like cell line HL-1. Furthermore, in some cases the diamond MEAs showed up to four times better SNR than Au MEAs.

Synthetic diamond materials have become the subject of interest due to their tuneable properties and chemical stability. By varying the growth parameters and dopants in synthetic diamond films, the crystal size ranges from nanoscale to macroscopic, and conductivity can be tuned from 10^{-6} to 10^4 S m⁻¹. [1] Furthermore, diamond devices have high biocompatibility and a large electrochemical window in solution. [2] The three types of diamond we discuss here are the conducting boron doped nanocrystalline diamond (BNCD) film, isolating undoped nanocrystalline (NCD) films, and dispersed nanodiamond (ND) slurry.

We show that MEAs with (BNCD) electrodes can detect APs, and present a method for patterned growth of isolating NCD on top of structured BNCD to generate an all diamond chip surface by non-reductive methods. [3] Au MEAs with SiO₂ passivation surface, BNCD MEAs with SiO₂ passivation surface, and BNCD MEAs with NCD passivation were compared in electronic and cell culture tests.

BNCD electrodes were generated by first applying a 140 nm TiSi₂ adhesion layer to an oxidized Si wafer. Nanodiamond seeds (NDs) were then applied to the surface. BNCD was grown from the NDs to a 350 nm thick film. An RIE process was then developed to generate smooth BNCD structures using a 5:35 O₂:Ar mixture (FIG 1a i-iii). These electrodes could be passivated by deposition of SiO₂/Si₃N₄ stacks (ONO) or by selective growth of NCD. To achieve patterned growth of NCD (FIG 1a iv-vii), NDs were applied to

the patterned BNCD wafer. Cr caps were deposited on the electrode and bond pad openings that were to remain free of passivation. NCD growth produced a confluent film over the areas where NDs were exposed. Chrome etch was then used to remove the caps and a brief RIE to remove the NDs that had been capped. The NCD growth and the final etch steps result in a leak-tight film 60% thinner than Si materials.

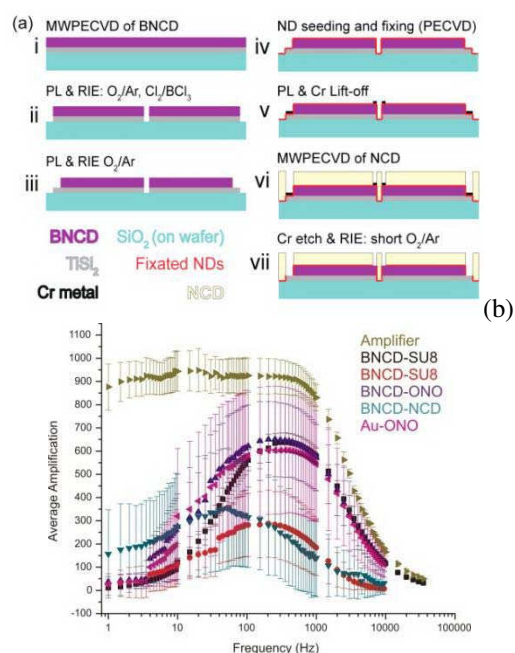


FIG. 1: Fabrication and performance of BNCD MEAs. a) BNCD is deposited on a TiSi₂ adhesion layer (i) and patterned by RIE.(ii). The bondpads are opened to the TiSi₂ (iii). To passivate with patterned NCD growth, ND seeds are applied to the whole wafer (iv). Areas to remain open are capped with Cr (v). After NCD growth (vi), Cr and NDs are removed (vii). b) The relative performance of BNCD MEAs with varying passivations vs. Au MEAs when a varying sine signal is applied to the bath. The theoretical maximum amplification is 1022x.

MEAs with BNCD electrodes and either conventional or NCD passivation were compared to equivalent devices with gold electrodes and traditional passivation materials in terms of signal shape, and signal to noise ratio (SNR).

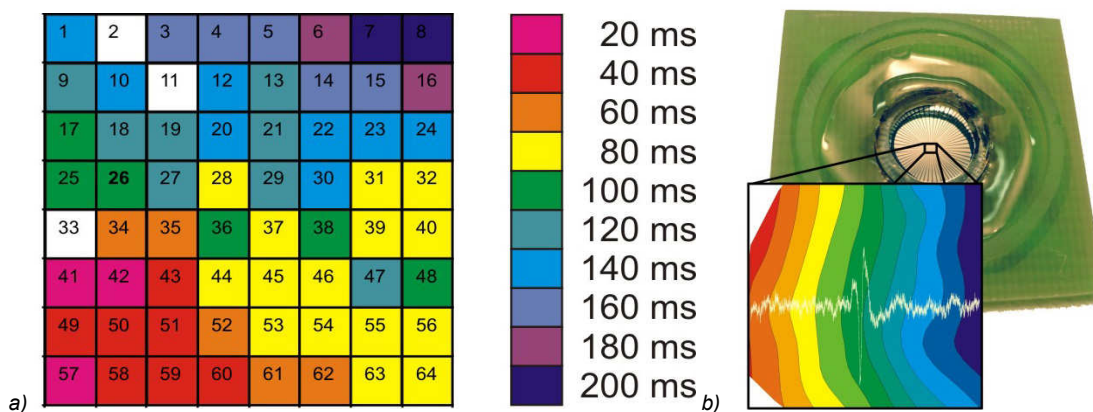


FIG. 2: a) The time of arrival of an AP at each electrode is color coded so that the propagation of the signal across the sheet of HL-1 cells can be visualized. b) A photo of the encapsulated chip shows the culture area where HL-1 cells grow and an inset of the wave propagation overlaid by the recording of a single AP recording in white.

A varying frequency sine signal applied to the MEA bath allowed characterization of the device bandwidth. Diamond devices were not significantly different from Au MEAs in terms of bandwidth, but tended to a slightly higher cut-off frequency in the slower regime. When measuring APs, this would favor detection of the ~ 1000 Hz voltage gated sodium response of neurons and muscle cells, while reducing the impact of 50 Hz noise, the dominant artificial background interference.

Further evaluation used confluent cultures of HL-1 cells on the MEAs to spontaneously generate waves of APs that propagate across the tissue (FIG 2). Diamond MEAs had sufficient detection of APs to determine the propagation speed and direction of the AP wave in culture. Furthermore, despite electronic measurements that suggest NCD passivated BNCD MEAs utilize less than 1/3 of the theoretical amplification possible, the peak to peak amplitude of the APs detected on these devices could be very high (up to 1 mV, whereas unstructured Au typically yields 600-700 μ V peak to peak).

Two factors may contribute to the improved SNR of all diamond chips. First, the rough structure of NCD and BNCD increases the surface area of the material by approximately 15%. For the electrode, this increase in surface area will improve the impedance. For the interface between the cell and the diamond, this roughness not only increases the available contact area, but may also induce the cell to form a tighter adhesion with the surface as has been shown for other cell cultures responding to a structured substrate. The second reason is that the height of the cleft between the cell and electrode when the electrode is sized similar to a single cell (FIG 3). The thinner passivation films formed by the NCD patterning process result in a smaller cleft between the cell and the electrode. This increase in proximity is expected to greatly enhance the signal detection by the electrode.

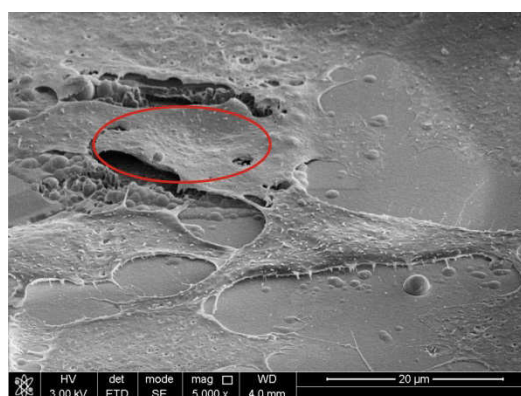


FIG. 3: SEM image of an HL-1 cell growing over a BNCD electrode (outlined in red), passivated with ONO, showing the importance of cleft height in cell-device coupling.

In summary, we have shown that non-reductive patterning of NCD on BNCD is a suitable method for generating all diamond MEAs. The roughness of the surface and the lower passivation thicknesses are hypothesized to be responsible for the performance of all diamond MEAs. On average, the diamond MEAs were not significantly different from Au MEAs, however, in some cases diamond performed up to four times better than Au in SNR. This suggests that further improvements in the consistency of diamond MEA production can make BNCD/NCD MEAs competitive with current materials.

-
- [1] Y. Pleskov, Russ. J. Electrochem. 38, 1275 (2002)
 - [2] P. Ariano, O. Budnyk, S. Dalmazzo, D. Lovisolo, Ch. Manfredotti, P. Rivolo, E. Vittone, Eur. Phys. J. E 30, 149 (2009)
 - [3] V. Maybeck, R. Edgington, A. Bongrain, J. Welch, E. Scorsone, P. Bergonzo, R. B. Jackman, A. Offenhausser, Adv. Healthcare Mater. DOI:10.1002/adhm (submitted)

Theory and Simulation of Cortical Networks

SJ v Albada¹, T Tetzlaff¹, M Diesmann^{1,2}, and S Grün^{1,3}

¹ Institute of Neuroscience and Medicine-6: Computational and Systems Neuroscience & Institute for Advanced Simulation-6: Theoretical Neuroscience, Forschungszentrum Jülich, Germany

² Computational Neuroscience, Faculty of Medicine, RWTH Aachen University, Germany

³ Theoretical Systems Neurobiology, Faculty I, RWTH Aachen University, Germany

Understanding the relation between the structure and dynamics of the cortical network is a prerequisite for the investigation of its function. To this end, we develop analytical tools to study general principles of recurrent-network dynamics (e.g. the role of inhibitory feedback on correlations in neural activity; see [1]), and employ simulations to investigate the complex dynamics of network models accounting for realistic features of the neocortex (e.g. the cell-type and layer-specific connectivity of local cortical microcircuits; see [2]). The investigation of brain-scale networks by means of computer simulations depends to a large extent on the development of novel algorithms and high-performance parallel computing strategies. In [3], for example, we show how memory consumption can be minimized by developing data structures exploiting the sparseness of the local network representation. Finally, to foster the implementation of neural-network models on neuromorphic hardware we investigate the effects of hardware limitations on the network dynamics (e.g. spike-timing-dependent plasticity in neural networks; see [4]).

Correlations in spike-train ensembles can seriously impair their capacity for encoding information. An inevitable source of correlation in finite neural networks is common presynaptic input to pairs of neurons. Recent studies demonstrate that spike correlations in recurrent neural networks are considerably smaller than expected based on the amount of shared presynaptic input. In [1], we explain this observation by means of a linear network model and simulations of networks of leaky integrate-and-fire (LIF) neurons. We show that inhibitory feedback efficiently suppresses pairwise correlations and, hence, population-rate fluctuations. We quantify this decorrelation by comparing the responses of the intact recurrent network (feedback system) and systems where the statistics of the feedback channel is perturbed (feedforward system). Neglecting correlations within the ensemble of feedback channels or between the external stimulus and the feedback amplifies population-rate fluctuations by orders of magnitude (Fig.1). It is found that, in purely inhibitory networks, shared-input correlations are canceled by negative spike-train correlations. In excitatory-inhibitory networks, spike-train correlations are typically positive. Here, the

suppression of input correlations is not a result of the mere existence of correlations between excitatory (E) and inhibitory (I) neurons, but a consequence of a particular structure of correlations among the three possible pairings (EE, EI, II).

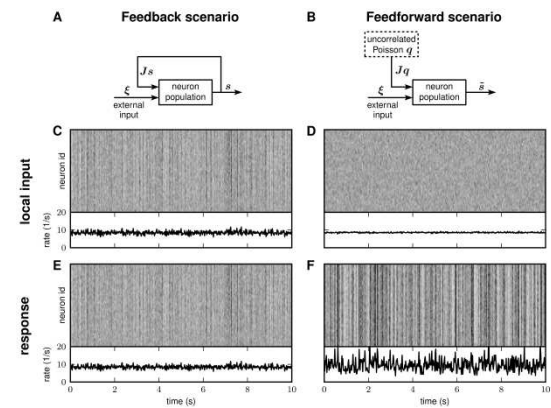


FIG. 1: Spiking activity in excitatory-inhibitory LIF networks with intact (left column; feedback scenario) and opened feedback loop (right column; feedforward scenario). A,B: Network sketches. C,D: Spiking activity (top panels) and population averaged firing rate (bottom panels) of the local presynaptic populations. E,F: Response spiking activity (top panels) and population averaged response rate (bottom panels). In the top panels of C–F, each pixel depicts the number of spikes (gray coded) of a subpopulation of 250 neurons in a 10ms time interval. In both the feedback and the feedforward scenario, the neuron population $\{1, \dots, N\}$ is driven by the same realization $\xi(t) = (\xi_1(t), \dots, \xi_N(t))^T$ of an uncorrelated white-noise ensemble; local input is fed to the population through the same connectivity matrix J . In-degrees, synaptic weights and shared-input statistics are thus exactly identical in the two scenarios. In the feedback case (A), local presynaptic spike-trains are provided by the network's response $s(t) = (s_1(t), \dots, s_N(t))^T$, i.e. the pre- (C) and postsynaptic spike-train ensembles (E) are identical. In the feedforward scenario (B), local presynaptic spike trains are replaced by an ensemble of N independent realizations $q(t) = (q_1(t), \dots, q_N(t))^T$ of a Poisson point process (D). Its rate is identical to the time- and population-averaged firing rate in the feedback case. Figure from Tetzlaff et al., 2012.

A more physiology-based approach to understanding the link between cortical structure and dynamics is taken in [2]. While available connectivity maps of local cortical networks have been used in various computational studies, prominent features of the simulated activity such as the spontaneous firing rates do not match the

experimental findings. In [2], we compile an integrated connectivity map incorporating insights on the specific selection of target types, and perform full-scale spiking network simulations of the local cortical microcircuit. The simulated spontaneous activity is asynchronous irregular and cell-type specific firing rates are in agreement with in vivo recordings in awake animals (Fig. 2).

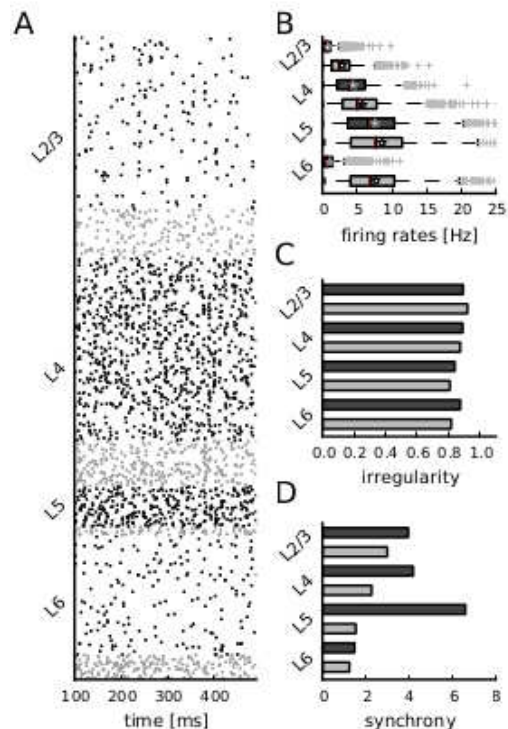


FIG 2: Simulated spontaneous cell-type specific activity. (A) Raster plot of spiking activity recorded for 400 ms of biological time of layers 2/3, 4, 5, and 6 (from top to bottom; black: Excitatory, gray: Inhibitory). Relative number of displayed spike trains corresponds to the relative number of neurons in the network (total of 1862 shown). (B–D) Statistics of the spiking activity of all 8 populations in the network based on 1000 spike trains recorded for 60 s (B and C) and 5 s (D) for every population. (B) Boxplot of single-unit firing rates. Crosses show outliers, stars indicate the mean firing rate of the population. (C) Irregularity of single-unit spike trains quantified by the coefficient of variation of the interspike intervals. (D) Synchrony of multiunit spiking activity quantified by the variance of the spike count histogram (bin width 3 ms) divided by its mean. Figure from Potjans and Diesmann, 2012.

The cortical microcircuit studied in [2] contains on the order of 10^5 neurons and 10^9 synapses, and has been simulated on a high-performance cluster. However, brain-scale networks are orders of magnitude larger in terms of numbers of neurons and synapses, and thus computational load. Such networks have been investigated in individual studies, but the underlying simulation technologies have neither been described in sufficient detail to be reproducible nor made publicly available. In [3], we discover that as network models approach the meso- and macroscale, memory consumption on individual compute nodes becomes a critical bottleneck. This is especially relevant on modern

supercomputers such as the Blue Gene/P architecture where the available working memory per CPU core is rather limited. We develop a simple linear model to analyze the memory consumption of the components of neuronal simulators as a function of network size and the number of cores used. The model enables identification of key contributing components to memory saturation and prediction of the effects of potential improvements to code before any implementation takes place. Applying the model to our freely available NEural Simulation Tool (NEST), we identify the software components dominant at different scales, and develop general strategies for reducing the memory consumption, in particular by using data structures that exploit the sparseness of the local representation of the network. We show that these adaptations enable our simulation software to scale up to the order of 10,000 processors and beyond.

The choice of representation of network components is also important for making optimal use of chip resources in large-scale neuromorphic hardware systems. When implementing spike-timing dependent plasticity, a natural modification that saves resources is to reduce synaptic weight resolution. In [4], we estimate the impact of synaptic weight discretization on different levels, ranging from random walks of individual weights to computer simulations of spiking neural networks. The FACETS wafer-scale hardware system offers a 4-bit synaptic weight resolution, which is shown to be sufficient within the scope of our network benchmark. Our findings indicate that increasing the resolution may not even be useful in light of further restrictions of customized mixed-signal synapses. In addition, variations due to production imperfections are investigated and shown to be uncritical in the context of the presented study. We suggest how weight discretization could be considered for other back-ends dedicated to large-scale simulations. Thus, our proposition of a good hardware verification practice may increase synergy between hardware developers and neuroscientists.

This work was partially funded by the Research Council of Norway (eVita [eNEURO], NOTUR), EU Grant 15879 (FACETS), EU Grant 269921 (BrainScaleS), BMBF Grant 01GQ0420 to BCCN Freiburg, Next-Generation Supercomputer Project of MEXT, Japan, and the Helmholtz Alliance on Systems Biology.

- [1] T. Tetzlaff, M. Helias, G.T. Einevoll, M. Diesmann (2012) PLoS Comput. Biol. 8(8), e1002596.
- [2] T.C. Potjans, M. Diesmann (2012) Cereb. Cortex, online first.
- [3] S. Kunkel, T.C. Potjans, J.M. Eppler, H.E. Plesser, A. Morrison, M. Diesmann (2012) Front. Neuroinform. 5, 35.
- [4] T. Pfeil, T.C. Potjans, S. Schrader, W. Potjans, J. Schemmel, M. Diesmann, K. Meier (2012) Front. Neuromorph. Eng. 6, 90.

Chemical Surface Modeling of GeTe, an Archetypical Functional Material

M. Lumeij, V. L. Deringer, and R. Dronskowski

Institute of Inorganic Chemistry, RWTH Aachen University, Germany

In modern society, data are virtually everywhere. Digital television on hard-disk receivers, “smart” (or pesky) cell-phones and their contents are just a few examples of things we certainly need to preserve forever and beyond. A great challenge lies in developing new technologies and materials which can fulfill these demands. Phase-change materials (PCM) store information by fast and reversible switching between two solid-state forms [1–4]. As a prominent example, a Ge–Sb–Te alloy is the active basis of re-writable Blu-Ray™ disks. Germanium telluride (GeTe) not only forms the basis of these PCMs but is a phase changer itself. Miniaturization of storage devices leads to an increase of their surface–volume ratio; subsequently, knowledge about surface morphologies and reconstructions is becoming more and more important. Here we present a fundamental *ab initio* study dealing with the archetypical GeTe(111) surfaces—a study that needs a little help from very “classical” structural chemistry.

GeTe seems to have a very simple solid-state structure. Its low-temperature polymorph, α -GeTe, is of a slightly distorted rocksalt type such that the cell exhibits rhombohedral symmetry with three shorter and three longer Ge–Te bonds in each coordination polyhedron [5]. At higher temperatures, α -GeTe appears to transition into a perfect rocksalt type, leading to indistinguishable Ge–Te bond lengths, an undistorted octahedral coordination, and the designation β -GeTe [6]. The relationship between both phases is best seen if we draw the structures in hexagonal unit cells (Figure 1): germanium and tellurium layers are stacked along the conventional [111] direction. Cleaving a GeTe crystal to expose these faces leads to the arguably most relevant GeTe(111) surfaces which have been recently studied by experimental means [7]. GeTe bilayers form the central structural motif in α -GeTe, and they have been sketched in Figure 1. Looking beyond simple binary GeTe, the feature of three long and three short bonds is present in a remarkable number of Ge–Sb–Te-based PCMs, although a simple “distorted rocksalt” model is often employed for convenience. Very recently, GeTe has been re-investigated, and it was discussed in the literature [8] that β -GeTe should not be a separate phase with a clear-cut transition; instead, it can be described as an “average” structure which consists of different α -phase-like local distortions that average out at increased temperatures. It seems

that a quite simple and long-known structure like GeTe still causes some issues.

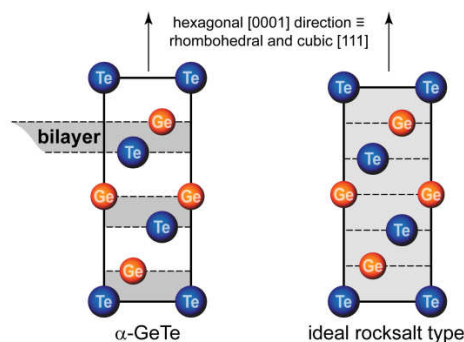


FIG. 1: Schematic view of α -GeTe (left) and idealized β -GeTe (right) focusing on their close resemblance and showing the GeTe bilayers in the case of α -GeTe.

Here, we search for a density-functional theory (DFT) model to make reasonable predictions for α -GeTe(111) surfaces. Since rocksalt-like (111) surfaces are polar and we intend to compute absolute surface energies, it is necessary to have the same termination at *both* sides of the slab, top and bottom. Moreover, a symmetric slab is desirable because much precious computing time can be saved by, in principle, looking only at one half of the slab while the other half is reproduced by symmetry operations. This symmetry operation (*i.e.*, an inversion center in the middle of the cell) is available in the rocksalt type (Figure 1, right) and many ternary Ge–Sb–Te alloys, but not in α -GeTe. If one seeks to cut a slab terminated by, say, tellurium at the top and bottom from the structure shown in Figure 1 (cutting along the dashed lines), one will always need to cut one bilayer in half. Consequently, such a model undergoes large distortions and is certainly not desirable [9].

To solve this problem, we exploit the close chemical relationship between both structure types. Figure 1 evidences that, in fact, both differ mainly in how the Ge and Te layers are stacked: bilayers are found in α -GeTe while all layers in the more symmetric rocksalt structure are equidistant. Since the energetic difference between both models is small, leading to an error of approximately $< 1 \text{ meV } \text{\AA}^{-2}$ [9], we constructed a symmetric model by choosing the central part to be bulk-like (*i.e.*, have the layer spacing of β -GeTe and hence introducing inversion symmetry); the surface layers faithfully resemble the bilayers found in α -GeTe and are allowed to fully relax.

One of the quantum-chemically optimized surface models is shown in Figure 2. We are particularly interested in the surface energies which are therefore calculated for different atomic structures at the surface: the lower a particular motif's surface energy, the more stable it is. Our calculations show that the pristine Te-terminated surface (which is also seen in Figure 2) is the most stable overall, independent of chemical surrounding (potential), which can quite intuitively be illustrated as the frontier orbitals of the tellurium anions are filled (the atoms at the surface should be close to "noble-gas" configurations). A naked, purely Ge-terminated surface is very unlikely to be seen; it might lower its surface energy by various reconstruction motifs (dashed and dotted lines in Figure 3a).

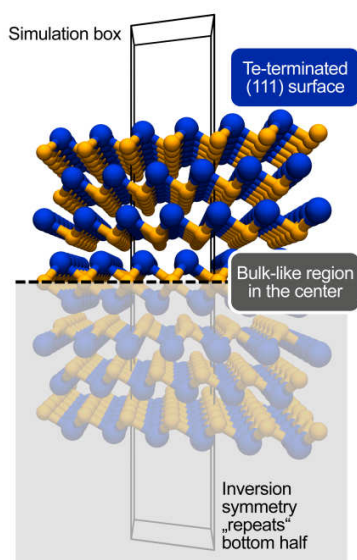


FIG. 2: Schematic of the modeling approach, representing a tellurium-terminated surface. Artificial "vacuum" areas are visible at the top and bottom. The center five regions of the slab have been held fixed in the computation, which is required to constrain the slight distortion to the center region.

With this newly developed set of surface models available, the prediction of surface properties is possible. One example is in Figure 3b–d: from the computed charge density, one may simulate scanning tunneling microscopy (STM) images to corroborate experiments yet to be performed (see [9] for detailed description and references); the interplay of both, computed and measured STM pictures, has contributed much to the present, precise knowledge about the atomic structure at many materials' surfaces. Besides their relationship to experiment, the computed STM images also illustrate features of the electronic band structure at a glance: for anion-terminated surfaces, the electronic surface states are localized in the filled bands ($U_{\text{sim}} < 0$), and the filled bands (left panel in Figure 3c) light up bright compared to the unoccupied areas above ε_F . The opposite is true for Ge-terminated, reconstructed motifs, which may be helpful for future experiments where both positive and negative bias voltage may be easily applied.

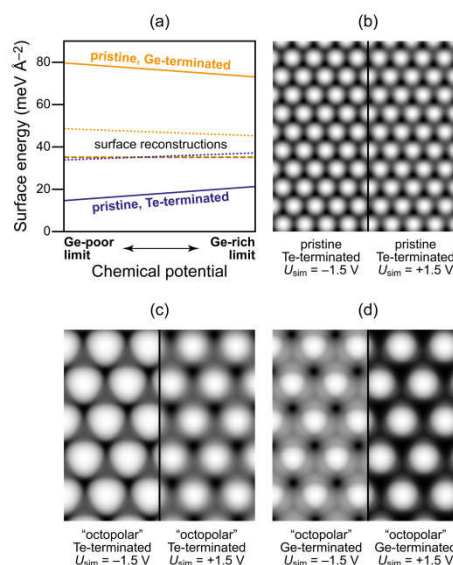


Fig. 3: (a) Surface phase diagram (at $T = 0$ K) computed for rhombohedral GeTe(111). The orange lines indicate Ge-terminated surfaces whereas the Te-terminated surface energies are plotted in blue. (b–d) Simulated STM images of unoccupied bands of pristine Te-terminated and "octopolar" Ge-terminated surfaces. Data taken from Ref. [9].

This work was supported by the Deutsche Forschungsgemeinschaft (SFB 917 "Nanoswitches"). Computer time was provided by the Center of Computing and Communication at RWTH Aachen University. V.L.D. gratefully acknowledges a scholarship from the Studienstiftung des deutschen Volkes.

- [1] W. Wehn, A. Pamungkas, R. Detemple, C. Steimer, S. Blügel, M. Wuttig, *Nature Mater.* 5, 56 (2006).
- [2] M. Wuttig, D. Lüsebrink, D. Wamwangi, W. Wehn, M. Gilleßen, R. Dronskowski, *Nature Mater.* 6, 122 (2007).
- [3] D. Lencer, M. Salinga, M. Wuttig, *Adv. Mater.* 23, 2030 (2011).
- [4] In *Phase Change Materials: Science and Application*; S. Raoux, M. Wuttig, Eds.; Springer: New York, 2009.
- [5] J. Goldak, C. S. Barrett, D. Innes, W. Youdelis, *J. Chem. Phys.* 44, 3323, (1966).
- [6] T. Chattopadhyay, J. X. Boucherle, H. G. von Schnering, *J. Phys. C: Solid State Phys.* 20, 1431 (1987).
- [7] L. V. Yashina, R. Püttner, V. S. Neudachina, T. S. Zyubina, V. I. Shtanov, M. V. Poygin, *J. Appl. Phys.* 103, 094909 (2008).
- [8] X. Biquard, M. Krbal, A. V. Kolobov, P. Fons, R. E. Simpson, B. Hyot, B. André, J. Tominage, T. Uruga, *Appl. Phys. Lett.* 98, 231907 (2011).
- [9] V. L. Deringer, M. Lumeij, R. Dronskowski, *J. Phys. Chem. C* 116, 15801 (2012).

In situ transmission electron microscopy study of the crystallization of bits in $\text{Ag}_4\text{In}_3\text{Sb}_{67}\text{Te}_{26}$

M. Bornhöfft^{1,2}, A. Kaldenbach³, M. Wuttig³, and J. Mayer^{1,2}

¹ Central Facility for Electron Microscopy, RWTH Aachen University, Germany

² Ernst Ruska-Centrum, Forschungszentrum Jülich and RWTH Aachen, Jülich, Germany

³ I. Physikalisches Institut A, RWTH Aachen University, Germany

In the present work, the crystallization of local amorphous marks (bits) in a crystalline layer of the phase-change material $\text{Ag}_4\text{In}_3\text{Sb}_{67}\text{Te}_{26}$ is investigated by in situ transmission electron microscopy (TEM) methods. The bits with a diameter of $0.6\ \mu\text{m}$ are produced by heating with laser radiation and melt quenching in a $30\ \text{nm}$ thick crystalline phase-change layer. The employed TEM in situ methods are crystallization by in situ heating and in situ irradiation. The temperature of the “Phillips PW 6592” in situ heating holder in the heating experiment is $110\ ^\circ\text{C}$ and the bit is completely crystallized in around 30 minutes. In the in situ irradiation experiment, the bits are partly crystallized by a focused electron beam of a FEI Tecnai F20 transmission electron microscope. The crystallization in both experiments is growth dominated.

Phase-change materials are promising candidates for non volatile data storage applications. Already used in rewritable optical data storage [1], they are also candidates for non-volatile electronic memory applications [2]. The understanding of crystallization kinetics of the phase-change materials is necessary to develop reliable and fast phase-change data storage devices, which can further improve actual data storage technology. The crystallization kinetics is the limiting factor of writing speed and memory stability. A recent topic of interest is the role of nucleation and growth in phase-change materials at different conditions. Crystallization dominated by growth promises faster data storage through increasing the writing speed by decreasing the bit size. Both in situ experiments show the growth dominated crystallization of $\text{Ag}_4\text{In}_3\text{Sb}_{67}\text{Te}_{26}$.

The $30\ \text{nm}$ thick phase-change layer is embedded in a supporting multilayer stack on a silicon substrate (Figure 1(a)). The supporting multilayer stack has three main purposes. Oxidation of the phase-change layer is prevented by the $100\ \text{nm}$ thick capping of ZnS-SiO_2 on top of the phase-change layer. The $50\ \text{nm}$ Si_3N_4 layer on top of the silicon substrate acts as an etch stop in the TEM sample preparation. An additional $10\ \text{nm}$ thick layer of ZnS-SiO_2 below the phase-change layer together with the capping layer decreases the necessary power to melt the phase-change layer. The multilayer stack was sputtered on a

$500\ \mu\text{m}$ thick silicon substrate and heated to crystallize the phase-change layer. The supporting layers stay amorphous. To produce the bits the crystalline phase-change layer is locally heated above the melting point by means of laser radiation. After terminating the laser pulse the heated area is melt quenched. The silicon substrate acts as a heat sink during the melt quenching.

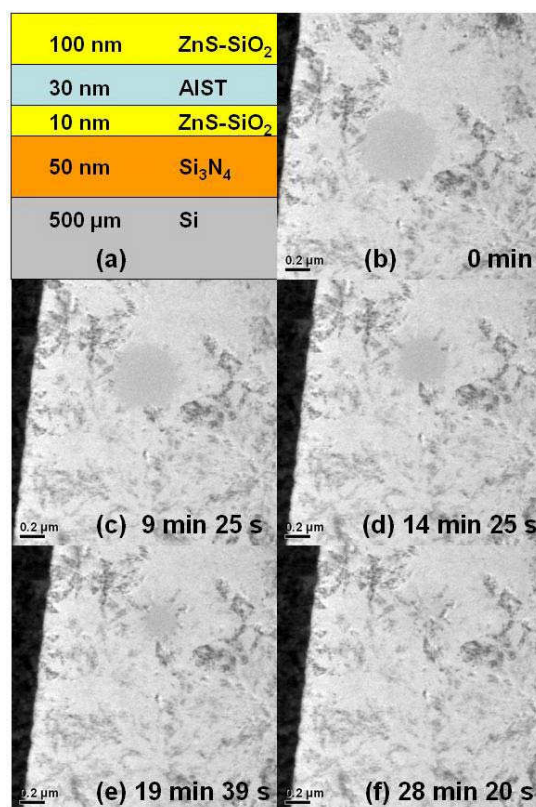


FIG. 1: a. Schematic image of the multilayer stack on silicon substrate before etching.

b-f. Transmission electron microscope brightfield images of an amorphous melt quenched region heated in situ to $110\ ^\circ\text{C}$ in crystalline $\text{Ag}_4\text{In}_3\text{Sb}_{67}\text{Te}_{26}$. Time is related to the start of heating. The size of the amorphous mark linearly decreases with time.

Samples with diameters of $3\ \text{mm}$ are extracted through ultra sonic disc cutting. The silicon of the extracted discs is ground to a thickness of $150\ \mu\text{m}$. Dimple grinding reduces the thickness further to $20\ \mu\text{m}$ in the center of the discs while a $150\ \mu\text{m}$

thick edge is preserved to enhance mechanic stability. Potassium hydroxide is used to remove the remaining 20 μm silicon substrate by etching at 70 °C. The Si_3N_4 layer prevents damage of the multilayer stack. All in situ experiments are carried out in a FEI Tecnai F20 at 200 kV.

Despite the relative high thickness of 190 nm of the multilayer stack the bits are clearly visible in the crystalline layer in the transmission electron microscope brightfield images. This is possible because all layers except the matrix of the phase-change layer are amorphous. The diffraction contrast between the crystalline matrix and the bits is much stronger than the mass thickness contrast of the other layers. Therefore the other layers basically reduce only the observable intensity. Moreover selected area diffraction patterns are taken to prove that the bits are completely amorphous.

In the in situ heating experiment the samples are heated with a Phillips PW 6592 in situ heating holder. The sample is first heated from room temperature to 70 °C and then heated to 110 °C after the thermal drift has faded. The crystallization of the bit is observed in brightfield imaging mode with inserted contrast aperture. The contrast is further enhanced by removal of inelastic scattering by means of energy filtering. The bits crystallize by inward growth from the crystalline rim towards the center of the bit. The crystalline rim grows homogeneously into the bit. At 110 °C The crystallization of a complete bit takes around 30 minutes after the heating starts. No nucleation is observed inside the bit. This shows clearly the growth dominated crystallization behavior. Bending contours created during crystallization follow approximately the crystal growth direction. Even with these bending contours, the crystallized area shows little difference in morphology to its surrounding crystalline matrix (Fig. 1b-f).

In the in situ irradiation experiment, the electron beam is focused onto the bit. Sufficient exposure by the focused electron beam produces a round crystalline mark inside the bit. The size of the crystallized mark and the time to crystallize depends on the spot size of the electron beam. To crystallize a round mark with 0.16 μm in diameter, it has to be exposed to the focused electron beam for approximately 35 seconds. The spot size was manually controlled and slightly bigger than the crystallized area. The crystallized area also shows bending contours, but they do not show a directional preference (Fig. 2a). Selected area diffraction proves that the area is crystalline and only consists of a few grains, because only a few diffraction spots are generated (Fig. 2b). The diameter of the selected area diffraction aperture is 200 nm. This confirms that the crystallization of the mark is primary growth dominated after the first nuclei have formed, even in conditions that promote nucleation in other phase-change materials [3]. The diffuse rings in the diffraction images are generated from the amorphous supporting layers and the amorphous surrounding of the crystallized mark.

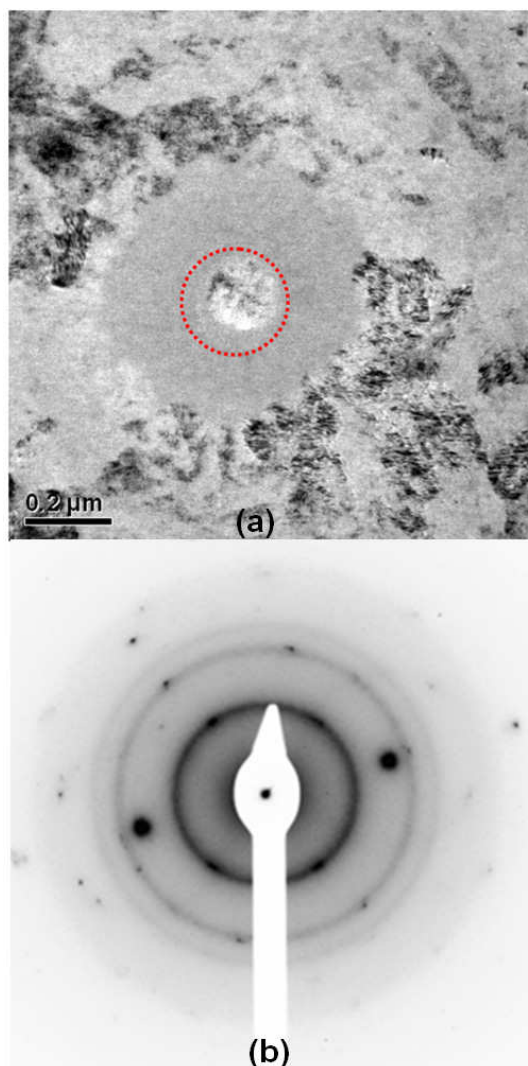


FIG. 2: a. Transmission electron microscope brightfield image of an amorphous region exposed to a focused electron beam. A round area in the middle of the amorphous region has crystallized. The dashed circle marks the position and size of the diffraction aperture. b. Inverted diffraction pattern of the crystallized area.

The authors gratefully acknowledge funding from the DFG in the framework of the SFB 917 "Nanoswitches".

-
- [1] E. Meinders, A. Mijiritskii, L. Pieterse, M. Wuttig, Optical Data Storage: Phase-change Media and Recording, Springer (2006).
 - [2] M. Wuttig and N. Yamada, Nature Materials 6, 824 (2007)
 - [3] B. Kooi, W. Groot, J. De Hosson, J. Appl. Phys. 95, 924 (2004)

Resonating valence bond states in the PEPS formalism

N. Schuch^{1,2}, D. Poilblanc³, J.I. Cirac⁴, and D. Pérez-García⁵

¹ Institut für Quanteninformation, RWTH Aachen University, Germany

² Institute for Quantum Information, California Institute of Technology, Pasadena CA 91125, U.S.A.

³ Laboratoire de Physique Théorique, C.N.R.S. and Université de Toulouse, 31062 Toulouse, France

⁴ Max-Planck-Institut für Quantenoptik, Garching, Germany

⁵ Dpto. Analisis Matematico and IMI, Universidad Complutense de Madrid, E-28040 Madrid, Spain

Using the formalism of Projected Entangled Pair States (PEPS), we study Resonating Valence Bond (RVB) states and, using a combination of analytical and exact diagonalization type methods, provide compelling evidence for their topological spin liquid nature. Using symmetries of their PEPS description, we can smoothly connect RVB states to known topological models and thereby prove their topological nature, while by exact diagonalization of the transfer operator, we can rule out any type of symmetry breaking in the system and thus demonstrate its spin liquid nature.

Resonating valence bond (RVB) states have been proposed by Anderson as an ansatz for systems with antiferromagnetic interactions, in particular in the context of high-temperature superconductivity [1]. More recently, they have received considerable attention as candidates for topological spin liquids, this is, systems which do not break any symmetry despite the presence of strong antiferromagnetic interactions, yet exhibit a topological ground state degeneracy. Particular interest, both theoretically and experimentally, has been devoted to frustrated magnets on the kagome lattice, as those systems are realized in actual materials and form candidates for the first experimental observation of a topological spin liquid [2].

Unfortunately, models with potential RVB ground states are typically difficult to study. This is both due to their high degree of frustration as well as the fact that different singlet configurations are not orthogonal, which has e.g. prevented a full understanding of how RVB states appear as ground states of local Hamiltonians [3]. To overcome this problem, simplified dimer models where different dimer configurations are orthogonal have been studied [4], for which e.g. the topological ground space structure on the kagome lattice could be shown [5].

More recently, Projected Entangled Pair States (PEPS) have been introduced as a tool to study quantum many-body wavefunctions [6,7]. PEPS provide a description of quantum many-body states based on their entanglement structure in terms of local tensors, and form a framework which allows to both analytically understand these

wavefunctions, and numerically study their properties. In particular, it is well understood how certain classes of PEPS, including those with topological order, arise as ground states of local Hamiltonians [8], based on the symmetry properties of the underlying tensor representation. Numerically, PEPS form a tool for computing quantities such as arbitrary correlations efficiently with very high accuracy, using transfer operators of matrix product form [7].

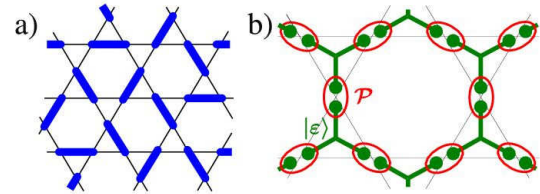


Figure 1. a) Dimer covering of the kagome lattice. b) PEPS construction for the RVB state.

In our work, we apply the PEPS formalism to the RVB state, and use it to prove the topological spin liquid nature of the RVB on the kagome lattice. Fig. 1(a) shows a *dimer covering* D of the kagome lattice. By associating a singlet to each dimer, we obtain a state $|\sigma(D)\rangle$ on the lattice; the RVB state is now defined as the equal weight superposition over all dimer coverings of the lattice, $|\Psi_{RVB}\rangle = \sum_D |\sigma(D)\rangle$. Alternatively, we can associate each dimer with a state $|D\rangle$ with $\langle D|D'\rangle = \delta_{D,D'}$, which gives rise to the (orthogonal) *dimer state* $|\Psi_{dimer}\rangle = \sum_D |D\rangle$. A PEPS description of the RVB state [9] is obtained by first placing 3-qutrit states

$$|\varepsilon\rangle = \sum_{i,j,k=0}^2 \varepsilon_{ijk} |ijk\rangle + |222\rangle$$

inside each triangle of the kagome lattice, as depicted in Fig. 1(b), with ε_{ijk} the completely antisymmetric tensor. This corresponds to having either one or no singlet in the $\{|0\rangle, |1\rangle\}$ subspace in the triangle, the absence of a singlet being marked by $|2\rangle$. Second, we apply the map $P = |0\rangle\langle 02| + |20\rangle\langle 20| + |1\rangle\langle 12| + |21\rangle\langle 21|$ at each vertex, which selects exactly one singlet per vertex; it is easy to check that the resulting state is indeed the RVB state. If we replace P by $P_{\perp} = |02\rangle\langle 02| + |12\rangle\langle 12| + |20\rangle\langle 20| + |21\rangle\langle 21|$

we obtain a representation of the dimer state instead. Moreover, it is possible to devise a smooth interpolation P_θ between $P(\theta=0)$ and $P_\perp(\theta=1)$, which yields an interpolation between the RVB and the dimer state.

The central observation is now that all objects involved in the PEPS description are invariant under a Z_2 symmetry (with representation $\{I, \text{diag}(1,1,-1)\}$). Even more, when blocking all the sites in one star, the resulting map (consisting of all P 's and all $|\varepsilon\rangle$'s completely contained in the star) becomes Z_2 -injective [8], i.e., injective on the invariant subspace. The same is true if we replace P by P_\perp or P_θ . From this, we can deduce that there is a local invertible map $\Lambda^{\otimes N}$ which transforms between the RVB state, the dimer state, and indeed any state along the interpolation [the latter with a smooth dependence $\Lambda \equiv \Lambda(\theta)$]. In turn, this implies that if the dimer state is the ground state of a local frustration free Hamiltonian $H = \sum h_i$ (i.e., $h_i \geq 0$, and $h_i |\Psi_{\text{dimer}}\rangle = 0$), then the RVB state $|\Psi_{\text{RVB}}\rangle = \Lambda^{\otimes N} |\Psi_{\text{dimer}}\rangle$ is the ground state of a local frustration free Hamiltonian $h_i = (\Lambda^{-1\dagger})^{\otimes K} h_i (\Lambda^{-1})^{\otimes K}$ where $(\Lambda^{-1})^{\otimes K}$ only acts on the sites which overlap with h_i . This is, the ground spaces of the RVB and the dimer state are related by the invertible map $\Lambda^{\otimes N}$, and thus, the RVB state and the dimer state have the same ground space structure. Even more, by the same argument there is a smooth local interpolation $H(\theta) = \sum h_i(\theta)$ between the RVB and the dimer state.

We can now use the known fact that the dimer model is local unitarily equivalent to Kitaev's toric code [10,11] (which can alternatively be shown using the Z_2 symmetry of the PEPS) to infer that the RVB state is the ground state of a local Hamiltonian with a topological ground space degeneracy equivalent to the toric code, i.e., a Z_2 topological model. Even more, this mapping allows

us to construct the full ground space manifold of the RVB model based on the symmetries in its PEPS description, just as for the toric code [8]: We thus obtain an exact parametrization of the full ground space of the RVB state, allowing for its numerical study [12].

We have subsequently used exact diagonalization techniques to study whether the RVB is a spin liquid, i.e., whether it breaks any symmetries. PEPS are particularly suited for this endeavor, since any type of correlation is mediated by the PEPS transfer operator; this is, symmetry breaking is reflected by a degeneracy in the spectrum of the transfer operator. The spectrum of the transfer operator can be determined using standard PEPS techniques; by restricting to cylinders of diameters up to 10 elementary cells (with 3 spins per cell) we can use exact boundary vectors, which allows us to apply exact diagonalization to the transfer operator and thus obtain machine precision data which gives extremely accurate finite size scaling results. In Fig. 2, we show the second largest eigenvalue of the transfer operator above the two-fold degenerate largest eigenvector (whose degeneracy reflects the topological nature of the state), for the interpolation from the RVB state (left) to the dimer state (right). Evidently, for the RVB state this eigenvalue remains bounded away from 1 in the $N \rightarrow \infty$ limit, demonstrating the spin liquid nature of the RVB state. Moreover, we find that also along the interpolation to the dimer/toric code state there is no sign of a phase transition in the transfer operator, which altogether provides compelling evidence that the RVB state is a Z_2 topological spin liquid in the same topological phase as the toric code model.

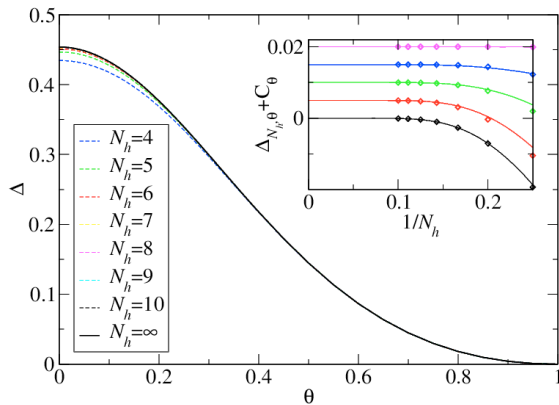


Figure 2. Gap of the transfer operator Δ as a function of θ along the RVB-dimer interpolation for $N_h=4, \dots, 10$ and periodic boundary conditions. The $N_h=\infty$ data has been obtained from a finite size scaling analysis, shown in the inset for $\theta=0, 0.1, 0.2, 0.3, 0.5$.

- [1] P. W. Anderson, *Mater. Res. Bull.* **8**, 153 (1973).
- [2] P. Mendels *et al.*, *Phys. Rev. Lett.* **98**, 077204 (2007); S. Yan *et al.*, *Science* **332**, 1173 (2011).
- [3] Seidel, *Phys. Rev. B* **80**, 165131 (2009).
- [4] D. S. Rokhsar and S. A. Kivelson, *Phys. Rev. Lett.* **61**, 2376 (1988).
- [5] G. Misguich, D. Serban, and V. Pasquier, *Phys. Rev. Lett.* **89**, 137202 (2002).
- [6] F. Verstraete and J. I. Cirac, *Phys. Rev. A* **70**, 060302 (2004).
- [7] F. Verstraete and J. I. Cirac, *cond-mat/0407066*.
- [8] N. Schuch, I. Cirac, and D. Pérez-García, *Ann. Phys.* **325**, 2153 (2010).
- [9] F. Verstraete, M. M. Wolf, D. Perez-Garcia, and J. I. Cirac, *Phys. Rev. Lett.* **96**, 220601 (2006).
- [10] Kitaev, *Ann. Phys.* **303**, 2 (2003).
- [11] Nayak and K. Shtengel, *Phys. Rev. B* **64**, 064422 (2001).
- [12] Poilblanc, N. Schuch, D. Pérez-García, and J. I. Cirac, *Phys. Rev. B* **86**, 014404 (2012).

Disorder-driven Metal-insulator Transitions in Crystalline Phase-change Materials

W. Zhang¹, A. Thiess², P. Zalden³, R. Zeller², P. H. Dederichs², J.-Y. Raty⁴, M. Wuttig³, S. Blügel², and R. Mazzarello¹

¹ Institute for Theoretical Solid State Physics, RWTH Aachen University, Germany

² Peter Grünberg Institute-2 & Institute for Advanced Simulation-3, Forschungszentrum Jülich, Germany

³ I. Institute of Physics A, RWTH Aachen University, Germany

⁴ Condensed Matter Physics, B5, University of Liege, Belgium

The study of metal–insulator transitions (MITs) in crystalline solids is a subject of crucial importance to understand the transport properties of these materials. Recently, evidence for a MIT exclusively due to disorder was observed in the crystalline phase-change material GeSb_2Te_4 [1]. Phase-change materials are considered to be promising candidates for non-volatile memories of next generation [2], due to their ability to switch rapidly and reversibly between the crystalline and the amorphous phase upon heating and to the pronounced resistivity contrast between the two phases. Here we report on calculations employing density functional theory, which identify the microscopic mechanisms that localize the wave functions and drive the MIT [3]. We show that, in the insulating phase, the electronic states responsible for charge transport are localized inside regions having large vacancy concentrations. The transition to the metallic state is driven by the dissolution of these vacancy clusters and the ordering of the vacancies into layers. These results open up the possibility of tuning the resistance of phase-change devices in a controlled way, which could lead to the development of novel devices based on multiple resistance states.

Experimentally, as-deposited amorphous GeSb_2Te_4 crystallizes into a cubic phase or a hexagonal phase at low and high annealing temperatures, respectively. The metastable cubic phase is always insulating at sufficiently low temperatures, whereas the hexagonal phase displays the MIT [1]. To shed light on this behavior, we have carried out a comprehensive computational study of the structural and electronic properties of both crystalline phases [3]. For this purpose, a large number of cubic and hexagonal models of GeSb_2Te_4 containing different amount of disorder in the form of randomly arranged vacancies and substitutional Ge/Sb disorder were generated and optimized using density functional theory. The KKRnano [4] and CP2K [5] packages were employed for these simulations. We start our analysis discussing the fully disordered cubic rock-salt phase. This metastable phase is also obtained in phase-

change memories upon fast recrystallization of the amorphous bits induced by heating. There is experimental evidence that one sublattice is occupied by Te atoms only, whereas in the second one 25% Ge, 50% Sb and 25% vacancies are arranged in a random fashion. To describe this phase, we considered two supercells of GeSb_2Te_4 composed of 875 and 3584 atoms, in which vacancies, Ge and Sb were placed on the second sublattice employing a random number generator.

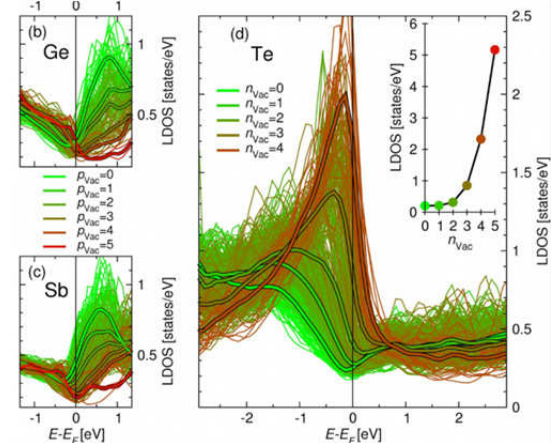


FIG. 1: Local density of p states of Ge, Sb and Te atoms in a $\text{Ge}_{125}\text{Sb}_{250}\text{Te}_{500}$ unrelaxed supercell. Te atoms are grouped with respect to the number of nearest-neighbor vacancies (n_{Vac}), whereas Ge and Sb atoms are grouped according to the number of third nearest-neighbor vacancies (p_{Vac}). One can clearly see that the presence of neighboring vacancies shifts the Te p states upwards in energy, close to E_F . Structural relaxation does not change this picture qualitatively, but for the opening of a pseudo gap above E_F .

Atomic p orbitals govern the electronic structure of GeSb_2Te_4 at the Fermi energy E_F . Hence, we have analyzed the local density of states (LDOS) of the p states on each atomic site to reveal the influence of chemical disorder on the electronic properties of GeSb_2Te_4 (Fig. 1). Since, for Te atoms, disorder occurs on the nearest-neighbor sites, the LDOS of Te atoms is much more sensitive to randomness. Figure 1 (right) shows the LDOS averaged over all Te atoms having the same number of nearest-neighbor vacancies, n_{Vac} : the LDOS in the vicinity of E_F increases markedly with n_{Vac} and, for the

relatively rare configurations $n_{\text{vac}}=3$ and $n_{\text{vac}}=4$, pronounced peaks appear slightly below or at E_F .

Given a configuration $n_{\text{vac}}=3$ or 4, the hybridization of the Te p states with states of neighboring Te atoms is hindered. Hence, the p states of the Te atoms located in regions having a high vacancy concentration are expected to give rise to spatially localized electronic states near E_F .

Next, we considered a sequence of large models of GeSb_2Te_4 containing 1,008 atoms to identify the structural rearrangement, which is responsible for the transition to the metallic state. We started from a Poisson distribution of Ge, Sb and vacancies in cubic GeSb_2Te_4 . Subsequently, the amount of disorder in the system was reduced, until a perfectly ordered hexagonal phase was obtained. Three important ingredients play a role in this sequence: the distribution of vacancies, the substitutional Ge/Sb disorder and the arrangement of the crystalline planes (cubic or hexagonal).

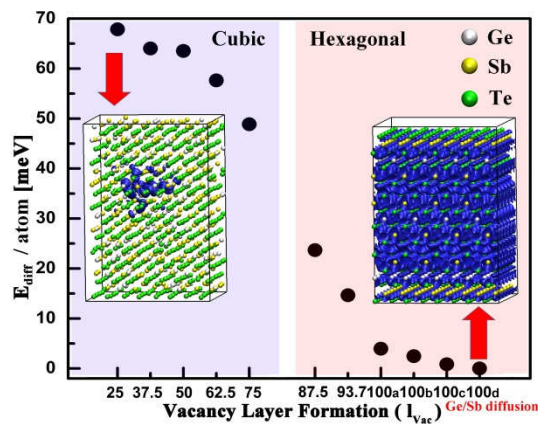


FIG. 2: Total energy per atom of 1008 atoms models of the disordered cubic phase of GST (first point on the left), perfect hexagonal GST (last point on the right) and several intermediate structures with varying degree of disorder. The formation of vacancy layers yields a large reduction in energy. The two insets show a snapshot of the HOMO state of the random cubic GST (left) and hexagonal GST (right). The first state is exponentially localized on about 20-30 atomic sites. The second state is completely delocalized.

The formation of the vacancy layers yields a very significant reduction in energy, of the order of 50 meV per atom (Fig. 2). Furthermore, our results indicate that the hexagonal phase becomes lower in energy than the corresponding structure with cubic stacking before vacancy layers have formed completely. Hence, the ordering of vacancies drives the structural transition.

The reduction of substitutional disorder also leads to a decrease in energy, however energy difference between models with vacancy layers and different degree of substitutional disorder are small, less than 5 meV per atom, and are comparable to the configurational entropy contribution of the disordered phases.

Subsequently, we have investigated the electronic structure of these models by evaluating the inverse participation ratio (IPR) and the charge density distribution of the electronic states near E_F .

For an extended state, the IPR is equal to zero in infinitely large systems. On the contrary, for localized states, it remains finite and provides an estimate for the inverse of the number of atoms on which the state is localized. In the disordered phases containing randomly arranged vacancies, evaluation of the IPR values and the charge density distributions shows that the states around E_F are localized in relatively small regions of the crystals, corresponding to vacancy clusters (Fig. 2, left inset). On the other hand, in the hexagonal phases where vacancy layers have formed, the IPRs values of the states at E_F are an order of magnitude smaller, reflecting the fact that the states are extended and spread over the whole cell (right inset). Hence, the transition to the metallic state is driven by the formation of ordered vacancy layers. Substitutional disorder and structural distortion do not play an important role.

Transport measurements indicate that both phases have typically a relatively large density of carriers (in the range of $1\text{--}2 \times 10^{20} \text{ cm}^{-3}$ [1]). These carriers are due to non-stoichiometric Ge/Sb vacancies, which turn crystalline GeSb_2Te_4 into a p-type degenerate semiconductor. Such defects have not been included in the models of Fig. 2 but we have been able to show that, since the concentration of excess vacancies compatible with said carrier densities is small, inclusion of these defects in the disordered models does not shift E_F away from the region of localized states [3].

In conclusion, the analysis of our set of models of GeSb_2Te_4 provides clear evidence for the occurrence of a structural transition involving a change of stacking sequence and an Anderson MIT, both of them driven by vacancy ordering. It also indicates that the structural transition takes place well before the vacancy layers are completely formed. This implies that there is still a significant amount of randomly distributed vacancies in hexagonal GeSb_2Te_4 in the vicinity of the structural transition point, which induce localization of states at E_F . These findings are in agreement with experiments, which show that the MIT occurs in the hexagonal phase. Hence, although the two transitions are driven by the same mechanism (vacancy ordering), they are of different nature and independent from each other.

The identification of the microscopic mechanism leading to the MIT provides a step towards the goal of controlling the degree of disorder in phase-change devices, so as to tune their resistance in a reproducible fashion.

- [1] T. Siegrist, P. Jost, H. Volker, M. Woda, P. Merkelbach, C. Schlockermann, and M. Wuttig, *Nature Mater.* **101**, 202 (2011).
- [2] M. Wuttig and N. Yamada, *Nature Mater.* **6**, 824 (2007).
- [3] W. Zhang, A. Thiess, P. Zalden, J.-Y. Raty, R. Zeller, P. H. Dederichs, M. Wuttig, S. Blügel, and R. Mazzarello, *Nature Mater.* **11**, 952 (2012).
- [4] Thiess, R. Zeller, M. Bolten, P. H. Dederichs, and S. Blügel, *Phys. Rev. B* **85**, 235103 (2012).
- [5] J. VandeVondele *et al.*, *Comput. Phys. Commun.* **167**, 103 (2005).

Iron-Pnictides: strong Coulomb correlations via Hund's coupling

A. Liebsch

Peter Grünberg Institute-1 & Institute for Advanced Simulation-1: Quantum Theory of Materials, Forschungszentrum Jülich, Germany

Hund's coupling in iron pnictides is shown to give rise to a significant depletion of spectral weight above E_F . DMFT calculations reveal that this pseudogap is associated with a collective mode in the self-energy caused by spin fluctuations. The pseudogap is remarkably stable over a wide range of Coulomb and exchange energies. The implications of this phenomenon for optical spectra of iron pnictides are discussed.

The discovery of superconductivity in iron pnictides has stimulated intense discussions concerning the role of correlation effects in these compounds. In contrast to high- T_c cuprates, which have antiferromagnetic Mott insulators as parent compounds, pnictides are correlated magnetic metals that show significant deviations from Fermi-liquid behavior. Moreover, as a result of the multi-band nature of pnictides, the interplay of Coulomb and exchange interactions gives rise to phenomena not found in cuprates. The importance of Hund coupling in pnictides has recently received wide attention. In particular, optical data on BaFe_2As_2 [1] reveal a high-energy pseudogap not compatible with normal metal behavior. This pseudogap differs from the low-energy gap in the antiferromagnetic spin-density wave phase. Also, ARPES data exhibit a depletion of spectral weight near E_F that differs from the superconducting gap.

To investigate the influence of Coulomb correlations on the electronic properties of iron pnictides, we use dynamical mean field theory (DMFT) combined with exact diagonalization (ED) as multi-orbital impurity solver [2]. As shown in Fig. 1(a), both the interacting and non-interacting Fe 3d density of states (DOS) reveal two main features separated by a minimum above E_F . Similar quasi-particle spectra were obtained by several groups for a variety of pnictides. It is not clear to what extent the pseudogap seen in these spectra is induced by Coulomb correlations or band structure effects.

To resolve this issue, we have performed DMFT calculations for five degenerate semi-elliptical bands [3]. Since in this case the DOS is featureless, correlation induced spectral modifications are easily identified. In addition, by scanning a wide range of Coulomb and exchange energies, it is feasible to investigate their respective roles. The main result of this work is that many-body effects are much more sensitive to the magnitude of Hund's rule coupling J than to the intra-orbital Coulomb repulsion U . In particular,

exchange interactions give rise to a pseudogap above E_F , which persists in the full range of realistic values of J , but disappears at small J . This is illustrated in Fig. 1(b) which shows DMFT spectra for $U = 3, \dots, 5$ eV and $J = 0.5$ eV. Spectra up to $J = 1.0$ eV are remarkably similar. Except in the limit $J = 0$, the interacting DOS exhibits peaks below

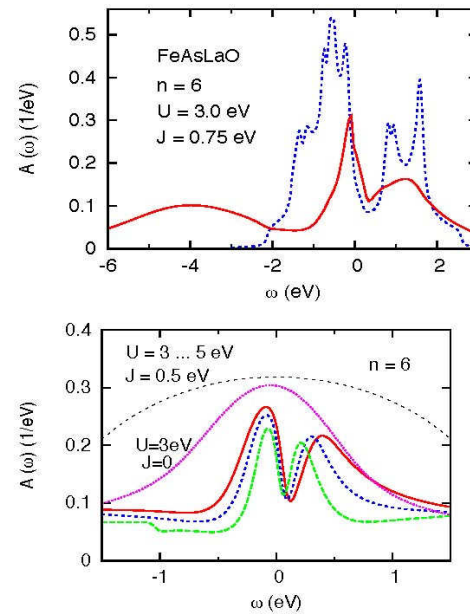


FIG. 1: (a) Fe 3d DOS of FeAsLaO. Solid curve: DMFT; dashed curve: LDA. (b) DMFT DOS of degenerate five-band model for several U and J . Black dashed curve: LDA.

and above E_F , separated by a pseudogap above E_F . The peak-dip structure near E_F is reminiscent of the one in the quasi-particle spectrum shown in panel (a). Since the bare DOS is smooth, the pseudogap is induced by the frequency-dependent self-energy. These results suggest that the pseudogap above E_F is a generic feature caused by correlations within the 3d shell and that its existence depends crucially on realistic values of Hund's coupling. The quasi-particle spectra of actual pnictides should therefore consist of a combination of correlation features associated with J and signatures related to the bare density of states.

To illustrate the effect of Coulomb correlations on the self-energy, we show in Fig. 2 the imaginary part of $\Sigma(i\omega_n)$ for several occupancies. For $n \geq 6.2$, $\text{Im} \Sigma(i\omega_n) \sim \omega_n$ at low energies, so that the system

is a correlated Fermi liquid with a doping dependent effective mass enhancement $m^*/m \approx 3, \dots, 6$. At smaller n , $\text{Im } \Sigma$ reveals a nonzero onset, associated with bad-metallic behavior. As shown previously [4], the spin correlation function then changes from Pauli to Curie Weiss behavior, indicating a spin freezing transition.

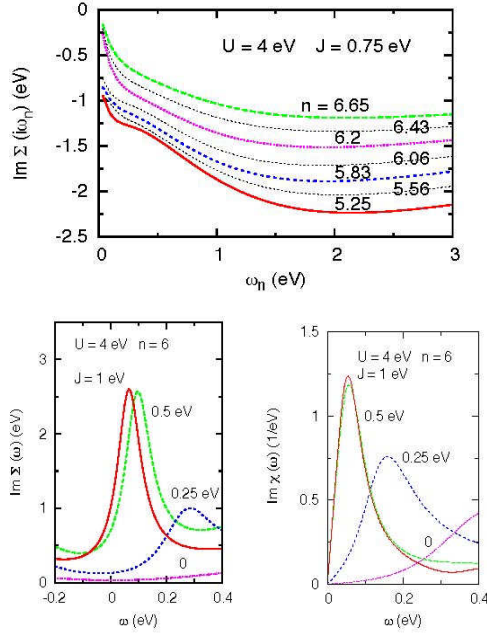


FIG. 2: (a) Self-energy for five-band model within ED DMFT for various occupancies. (b) Variation of self-energy (left) and spin susceptibility (right) with Hund's coupling.

In addition, $\text{Im } \Sigma(i\omega_n)$ exhibits a kink near $\omega_n \approx 0.1, \dots, 0.2$ eV, which is weak in the Fermi-liquid region, but becomes more intense at lower occupancy. As shown in panel (b), this kink is related to a resonance in $\text{Im } \Sigma(\omega)$, which is the origin of the pseudogap above E_F in the spectra shown in Fig. 1. Remarkably, the resonance disappears at small J . For $J = 0.5, \dots, 1.0$ eV, the local spin correlation function reveals a maximum below 0.1 eV, suggesting that the resonance in $\text{Im } \Sigma(\omega)$ corresponds to a collective mode induced by spin fluctuations associated with Hund's coupling. Thus, states in the resonance region have a greatly reduced lifetime. According to Kramers-Kronig relations, $\text{Re } \Sigma(\omega)$ exhibits a positive slope near the resonance, so that spectral weight is removed from the pseudogap region. Beyond this region, the slope of $\text{Re } \Sigma(\omega)$ becomes again negative, giving rise to a kink in the dispersion of energy bands.

A complementary understanding of the pseudogap can be achieved by realizing that the system at $n = 6$ occupancy exists in proximity to the $n = 5$ Mott insulator. As shown in Fig. 3, at half-filling the degenerate five-band model exhibits a Mott

transition at a critical Coulomb energy that depends sensitively on J , but is insensitive to U . In particular, U_c diminishes rapidly when J increases. Thus, for realistic U and J (see green box), the half-filled system is a Mott insulator composed of localized $S = 5/2$ spins. Upon doping, some of the localized states become itinerant, so that the DOS exhibits a narrow quasiparticle peak below E_F , and a minimum or pseudogap above E_F , in agreement with the spectra shown in Fig. 1. On the other hand, according to the phase diagram shown in Fig. 3, at small J the high orbital degeneracy yields a weakly correlated metal since $U \ll U_c$. This also holds at finite electron doping, so that the spectral distribution exhibits a broad quasi-particle peak, as indicated by the results for $U = 3$ eV, $J = 0$ in Fig. 1(b). It is evident, therefore, that the collective mode in the self-energy shown in Fig. 2 and the associated pseudogap obtained at realistic values of J are a consequence of Hund's coupling.

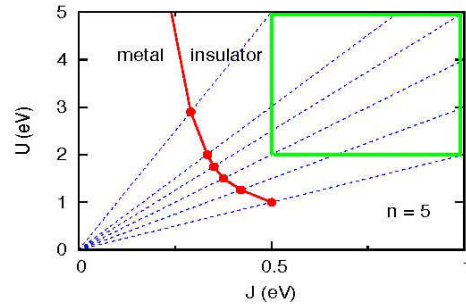


FIG. 3: Phase diagram of five-band model at half-filling. Dashed lines: fixed ratios $J/U = 1/10 \dots 1/2$. Dots: U_c of Mott transitions for these ratios. To the right (left) of the solid red curve, the system is insulating (metallic). Green box: range of U and J used in DMFT studies of iron pnictides.

At present there exists appreciable uncertainty concerning the experimentally determined values of U and J as well as their theoretical estimates. Nonetheless, the robustness of the pseudogap over a wide range of U and J and the persistence of the Mott phase at half-filling down to remarkably low Coulomb energies suggest that the characteristic peakdip structure near E_F seen in many quasiparticle spectra of pnictides is partially caused by Coulomb correlations intimately related to Hund's coupling.

-
- [1] A.A. Schafgans *et al.*, Phys. Rev. Lett. **108**, 147002 (2012), and references herein.
 - [2] A. Liebsch, H. Ishida, J. Phys. Condens. Matter **24**, 05320 (2012).
 - [3] A. Liebsch, Phys. Rev. B **84**, 180505(RC) (2011).
 - [4] H. Ishida, A. Liebsch, Phys. Rev. B **81**, 054513 (2010); A. Liebsch, H. Ishida, *ibid.* **82**, 155106 (2010).

Multiferroicity from charge ordering? a case study

M. Angst, J. de Groot, and T. Mueller

Peter Grünberg Institut-4, Forschungszentrum Jülich, Germany

Materials combining magnetism and ferroelectricity, termed multiferroics, have a high potential for applications in information technology, and are therefore attracting rapidly increasing research efforts. Out of various identified or proposed mechanisms of realizing the coexistence of magnetism and ferroelectricity, a mechanism where the latter is induced by the ordered arrangement of different valence states of an ion, so-called charge order (CO), is particularly intriguing because it could combine large polarizations with strong magnetoelectric coupling. However, examples of oxides where this mechanism is experimentally indicated to occur are exceedingly rare and none is really well understood. The prototypical example material LuFe_2O_4 was believed for many years to provide the “proof of principle” that this mechanism can work in real materials. However, our recent structural investigations indicate a non-ferroelectric charge order. New dielectric spectroscopy measurements concur with this, finding no indications of ferroelectricity, once contact effects are properly taken into account. Thus, proof of principle for multiferroicity originating from CO remains an open question.

Because any ferroelectric polarization is built from electric dipole moments, i.e. non-centrosymmetric charge distributions, any CO breaking inversion symmetry automatically induces a ferroelectric polarization, which may be very large. The presence of different valence states of an ion implies an active spin degree of freedom on the same ion. Therefore a strong magnetoelectric coupling may be expected as well, which makes “ferroelectricity from CO” very attractive from the point of view of prospective applications such as memory cells. However, while the concept [1] is straight-forward, there is a distinct lack of experimentally verified examples.

The idea of ferroelectricity from CO, received a large boost of attention when, in 2005, a plausible example was reported [2]: A proposed CO of Fe^{2+} and Fe^{3+} in the bilayers of LuFe_2O_4 (Fig. 1 left), consistent with the position of superstructure reflections, would render the bilayers polar. Accompanying measurements of dielectric spectroscopy and pyroelectric currents suggested a large ($28 \mu\text{C}/\text{cm}^2$) ferroelectric polarization below the charge ordering temperature of $\sim 320 \text{ K}$. Furthermore, subsequent dielectric measurements [3] indicated a giant effect of magnetic fields on

dielectric behavior, implying a large magnetoelectric coupling.

The combination of the plausible model of CO and the macroscopic indications of ferroelectricity made a strong case and led to the compound being considered as the prototypical example and “proof of principle” of the mechanism.

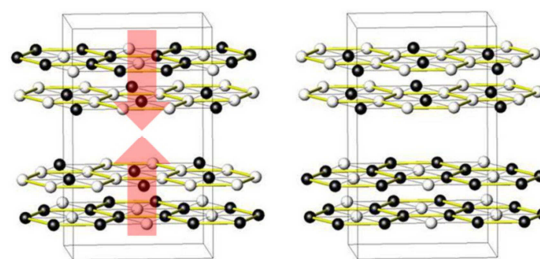


FIG. 1: Two models of the distribution of Fe^{2+} (white) and Fe^{3+} (black) ions in LuFe_2O_4 . Left: the originally proposed [2] uneven distribution of Fe^{2+} and Fe^{3+} over the two layers of a bilayer renders the latter polar (indicated by arrows). Right: the distribution consistent with structure refinements and circular dichroism [4] does not contain polar bilayers and is inconsistent with “ferroelectricity from CO”.

However, an alternative model of CO (Fig. 1 right), which does not contain polar bilayers and does not break inversion symmetry, leads to superstructure reflections at the same positions. Our structure refinements together with the bond-valence-sum method unambiguously identified a distribution of Fe^{2+} and Fe^{3+} ions as shown in Fig. 1 on the right [4]. This arrangement was furthermore independently verified by combining the spin structure with the spin-charge-coupling deduced by x-ray magnetic circular dichroism, casting much doubt on the occurrence of ferroelectricity from CO in LuFe_2O_4 .

The question of how to account for the macroscopic indications of ferroelectricity reported in [2] remained, however. To address this, we conducted broad-band dielectric spectroscopy on high-quality single crystals, in collaboration with the University of Cologne. The results (Fig. 2) show all the features of the corresponding data in [2]: extremely large dielectric constants at high temperatures and/or low frequencies, with a step at a frequency-dependent temperature. However, a strong impact of the electrode material as shown for the example of 100 kHz (different symbols) suggests significant contact effects. These may for example arise due to Schottky-type depletion layers at the contact interfaces, which act as additional capacitances. The whole data-set of real

and imaginary parts of the dielectric permittivity as functions of frequency and temperature could be well described with an equivalent-circuit model featuring contact-capacitance and –conductance in addition to sample hopping and dc conductivity and the sample capacity arising from the intrinsic dielectric constant of the material, with all parameters independent of frequency.

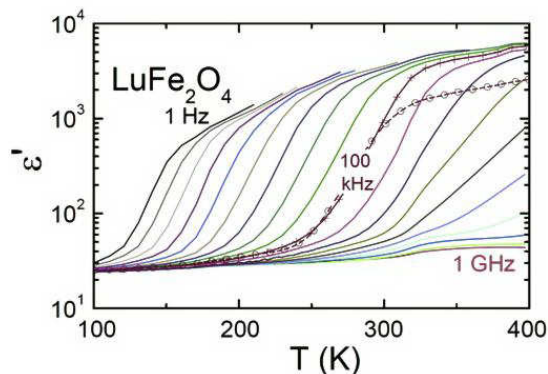


FIG. 2: Real part of the dielectric permittivity vs temperature in LuFe_2O_4 for frequencies between 1 Hz and 1 GHz (lines). Data additionally marked with symbols ($^\circ$, $+$) are both taken at 100 kHz, but with electrodes from different materials: Graphite ($^\circ$) and silver ($+$ and all other data). The large difference suggests the importance of contact contributions. After [5].

The modeling shows that the contact resistance is much larger than the sample resistance, and similarly the contact capacitance is much larger than the sample capacitance. For low frequencies or high temperature the circuit reduces to a leaky contact capacitance in series with the sample conductivity, while the sample capacitance is short-circuited, the apparent giant dielectric constants thus are of extrinsic origin, arising from the contact interface. Upon lowering the temperature the sample conductivity decreases and eventually the sample capacitance dominates, which leads to the characteristic step in the apparent dielectric constants. Because the step depends mainly on contact capacitance and sample resistance, a magneto-resistance will lead to an apparent magneto-dielectric response. This can account for the results of Subramanian and coworkers [3].

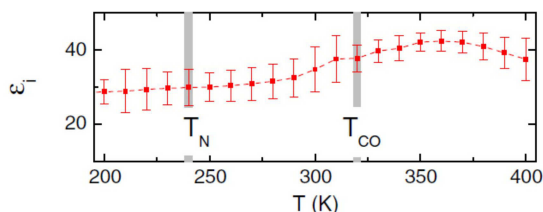


FIG. 3: Temperature-dependence of the intrinsic dielectric constant of LuFe_2O_4 , obtained by modeling the data of Fig. 2 with an equivalent circuit incorporating sample and contact contributions to resistance and capacitance. The absence of anomalies at the magnetic (T_N) and charge ordering (T_{CO}) temperatures counter indicates ferroelectric transitions at these temperatures. After [5].

The fitted intrinsic dielectric constant (Fig. 3) is only around 30 and does not show any indications of ferroelectric or antiferroelectric transitions. The

polarization is directly linked with the dielectric constant, and correspondingly the intrinsic polarization behavior may not be observed at low frequencies where contact contributions dominate. Indeed, the reported [2] anomalies in pyroelectric current measurements are naturally explained in the indicated conductivity dominated scenario: Charges are trapped inside the sample-contact interface region for low conductivity values at low temperatures and released when the conductivity increases again upon warming. Thus the dielectric spectroscopy results [5], in agreement with the finding of a non-polar CO [4], indicate that the prototypical example of ferroelectricity from CO is not ferroelectric after all.

In summary, a thorough reexamination of “multiferroicity from charge ordering” in the prototypical example LuFe_2O_4 indicates that neither the microscopic indications of a ferroelectric CO nor the macroscopic indications of ferroelectricity hold up to scrutiny. Although the position of CO superstructure reflections is compatible with a ferroelectric CO, a refinement of their intensity shows that a non-ferroelectric CO is actually realized. Furthermore, the reported macroscopic anomalies in pyroelectric current measurements and dielectric spectroscopy, which were taken as indications of ferroelectricity, are now shown to arise from contact effects and thus to be of extrinsic nature. LuFe_2O_4 does not only have no ferroelectricity originating from CO, it not ferroelectric at all. As this material has been generally acknowledged to be the “proof of principle” example showing that the mechanism of “ferroelectricity from CO” works, our result implies that an experimental proof of principle of the mechanism is still outstanding. Because of the advantages of large polarization and strong magnetoelectric coupling that this mechanism is expected to yield, identifying an alternative material where the mechanism works has now a high priority. Preliminary results indicate that classical magnetite could be such a material.

We gratefully acknowledge our collaborators: D. Niermann, F. Waschkowski, J. Hemberger, R.A. Rosenberg, D.J. Keavney, Z. Islam, J.-W. Kim. This work was supported by the initiative and networking fund of the Helmholtz Association through funding the Helmholtz-University Young Investigator Group VH NG-510 “Complex Ordering Phenomena in Multifunctional Oxides”, by the DFG through SFB608, and by the US Department of Energy, Office of Science.

- [1] J. van den Brink and D. I. Khomskii, J. Phys.: Condens. Matter **20**, 434217 (2008).
- [2] N. Ikeda *et al.*, Nature **436**, 1136 (2005).
- [3] M. A. Subramanian *et al.*, Adv. Mater. **18**, 1737 (2006).
- [4] J. de Groot *et al.*, Phys. Rev. Lett. **108**, 187601 (2012).
- [5] D. Niermann *et al.*, Phys. Rev. Lett. **109**, 016405 (2012).

Insulating Ground State of an Interface with Polar Discontinuity: DyScO₃/SrTiO₃

K. Rahmanizadeh¹, G. Bihlmayer¹, M. Luysberg², and S. Blügel¹

¹ Peter Grünberg Institut-1 & Institute for Advanced Simulation-1, Forschungszentrum Jülich, Germany

² Peter Grünberg Institut-5 & Ernst Ruska-Centre, Forschungszentrum Jülich, Germany

Polar discontinuities, as they arise e.g. at the (001) oriented LaAlO₃/SrTiO₃ interfaces, have received a lot of attention due to the two-dimensional (2D) electron gas that can form at the boundary of these materials. This 2D electron gas results from charged (AlO₂)⁻ or (LaO)⁺ layers, that are not compensated by the neutral SrO or TiO₂ layers at the interface. In contrast, the chemically very similar DyScO₃ shows an insulating boundary to SrTiO₃ in epitaxial multilayer structures [1]. Experiments have shown that a charge compensation takes place that results from an off-stoichiometry of the layers at the interface, i.e. mixed (Sc,Ti)O₂ or (Dy,Sr)O layers. Total energy calculations, based on density functional theory, show that the ground state of this system is always insulating, irrespective of the stoichiometry of the interface, with preferential formation of a mixed, chemically ordered (Dy,Sr)O layer [2]. This allows us to identify the basic mechanisms for the formation of these layers.

In the last years, oxide interfaces have attracted considerable attention due to the emerging novel properties, which do not exist in the corresponding parent bulk compounds. E.g. joining the two band insulators LaAlO₃ and SrTiO₃ on the (001) faces can induce a wealth of new properties ranging from conductivity, to magnetism, even to superconductivity [3]. In a simple ionic model, an electric interface dipole is formed, which leads to a divergence of the electrostatic potential with increasing distance from the interface. This is claimed responsible for many peculiar properties at the interface. On the other hand, intermixing at the interface, defects, or the formation of a ferroelectric-like polarization in the insulators are mechanisms that may contribute to prevent the divergence of the electric potential as well.

Recently, using high-resolution scanning transmission electron microscopy (HR-STEM) and electron energy loss spectroscopy (EELS), intermixing of the cations at the interface layers was reported for the DyScO₃ / SrTiO₃ interface [1]. Dysprosium scandate exhibits the same polar layers as lanthanum aluminate: DyO layers have a nominal charge of +1 e per formula unit, while ScO₂ layers carry -1 e charge per formula unit. As a consequence of the chemical off-stoichiometry at the interface, multilayers of DyScO₃ and SrTiO₃ were found to be electrically insulating.

Despite obvious similarities to the well-investigated LaAlO₃ / SrTiO₃ interface, there are also considerable differences, as far as the structure of the parent compounds is concerned: While the polar insulator LaAlO₃ crystallizes (as high temperature phase) in an ideal cubic perovskite lattice, DyScO₃ is of the orthorhombic GdFeO₃ type (space group *Pbnm*). For the interface to the non-polar SrTiO₃ this implies that good lattice matching is achieved when the (110) surface of DyScO₃ is interfaced with a *p*(2x2) unit cell of the (001) surface of SrTiO₃, while in the LaAlO₃ case both (001) surfaces can be matched. These structural differences may lead to different stresses at the interfaces and influence the chemical composition of the interface layers.

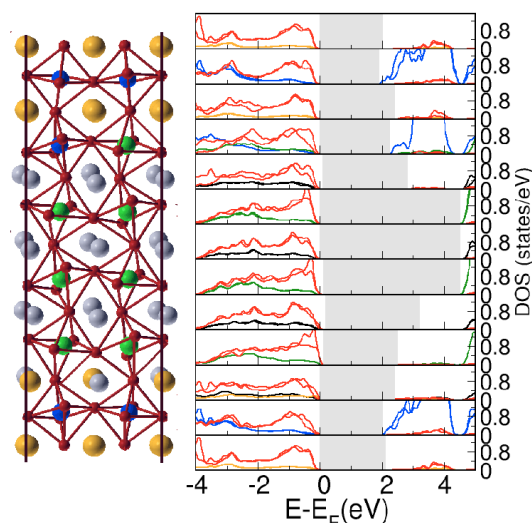


FIG. 1: Left: Relaxed structure of the DyScO₃ / SrTiO₃ with cation intermixing at the interface showing (red) oxygen octahedra with Sc (green) or Ti (blue) atoms in the center and gray and golden spheres representing the Dy and Sr ions. On the right we show the LDOS grouped by layers of the supercell, using the same color code as for the atoms. The gray shaded area indicates the band gap estimated from the LDOS of each layer.

To model the interfaces between DyScO₃ and SrTiO₃, we used supercells of *m* layers of DyO or ScO₂ and *n* layers of SrO or TiO₂. These structures, denoted shortly as (*m*,*n*) supercells, were then repeated periodically in the direction perpendicular to the interface. An in-plane *p*(2x2) unit cell with the lattice parameters of SrTiO₃ is used. For the (7,5) supercell with non-

stoichiometric interfaces [i.e. mixed (Dy,Sr)O and (ScTi)O₂ layers] shown in Fig.1 (left) the whole structure contains 120 atoms. Plots of the local densities of states (LDOS) for this structure resolving the atoms in each layer are shown in the right panel of Fig. 1. Throughout the structure a bandgap of at least 1.9 eV is obtained, indicating again the insulating character of the interface. The insulating property of the structure is furthermore verified by inspection of the total DOS (not shown). This confirms the proposal that an off-stoichiometry at the interface helps to avoid the formation of a two-dimensional electron gas at the interface of a polar to non-polar insulator.

In comparison to the chemically mixed interfaces, shown in Fig.1, we also set up supercells with stoichiometric layers at the interface between DyScO₃(110) and SrTiO₃(100). The resulting (6,6) structure was again relaxed and from the displacements of the cations with respect to the oxygen atoms in each layer we identify oppositely oriented polarizations in the two materials: on average, the oxygen anions move closer to the DyO/TiO₂ interface (nominally positively charged), while the cations relax towards the (nominally negative) ScO₂/SrO interface. Since SrTiO₃ is known as a highly polarizable material, the induced ionic polarization is larger in this material than in DyScO₃. From the layer resolved densities of states (not shown) it can be concluded that similar to the mixed interfaces also at the interfaces with sharp boundaries no metallic layer is formed at the interface. A similar mechanism of induced polarization was also discussed for the LaAlO₃ / SrTiO₃ interface. This supports the idea that strontium titanate can screen extra charges appearing at a polar interface. HR-TEM measurements actually confirmed the formation of cation / anion displacements around the interface [4]. We note here that this screening mechanism leads to a band insulator, in contrast to the Mott-insulating state. In our calculations, this can be realized by introducing strong correlation effects on the Ti atom that are not considered here.

To compare the stability of the mixed and sharp interfaces, we also considered a system with eight layers of DyScO₃ and four layers of SrTiO₃, a (8,4) supercell. Again, all internal coordinates and the lattice constant perpendicular to the interface were relaxed. Now, the energy gained by intermixing can be written as

$$\Delta E^{\text{mix}} = E^{(7,5)} - \left(E^{(6,6)} + E^{(8,4)} \right) = -65 \text{ meV}$$

i.e. we find that the intermixed interfaces are more stable than the sharp ones by 65 meV per $p(1 \times 1)$ in-plane unit cell.

Up to now, we considered in the mixed interfaces a checkerboard ordering of the cations in the $p(2 \times 2)$ unit cell. Actually, due to the rotations and tiltings of the oxygen cages in the DyScO₃ crystal structure, at the (110) interface an exchange of Dy and Sr atoms leads to a different interface structure with slightly lower energy (see Fig.2, black and orange boxes). Following this

observation, we considered several other chemical ordering patterns at the interface finding that a certain row-wise arrangement of the two different species gives the structural ground state.

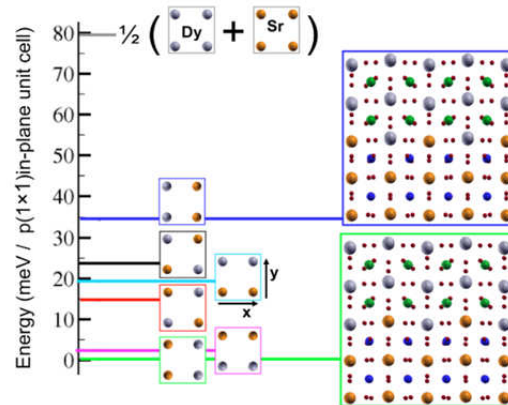


FIG. 2: Energetics of the cation ordering in the mixed (Dy,Sr)O layer: A checkerboard-ordering (black line) is 65 meV more stable than separated Dy and Sr layers. However, row-wise ordering of the two chemical species can lead to a further gain in energy (green). The reason for this behavior can be seen from the DyScO₃ structure (right) that accommodates ions of different size along distinct rows at the interface.

This particular type of ordering is also confirmed by STEM images, where the buckling of the mixed (Dy,Sr)O layer is clearly seen (cf. our simulations in the right part of Fig.2). Here, the matching of the different sizes of the Dy and Sr atoms and the DyScO₃ crystal structure are responsible for observed chemical ordering. It should be noticed that this mechanism is not effective at the mixed (Sc,Ti)O₂ interface, where the cations sit in rather rigid oxygen cages.

Our results show that the electronic structure of oxide interface is highly sensitive to the exact structural details, the stoichiometry at the interface, the polarizability of the oxides and, therefore, to in-plane strain that might arise in multilayer systems. Despite the strong driving force to avoid delocalized charge carriers at the interface, this enormous sensitivity also offers the possibility to tune the electronic properties in a certain range.

This work was supported by funding from the European Community's Seventh Framework Programme (FP7/2007-2013) under grant agreement NMP3-LA-2010-246102. We gratefully acknowledge computing time from the Jülich supercomputing centre.

- [1] M. Luysberg, M. Heidelmann, L. Houben, M. Boese, T. Heeg, J. Schubert, and M. Roeckerath, *Acta Materialia* **57**, 3192 (2009).
- [2] K. Rahmanizadeh, G. Bihlmayer, M. Luysberg, and S. Blügel, *Phys. Rev. B* **85**, 075314 (2012).
- [3] M. Huijben, A. Brinkman, G. Koster, G. Rijnders, H. Hilgenkamp, and D. H. A. Blank, *Adv. Mater.* **21**, 1665 (2009).
- [4] C. L. Jia, S. B. Mi, M. Faley, U. Poppe, J. Schubert, and K. Urban, *Phys. Rev. B* **79**, 081405 (2009).

Analysis of polarization and lattice strains at the Interface of ferroelectric heterostructures on atomic scale by Cs-corrected scanning transmission electron microscopy (STEM)

D. Park^{1,2}, A. Herpers³, T. Menke³, R. Dittmann³, and J. Mayer^{1,2}

¹ Central Facility for Electron Microscopy, RWTH Aachen University, Germany

² Ernst Ruska-Centre, Forschungszentrum Jülich and RWTH Aachen, Jülich, Germany

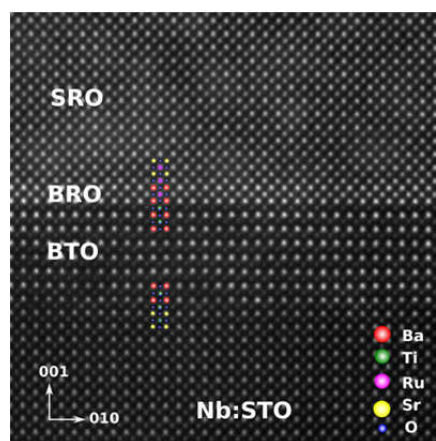
³ Peter Grünberg Institute-7, Forschungszentrum Jülich, Germany

Ferroelectric thin films are attractive candidates for capacitors in random access memory (RAM), in which a reversible spontaneous polarization is utilized to store information. However, below a critical thickness, the ferroelectric property usually disappears. The origin of the vanishing of the polarization is generally believed to be the existence of the depolarization field at electrode-ferroelectric interfaces. Therefore, to understand these obstacles the analysis of the atomic arrangement and chemical composition at interfaces is essential.

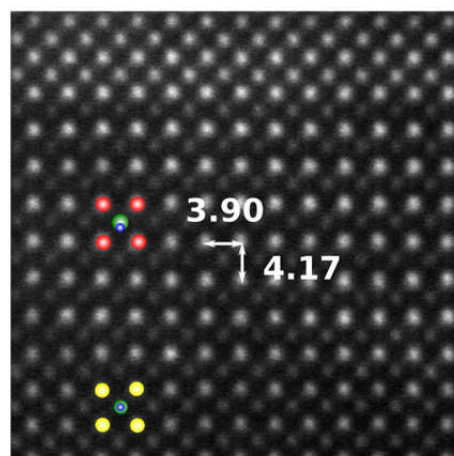
The Nb:SrTiO₃/BaTiO₃(7u.c.)/BaRuO₃(1.5u.c.)/SrRuO₃ heterostructures were grown by pulsed laser deposition (PLD) technique. The specimens for TEM investigation were prepared by focused ion beam (FIB) sectioning. To reduce artifacts during the FIB preparation the specimen is finally cleaned using Ar-ion milling with 2 keV.

To study the lattice distortions, sequential HAADF images are acquired and aligned by cross correlation with a reference frame selected from the sequence. A fast sequential acquisition in the scanning mode reduces the sample drift. A sum of images after the drift correction suppresses scan noise. In Figure 1, the perfect drift corrected HAADF image of the ferroelectric heterostructure is shown. The intensity of the HAADF image follows the Rutherford scattering model which is roughly proportional to Z^2 , where Z is the atomic number. The HAADF image is therefore also referred to as Z-contrast image. The HAADF image in Figure 1 shows clearly the Z-contrast dependence with the atomic number. Atomic columns of Ba ($Z=56$, red) appear brightest, followed by Ru ($Z=44$, pink), Sr ($Z=38$, yellow), Ti ($Z=22$, green) and O ($Z=8$, blue). Therefore, direct interpretation of the HAADF image is feasible.

In Figure 2 the intensity of the HAADF image and lattice parameters are quantitatively analyzed by a peak finding algorithm using the Gaussian fitting



(a)



(b)

Fig. 1: (a) the drift corrected HAADF image of the ferroelectric heterostructure along the [100] direction. (b) in-plane and out-of-plane lattice parameters of BaTiO₃ are indicated and a small shift of Ti column is visible.

method. According to the intensity analysis in Figure 2 (a), 7 unit cells of BaTiO₃ and 1.5 unit cells of BaRuO₃ are verified.

The critical thickness depends on the termination of the ferroelectric thin film at the electrode interfaces. To achieve a single termination of TiO_2 the Nb: SrTiO_3 substrate was etched by means of a buffered hydrofluoric acid-solution (BHF) and checked by atomic force microscopy (AFM). In the HAADF-STEM images, the layer sequence of $(\text{BaO-TiO}_2)_x$ and $\text{BaO-RuO}_2\text{-BaO}$ on the substrate is identified by the intensity analysis. Additional $\text{BaO-RuO}_2\text{-BaO}$ layers are deposited to change the TiO_2 -termination of BaTiO_3 . It is reported that a BaTiO_3 layer with BaO -termination exhibits a more stable ferroelectric polarization compared to TiO_2 -termination [1, 2]. By using interface engineering, the TiO_2 termination of BaTiO_3 is successfully changed into the BaO -termination.

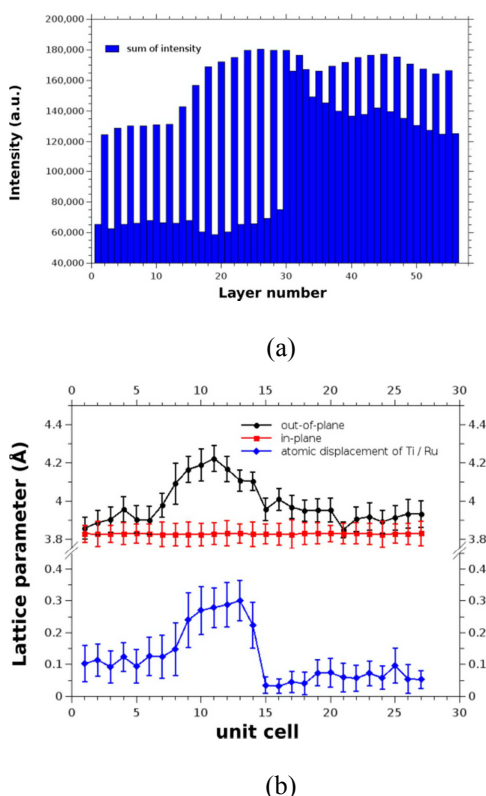


Fig. 2: (a) Intensity analysis (b) in-plane and out-of-plane lattice parameter analysis of the HAADF image

Using smaller in-plane lattice parameter of the substrate induces epitaxial strain which results in enhanced ferroelectric distortion. In this study, niobium doped SrTiO_3 is used as a substrate due to its 2.2% smaller lattice parameter compared to BaTiO_3 . In Figure 2(b), in-plane and out-of-plane lattice parameters measured by the peak finding algorithm are shown. In the BaTiO_3 layer, the enhanced tetragonal distortion strained by the substrate is clearly visible, whereas SrTiO_3 and SrRuO_3 show almost cubic symmetry. Averaged in-plane and out-of-plane lattice parameter of BaTiO_3 are respectively 3.83 Å and 4.15 Å.

To verify the enhanced tetragonal distortion of the ultrathin strained BaTiO_3 layer the energy-loss near-edge structure of the Ti-L_{23} edge of Nb: SrTiO_3 and BaTiO_3 are measured using the StripeSTEM technique [3]. The StripeSTEM

technique reduces beam damage during EEL spectra measurement. As a reference, the Ti-L_{23} edge of bulk BaTiO_3 is measured. In Figure 3, measured Ti-L_{23} edges are compared. Here, for ultrathin BaTiO_3 layer (with tetragonal symmetry) the crystal field splitting (CFS) of $\text{Ti } 3d e_g$ and t_{2g} orbitals is expected to decrease due to the reduction in symmetry from the cubic perovskite structure. The CFS energy of the strained BaTiO_3 shows 1.93 eV, whereas SrTiO_3 shows 2.24 eV. The reduction in the CFS energy of BaTiO_3 accounts for the tetragonal distortion. Moreover, compared to a bulk BaTiO_3 (2.01 eV) the CFS energy is slightly smaller. It reveals the enhanced tetragonal distortion strained by the substrate with a small lattice parameter.

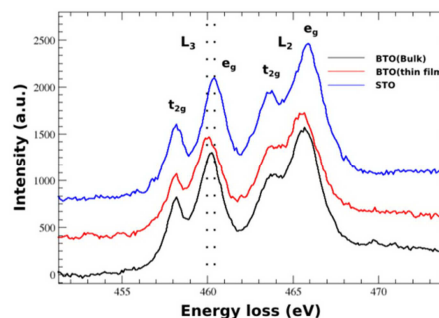


Fig. 3: The analysis of the energy-loss near-edge structure of the Ti-L_{23} edge.

A fast sequential acquisition of HAADF images and the sum of images after the drift correction minimize the image distortion and scan noise in the scanning mode. This approach enables to analyze atomic column positions and the intensity quantitatively. The tetragonal distortion ($c/a = 1.07$) of ultrathin BaTiO_3 film strained by SrTiO_3 is confirmed by the lattice parameter analysis which shows a good agreement with experimental and theoretical values [4]. Terminations at interfaces are identified by the Z-contrast analysis. To stabilize the ferroelectricity TiO_2 termination of BaTiO_3 is successfully changed into BaO termination by using interface engineering. The change of crystal field splitting energy on Ti-L_{23} edges due to the tetragonal distortion is verified in EEL spectra using the StripeSTEM technique.

The authors acknowledge support by the DFG in projects MA1280/32-1 and DI919/3-1.

- [1] M. Stengel, D. V. M. Stengel, D. Vanderbilt and N. Spaldin, *Nature Materials* 8, 392-397 (2009)
- [2] Umeno, Y., Albina, J. M., Meyer, B., Elsäßer *Physical Review B* 80 (2009)
- [3] M. Heidelmann, J. Barthel and L. Houben, *Ultramicroscopy* 109, 1447 (2009).
- [4] A. Petraru, N. A. Pertsev and R. Waser et. al *J. Appl. Phys.* 101, 114106 (2007).

In-situ Structural Investigations of Non-stoichiometric HfO_{2-x} Films Using QEXAFS

M. Liu¹, T. Leichtweiß², J. Janek², and M. Martin¹

¹ Institute of Physical Chemistry, RWTH Aachen University, Germany

² Institute of Physical Chemistry, Justus-Liebig-University Giessen, Germany

Thin films of amorphous, non-stoichiometric hafnium oxide (HfO_{2-x}) were synthesized by Pulsed Laser Deposition (PLD). During the deposition, gas atmospheres of O_2 , Ar and Ar/ H_2 were used. Electron Probe Micro Analysis (EPMA) and X-ray Photoelectron Spectroscopy (XPS) measurements show that films deposited in Ar or Ar/ H_2 are oxygen deficient, while films deposited in O_2 are stoichiometric. X-ray Diffraction (XRD) of as-prepared samples proofed them to be amorphous, while annealed films show signals of the monoclinic HfO_2 phase. *In-situ* Quick-scanning Extended X-ray Absorption Fine Structure (QEXAFS) measurements carried out at elevated temperatures up to 440 °C showed an increase in the Hf-Hf order. From the time-resolved data the crystallization kinetics is extracted and analyzed using the Avrami model.

Hafnium oxide is a promising candidate to replace SiO_2 as a gate dielectric in metal-oxide-semiconductor (MOS) transistors, as the downscaling of these devices gives rise to problems such as tunneling currents [1]. A way to avoid these tunneling currents is the use of a high- κ material, like HfO_2 ($\kappa \sim 22-25$) [2], as these materials enable the use of a thicker MOS layer, while maintaining the performance. Other advantages of HfO_2 are the wide band gap (5.55-5.7 eV) [1, 3] and the thermal stability with silicon [4]. Another application of hafnium oxide is the use in nonvolatile memory devices, where the resistive switching between states with low and high resistivity is important. For these applications, non-stoichiometric HfO_{2-x} is used, as for example Lee *et al.* [5] reported earlier. These two very different applications, one using hafnium oxide as an insulator, the other using it as a resistive switching material, hint at the large difference between stoichiometric and oxygen deficient hafnium oxide.

Here we investigate amorphous HfO_{2-x} films with varying stoichiometry x and analyze the structure and stability of these films. To further understand the kinetics of the crystallization, the films were examined during thermal treatment by means of time-resolved *in-situ* QEXAFS measurements.

Thin films of hafnium oxide were prepared on amorphous SiO_2 substrates at room temperature by PLD using a 248 nm KrF Excimer laser. A

ceramic target was used, which was prepared from commercially available HfO_2 powder through pressing and subsequent sintering. Before deposition, the chamber was evacuated to at least $6.7 \cdot 10^{-7}$ mbar. During the deposition a total pressure of $40.0 \cdot 10^{-3}$ mbar of O_2 , Ar or a mixture of Ar and H_2 was used. For all films, the laser energy was set to 200 mJ per shot with a total of 72000 shots used per deposition. The target substrate distance was constantly kept at 50 mm.

The stoichiometries of the samples were determined by EPMA and XPS measurements. The XPS measurements were first carried out on the surface of the sample and subsequently after sputtering with argon ions. As it is known that preferential sputtering of oxygen ions may occur, the bulk stoichiometries determined by XPS were corrected under the assumption that the film deposited in O_2 is fully stoichiometric, which is in accordance with the EPMA results. Furthermore, stoichiometries were obtained from the Fourier transformed (FT) EXAFS spectra (see below). The resulting stoichiometries for all methods are given in Table 1 as ratios of O/Hf.

Gas	O_2	Ar	Ar/ H_2
EPMA	2.07(3)	1.83(2)	1.75(1)
XPS surface	1.97(10)	1.94(10)	2.00(10)
XPS bulk	2	1.9(1)	1.7(1)
EXAFS 1 st shell fit	1.99(10)	1.87(11)	1.81(11)

TABLE 1: O/Hf ratios of films deposited in different gas atmospheres.

X-ray diffraction shows that all films are amorphous in the as-prepared state (not shown).

The EXAFS measurements were carried out at beamline C of HASYLAB in Hamburg, Germany at the Hf L_{III} edge. First, spectra of films in the as-prepared state were measured. In Fig. 2 the FT EXAFS spectra of films deposited in different atmospheres together with a reference spectrum of a sintered HfO_2 powder sample are shown. It can be seen that the first peak, which correlates to the first shell, is almost unchanged in the films, while the second peak, correlating to the Hf-Hf distance is greatly diminished. This can be interpreted as an almost unchanged first coordination shell with missing long-range order.

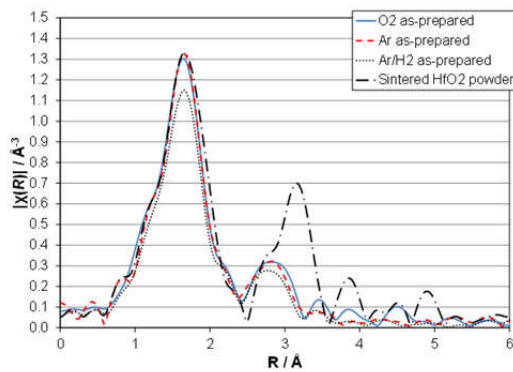


FIG. 1: FT EXAFS spectra of amorphous HfO_{2-x} films deposited in different gas atmospheres in the as-prepared state.

To determine the stoichiometry of the films, the first peaks (1.0-2.4 Å, R-space) of the FT EXAFS spectra were fitted with a structure model obtained from crystalline, monoclinic hafnium oxide (structural parameters taken from [6]). With this model, a total of seven oxygen atoms around the hafnium absorber atom are given. To obtain the coordination number the total occupancy of the seven scattering paths was fitted, while each individual path was given N/7 occupancy. If one assumes that Hf atoms in the amorphous film are sevenfold coordinated by oxygen, as in monoclinic HfO_2 , the stoichiometry can be calculated from the coordination number.

The crystallization kinetics of the films was investigated by in situ, time-resolved QEXAFS measurements. Fig. 2 shows the FT EXAFS spectra of an HfO_2 film deposited in O_2 during crystallization at 370 °C. Below this temperature, no crystallization could be observed within two hours. The second peak in the spectra intensifies over time, which is an indicator for increasing crystallinity, as the increased order in the second shell may be due to a more narrowly defined range of Hf-Hf distances in the crystallized state. The FT transformed EXAFS spectra for films deposited in Ar and Ar/H_2 were measured in the same way at 430 °C and 440 °C. Qualitatively, they exhibit the same behavior (not shown).

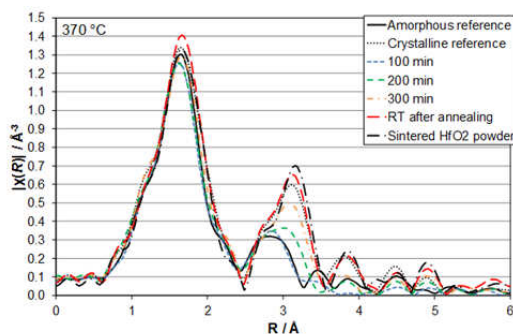


FIG. 2: In-situ FT EXAFS spectra of an HfO_2 film deposited in oxygen atmosphere during crystallization.

The FT EXAFS spectra were then fitted with a linear combination fit, where an amorphous and a crystalline EXAFS spectrum were used as references, to determine the crystalline phase

fraction α . Afterwards, α was plotted against time t and evaluated after the Avrami method [7] (see Fig. 3).

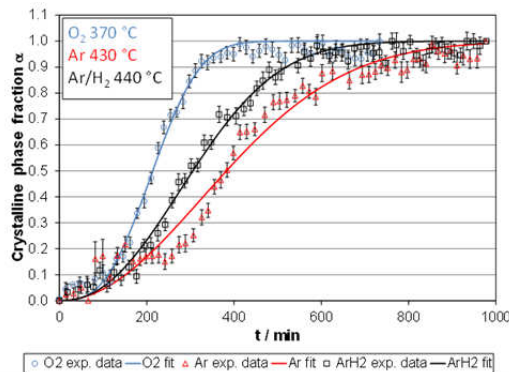


FIG. 3: Crystallization kinetics of HfO_{2-x} films deposited in different atmospheres obtained by a linear combination fit (symbols) and Avrami fits (solid lines).

In Table 2, the results of the Avrami fits are summarized.

Gas	O_2	Ar	Ar/ H_2
T / °C	370	430	440
n	2.89(13)	2.03(10)	2.26(7)
k / 10^{-3} min^{-1}	4.12(5)	2.18(4)	2.78(3)

TABLE 2: Avrami exponents n and rate constants k of HfO_{2-x} films deposited in different gas atmospheres at temperatures T , as obtained from the Avrami model $\alpha(t) = 1 - \exp(-(k \cdot t)^n)$.

In summary, our investigations show that amorphous, highly non-stoichiometric HfO_{2-x} films with x up to 0.25 can be prepared by PLD. The highly oxygen deficient films are stable up to temperatures of about 400 °C, which is important for resistive switching applications. The stoichiometric films are stable up to about 350 °C, which is of importance for gate dielectric applications.

This work was financially supported by the DFG within the priority program SPP 1415.

- [1] G.D. Wilk, R.M. Wallace, J.M. Anthony, J. Appl. Phys. 89, 5243 (2001).
- [2] M. Balog, M. Schieber, M. Michman, S. Patai, Thin Solid Films 41, 247 (1977).
- [3] J.G. Bendoraitis, R.E. Salomon, J. Phys. Chem. 69, 3666 (1965).
- [4] F.-C. Chiu, J. Appl. Phys. 100, 114102 (2006).
- [5] H.Y. Lee, Y.S. Chen, P.S. Chen, T.Y. Wu, F. Chen, C.C. Wang, P.J. Tzeng, M.J. Tsai, C. Lien, Electron Device Letters, IEEE 31, 44 (2010).
- [6] K.R. Whittle, G.R. Lumpkin, S.E. Ashbrook, J. Solid State Chem. 179, 512 (2006).
- [7] M. Avrami, J. Chem. Phys. 12, 1103 (1939), J. Chem. Phys. 8, 212 (1940), J. Chem. Phys. 9, 177 (1941).

Pulsed laser ablation of complex oxides: the role of congruent ablation and preferential scattering for the film stoichiometry

S. Wicklein¹, A. Sambri², S. Amoruso², X. Wang², R. Bruzzese², A. Koehl¹, and R. Dittmann¹

¹Peter Grünberg Institut-7, Forschungszentrum Jülich, Germany

²CNR-SPIN and Dipartimento di Scienze Fisiche, Complesso Universitario di Monte Sant'Angelo, Napoli, Italy

By combining structural and chemical thin film analysis with detailed plume diagnostics and modeling of the laser plume dynamics, we are able to elucidate the different physical mechanisms determining the stoichiometry of the complex oxides model material SrTiO₃ (STO) during pulsed laser deposition. Deviations between thin film and target stoichiometry are basically a result of two effects, namely, incongruent ablation and preferential scattering of lighter ablated species during their motion towards the substrate in the O₂ background gas. On the one hand, a progressive preferential ablation of the Ti species with increasing laser fluence leads to a regime of Ti-rich thin film growth at larger fluences. On the other hand, in the low laser fluence regime, a more effective scattering of the lighter Ti plume species results in Sr rich films.

Complex transition metal oxides exhibit a large variety of interesting physical properties comprising high temperature superconductivity, piezoelectricity, multiferroicity and redox-based resistive switching. Due to the strong impact of slight deviations from the ideal stoichiometry on the physical properties of oxide thin films and heterostructures, the understanding and precise control over the formation of vacancy defects is one of the key challenges for the oxide thin film growth community. Pulsed laser deposition (PLD) is the most widely spread method for the growth of complex oxides, since it has been generally assumed in the past that above a certain laser fluence threshold the target stoichiometry is properly transferred to the thin film. However, it has been demonstrated by several groups that the Sr/Ti ratio of homoepitaxially grown STO thin films strongly depends on the laser fluence, and that a stoichiometric transfer is only obtained for a certain laser fluence [1]. Nonetheless, the physical mechanisms underlying this phenomenon has not yet been clarified up to now.

In order to clarify the origin of this generally observed fluence dependence of the thin film composition for the model material STO, we

carried out systematic PLD growth conditions studies, where we combine the characterization of the STO plume with thin film chemical analysis via X-ray photoelectron emission spectroscopy (XPS).

Figure 1 shows the deviation of the c-axis from the STO bulk value, Δc , as a function of the laser fluence, F , for three different values of the target to substrate distance, D_{TS} , (40, 44 and 48 mm). As reported earlier [1], STO thin films exhibiting c-axis values of bulk STO can be regarded as stoichiometric, whereas thin films with expanded c-axis exhibit a significant non-stoichiometry. Figure 1 also exemplifies that at a given fluence, e.g. $F=1.5 \text{ J/cm}^2$, the films can be nearly stoichiometric ($D_{TS}=44\text{mm}$) but also extremely non-stoichiometric with a Ti-rich ($D_{TS}=40\text{mm}$) or a Sr-rich ($D_{TS}=48\text{mm}$) composition, depending on the target-to-substrate distance. This is an indication that time-of-flight effects have to be considered as origin of the observed non-stoichiometry.

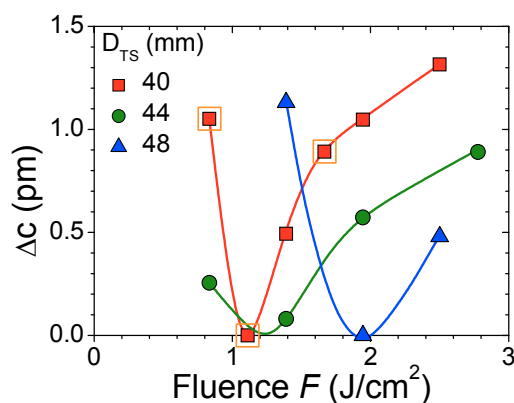


FIG. 1: c-axis expansion, Δc , of epitaxial STO thin films vs laser fluence, F , at three different target-to-substrate distances (D_{TS}) grown at a substrate temperature $T_S=720^\circ\text{C}$ in 0.2 mbar of oxygen background gas. The curves are visual guides. The orange squares mark the conditions for which XPS analyses of the thin films and of the corresponding ablation spots on the target were carried out.

XPS analysis of the STO thin films and of the corresponding ablation spots on the STO target were carried out for three experimental conditions

marked by squares in figure 1, corresponding to $D_{TS}=40$ mm and laser fluencies of 0.8, 1.1 and 1.7 J/cm². STO thin films which show no c-axis expansion have a Sr/Ti ratio of ~ 1 . Films exhibiting a c-axis expansion reveal a Sr/Ti ratio $\neq 1$. In particular, films grown at low laser fluence show a Sr-rich composition, while those grown at high laser fluence, exhibits a Sr/Ti ratio < 1 , i.e. a Ti-rich composition. Moreover, XPS analysis of the ablation spots revealed that the Sr/Ti ratio on the STO target increases with increasing laser fluence. This indicates a preferential ablation of Ti species from the target for higher laser fluencies leaving behind a Sr-rich STO surface. This unidirectional trend of the Sr/Ti ratio on the target, however, does not explain the observed variation of the film stoichiometry with the target-to-substrate distance, at a fixed fluence (see Fig. 1), and the increase of the Sr/Ti ratio of the thin films deposited at 0.8 J/cm².

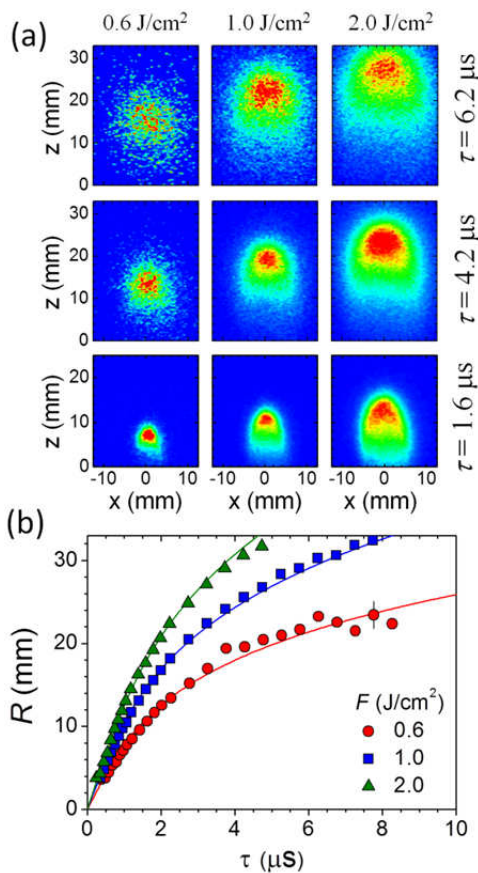


FIG. 2: (a) 2D images of the STO plume emission for three different values of the laser fluence, F , at three delays, τ , after the laser pulse. (b) Position-time R - τ plots of the plume front for the three different values of the laser fluence of Fig. 1(a). The solid lines are fits according to the expansion mode [2].

In order to further assess these issues, an analysis of the STO plume dynamics and composition was carried out, by using time-resolved optical spectroscopy of the expanding plume [1]. Fig. 2(a) reports single-shot images of the STO plume emission collected by an intensified-charge-coupled device (ICCD), at three different fluences, and for three succeeding temporal delays, τ , after

the laser pulse. In Fig. 2(a), each image is normalized to its own maximum intensity, to facilitate the comparison. From sequences of images such as those in Fig. 2(a), the temporal evolution of the plume front position, R , was obtained, and shown in Fig. 2(b). The solid curves in Fig. 2(b) are fits according to the plume propagation model. By reducing the fluence, the initial driving energy of the STO plume decreases, and the braking effect of the background gas correspondingly increases. Therefore, the plume is significantly braked, eventually stopping before reaching the substrate. In such a regime, the diffusion-like flow of the plume species towards the substrate can be significantly non-stoichiometric as a consequence of the collisional processes between ablated species and background gas molecules and the preferential scattering of the lighter Ti plume species. This explains the larger content of Sr observed in the STO thin films deposited at lower fluences, even if the nascent plume is stoichiometric.

On the contrary, an increase of the laser fluence progressively reduces the background gas confinement, and the plume impacts on the substrate at earlier times (see Fig. 2). In such a condition, the plume composition is closer to that of the nascent plume observed at short distance from the target surface, i.e., a Ti-rich plume. At any fixed target-to-substrate distance, the intricate interplay between the progressive variation of the plume composition, due to the incongruent ablation of the STO target, and the transition from an halted to a progressively more free plume propagation, allows passing from Sr-rich to Ti-rich STO films, going from low to high fluence, with a stoichiometric deposition occurring at an intermediate fluence, as observed in Fig. 1.

In the case of incongruent target ablation of complex oxides, as for STO, the results discussed above also indicate that, at a fixed oxygen background gas pressure, it is possible to compensate for a larger content of the lighter species in the nascent ablation plume (e.g. Ti in STO) by appropriately selecting the target-to-substrate distance. Another approach could be to use an ablation target with an enriched content of the lighter species. Our findings are of general importance for the growth of complex oxides containing elements with significant difference in atomic weight, and they open up the way for a more defined control of the deposited thin film stoichiometry.

This work was financially supported by the SFB 917 "Nanoswitches"

- [1] D.J. Keeble, S. Wicklein, R. Dittmann, L. Ravelli, R.A. Mackie, and W. Egger, PRL 105, 226102 (2010)
- [2] S. Wicklein, A. Sambri, S. Amoroso, X. Wang, R. Bruzzese, A. Koehl, and R. Dittmann, APL 101, 131601 (2012)

Heavily Donor-Doped Optically Translucent BaTiO₃-Ceramics through Defect Chemical Engineering

C. Pithan¹, H. Katsu², R. Waser¹, G. Roth³, and H. Takagi²

¹ Peter Grünberg Institut-7, Forschungszentrum Jülich, Germany

² Murata Manufacturing Corporation Limited, Kyoto, Japan

³ Institute of Crystallography, RWTH Aachen University, Germany

Ferroelectric, translucent and heavily donor-doped BaTiO₃-ceramics with TiO₂-excess were prepared by the conventional solid state route, processed by subsequent sintering and annealing at high partial pressures of oxygen. The resulting ceramics possess very high densities and a remarkably fine-grained microstructure. Under oxidizing conditions large amounts of the donor – in this case La – can be incorporated into the perovskite lattice during sintering. Electrons released from these donors are captured most probably by vacancies of titanium, acting as acceptors. The optical properties are largely determined by the defect chemistry and in particular by the concentration of free conducting electrons. Reducing the number of free electrons is thought to be the origin for the high degree of optical translucency. Normalized values of the optical transmittance reach or even exceed the best values reported so far for nano-crystalline chemically derived barium titanate thick films or ceramics, that partly have to be consolidated by pressure assisted techniques. In contrast to these examples reported in the literature, however, the electro-optical materials presented in here are fabricated by conventional ceramic technological methods and by exploiting the chemical principles of lattice disorder.

Electronic ceramics based on the ferroelectric perovskite type compound BaTiO₃ generally appear optically opaque, even though they have a rather large bandgap of approximately 3 eV. In the case of insulating acceptor-doped dielectric materials, as they are used in capacitor applications, BaTiO₃ appears light yellow in color. Donor-doped semiconducting ceramics containing a large number of electrons in the conduction band, on the other hand, have a dark blue color, because the high concentrations of free electrons absorb the low frequency range of the spectrum of the visible light. For the realization of translucent ceramics based on BaTiO₃ an ultrafine grained and highly dense microstructure with only little and extremely small residual pores represent unavoidable prerequisites to be met. In the past several attempts to reach this goal, including the use of nanocrystalline powders, deposited as thick films or consolidated to ultrafine grained and

dense ceramics using pressure assisted techniques have been reported [1 – 4] (Table 1). In the present report a different approach has been followed. The possibility of preparing heavily donor-doped translucent ferroelectric ceramics on BaTiO₃-basis exploiting the defect chemistry and the phenomenon of the so-called grain growth anomaly [5] has been examined on the basis of entirely conventional methods and tools of ceramic technology, avoiding any complicated or costly synthesis route for powder preparation and neglecting any consolidation technique other than natural and pressureless sintering. La-doped BaTiO₃ ceramics powders with a donor concentration of either 1, 1.5 or 2 mol.%, containing a TiO₂ excess of 0.5 mol.% were prepared by the usual solid state route. Compacts of these powders were then consolidated to translucent bulk ceramic pellets through sintering for 2 hours at 1350 °C under pure oxygen. Eventually an additional heat treatment for 30 hours at 1000 °C equally in pure oxygen followed. Fig. 1 shows a representative example of the materials microstructure obtained.

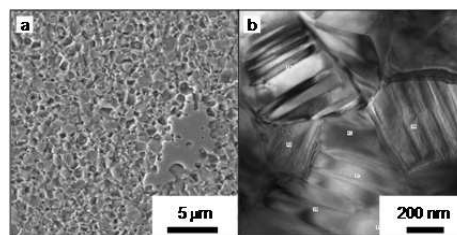


FIG. 1 Microstructure of $(\text{Ba}_{0.99}\text{La}_{0.01})\text{Ti}_{1.005}\text{O}_3$ sintered in pure oxygen at 1350 °C: (a) SEM-micrograph of a mechanochemically polished surface showing a fine grained dense matrix of barium titanate with a few large inclusions of the secondary Ti-rich phase $\text{Ba}_6\text{Ti}_{17}\text{O}_{40}$. (b) Corresponding TEM-micrograph. The average grain-size amounts to a few hundreds of nm only.

Characterization by XRD in combination with Rietveld refinements suggest that the donor added is largely dissolved in the crystal lattice of barium titanate under these preparation conditions and results in a considerable decrease of the tetragonal distortion of the unit cell expressed by the ratio of the lattice parameter c and a , c/a , down to approximately 1.0045 at a maximum La-concentration of 2 mol.%. Recording the temperature dependence of the dielectric

permittivity revealed in a depression of the Curie-temperature by around 50 K compared to pure barium titanate in the case of the highest La-content of 2 mol.%. Fig. 2 illustrates the optical properties of a ceramic containing such a high level of donor-doping. Defect chemically the incorporation of these high concentrations of La into the perovskite lattice and the expulsion of Ti resulting in the formation of Ti-vacancies can be expressed as follows:

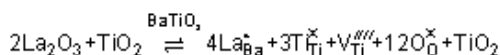


FIG. 2 Translucent 0.78 mm thick BaTiO_3 ceramic pellet containing 2 mol.% of La-addition after sintering for 2 hours at 1350 °C and subsequent annealing for 30 hours at 1000 °C in pure oxygen. The nominal composition is $(\text{Ba}_{0.99}\text{La}_{0.02})\text{Ti}_{1.005}\text{O}_3$. The white bar in the right bottom corner of this image indicates 10 mm in length.

At an optical wavelength of 800 nm the normalized transmittance of the sample shown in figure 2 is as high as 21 %. Fig. 3 shows a comparison of as sintered ceramics with different La-contents for the whole electromagnetic spectrum up to 1300 nm.

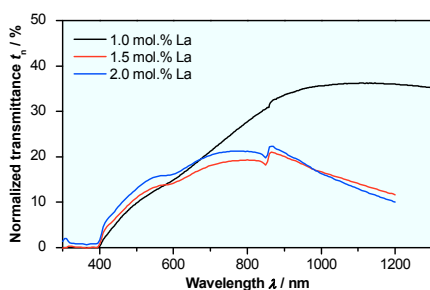


FIG. 3 Normalized optical transmittance t_n in dependence of the optical wavelength λ for BaTiO_3 in the as sintered condition containing 1 to 2 mol.% La as donor.

The best transmittance values are obtained for 1.0 mol.% of La-doping. Further improvement can be achieved if samples with a high La-content above 1 mol.% are additionally annealed in pure oxygen at 1000 °C for 30 hours. Impedance spectroscopic characterization then reveals that this heat treatment at high partial pressures of oxygen significantly increases resistivity obviously through the formation of additional metal vacancies $\text{V}_{\text{Ti}}^{\text{eff}}$, which trap free electrons. At an optical wavelength of 800 nm normalized values as high as 38 % could be realized. The presence of ferroelectric domains in the microstructure (fig. 1), reduced values of the tetragonality ratio c/a as well as

measurements of the ferroelectric hysteresis and of the temperature dependence of the dielectric constant (Curie – Weiss behavior) clearly demonstrated the polar character of the translucent ceramics. The determination of the real and imaginary part of the refractive index after poling at a maximal field strength of 1.26 kV/mm and after subsequent thermal depolarization (annealing above the Curie-temperature) proved that the refractive index of the optically translucent ceramics can be switched by an electrical field, refer to fig. 4.

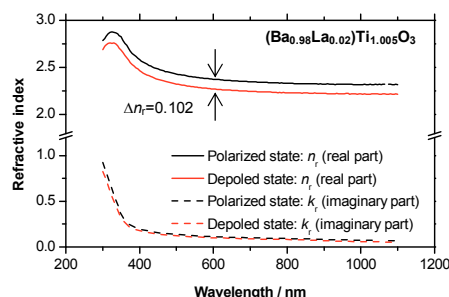


FIG. 4 Wavelength dependence of the refractive index of translucent $(\text{Ba}_{0.99}\text{La}_{0.02})\text{Ti}_{1.005}\text{O}_3$ in the poled und unpoled condition.

A rigorous analysis of the wavelength dependence of the refractive indices in the polarized and depolarized condition showed that the optical refraction can be reasonably explained in the framework of the theory of a single oscillator model [6].

Morphology	Powder / Process	d [mm]	t [%]	t_n [%]	Ref.
Thick films	Sol-Gel / Sintering	0.34	16	0.5	[1]
		0.20	32	0.3	[2]
Ceramics	Oxalate / Hot pressing	1.07	22	24	[3]
	Commercial / SPS	0.87	32	27	[4]
	Solid state / Sintering in O_2	0.76	38	28	*

Table 1 Materials parameters regarding the measurements of the optical transmittance in relation to processing conditions for the present work (marked with *) in comparison to results from literature.^{[1]-[4]} The optical transmittance t , and the values t_n normalized with respect to the sample thickness d correspond to the ones determined at an optical wavelength $\lambda=800$ nm.

- [1] H. Shimaoka, S. Kohiki, T. Kobayashi, M. Kuwabara, J. Mater. Chem. 10, 1511 (2000).
- [2] J.-H. Cho, W.-Y. Choi, S.-H. Kim, M. Kuwabara, Integrated Ferroelectrics 69, 287 (2005).
- [3] H. Yamamura, H. Haneda, A. Watanabe, S. Shirasaki, Jap. J. Appl. Phys. 24, Suppl. 24-2, 433 (1985).
- [4] J. Liu, Z. Shen, W. Yao, Y. Zhao, A. K. Mukherjee, Nanotechnology 21, 075706 (2010).
- [5] G. H. Jonker, Solid-State Electron. 7, 895 (1964).
- [6] M. DiDomenico Jr., S. H. Wempel, J. Appl. Phys. 40, 720 (1969).

Structural Characterization of Resistively Switching Thin SrTiO_3 Films by Grazing Incidence Small Angle X-ray Scattering

O. Faley¹, S. Stille¹, R. Dittmann², J. Perlich³, S.V. Roth³, R. Waser^{2,4}, and U. Klemradt¹

¹ II. Physikalisches Inst. B, RWTH Aachen University, Germany

² Peter Grünberg Institute-5, Forschungszentrum Jülich, Germany

³ HASYLAB at DESY, Hamburg, Germany

⁴ Institute of Materials in Electrical Engineering 2, RWTH Aachen University, Germany

We investigated the grazing incidence small angle X-ray scattering (GISAXS) signature in metal-insulator-metal (MIM) memory cells with predicted conductive filaments that originate from migration of oxygen vacancies. Various electrode materials such as Pt, Ti and Al have been investigated with respect to their suitability for resistive switching, as well as their suitability for X-ray scattering methods. Measurements on samples with Ti electrodes show a clear signature of structures in the insulating layer. First 2D simulations indicate a tapered form of the filamentary structures.

The understanding of the material properties is essential for the development of the next memory generation for information technology. Resistively switching oxides is a promising candidate for their change of the electrical resistance due to the change of valences in the contained cations [1]. This effect can be observed in many transition metal oxides like titanates [2], manganates [3, 4] and zirconates [5]. In SrTiO_3 , bipolar resistive switching was first observed around 12 years ago [2]. In our studies we use iron doped SrTiO_3 (Fe:STO) as the resistively switching material. Since SrTiO_3 is well understood with respect to its structural and electronic properties, it provides a useful model system to obtain further insight into the physical mechanisms of resistive switching due to valence changes. The change in resistance originates from n-doping by introduction of oxygen vacancies. The switching is caused by voltage applied to the electrodes leading to a local electrochemical redox reaction and is accompanied by a massive migration of ions and anion vacancies along extended defects thus forming conductive filaments [6]. A subsequent change of the stoichiometry and a valence change of the cation sublattice lead to a resistance change at the electrode interface. Usually a first irreversible forming step is needed to form the filamentary structures [7, 8], however if reactive electrode materials are used no forming step may be necessary [9-11]. The detailed switching mechanisms are the subject of intense current

research efforts [16]. However, the exact nature and the atomic and electronic structure of the conductive paths have not been clarified up to now. Grazing incidence small angle X-ray scattering (GISAXS) provides a suitable technique to resolve structures buried below the surface without destroying the sample. In essence, filaments in valence-change materials exhibit an electron density contrast of about 10-20 % with respect to the surrounding matrix and can thus be detected by small angle X-ray scattering. However, other scattering contributions (interfacial roughness, electrodes with heavy scatterers) easily mask the signal unless specific measures are taken. Recent experimental progress was achieved by Stille et al. using Ti top electrodes for GISAXS experiments and numerical simulations to assess filament diameters and distances in Fe:STO films [12].

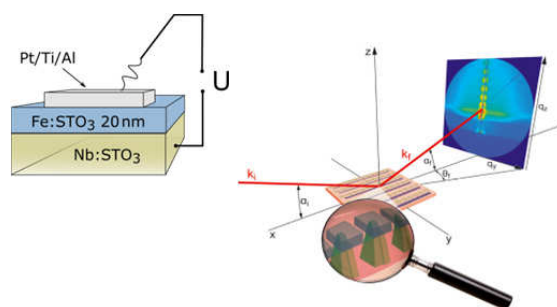


FIG. 1: (a) Sketch of the sample geometry. (b) Sketch of the geometry for GISAXS measurements. The electrodes have been arranged in arrays due to the large x-ray footprint under the small incidence angle of 0.7° . The magnification glass shows an artist's view of the conducting filaments under the electrode pads [12].

Memory cells in metal-insulator-metal (MIM) geometry have been studied by GISAXS at HASYLAB beamlines BW4 and P03. The sample geometry is sketched in Fig. 1(a). The metallic conductive Nb-doped SrTiO_3 (Nb:STO) substrate is used as the bottom electrode. The 20 nm thick active layer, consisting of Fe:STO has been deposited by pulsed laser deposition. Pt, Ti and Al were used for the top electrodes so far with the efforts going into optimizing the use of light

materials like Ti and Al owing to their small scattering cross section for X-rays. The reactivity of Ti gives rise to forming-free memory devices, thus removing the necessity of a preceding forming step. The memory cells have been laterally patterned by optical lithography into long arrays of electrodes for the optimal coverage by the long footprint of the X-ray beam under the used grazing angle of 0.7° as shown in Fig. 1(b) [12].

Fig. 2(a) shows experimental results for the sample with 10 nm thick Ti electrodes. The oscillations in q_z directions correspond to c.a. 22 nm high structures which is in accordance with the thickness of the active Fe:STO layer. The lateral maxima show an offset by half a period in relation to central peaks. First 2D simulations as shown in Fig. 2(b) based on experimental data indicate that this GISAXS signature can only be caused by tapered structures as opposed to strictly vertical cylindrical structures as previously assumed.

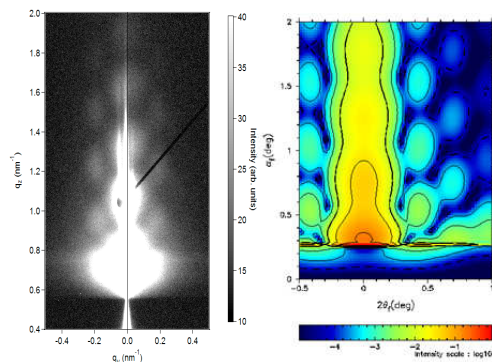


Fig. 2: (a) GISAXS pattern for a 5 nm Ti / 20 nm Fe:STO / Nb:STO with filamentary structures [12]. (b) 2D simulation with lsGISAXS [15] based on cone-like form-factor shows the half a period shift of the lateral maxima as seen in the measured data in (a).

Further simulations were done using FitGISAXS [13] to investigate the lateral scattering by the layer interfaces and their contribution to the background in our measurements. Simulations show that the background dominates over the filamentary signature in samples with Pt electrodes, while the filamentary signature is dominant in samples with Ti electrodes. In samples with Al electrodes the lower absorption of Al compared to Ti leads to a higher intensity of the filamentary signal, however the high roughness of Al also leads to a higher background scattering [14].

In conclusion, it can be stated that GISAXS is a useful characterization technique to gain novel insights into resistive switching in thin film devices. The GISAXS signature shows that electroforming results in the formation of filaments rather than a homogeneous modified material beneath the electrode and allows insight into the shape of the filaments. Information on the mean lateral size and distance of filamentary structures, not only at the surface but also inside the whole thin film, could be obtained. Therefore, GISAXS experiments are a powerful tool to provide essential contributions to the assessment of the ultimate scaling limits of future RRAM devices.

The presented research is a part of the efforts of the Collaborative Research Group (SFB 917) on the topic of "Resistively Switching Chalcogenides for Future Electronics – Structure, Kinetics and Device Scalability" [16].

- [1] R. Waser, R. Dittmann, G. Staikov, and K. Szot, *Adv. Mater.* **21**, 2635 (2009).
- [2] Y. Watanabe, J. Bednorz, A. Bietsch, C. Gerber et al., *Appl. Phys. Lett.* **78**, 3738 (2001).
- [3] H. Oshima, K. Miyano, Y. Konishi, M. Kawasaki, and Y. Tokura, *Appl. Phys. Lett.* **75**, 1473 (1999).
- [4] A. Asamitsu, Y. Tomioka, H. Kuwahara, and Y. Tokura, *Nature* **388**, 50 (1997).
- [5] A. Beck, J. Bednorz, C. Gerber, C. Rossel, and D. Widmer, *Appl. Phys. Lett.* **77**, 139 (2000).
- [6] K. Szot, W. Speier, G. Bihlmayer, and R. Waser, *Nature Mater.* **5**, 312 (2006).
- [7] T. Menke, R. Dittmann, P. Meuffels, K. Szot, and R. Waser, *J. Appl. Phys.* **106**, 114507 (2009).
- [8] R. Muenstermann, T. Menke, R. Dittmann, S. Mi, C.-L. Jia et al., *J. Appl. Phys.* **108**, 124504 (2010).
- [9] Y.S. Chen, H.Y. Lee, P.S. Chen, T.Y. Wu et al., *IEEE Electron Device Lett.* **31**, 1473 (2010).
- [10] C. Hermes, R. Bruchhaus, and R. Waser, *IEEE Electron Device Lett.* **32**, 1588 (2011).
- [11] W. Wang, S. Fujita, and S. Wong, *IEEE Electron Device Lett.* **30**, 763 (2009).
- [12] S. Stille, Ch. Lenser, R. Dittmann, A. Koehl, I. Krug, R. Muenstermann, J. Perlich, C. M. Schneider, U. Klemradt, R. Waser, *Appl. Phys. Lett.* **100**, 223503 (2012).
- [13] D. Babonneau, *J. Appl. Crystallogr.* **43**, 929 (2010).
- [14] S. Stille, C. Baeumer, S. Krannich, C. Lenser, R. Dittmann, J. Perlich, S. V. Roth, R. Waser, U. Klemradt *J. Appl. Phys.* **113**, 064509 (2013).
- [15] R. Lazzari, *J. Appl. Cryst.* **35**, 406-421 (2002)
- [16] Further information on the homepage of SFB 917: <http://www.sfb917.rwth-aachen.de>.

Chemical insights into electroforming of resistive switching manganate heterostructures

C. Park¹, F. Borgatti², A. Herpers¹, F. Offi³, Y. Yamashita⁴, A. Yang⁴, M. Kobata⁴, K. Kobayashi⁴, G. Panaccione⁵, and R. Dittmann¹

¹ Peter Grünberg Institut-7, Forschungszentrum Jülich, Germany

² CNR-SPIN CNR – Istituto per lo Studio dei Materiali Nanostrutturati (ISMN), Bologna, Italy

³ CNISM and Dipartimento di Fisica, Università Roma Tre, Rome, Italy

⁴ NIMS beamline Station at Spring-8, National Institute for Materials Science, Hyogo, Japan

⁵ Istituto Officina dei Materiali (IOM)-CNR, Laboratorio TASC, Trieste, Italy

We have investigated the chemical changes induced during electroforming of resistive switching Pt/Ti/Pr_{0.5}Ca_{0.5}MnO₃ (PCMO) /SrRuO₃ devices by hard X-ray photoelectron spectroscopy (HAXPES). We could demonstrate that the higher resistance state induced by electroforming of as-prepared devices is strictly correlated to the oxidation of the top electrode Ti layer through field-induced electromigration of oxygen ions. Conversely, the PCMO exhibits oxygen depletion and downward change of the chemical potential for both resistive states. In combination with impedance spectroscopy measurements we could conclude, that the main contributions to the resistance in the initial state and the electroformed states are the reduced PCMO at the Ti electrode and the anisotropic n-p junction between the TiO_{2-x} and PCMO, respectively.

Besides a large variety of binary oxides, complex transition metal oxides, e.g. manganites titanates and zirconates, exhibit different resistance states at opposite polarities of electrical stimulation and could thereby be employed as resistance random access memory (RRAM) [1]. It has become widely accepted that this resistive switching in oxides is in most cases connected with a voltage-driven redox process. However, the current knowledge of the microscopic details of this redox-processes is very limited. Ti/PCMO devices are very interesting from the circuit design point of view because, in contrast to most other resistive switching oxides, it was demonstrated that the high and low resistive state currents scale with the electrode area [1]. As a result of the use of non-noble metal Ti, an interface oxide layer is formed which in principle could also be directly involved in the switching effect. Therefore, a key question for this multilayer system is, which sublayers perform a valence change during electroforming and switching and how these chemical changes influence the electronic transport in the manganite heterostructures.

In this work we have studied the influence of electroforming on the electronic structure of the Ti/

PCMO interface region by performing HAXPES measurements at the NIMS beamline at spring-8, which allows for the nondestructive study of buried interfaces.

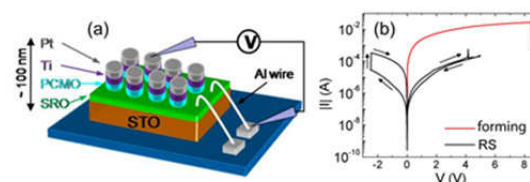


FIG. 1: (a) Schematic of the sample. For the HAXPES experiments a Pt layer thickness of 4 nm and a Ti thickness of 7 nm and 10 nm are used; (b) The forming and the subsequent strong asymmetric switching hysteresis.

The stack sequence of the Pt/Ti/PCMO/SrRuO₃ switching cells is sketched in Fig. 1(a). For this system a so called electroforming process occurs when a positive threshold voltage of the order of 8-10 V is applied to the as-prepared system, (red curve in Fig. 1(b)) leading to a raise of the resistance up to about one order of magnitude. After forming, the I-V curves exhibit a reversible hysteresis which is more pronounced in the negative branch (Fig. 1(b)). The core-level spectra for all the elements of interest of Pt/Ti/PCMO/SrRuO₃ devices in the initial resistive state (IRS) and the high resistive electroformed (HRS) states are summarized in Fig. 2. Details about the performed measurements are described in Ref. [2]. The core levels spectra of all PCMO elements (figure 2 (b)-(e)) exhibit binding energy (BE) shifts with respect to the reference spectra of the bare materials. The core level shifts towards higher BE for Pr 3d, Ca 2p and towards lower BE for Mn 2p are identical for both resistive states, indicating that the main changes in the PCMO occur during the deposition of the Ti top electrode rather than during the electrical treatment. The lowering of the PCMO chemical potential at the Ti/PCMO boundary is the fingerprint of oxygen depletion inside the PCMO raising up the PCMO resistivity. The different sign of the Mn 2p BE shift results from the progressive change of the Mn⁴⁺ species to lower valence states (Mn³⁺) due to the

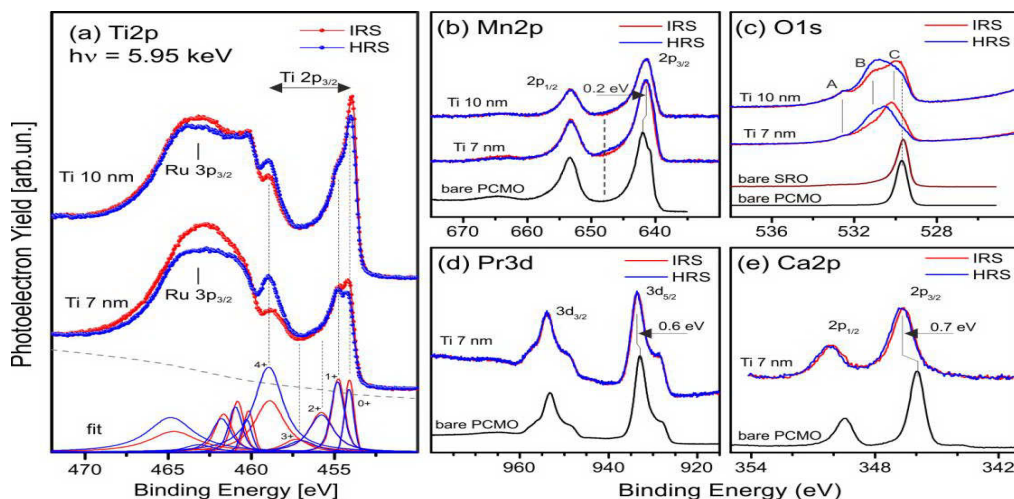


FIG. 2: (a) Ti2p and (b-e) PCMO-related core-level spectra of the IRS (red) and HRS (blue) samples and the bare PCMO (black) and SRO (brown). Photon energy was about 5.95 keV. The fit results for the Ti layer of 7 nm is shown at bottom of panel (a) for both IRS (red) and HRS (blue) spectra. [2]

release of surrounding oxygen atoms. The shape of the Mn2p, Ca2p and Pr3d spectra do not show strong spectral features indicative of chemical interaction.

The Ti 2p_{3/2} component exhibits two distinct features at 454 eV and 459 eV which, on the basis of the binding energy values in the literature, are associated to Ti⁰ (metallic) and Ti⁴⁺ ion valence states, respectively. The detailed fit analysis performed for the Ti2p spectra, reported in Fig. 2(a) for the Ti layer of 7 nm show that all of them include intermediate valence terms and that the strength of the Ti⁰ component is always less than 15% of the overall Ti 2p photoelectron yield, confirming that even for the as-prepared IRS systems there is a large chemical interaction with the underlying PCMO. We notice that the Ti⁴⁺ spectral term for the IRS case cannot be exclusively related to formation of TiO₂ but could be partially ascribed to Ti⁴⁺ ions distributed within the PCMO-Ti mixed region, with the formation of Ca doped TiO_{2-x} compounds (see ref. [2]), thereby contributing to the degradation of the system metallicity. After the forming to the HRS state the Ti⁰/Ti⁴⁺ peak intensity ratio is reduced from 0.32 (0.56) to 0.17 (0.42) for the Ti layer of 7 (10) nm, while the strength of the intermediate valence states is reduced just by 2-6%, showing that formation of TiO₂ through the diffusion of oxygen ions in the Ti layer plays a crucial role for the change of the resistivity.

In order to further assign the observed chemical changes during electroforming in this device system to the resistance change, impedance measurements of both resistive states have been performed. Both Cole-Cole plots of the impedance for IRS and HRS states contain two semi-circles which have been fitted by two parallel Resistance (R)-Capacitance (C) components in series. For the IRS sample, we attribute these R-C circuits to the

Ca-doped TiO_x interface layer observed by EELS analysis [2] and to the oxygen-deficient PCMO layer which is naturally formed during the deposition of the Ti top electrode. The electroforming process increases both resistance contributions by one order of magnitude. Our simulations suggest that the entire reduced PCMO interface in the HRS could belong to the p-type depletion layer. Therefore the two parallel R-C circuits of the impedance spectra in the HRS case can be associated with the two depletion layers on the two sides of the anisotropic n-p junction. The corresponding band diagrams in IRS and HRS are depicted in figure 3.

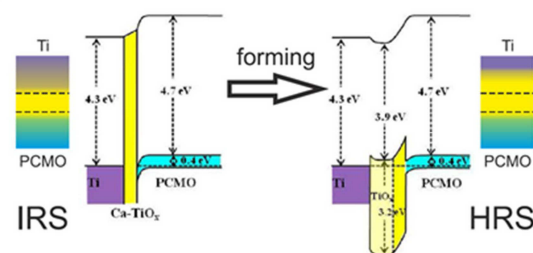


FIG. 3: (a) Suggested change of the energy bands after electroforming

Based on the comparison between the chemical analysis and our impedance spectroscopy data, we could extract the reduced PCMO interface layer to be the dominant resistance contribution in the IRS and the pn junction between the TiO_{2-x} and the PCMO the dominating resistance contribution in the HRS.

This work was funded by the European Union Council under the 7th Framework Program (FP7) grant nr. 246102 IFOX.

- [1] A. Sawa, Mater. Today, 11, 28 (2008)
- [2] F. Borgatti, C. Park, A. Herpers, F. Offi, R. Egoavil, Y. Yamashita, A. Yang, M. Kobata, K. Kobayashi, J. Verbeeck, G. Panaccione and R. Dittmann, Nanoscale 5 (9): 3954-60 (2013).

Simulation of Multilevel Switching in Electrochemical Memory Cells

S.Menzel¹, U. Böttger², and R. Waser^{1,2}

¹ Peter Grünberg Institut-7, Forschungszentrum Jülich, Germany

² Institut für Werkstoffe der Elektrotechnik 2, RWTH Aachen University, Germany

A simulation model for bipolar resistive switching in electrochemical metallization memory cells is presented. The model is based on an electrochemical driven growth and dissolution of a metallic filament. The origin of the multilevel switching is proposed to be a direct tunnelling between the growing filament and the counter electrode. The model fully reproduces the experimental data and allows for an explanation of the transition from bipolar to unipolar switching.

Electrochemical metallization memory (ECM) cells as a variant of redox-based random access memories (ReRAM) are a promising candidate for next generation non-volatile, high speed and highly scalable memory cells [1,2]. The switching is attributed to the electrochemical growth and dissolution of a Cu or Ag nano-sized filament. Typically, ECM cells consist of a Cu or Ag active electrode, an ion conducting switching layer (SL) and an inert electrode. During the SET process a positive potential is applied to the active electrode which is oxidized. Ag or Cu cations are created at the active electrode and migrate through the switching layer. At the inert cathode, the cations are reduced and a metallic filament grows towards the anode resulting in a low resistive state (LRS). To RESET the device to a high resistive state (HRS), the voltage polarity is reversed and the filament dissolves. Based on this switching mechanism we developed a dynamic simulation model for multilevel switching in ECM cells [3]. The origin of multilevel switching is proposed to be direct tunneling between the growing filament and the active electrode. It is shown that the different low resistive states (LRS) are achieved by modulation of the corresponding tunneling gap. The nonlinear switching kinetics is modeled by the electron transfer reaction, which occurs at the electrode/ insulator interfaces.

Fig. 1 shows a schematic of the simulation model. The metallic cylindrical filament growth from the inert bottom electrode through the SL and modulates the tunneling gap x . Within the SL ionic and electronic tunneling currents are present. The ionic current path is modeled by two voltage controlled current sources (η_{ac} , η_{fil}), which represent the electron-transfer reactions at the boundaries (see explanation below), and the resistance due to ionic drift $R_{ion}(x)$. The electronic current path is attributed to electronic tunneling,

represented by one voltage controlled current source V_{Tu} . The LRS is reached as the tunneling gap is small enough to enable significant tunneling current.

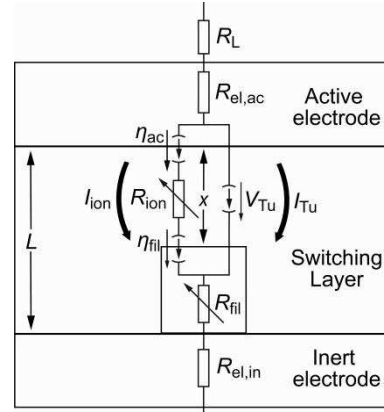


FIG. 1: Schematic of the switching model with equivalent circuit diagram. The switching layer of thickness L is sandwiched between the active top electrode and the inert bottom electrode. A cylindrical filament growth within the SL and modulates the tunneling gap x between filament and active electrode. The elements of the equivalent circuit are an optional load resistor R_L , the electrode resistors $R_{el,ac}$ and $R_{el,in}$ and the filament resistor $R_{fil}(x)$. (Redrawn from [3])

The filament growth/dissolution and thus the change of x can be described using Faradays law

$$\frac{\partial x}{\partial t} = - \frac{M_{Me}}{ze\rho_{m,Me}} J_{Me^{z+}}$$

Here, $J_{Me^{z+}}$ is the ionic current, z the charge transfer number, M_{Me} the atomic mass and $\rho_{m,Me}$ the mass density of deposited metal. The redox reactions at the electrodes involve an electron transfer reaction. The resulting current density due to this charge transfer is described by the Butler-Volmer equation and defines the ionic current

$$J_{Me^{z+}} = j_0 \left\{ \exp\left(\frac{(1-\alpha)ez}{kT}\eta\right) - \exp\left(-\frac{\alpha ez}{kT}\eta\right) \right\}$$

Here j_0 is the exchange current density, α the charge transfer coefficient and η the overpotential. The tunneling current I_{Tu} can be calculated according to Simmons as

$$I_{Tu} = \frac{eA_{fil}}{2\pi\hbar x^2} \left(\varphi_0 - \frac{eV_{Tu}}{2} \right) \exp \left(-K_x \sqrt{\varphi_0 - \frac{eV_{Tu}}{2}} \right) - \frac{eA_{fil}}{2\pi\hbar x^2} \left(\varphi_0 + \frac{eV_{Tu}}{2} \right) \exp \left(-K_x \sqrt{\varphi_0 + \frac{eV_{Tu}}{2}} \right)$$

where $K = 4p/\hbar \sqrt{2m_{eff}}$. Due to the exponential dependence of I_{Tu} on x , the LRS is very sensitive to small variations in x . For small voltages V_{Tu} the tunnel junction shows an ohmic behavior, which is consistent with the experimentally observed characteristic of LRS in ECM cells. Using Kirchhoffs laws, an implicit equation for the filamentary overpotential can be obtained and the equation system can be solved.

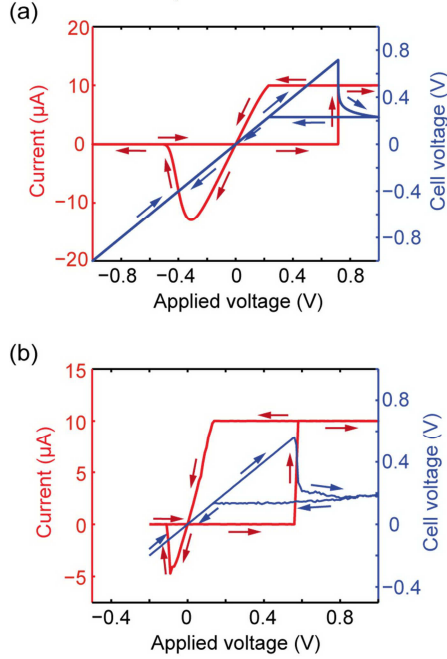


FIG. 2: (a) Simulated I - V curve (red) and corresponding relation between V_{cell} and $V_{applied}$ (blue). (b) Experimental I - V characteristic for a $Cu/SiO_2/Pt$ cell. (Redrawn from [3]).

As a model system for the simulations, a cylindrical $Cu/SL/Pt$ structure is used. Both electrodes have a thickness of 20 nm and a 100 nm radius, which leads to an electrode resistance $R_{el} = 76$ m Ω . R_L is zero in all simulations. The SL thickness is $L = 20$ nm. Due to numerical simplicity we set $A_{ion} = A_{ac} = A_{fil} = \pi r_{fil}^2$. Further parameters are $z = 2$, $\rho_{m,Cu} = 8.95$ g/cm³, $M_{Cu} = 1.06 \cdot 10^{-22}$ g and $T = 300$ K. As reference material in the simulations we choose SiO_2 and thus $\varphi_{0Cu/SiO_2} = 4.2$ eV and $m_{r,SiO_2} = 0.86$. The remaining reference values are $\rho_{ion} = 10^{-2}$ Ωm , $j_0 = 10^{-2}$ A/m² and $r_{fil} = 2$ nm. Fig. 2(a) shows the simulated I - V characteristic (red solid line) using a current compliance of 10 μA . The ECM cell is initially in HRS. As excitation a triangular voltage with 1V amplitude and 1s rise time is used in all simulations. During SET operation the actual cell voltage is not equal to the applied voltage (cf. blue curve in Fig. 2(a)). As soon as the set I_{SET} is

reached, V_{cell} first drops abruptly. Afterwards it decreases gradually during the current control. The simulation results are in good agreement to experimental data shown in Fig. 2(b).

In order to study the multilevel programming, we performed simulations with varying set current I_{SET} . The simulated LRS values are shown in Fig. 3(a) along with experimental data. Evidently, the proposed tunneling model is capable of explaining multilevel switching over the full range of SET currents. The remaining gap x_{min} is proportional to $\log(I_{SET}) = -1$ and changes from 1.10 nm at 1 pA to 0.13 nm at 398 μA . At higher SET currents the gap is closed completely resulting in a metallic contact. Also for the relation between RESET and SET current experimental data and simulation data are consistent (cf. Fig. 3(b)).

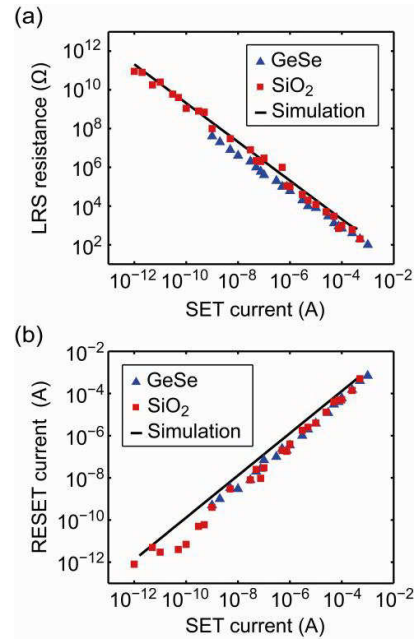


FIG. 3 (a) LRS resistance vs. SET current and (b) corresponding RESET current vs. SET current. The simulation results for (a) and (b) are depicted as black solid lines. Experimental data is displayed as blue triangles for a $Ag:GeSe$ system [4] and as red squares for a $Cu:SiO_2$ system.[4] The filament radius is $r_{fil} = 8$ nm. (Redrawn from [3])

In conclusion, we presented a physical simulation model for resistive switching in ECM cells. We proposed tunneling as the origin of multilevel switching rather than filament diameter variation, whereas the LRS level is controlled by I_{SET} . A metallic contact is still possible for a high I_{SET} . This allows for an explanation of the transition from bipolar to nonpolar switching.

- [1] R. Waser, M. Aono, Nat. Mater., 6 (2007) 833.
- [2] I. Valov, R. Waser, J. R. Jameson, M. N. Kozicki, Nanotechnology, 22 (2011) 254003/1.
- [3] S. Menzel, U. Böttger, R. Waser, J. Appl. Phys., 111 (2012) 014501.
- [4] C. Schindler, PhD thesis, RWTH Aachen, 2009.

Area-Delay Metric Optimization for Hybrid RS/CMOS Memories based on Passive Nanoelectronic Crossbars

Q. Wang, A. Heitmann, T.G. Noll

Electrical Engineering and Computer Systems, RWTH Aachen University, Germany

An area-delay metric (AT) of hybrid resistive-switches/CMOS memory architectures with small storage capacity is discussed. The proposed memory circuit is modeled by a passive nanoelectronic crossbar comprising electrochemical metallization cells (ECM) as memory elements. Additionally, CMOS circuits are included at the periphery of the passive crossbar which provide appropriate voltage levels for robust write and read operations. For specific memory configurations as well as particular values for the low resistive state (LRS) or the ECM cells the driving capabilities of the peripheral circuits are optimized by consideration of the overall circuit area and the delay of the read operation. Additionally, boundary conditions were considered with respect for a maximum allowed read margin loss as well as a maximum allowed loss of the effective write voltage which is required to tune the state of the ECM cell. Since the dominating parasitic capacitances determining the read speed are a function of the transistors' driving capabilities (and hence of the circuit area), the AT tradeoff can be optimized for given values of the LRS. The optimization of the CMOS periphery was done for a 40-nm CMOS technology, and especially in regard to the physical properties of ECM cells. The evaluation of the AT-tradeoff finally shows that the exploitation of the area benefit of ECM cells is directly linked with an increase of the read latency.

The outstanding scaling potential as well as a high storage density designates nanoelectronic resistive switches (RS) as promising candidates to substitute conventional storage devices in future integrated circuits [1]. However, due to the passiveness of RS their application requires additional active circuits for signal amplification, signal recovery, and selection. Consequently, prospective circuit architectures comprising RS as storage elements will be hybrid ones, e.g. including CMOS circuits which provide the active circuit parts. In order to exploit the full potential of RS devices the joint interaction between RS and active CMOS has to be considered. Particular interactions for instance are coming up during the programming of RS when a specific voltage-current profile has to be delivered in order to set either the low resistive state (LRS) or the high resistive state (HRS) of an RS in a defined way.

Also, the read operation requires well-defined voltage-current profiles delivered from the periphery in order to maximize the read margin and to guarantee sufficiently low bit error rates. In order to derive a reasonable area-delay (AT) metric for scaled hybrid RS/CMOS memory arrays both factors (reliable read operation, reliable write operation) were set as boundary condition for the circuit optimization.

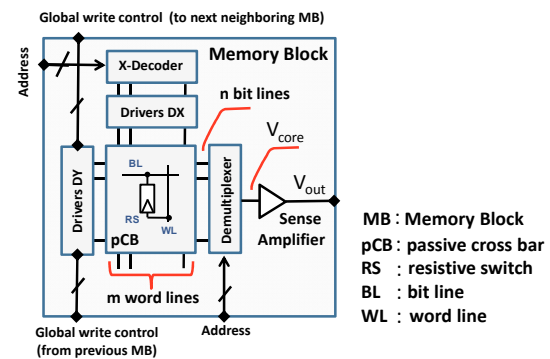


Figure 1: Architecture of a memory block (MB) which is based on a passive crossbar comprising resistive switches.

The analyzed architecture of an RS-based memory block (MB) is shown in Fig.1. The MB consists of a passive crossbar (pCB) with m word lines and n bit lines comprising $M=n \times m$ ECM memory cells (cf. Fig. 2a) in total. During a read operation, i.e. the circuit maps the address input onto an output bit, some address bits are used to select appropriate voltage levels for the word lines via the X-decoder. The remaining address bits are used to select a particular bit line via a demultiplexer. After an architecture-dependent delay, the voltage V_{core} is equal to the voltage level obtained at the selected bit line. The voltage V_{core} represents the associated logic state and is transformed via the sense amplifier to a full-swing output signal.

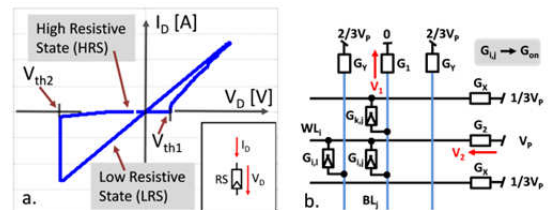


Figure 2: a. ECM characteristics with set voltage V_{th1} and reset voltage V_{th2} . b. equivalent circuit for setting G_{ij} to R_{on} (LRS)

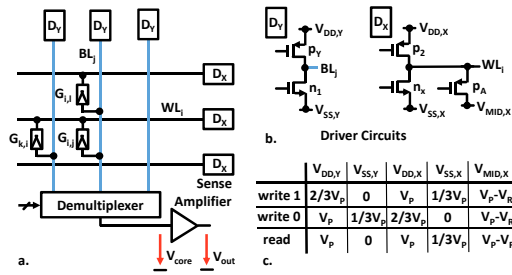


Figure 3: a. pCB with driver circuits DX, DY, and demultiplexer. b. circuit implementation of DX and DY. c. voltage levels of the supply lines for read and write operation. $V_{DD}=V_p=0.9V$, $V_R=0.2V$

In order to comply with the electrical requirements for ECM cells particular driver circuits are added at the crossbar periphery (cf. Fig. 3). For particular memory capacities M (here: 16 bit, 32 bit, and 64 bit) and partitioning into different sets of word lines m and bit lines n optimal decoder circuits and demultiplexer circuits were derived and characterized with regard to area and latency (note: a 40 nm CMOS technology was assumed here). Additionally, the driver circuits DX and DY (cf. Fig. 3) were optimized. Due to the (almost) linear I-V characteristics of ECM cells [3] parasitic sneak paths complicate the analysis. By numerical optimization lower bounds for the required transistor conductances (cf. Fig.2b and Fig.4a) were derived in respect to the ON-resistance of the RS and in respect to different array configurations. Based on the transistor sizes as well as based on a interconnect model parasitic capacitances were determined which allowed for the analysis of the read latency. The definition of reasonable boundary conditions for the write operation ended up in an effective allowed write voltage loss of fractions of the temperature voltage $V_T=k_B T/q$ (k_B : Boltzmann constant, T : temperature, q : elementary charge). For the read operation, the maximum allowed read margin loss (cf. Fig. 4b) was set to fractions of $V_R/2m$ (V_R : read voltage).

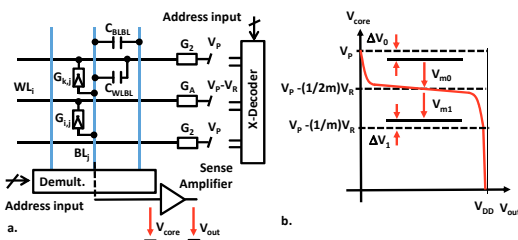


Figure 4: a. word line configuration for accessing G_{ij} . b. sense amplifier transfer characteristics (the red curve), worst case core voltage and signal margins V_{m1} (reading a one) and V_{m0} (reading a zero) and margin loss ΔV_0 , ΔV_1

The optimization results are shown in Fig.5. For different ON-resistances the optimization of the AT metric results in a specific total circuit core area (including drivers, decoders, and demultiplexer) as well as an associated delay. Architectures with a larger number of word lines show clear benefits in regard to read latency at a given core area. Also architectures with higher storage capacity clearly provide a better area efficiency (taking the

effective area per bit as metric) compared to low capacity arrays.

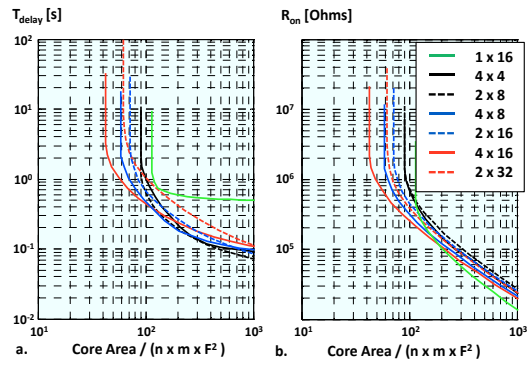


Figure 5: Effective area per bit in relation to F^2 (F : lithographic resolution) for different array configuration, b. Minimum On-resistance R_{ON}

Finally, reasonable (recommended) values for the ON-resistance of ECM cells have to be chosen above 100k Ω . The main limiting factor under worst case conditions is the presence of sneak paths [4] and the necessity to deliver high currents to the passive crossbar.

- [1] Wei Lu, Charles M. Lieber, "Nanoelectronics from the bottom up", Nat. Mater. 6, pp. 841–850 (2007)
- [2] R.Waser, "Electrochemical and Thermochemical Memories", IEDM, pp 1-4 (2008)
- [3] S.Menzel, U.Böttger, and R.Waser, "Simulation of Multilevel Switching in Electrochemical Metallization Memory Cells", Journal of Applied Physics Vol. 111, pp.014501-014501-5, (2012)
- [4] A. Flocke, T.G. Noll, "Fundamental analysis of resistive nano-crossbars for the use in hybrid Nano/CMOS-memory," Proceedings of the 33rd European Solid-State Circuits Conference, pp. 328-331 (2007)

Nanobatteries inside Redox-Based Memristive Elements

I. Valov¹, E. Linn², S. Tappertzhofen², S. Schmelzer², J. van den Hurk², F. Lentz¹, and R. Waser^{1,2}

¹Peter Grünberg Institut-7, Forschungszentrum Jülich, Germany

²Institut für Werkstoffe der Elektrotechnik 2, RWTH Aachen University, Germany

Being theoretically proposed by Leon Chua in 1971 [1], memristors are known to be the missing fourth basic circuit element. While they are still missing today, the much more general 'memristive device' introduced in 1976 has recently been linked to nanoscale redox-based resistive memory cells (ReRAMs). These devices are studied for their potentially promising energy-efficient memory and neuromorphic logic applications. However, the model of memristive devices is based on a hysteresis current/voltage loop, pinched at the origin. Here we show that operation of these devices inherently results in the generation of non-equilibrium states similar to processes in batteries violating the existing theory.

On the way towards further integration of memory and logic devices new technological approaches beyond the conventional von Neumann architecture are in the scope of nanoelectronics research. The ReRAM is considered as one of the most ambitious concepts to overcome the current limitations of state-of-the-art FLASH technology due to the prospect of high scalability to a nearly atomic level, fast access times and low power consumption [2]. In ReRAMs resistance transition can be achieved by voltage or current pulses and nanoionic driven redox reactions have been unveiled as the underlying mechanism [3]. For device fabrication typically transition metal-oxides (such as SrTiO_3 or Ta_2O_5) sandwiched between electrodes with a low and a high oxygen affinity (e. g. TiN and Ti) are used in the case of ReRAMs based on the valence change mechanism (VCM). Here, the switching mechanism is attributed to the drift of oxygen vacancies. Another type of ReRAM cells, so called electrochemical metallization (ECM) cells, is based on the electrochemical growth and dissolution of a metal filament within an insulating but (on the nanoscale) ion conducting thin film (eg. SiO_2 , GeS_x or AgI). In these cells, electrochemically active metals such as Ag or Cu as active electrode and Pt or TiN as inert electrode are used.

Recently, ReRAM cells were identified as memristive devices [4]. This circuit element is a passive non-linear two-terminal device relating the voltage $V(t)$ and the current $I(t)$ by a conductance $G(x, V)$ which depends on an internal state variable x :

$$I(t) = G(x, V) \cdot V(t) \quad (1)$$

In order to represent ReRAM cells, memristive devices are supposed to fulfil certain requirements such as a state variable x which is compositional and shows limited upper and lower values.

A fingerprint of memristors and memristive devices is the existence of a zero-crossing hysteresis loop based on eq. (1). In our study we show that during device operation of redox-based resistive switches ion concentration gradients are repeatedly generated resulting in non-equilibrium states and the formation of an electromotive force (emf voltage) [5]. This leads to a non-zero-crossing hysteresis loop inconsistent with the existing theory of memristive devices. Moreover, the observed processes are of high practical interest and may explain hitherto unsolved questions of the resistive switching effect.

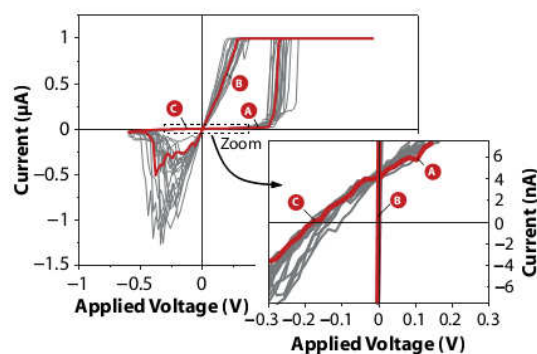


Fig. 1: Resistive switching of a $\text{Cu/SiO}_2/\text{Pt}$ ECM-type cell. For readability labels are shown indicating the switching direction. The zoom clearly reveals the non-pinched hysteresis.

Resistive switching of a $\text{Cu/SiO}_2/\text{Pt}$ cell is shown as an example in Fig. 1. The zoom clearly reveals the non-pinched hysteresis characteristic. For switching to the ON state, anodic oxidation of the Cu electrode takes place first and subsequently the oxidized Cu^{z+} ions (with charge number z) are reduced at the Pt electrode forming a nanoscale Cu filament short circuiting both electrodes. After RESET to the OFF state (dissolution of the filament) the concentration gradient of ions still exists. We found three factors depicted in Fig. 2 which result in non-equilibrium states during device operation and thus the generation of an emf voltage: (1) the Nernst potential (Fig. 2a), (2) the diffusion potential (Fig. 2b) and (3) the Gibbs-

Thomson potential (Fig. 2c). When the cell is programmed to a metallic ON state no emf can be measured due to the short circuit. However, the driving force for the emf still remains and may lead to internal changes also in the ON state.

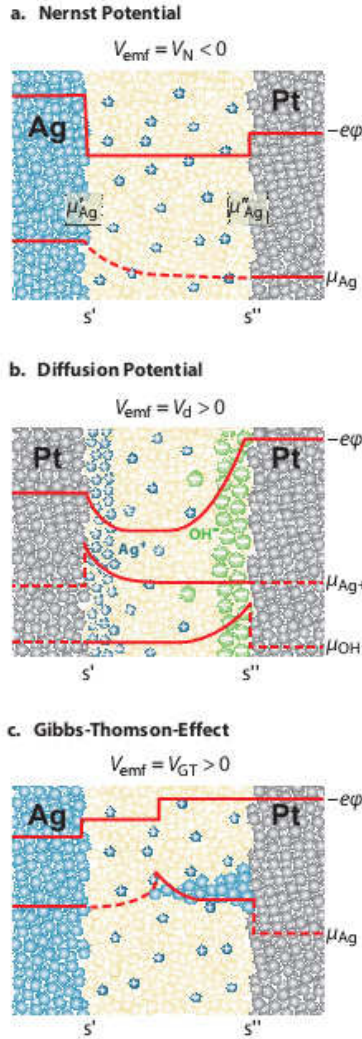


Fig. 2: Three factors resulting in the generation of an electromotive force: (a) Nernst potential, (b) diffusion potential and (c) the Gibbs-Thomson-Effect. Depending on the particular system at least one of these non-equilibrium states is repeatedly induced during device operation.

Emf voltages of various material systems for ECM- and VCM-type ReRAM cells have been measured as shown in Fig. 3. The measureable emf V_{Cell} strongly depends on the electronic partial conductivity. VCM cells show typically a much higher electronic than ionic partial conductivity compared to ECM cells resulting in a lower absolute value of the measureable cell voltage. We also performed short circuit current measurements ($V = 0$) after RESET. The overall charge is about three orders of magnitude larger than the dielectric capacitance charge, again confirming the nanobattery effect.

Based on the measurements and electrochemical theory discussed in our work we present a modified model which we call “extended

memristive device” and which is an active circuit element and accounts for the electromotive force.

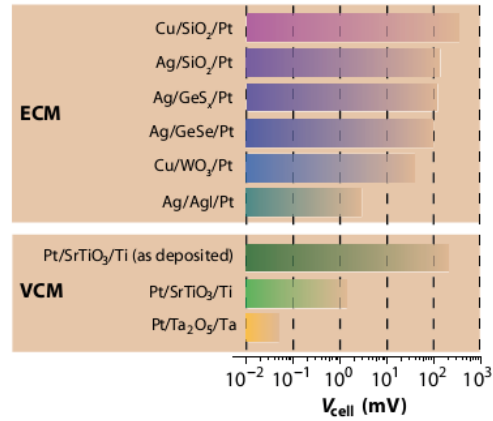


Fig. 3: Typical cell voltage values for various material systems covering both ECM- and VCM-type resistive switches.

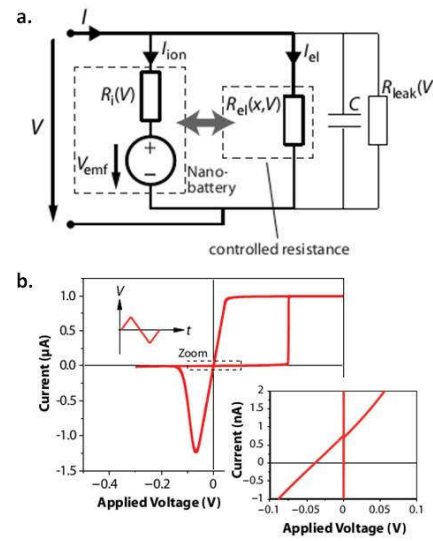


Fig. 4: (a) Equivalent circuit representing the extended model of memristive devices which accounts for the nanobattery effect. (b) Simulation results based on the circuit model in (a).

The equivalent circuit model of our extended model is shown in Fig. 4a. In contrast to the existing theory, the ionic current path $R_i(V)$ is separated in parallel from the controlled electronic device resistance $R_{el}(x,V)$ (x is the state variable). Moreover, the ionic current path can be considered a nanobattery representing the emf. The simulation results (for Cu/SiO₂/Pt as an example) are depicted in Fig. 4b and fit well to our measurement shown in Fig. 1.

- [1] L.O. Chua, IEEE Trans. Circuit Theory CT-18, 507 (1971).
- [2] R. Waser and M. Aono, Nat. Mater. 6, 833 (2007).
- [3] K. Szot, W. Speier, G. Bihlmayer, and R. Waser, Nat. Mater. 5, 312 (2006).
- [4] D. B. Strukov, G. S. Snider, D. R. Stewart, and R. S. Williams, Nature 449, 80 (2008).
- [5] I. Valov et al., Nature Communications (2013).

Atomic Manipulation of Electrochemical Interfaces for Resistive Switching

I. Valov¹, I. Sapezanskaia², A. Nayak³, T. Tsuruoka³, T. Bredow⁴, T. Hasegawa³, G. Staikov¹, M. Aono³, and R. Waser^{1,2}

¹Peter Grünberg Institut-7, Forschungszentrum Jülich, Germany

²Institut für Werkstoffe der Elektrotechnik 2, RWTH Aachen University, Germany

³National Institute of Materials Science (WPI-MANA), Tsukuba, Japan

⁴Institute of Theoretical Chemistry, University of Bonn, Germany

Electrochemical equilibrium and the transfer of mass and charge through interfaces at atomic scale are of a fundamental importance for the microscopic understanding of elementary physicochemical processes. Approaching atomic dimensions, phase instabilities and instrumentation limits restrict the resolution. Here we show an ultimate lateral, mass and charge resolution during electrochemical Ag phase formation at the surface of RbAg₄I₅ superionic conductor thin films. We demonstrate that Ag critical nucleus formation is rate limiting. Our approach is crucial to elucidate the mechanism of atomic switches and highlights the possibility of extending this method to a variety of other electrochemical systems [1].

The ability to control at the atomic scale the physicochemical properties of surfaces is of primary interest for a wide range of fields, including energy conversion, nanoelectronics and information technology, and nanoionics [2].

An electrochemically formed new phase consisting of a few to some tens of atoms in contact with foreign substrate is expected to be thermodynamically unstable (as far it can be physically defined as a phase). The charge, transferred in the elementary act(s) cannot exceed these tens of e^- which is beyond the sensitivity limits of modern instrumentation. An uncertainty is additionally introduced by the fact that the well-defined macroscopic quantities are averaged and even single crystalline substrates show local structural defects leading to microscopic inhomogeneities of the material properties. Therefore, the atomically resolved measurements of electrochemical processes require a high precision in detecting mass and charge flow, a stabilisation of thermodynamically meta-stable clusters of few atoms and knowledge of the local atomic structure and topography.

Despite that scanning tunnelling microscope (STM) provides atomic resolution and an ability to manipulate surfaces, no reports can be found on STM measurements of superionic conducting solid electrolytes. The reason is the poor electronic conductivity of this class of materials suppressing the quantum mechanical tunnelling required by STM. However, mixed electronic-ionic conducting solids with prevailing electronic conductivity were

the subject of STM experiments and lead to the development of the concept of the atomic switch demonstrating the ultimate scalability of the cation based resistive switching memories and the memristive systems.

The so-called 'atomic switch' is based on electrochemical surface reaction of formation and dissolution, respectively, of nano-sized metallic cluster of Ag or Cu upon applying a short voltage pulse in the vacuum gap between STM tip and a mixed electronic/ionic conducting solid, e.g. Ag₂+₆S and Cu₂+₆S. It has been introduced by Terabe et al. [3] and was further developed as a technique to manipulate the resistance in the tunnel gap, where attempts have been made to elucidate the detailed mechanism of the atomic switch [4].

The kinetics of the electrochemical formation of the small cluster (new phase) can be limited by the electron charge transfer or by the statistical process of (re)arrangement of the deposited atoms in an energetically stable configuration, i.e. the formation of a critical nucleus. If the number of atoms (N_c) constituting the critical nucleus is lower than approximately 20, the thermodynamics and kinetics of the cluster is given by the atomistic theory of nucleation, accounting for the discrete character of the system.

Once formed, the nucleus may further grow establishing a single atomic contact to the STM tip (Fig. 1). This mechanical contact stabilises thermodynamically the cluster and the tip-sample distance, the number of the atoms in the cluster, the partial charge used in the redox process, and the Faraday efficiency can be estimated.

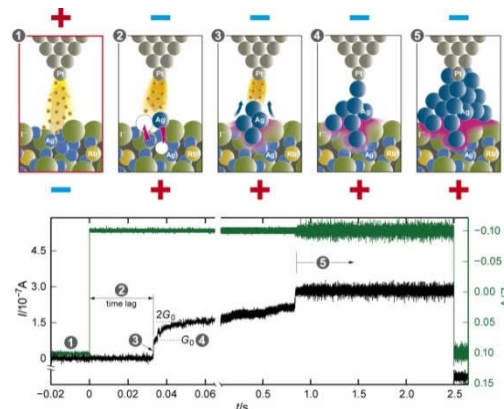


Fig. 1: Nucleation and resistive switching in RbAg₄I₅-based atomic switch.

An applied voltage shifts the Fermi level of the STM tip relative to the sample ($\Delta E_F(\text{tip}) = -e\Delta\phi$) and an effective tunnelling current is induced.

Electrons arriving at the RbAg_4I_5 surface with energy lower than the Fermi energy of the redox reaction (1), i.e., $E_F < E_F(\text{Ag}^+/\text{Ag})$ can only tunnel but cannot contribute to the electrochemical reaction. After achieving the energy level of $E_F > E_F(\text{Ag}^+/\text{Ag})$ the tunnel electrons can overcome the energy barrier for the Ag^+/Ag redox reaction. Thus, at $E_F < E_F(\text{Ag}^+/\text{Ag})$ we performed the STM imaging and at $E_F > E_F(\text{Ag}^+/\text{Ag})$ we performed electrochemical measurements of the reaction kinetics.

Fig. 2 shows for the first time atomically resolved STM images of superionic solid electrolyte.

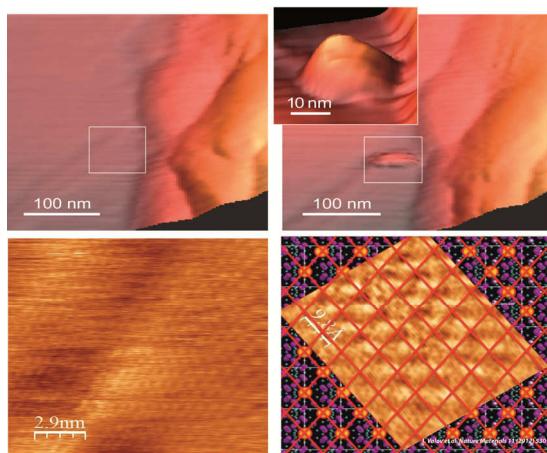


Fig. 2: STM images of initial state of the surface (a) and after the formation of the Ag nucleus (b). In (c) and (d) an atomically resolved STM image is presented.

Next, the initial stages of Ag cluster formation were studied by applying a negative voltage to the STM tip according to:

$$E_F(\text{tip}) + e\Delta\phi > E_F(\text{Ag}^+/\text{Ag})$$

Due to the specifics of the system no steady state measurements can be performed but only rather short voltage pulse experiments. Applying a negative voltage pulse, a switching event occurs (short circuiting the vacuum gap) in times ranging between some ms and ns, with switching times t_s being exponentially dependent on the value of the applied potential.

We unequivocally relate the short circuiting of the tunnel gap to a formation of an Ag nucleus induced by the electrochemical reaction given by equation (1). The elementary steps of formation of one or few Ag atoms at the RbAg_4I_5 surface represent an electrochemical reaction limited by the initial stage(s) of the formation of a new phase (Ag) on a foreign substrate i.e., the nucleation. The nucleation time t_n / s is given in accordance to the atomistic model for electrocrystallisation:

$$t_s = t_0 \exp\left(\frac{(N_c + \alpha)e\Delta\phi}{kT}\right) \quad (1)$$

As shown in Fig. 3 two linear regions can be distinguished - *Region 1* between -75 mV and -300 mV and *Region 2* between -300 mV and -600 mV. The corresponding reciprocal slopes were calculated to be $b_1 = 21$ mV and $b_2 = 125$ mV. In *Region 1* we found $N_c = 1$ and in *Region 2* $N_c = 0$. $N_c = 1$ has the physical meaning that each atom of Ag created at the RbAg_4I_5 surface can be considered as a nucleus of the new phase, and $N_c = 0$ means that an empty nucleation site acts as a critical nucleus and the single created Ag atom represents a supercritical cluster of the new phase.

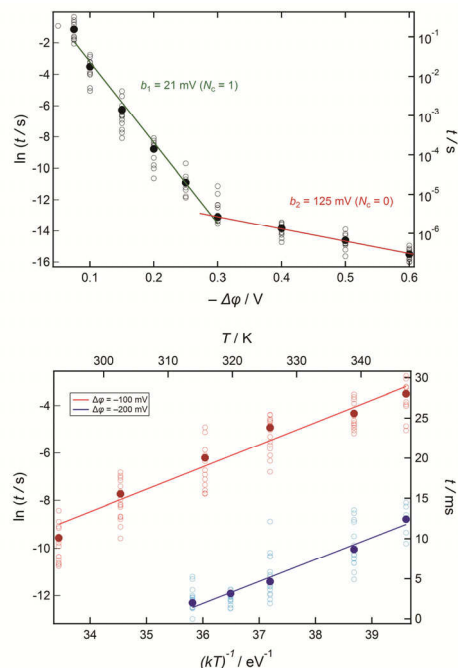


Fig. 3: (a) Dependence of the switching time t_s (a) on the applied voltage for $T = 300$ K, and (b) on the temperature at two constant voltages.

The activation energy of the nucleation process (~ 1 eV) was obtained from the temperature dependence of the switching time.

In this study we offer an alternative approach for studying electrochemical reactions on a microscopic level with an ultimate lateral, mass and charge resolutions based on the atomic switch concept. We demonstrate that the very initial stage of an electrochemically driven formation of a new phase is limited by the critical nucleus formation.

We suggest the possibility of extending our method to other solid- and liquid-based ionic conductors which are used in sensors, fuel cells, and catalysts.

- [1] Valov, I. *et al. Nat. Mater.* **11**, 530 (2012).
- [2] Waser, R. & Aono, J. *Nat. Mater.* **6**, 833 (2007).
- [3] Terabe, et al. *Nature* **433**, 47 (2005).
- [4] Nayak, A. *et al. J. Phys. Chem. Lett.* **1**, 604 (2010).

Versatile scanning tunneling microscopy with 120 ps time resolution

C. Saunus, J. R. Bindel, M. Pratzer, and M. Morgenstern

II. Institute of Physics, RWTH Aachen University, Germany

We describe a fully ultra-high vacuum compatible scanning tunneling microscope (STM) optimized for radiofrequency signals. It includes in-situ exchangeable tips adapted to high frequency cabling and a standard sample holder, which offers access to the whole range of samples typically investigated by STM. We demonstrate a time resolution of 120 ps by using the nonlinear $I(V)$ -characteristic of the surface of highly oriented pyrolytic graphite (HOPG). We provide atomically resolved images in pulse mode related to a spatially varying nonlinearity of the local density of states of the sample, thus, demonstrating the possible spatial resolution of the instrument in pulse mode.

It is very complex to combine the unmatched spatial resolution of an STM with a high time resolution, since the measurement bandwidth of common high-gain current amplifiers does typically not exceed a few kilohertz at a sufficient noise level. In order to overcome these limits, Nunes and Freeman combined an STM with the pump-probe technique known from time resolved optical probing and demonstrated 20 ps time resolution combined with 1 nm spatial resolution.[1,2] Their high temporal resolution relies on the careful guiding of the voltage pulses on the sample towards the tunneling junction by the use of impedance matched transmission lines. Thus, their approach is not versatile with respect to sample preparation. Recently, S. Loth *et al.* detected electron-spin relaxation with atomic resolution using an all-electrical pump-probe scheme and a standard, thus, versatile STM system.[3] In their work the shortest measured relaxation times were 50 ns using a probe pulse width of 100 ns.

Here, we present a home-built STM head using radio-frequency (RF) optimized tips, which achieves a time resolution of 120 ps while maintaining atomic resolution. While the presented experiments are performed at ambient conditions, the STM is fully compatible with ultra-high vacuum (UHV), low temperature (5 K) and high magnetic fields since only slightly modified with respect to established designs.[4] Tunneling tips and samples are exchangeable in-situ and the sample holder is identical to that used for conventional STM giving full access to the plethora of known UHV sample preparation methods as well as coating of the tip by ferromagnetic or anti-ferromagnetic materials for the purpose of spin-polarized STM. To optimize the radio frequency response of the microscope, the tunneling voltage is guided towards the tip by an RF-coaxial cable

with cut-off frequency $f_{3\text{db}} = 18\text{ GHz}$. Applying the voltage to the tip rather than the sample avoids complex RF-optimized sample designs as long as the sample is well grounded capacitively. To allow in-situ tip exchange, the coaxial cable is terminated by an SMP type coaxial plug, which is fixed to the back of the microscope body. The counter jack is mounted on a modified standard tip carrier with the short tunneling tip (2 mm) glued to the center conductor of the jack. The whole tip assembly can be exchanged as plug-in board in-situ using a wobble stick.

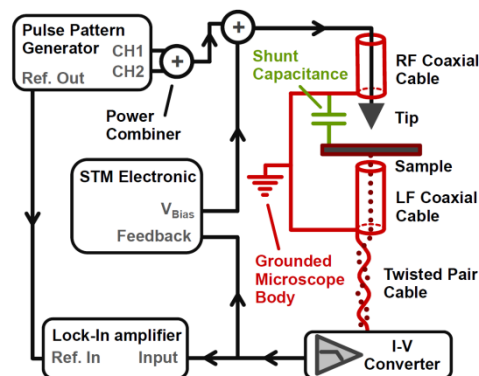


FIG. 1: Setup scheme for pulsed STM measurements, indicating the tunneling voltage generation by PPG and STM electronics, the RF coaxial connection to the tip and the current analysis by STM electronics and lock-in amplifier. For pulse superposition measurements (Fig. 2) the lock-in output is displayed as a function of pump-probe delay.

The pulse measurement setup is shown in Fig. 1 consisting of a pulse pattern generator (PPG) and a lock-in amplifier. The PPG has two independent output channels which provide voltage pulses of up to 2 V at 50 Ω and a full width at half maximum (FWHM) measured to go down to 120 ps (nominally 100 ps). The channels can be internally delayed and are summed by a resistive power combiner at the output of the PPG. A second power combiner adds the bias voltage of the STM electronics to the voltage pulses before the signal is guided to the tunneling tip by the RF cable. The resulting tunneling current is first amplified by 10^9 V/A at a bandwidth of 1 kHz and then analyzed by the feedback electronics and the lock-in amplifier simultaneously. In pulse STM operation, the PPG sends two continuous pulse trains, a “pump” pulse train and a delayed “probe” pulse train, to the junction. The time delay between the two can be swept to scan the time evolution of a signal. To enable lock-in detection, the time delay is modulated with a fixed reference frequency around the time delay of interest to allow lock-in

detection. The lock-in amplifier displays a value proportional to the average excess current generated by the probe pulses at the time delay of interest.

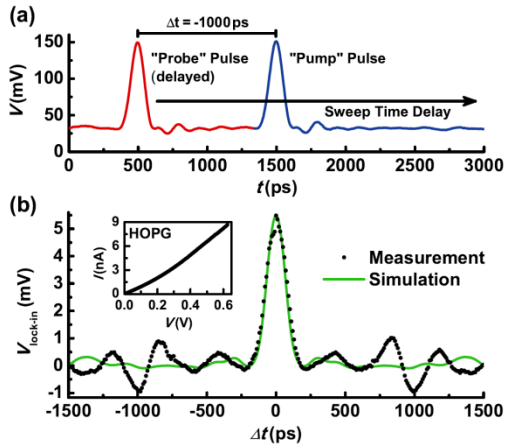


FIG. 2: A. Voltage pulse train generated by the PPG combined with the DC bias as measured by 50 Ω oscilloscope. B. Lock-in output $V_{\text{lock-in}}$ as a function of Δt for an HOPG sample and a PtIr tip. The inset shows the measured $I(V)$ -characteristic.

The time resolution of a pump-probe measurement is limited by the width of the voltage pulses directly at the tunneling junction.[1] It cannot be measured directly by an oscilloscope without affecting the voltage drop across the junction. Thus, one has to use a different approach. Figure 2(b) shows the result of a pulse superposition measurement on HOPG under ambient conditions. The acquired lock-in voltage $V_{\text{lock-in}}$ is shown as a function of the time delay Δt between the two pulse trains. The pulses as measured by an oscilloscope directly connected to the second power combiner (see Fig. 1) are displayed in Fig. 2(a). They have a full width at half maximum (FWHM) of 120 ps and an amplitude of 121 mV (nominally 2 V) at the 50 Ω input impedance of the oscilloscope. The voltage amplitude at the tunneling junction is nearly twice as large due to its \sim G Ω impedance.

The tunneling junction consists of a PtIr tip above a flat HOPG terrace produced by cleavage. The tip is stabilized at a bias voltage of $V_{\text{bias}} = 54$ mV and a tunneling current of $I_{\text{set}} = 500$ pA in order to characterize the junction by the $I(V)$ -curve shown in the inset of Fig. 2(b). The current rises non-linearly with increasing voltage, i.e. $I(V)$ offers a positive curvature. Then, the PPG output is enabled and the lock-in value is recorded during a time delay sweep. The non-linear $I(V)$ -characteristic of HOPG leads to a gain in average current per cycle when pump and probe pulses start to overlap ($\Delta t \rightarrow 0$) as seen in Fig. 2(b).[1] Since the average current of separated pulses is subtracted by the lock-in amplifier, Fig. 2(b) only shows contributions from the excess current which approaches 0 at low and high time delays ($\Delta t \rightarrow \pm 1.5$ ns). A parameter free simulation of the expected lock-in output (solid curve in Fig. 2(b)) using the recorded pulse train out of Fig. 2(a) and the measured $I(V)$ -curve from the inset of Fig. 2(b) exhibits excellent agreement with the measured

data in the region of overlap. Hence, we deduce that the voltage pulses at the tunneling junction are nearly identical to the ones provided by the PPG, respectively, we establish a time resolution of 120 ps.

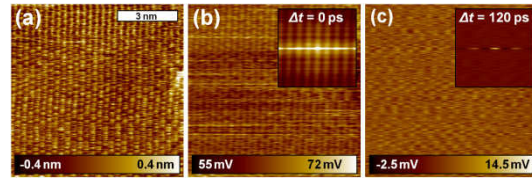


FIG. 3: A. 8.6 nm x 8.6 nm constant-current image of HOPG with atomic resolution. B,C. Simultaneously acquired lock-in data using time delays Δt as marked.

Finally, we demonstrate atomic resolution in pulsed mode. Therefore, we image an 8.6 nm x 8.6 nm area of HOPG (Fig. 3(a)) and simultaneously acquire the lock-in output in PPG mode as a measure of the local non-linearity of the $I(V)$ -curve. Figures 3(b) and 3(c) show lock-in images on the same position with a fixed time delay of $\Delta t = 0$ ps and $\Delta t = 120$ ps using pulses of a measured width of 133 ps and a pulse height at the junction of 307 mV. Pulse image 3(b) shows atomic contrast in the real space image with a visibility of 5 % while the contrast disappears at 120 ps (Fig 3(c)), where the pulses hardly overlap. This result becomes even more striking within the autocorrelation images (insets), which exhibit atomic rows at $\Delta t = 0$ ps, but not at $\Delta t = 120$ ps. Thus, the applied voltage pulses probe at an atomic scale and there is no obvious reason that this would change for really time-varying signals. We can conclude that we probe the curvature of the $I(V)$ -curve, which is directly linked to the local density of states, at 120 ps time resolution.

In conclusion, a home built RF-STM is presented, where the tip is directly connected to an RF-cable with 18 GHz bandwidth. We demonstrate time resolution of 120 ps while maintaining atomic resolution in pulsed mode. While the measurements were performed at ambient conditions, the STM is compatible with UHV, low temperature, and magnetic field. Importantly, the spatiotemporal resolution is achieved without any additional restrictions to the sample with respect to standard STM, thus giving atomically resolved access, e.g., to charge carrier dynamics or mechanical motion of nano membranes.[5]

We acknowledge financial support from the DFG via SFB 917-A3 and Mo 858/8-2.

- [1] G. Nunes and M. R. Freeman, *Science* **262**, 1029 (1993).
- [2] N. N. Khusnatdinov, T. J. Nagle, and J. G. Nunes, *Appl. Phys. Lett.* **77**, 4434 (2000).
- [3] S. Loth, M. Etzkorn, C. P. Lutz, D. M. Eigler, A. J. Heinrich, *Science* **329**, 1628 (2010).
- [4] T. Mashoff, M. Pratzer, M. Morgenstern, *Rev. Sci. Instrum.* **80**, 053702 (2009).
- [5] T. Mashoff, M. Pratzer, V. Geringer, T. J. Echtermeyer, M. C. Lemme, M. Liebmann, and M. Morgenstern, *Nano Lett.* **10**, 461 (2010).

High-sensitivity SQUIDs with dispersive readout for scanning microscopy

J.-M. Mol¹, J. Arps¹, F. Foroughi¹, G.W. Gibson, Jr.³, K. Fung³, B. Klopfer², K. Nowack², P.A. Kratz², M.E. Huber⁴, K.A. Moler², J.R. Kirtley², and H. Bluhm¹

¹ II. Institute of Physics C, RWTH Aachen University, Germany

² Center for Probing the Nanoscale, Stanford University, Stanford, California

³ IBM Research Division, T.J. Watson Research Center, Yorktown Heights, New York

⁴ University of Colorado Denver, Denver, Colorado

In a scanning SQUID microscope, the high magnetic flux sensitivity of a SQUID is utilized to image magnetic properties of sample surfaces. So far, DC-SQUIDs have been widely used for this task. As an alternative, we present Nb SQUIDs for scanning with dispersive microwave readout, featuring a higher bandwidth and sensitivity. An on-chip shunt capacitor in parallel with the junction and flux pickup loops forms an LC resonator whose resonance frequency depends on the flux in the SQUID. The microwave-readout utilizes a phase-sensitive detection of the reflected drive signal at the SQUID's resonance frequency.

Scanning SQUID microscopy has been used successfully for a wide range of applications ranging from nondestructive material examination over materials physics studies to fundamental experiments in mesoscopic physics. Compared to other magnetic imaging techniques, the strengths of SQUID sensors lie in the (relatively) non-invasive measurements, high sensitivity, and a quantitative signal. Furthermore, field coils integrated in the sensor can be used for susceptibility and magnetic response measurements. Magnetic images are obtained by moving the sensor over the sample surface. By placing the sensor in vacuum directly above the sample, a spatial resolution in the micrometer range can be achieved. It is also possible to place the sensor above an object to record details of its magnetic response while using the scanning capability for background measurements and addressing different samples.

Traditionally, this technique is used with so called DC SQUIDs, whose I-V characteristic changes in response to a magnetic flux threading its sensing loop. Typical sensor noise levels exceed $0.2 \mu\Phi_0/\sqrt{\text{Hz}}$. We are developing devices which are instead read out by reflecting a microwave carrier. As for typical DC SQUIDs for scanning microscopy, the sensors are designed in a gradiometric layout with two counter-wound pickup coils. These are placed on opposite corners of a parallel-plate capacitor (Fig. 1a). Around each of the pickup loops, a field coil for local application of magnetic fields is located. The counter-wound geometry ensures an effective way to cancel out

externally applied flux by the field coils as well as possible background fields. The pickup-coils and the capacitor form an LC resonator with a flux dependent inductance due to a Josephson junction in one of the parallel arms of the resonator. Different designs feature resonance frequencies in the range of a few up to approximately 15 GHz. The backward field coil (or alternatively an inductively coupled wire with lower inductance) can also be used to apply a bias flux so that the sensor can be operated at its most sensitive point.

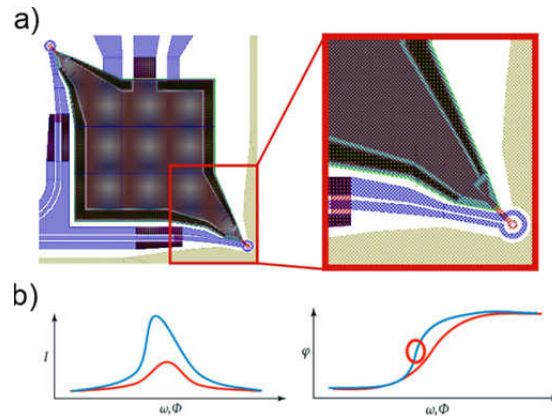


FIG. 1 (a) Schematic of the sensor chip. The multi-layer structure is defined by using high-resolution lithography. Pickup loop sizes (red loop in magnification) vary between 0.5 to 1.5 μm . (b) Signal amplitude and phase as functions of either frequency or flux. By tuning the flux-bias point of the device and setting the drive to higher powers, the resonator undergoes a change from the linear (red curve) to the nonlinear regime (blue curve). This increases slope of the phase change at resonance, $d\phi/d\Phi$, leading to higher sensitivity and parametric gain.

The microwave readout relies on a change of the resonance frequency in response to a flux signal seen by the SQUID, which is connected to a coaxial cable. As a result, a resonant excitation signal launched towards the SQUID is reflected with a flux-dependent phase (Fig. 1b). The highest sensitivity is achieved by making use of the inherent nonlinearity of the device arising from the nonlinear inductance of the Josephson junction. It leads to a steepening of the transfer function (and shift of the resonance frequency) at high excitation power (parametric gain, Fig. 1b). At even higher

power, the SQUID undergoes a bifurcation. Hence, a crucial factor for optimum noise performance is the fine tuning of the excitation power. The best working point is just before bifurcation sets in. This point is a function of external magnetic field (bias flux) and excitation frequency.

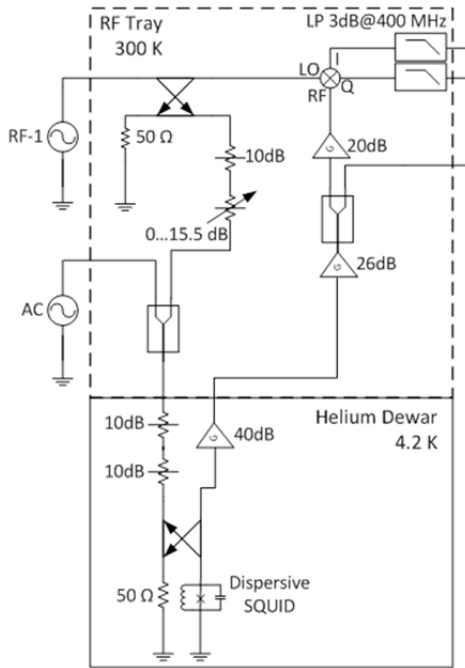


FIG. 2: Experimental setup for characterization. The excitation signal RF-1 is coupled to the SQUID excitation line. A digital step attenuator is used to change power in 0.5 dB steps. The reflected signal is amplified with a low temperature amplifier at LHe temperatures. After further amplification the signal is demodulated at room temperature.

We conducted first characterizations of different devices at 4.2 K. The setup used to characterize the RF SQUIDs is shown in Fig. 2. To shield the SQUID from room temperature noise, the excitation signal has to be attenuated at low temperatures. The phase of the reflected signal is read out with the help of an IQ mixer in order to extract a low frequency signal.

To find the best working point, frequency, power and applied flux have to be optimized. Fig. 3 shows the measured SQUID sensitivity for fixed external flux. Setting the power within an optimal working bias (dashed box, Fig. 3), a second scan is performed, sweeping the externally applied flux (Fig. 4) at fixed excitation power. Finally, biasing the device at the optimal working point, the overall flux noise is reduced to a minimum of $30 n\Phi_0/\sqrt{\text{Hz}}$, nearly an order of magnitude lower than comparable DC SQUIDs. A fit of the resonance frequency vs. flux yields a critical current of the Josephson junction of 3 μA , corresponding to approximately 30% of the planned design value. Improvements in the fabrication process could thus lead to even better sensitivities. Simulations and an extrapolation from our results indicate that values as low as $10 n\Phi_0/\sqrt{\text{Hz}}$ could be possible. With the sub-micron pickup loop diameter of our

devices, this noise level would correspond to a spin sensitivity near $1 \mu_B/\sqrt{\text{Hz}}$ and might thus enable the detection of individual electron spins.

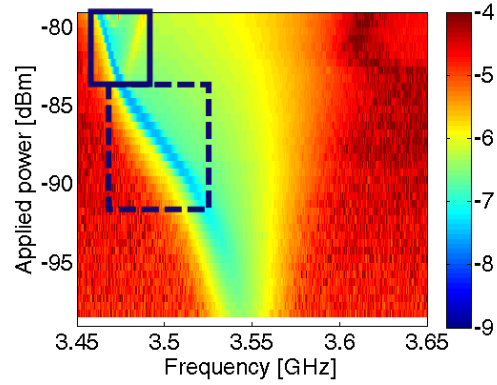


FIG. 3 Decadic logarithm of the estimate flux noise $S_\phi^{1/2} [\Phi_0/\sqrt{\text{Hz}}]$, where $\Phi_0 = h/2e$ at a flux bias of $0.2 \Phi_0$, obtained by dividing the change of reflected microwave signal with flux by the expected amplifier and drive line noise. The bifurcation is visible within the solid box. The optimal working bias lies within the dashed box at resonance.

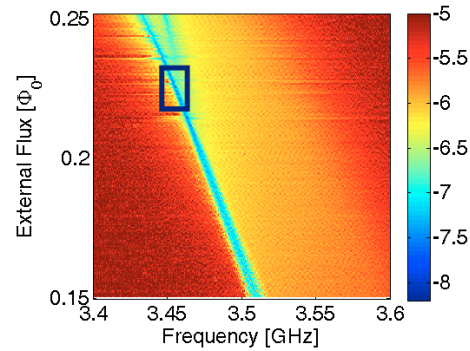


FIG. 4 Decadic logarithm of flux noise $S_\phi^{1/2} [\Phi_0/\sqrt{\text{Hz}}]$. The power is set to -87 dBm at optimal working bias. The solid box denotes the best working point in flux bias, minimizing the overall noise.

In conclusion, we implemented a novel type of SQUIDs using dispersive microwave readout and showed that their sensitivity can be expected to significantly exceed that of conventional SQUIDs. A key ingredient is to harness the nonlinearity of the device. Future work will include a characterization of the bandwidth, which is expected to exceed 100 MHz for the highest frequency devices, and a direct verification of the noise performance. We are also constructing a scanning microscope designed to operate at millikelvin temperatures. In conjunction with the SQUIDs, it will provide a powerful tool for the study of weak magnetic effects possibly down to the single spin level and quantum coherent phenomena.

This work was supported by NSF IMR-MIP grant No. 0957616 and the Alfred Krupp von Bohlen und Halbach – Foundation.

Detection of Liquids based on Reflectance Measurements with High- T_c Superconducting Sensors

M. Lyatti, U. Poppe, and Y. Divin

Peter Grünberg Institut-5, Forschungszentrum Jülich, Germany

Future checkpoint screening should include quick detection of liquids with a low rate of false alarms. An approach based on reflectance measurements in a spectral range of main dispersions of liquids, from a few GHz to a few THz, has been recently suggested. High-temperature (high- T_c) superconducting sensors, which operate in this spectral range with a power dynamic range of more than five orders, might guarantee high accuracy and short time of identification. Several set-ups of liquid identifiers, consisting of high- T_c superconducting Josephson sensors, radiation sources, quasioptical and waveguide coupling units have been developed and characterized. Comparison of quasioptical and waveguide coupling units shows advantages of waveguide approach in frequency range and selectivity of the detection of liquids.

Bottles with liquids, which might contain flammables, explosives or their components, are of severe security concern. To distinguish between benign and threat liquids, we have suggested an electromagnetic-wave concept based on our Hilbert spectroscopy and high- T_c superconducting Josephson sensors [1]. This approach covers a frequency range of main dispersions in liquids, from a few GHz to a few THz, and thus significantly enhances reliability of identification in comparison with conventional approaches, where only low-frequency measurements are used. The high- T_c Josephson sensors, due to high power dynamic range, guarantee fast operation of the identifier. Reliable identification of liquids, both benign and threat, within an accuracy of 0.3% was successfully demonstrated using quasioptical reflectance measurements in a special dielectric cell [2]. However, this quasioptical approach suffers from large diffraction losses at low frequencies. Here, we present the radiation coupling unit made from a dielectric waveguide, characterize our set-ups for broadband reflectance measurements and compare detection abilities of quasioptical and waveguide coupling units in identification of liquids.

The spectral range of dispersion in liquids due to Debye relaxation is rather broad and extends from 100 MHz to a few THz. The differences in reflectance for practically all pure liquids are relatively high, but the relative difference for water and H_2O_2 is only of a few percent. This difference

in reflectivity might be of different signs and even lower in absolute values for H_2O_2/H_2O mixtures [3].

Our high- T_c Josephson sensors can operate at this frequency range and demonstrate a power dynamic range of 50-60 dB for a postdetection bandwidth of 1 Hz [1]. Taking into account a noise level of a cryogenic amplifier of 0.15 nV/Hz^{1/2} and a value of the time constant of a lock-in amplifier of 1 ms, we might achieve a value of 32 dB for the power dynamic range. This signal-noise ratio is sufficient to distinguish between calculated reflectivities of H_2O and 30% H_2O_2/H_2O solution [3].

In these measurements we used an $YBa_2Cu_3O_{7-x}$ Josephson sensor integrated into a Stirling cooler. More details about our high- T_c sensors and Hilbert spectrometers, operating with Stirling coolers, and also their applications for identification of liquids can be found elsewhere [2]. To study identification process, we have developed two set-ups, where radiation is coupled to liquid in different ways. In the first set-up we used quasioptics (Fig. 1) and dielectric waveguides were used in the second set-up (Fig. 2).

In the quasioptical set-up (Fig.1), a polychromatic radiation from a composite radiation source was focused by a gold-plated elliptical mirror on a bottle, and the radiation, reflected from the bottle, was focused on the Josephson sensor with the help of the second elliptical mirror.

In set-up with waveguide coupling (Fig 2), the radiation from different radiation sources is coupled to a central waveguide by proximity radiation coupling. Then, the radiation is guided to a prism and coupled to the liquid. After reflection from the liquid the radiation is directed by another waveguide to the Josephson sensor. The waveguides and the prism were made of high-density polyethylene as one unit to avoid radiation losses.



FIG. 1. Demonstrator of liquid identifier with quasioptical coupling

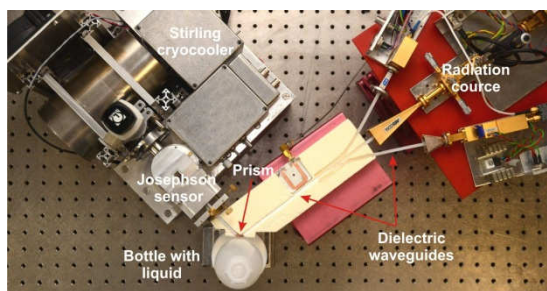


FIG. 2. Demonstrator of liquid identifier with waveguide coupling.

Several pure liquids such as water, acetone, methanol and ethanol were used to test both types of the liquid identifiers. The results of measurements for both types of identifiers are shown in Fig. 3 and Fig. 4 with respect to the average value of the response of water.

Data for quasioptical radiation coupling (Fig. 3) were reliably obtained at the frequency range from 30 to 300 GHz. A frequency-selective mode of a Josephson sensor was used, where information on frequencies and power levels of spectral lines is available. The reflection values varied in an extended amplitude range from maximum value of 1 for water to a minimum value of 0.16 for ethanol. Qualitatively, the response values follow to the reflection coefficients of the liquids, but for a quantitative analysis integration over a broad range of incidence angles should be considered.

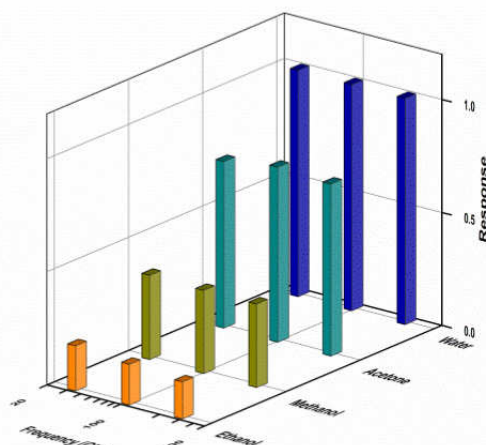


FIG. 3. Response of liquid identifier with quasioptical coupling on different liquids. Responses are normalized on that of water.

With waveguide coupling, reflection data are available in extended range from 1 to 300 GHz (Fig. 4). For measurements at frequencies below 30 GHz we have used a broadband mode of the Josephson sensor, where the response is proportional to total adsorbed radiation power.

At low frequencies, when a wavelength of radiation is comparable to the waveguide length, the waveguide can be considered as a resonator with multiple resonance frequencies. The resonance frequencies and the quality factor of such a

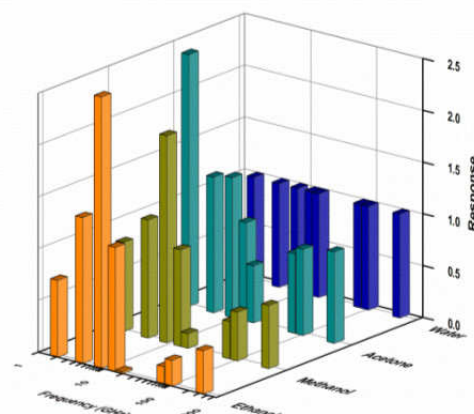


FIG. 4. Response of liquid identifier with waveguide coupling on different liquids. Responses are normalized on that of water.

resonator are changed when the cell with liquid is attached to the waveguide. Higher electromagnetic losses of liquid should result in lower values of response, because a Q-factor of the resonator decreases. A resonator model of this type is in agreement with our data.

At high frequencies, when radiation wavelength is smaller than all characteristic lengths of waveguides, the response of the Josephson sensor is proportional to the reflectivity of the PE-liquid interface. The reflectivity of substance with losses can be calculated from the Fresnel equations [4]. The measured reflectance values are in good agreement with calculated data.

The waveguide version of the identifier is leading to a more reliable liquid identification compared to the quasioptical version. Moreover, a more simple way of data recovery makes the waveguide approach preferable for scientific applications, when the knowledge of absolute values of the complex permittivity is required.

In this work we have tested quasioptical and waveguide versions of a liquid identifier. Due to an extended frequency range and a different measurement technique, the signature of liquids is more specific in the case of the waveguide coupling, which makes the liquid identification in this case more reliable, than in the case of the quasioptical coupling.

This work is supported by the joint project HRJRG-207 of Helmholtz Association of German Research Centers and Russian Fund for Basic Research (project 11-02-91321-SIG_a).

- [1] Y. Divin, U. Poppe, V. Gubankov, K. Urban, IEEE Sensors J., 8, 750-757 (2008)
- [2] M. Lyatti, Y. Divin, U. Poppe, K. Urban, Supercond. Sci. Technol., vol.22, 114005 (2009)
- [3] P. M. Gross, R.C. Taylor, J. Amer. Soc., 72, 2075-2080 (1950)
- [4] W. Leupacher and A. Penzkofer, Appl. Optics, vol. 23(10), pp.1554-1558 (1984)

High- T_c quantum interferometers for magnetoencephalography

M. I. Faley¹, U. Poppe¹, R. E. Dunin-Borkowski¹, M. Schiek², F. Boers³, H. Chocholacs³, J. Dammers³, E. Eich³, N. J. Shah³, A. B. Ermakov⁴, V. Y. Slobodchikov⁴, Y. V. Maslennikov⁴, and V. P. Koshelets⁴

¹Peter Grünberg Institut-5, Forschungszentrum Jülich, Germany

²Central Institute for Engineering, Electronics and Analytics ZEA-2, Forschungszentrum Jülich, Germany

³Institute of Neuroscience and Medicine-4, Forschungszentrum Jülich, Germany

⁴The Kotelnikov Institute of Radio Engineering & Electronics RAS, Moscow, Russian Federation

We have investigated the microstructural and electron transport properties of 45° step-edge Josephson junctions grown on MgO substrates and used them for the preparation of SQUID magnetometers intended for magnetoencephalography (MEG) measurement systems. The high- T_c SQUID magnetometers also incorporate 16 mm multilayer superconducting flux transformers on the MgO substrates and demonstrate a magnetic field resolution of ~ 4 fT/ $\sqrt{\text{Hz}}$ at 77 K. Results are illustrated for the detection of auditory evoked magnetic responses of the human cortex and compared between high- T_c SQUIDs and a commercial low- T_c MEG system. Our results demonstrate that MEG systems can be upgraded using high- T_c SQUIDs to make them independent of helium and more user-friendly, saving operating costs and leading to the widespread utilization of MEG systems in clinical practice and at universities.

Magnetoencephalography (MEG) systems are currently based on low- T_c superconducting quantum interference devices (SQUIDs), which are cooled by liquid helium. The increasing cost of liquid helium is one of the main obstacles for the acceptance of MEG in research and clinical practice. For most routinely used MEG systems, a magnetic field resolution of better than 10 fT/ $\sqrt{\text{Hz}}$ in the frequency range 1 Hz to 1 kHz would be sufficient. High- T_c SQUIDs with multilayer flux transformers have a good chance of being used as magnetic field sensors in future MEG systems because they have a magnetic field resolution of ~ 4 fT/ $\sqrt{\text{Hz}}$ at 77 K for a 16 mm sensor [1, 2].

Typically, the high- T_c SQUIDs with such resolution contain bicrystal Josephson junctions. The use of readily available and relatively cheap step-edge Josephson junctions on single crystal substrates instead of bicrystal Josephson junctions can further improve the sensitivity and reduce the cost of high- T_c sensors. However, better control of the parameters of the junctions is required. Here we describe the microstructural and electron transport properties of multilayer high- T_c DC SQUID magnetometers with step-edge Josephson junctions and compare MEG measurements obtained using a high- T_c system with those obtained using a commercial low- T_c system [3].

The high- T_c DC SQUID flip-chip magnetometers were fabricated with $\text{YBa}_2\text{Cu}_3\text{O}_{7-x}$ (YBCO) films deposited by high-oxygen-pressure magnetron sputtering from stoichiometric polycrystalline targets. An image of the inner part of the SQUID structure, taken using a scanning electron microscope (SEM), is shown in Fig. 1. The step-edge junctions on MgO substrate steps were prepared by using masks of AZ TX1311 photoresist patterned by deep-UV lithography, using a two-part milling process [4] with Ar ion beam etching (IBE).

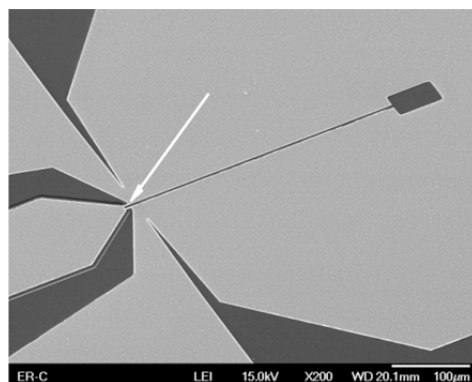


FIG. 1: SEM image of a high- T_c DC SQUID with two step-edge Josephson junctions and a 1 mm washer. The position of the step-edge junctions is marked by an arrow.

This second etching of the MgO substrate with steps using IBE produced linear trenches along [100] and [010] directions on the surface. SEM images of the step edge area made before lithography showed growth spirals with 1 nm steps on the surface of the grains, with the orientation of the a - or b - axes of the YBCO film aligned in-plane, normal to the corners of the step. Fig. 2 shows an SEM image of an individual step-edge Josephson junction on an MgO substrate. The surface morphology of the grains in the YBCO film indicates that the orientation of the c -axis of the YBCO film on the step edge surface differs from the film orientation on the plane surface.

FEI Helios Nanolab 400s FIB system was used to prepare a ~ 100 nm thick lamella for HRTEM. This lamella was transferred into a Philips CM-20 microscope and HRTEM images of the step-edge junction were taken.

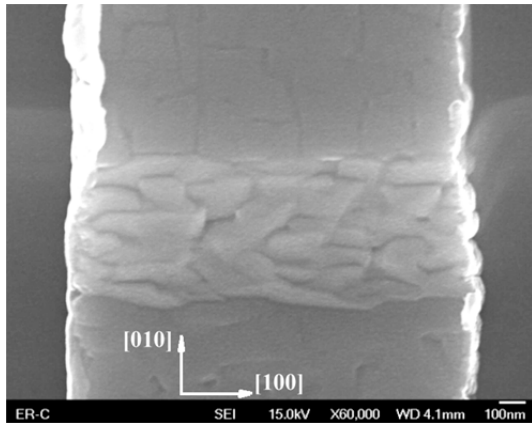


FIG. 2: SEM image of an individual step-edge Josephson junction on an MgO substrate. The orientation of the c -axis of the YBCO film on the step edge surface differs from the film orientation on the plane surface.

Fig. 3 shows an HRTEM image of the YBCO film deposited on the upper corner of the substrate step. The ab -planes of the film are not parallel to the surface of the edge, while the GB has exactly a 45° misorientation. The c -axis of the YBCO film is oriented parallel to the $[011]$ orientation of the MgO at the edge. This image shows a combination of graphoepitaxial in-plane and epitaxial out-of-plane growth of the YBCO film on the step edge of the MgO substrate. In contrast to [4], the c -axis of the YBCO film is not normal to the step edge surface but forms a near coincidence site lattice arrangement.

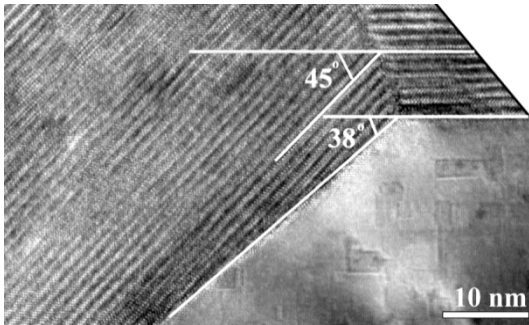


FIG. 3: HRTEM image of the YBCO film deposited on the upper corner of the substrate step.

The properties of the 45° $[100]$ -tilted GB of the step-edge junction are similar to those of the 22.5° $[001]$ -tilted GB of a standard bicrystal Josephson junction, according to the angular dependence of the superconducting gap function for the $d_{x^2-y^2}$ pairing symmetry in YBCO in momentum space:

$$\Delta(\vec{k}) \propto k_x^2 - k_y^2 = (\cos^2 \varphi - \sin^2 \varphi) \sin \theta = \cos(2\varphi) \sin \theta,$$

where φ is the in-plane misorientation angle along the $[001]$ axis and θ is the out-of-plane misorientation angle along the $[100]$ axis.

The magnetic field resolution of the high- T_c system was ~ 5 fT/ $\sqrt{\text{Hz}}$ with the high- T_c magnetometer operating at 77 K in the superconducting shield and ~ 7 fT/ $\sqrt{\text{Hz}}$ (white noise level) at 77 K. The MEG measurements were performed in a magnetically shielded room using both a one-channel high- T_c DC SQUID measurement system and a commercial 248-channel low- T_c MEG

system (9mm low- T_c SQUID magnetometers; "Magnes© 3600 WH" 4D-Neuroimaging) [2]. The analog output from the high- T_c system was connected to a 16-bit analog-to-digital converter port available on the low- T_c system with a sampling rate of 678 Hz and processed together with the signals from the low- T_c magnetometers.

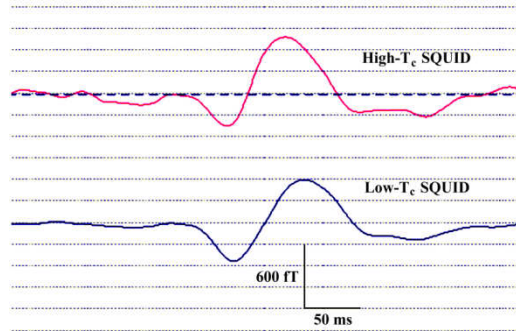


FIG. 4: Auditory evoked MEG signals acquired with the low- T_c whole-head system (lower curve) and the high- T_c system (upper curve).

Auditory signals were generated by electrostatic drivers outside the shielded room and the sound was transmitted via flexible tubes to the ears of the subject. Positions with maximum response obtained from whole-head recordings were used as starting positions for the high- T_c recordings. Fig. 4 shows an example of auditory evoked MEG signals acquired with the low- T_c whole-head system and the high- T_c system. Both data sets show averages over 100 epochs and were band-pass filtered from 3 to 30 Hz. The traces obtained from both the high- T_c and the low- T_c systems demonstrate similar signal-to-noise ratios in spite of the 18 times difference in the operating temperatures of the sensors.

- [1] M. I. Faley, "Epitaxial oxide heterostructures for ultimate high- T_c quantum interferometers," in: Applications of High- T_c Superconductivity, Adir Luiz editor, InTech; ISBN 978-953-307-308-8, pp.147-176, (2011).
- [2] M.I.Faley, U.Poppe, R. E. Dunin-Borkowski, M. Schiek, F. Boers, H. Chocholacs, J. Dammers, E. Eich, N. J. Shah, A. B. Ermakov, V. Yu. Slobodchikov, Yu. V. Maslennikov, and V. P. Koshelets "Magnetoencephalography using a multilayer high- T_c DC SQUID magnetometer", Physics Procedia, vol.36, pp.66-71 (2012).
- [3] M.I.Faley, U. Poppe, R. E. Dunin-Borkowski, M. Schiek, F. Boers, H. Chocholacs, J. Dammers, E. Eich, N. J. Shah, A. Ermakov, V. Yu. Slobodchikov, Yu. V. Maslennikov, and V. P. Koshelets, "High- T_c DC SQUIDS for magnetoencephalography", IEEE Transactions on Applied Superconductivity, v.23 Issue 3 part 1 p.1600705(5) (2013).
- [4] E. E. Mitchell and C. P. Foley, "YBCO step-edge junctions with high $I_c R_n$ ", Supercond. Sci. Technol. vol.23, pp. 065007(10pp) (2010).

Ultra-Compact Multi-Tip Scanning Tunneling Microscope

V. Cherepanov, E. Zubkov, H. Junker, S. Korte, M. Blab, P. Coenen, and B. Voigtländer

Peter Grünberg Institut-3, Forschungszentrum Jülich, Germany

We present a multi-tip scanning tunneling microscope (STM) where four independent STM units are integrated on a diameter of 50 mm. The coarse positioning of the tips is done under the control of an optical microscope or an SEM in vacuum. The heart of this STM is a new type of piezoelectric coarse approach called KoalaDrive[®]. The compactness of the KoalaDrive[®] allows building a four-tip STM as small as a single tip STM with a drift of less than 0.2 nm/min at room temperature and lowest resonance frequencies of 2.5 kHz (in xy) and 5.5 kHz (in z). We present as examples of the performance of the multi-tip STM four point measurements of silicide nanowires and graphene.

The controlled fabrication of self-organized nanostructures with dimensions in the single digit nanometer range is becoming possible. However, the measurement of charge transport through such nanostructures is still a challenge. Our approach is to establish contacts by a multi-tip STM in order to enable charge transport measurements at the nanoscale.

In order to perform stable electrical measurements at the nanoscale an ultimate mechanical stability of the instrument is required. We developed an instrument with currently unsurpassed stability using a new kind of nanopositioner, recently developed in Jülich: the KoalaDrive[®], which is described in detail in Ref. [1]. With this positioner as key element, it was possible to develop an ultra-compact multi-tip scanning probe instrument with an outer diameter of 50 mm and with a drift of less than 0.2 nm/minute at room temperature, as shown in Fig1 (a). The coarse motion of the four tips and the sample can be observed by an optical microscope from below, or in vacuum by a scanning electron microscope.

In the following we report on measurements performed with our multi-tip instrument. These results obtained demonstrate a proof of principle for electrical measurements on the nanoscale with a four tip STM. Performing electrical measurements with a four-tip STM is more than to have four tips and to be able to scan with them. Concerted measurements of currents and voltages with all four tips have to be performed on a real time basis.

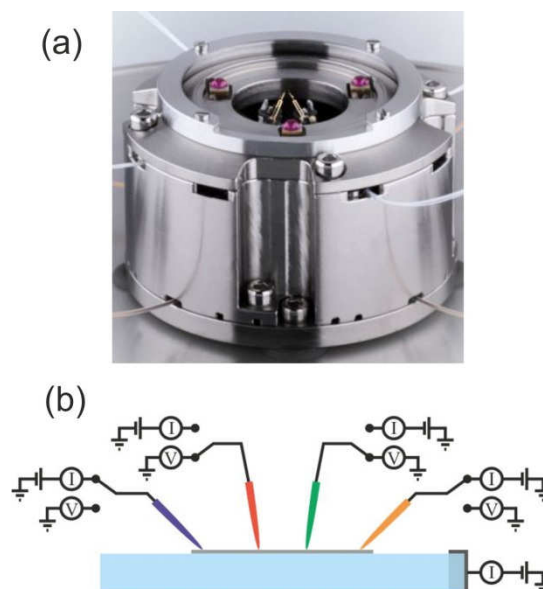


FIG. 1: (a) Photo of an ultra-compact four-tip STM with an outer diameter of 50 mm. (b) Each tip can be operated as current probe or voltage probe. Thus "concerted" spectroscopic measurements involving all four tips are possible.

Our electronics allows operating each tip either as current probe, or as voltage probe as shown in Fig1 (b). Before a n electrical measurement all four tips are scanning in STM mode and positioned to the desired positions at desired positions on the sample. A typical measurement is performed as follows: The feedback (e.g. for all four tips) is disabled and the tips are approached towards the sample by a desired distance. Subsequently, different I/V ramps are applied between different tips (and/or the sample).

In the simplest case a current is injected between the two outer tips and a potential difference is measured between the inner tips (classical four probe measurement). However, also various kinds of other measurements can be performed. If all desired voltage ramps are finished the tips are moved back to the original tunneling tip-sample distance and the feedback is resumed. In this way the electrical measurements on the nanoscale can be performed completely nondestructive.

As an example we show a four-tip measurement at an yttrium silicide nanowire. The yttrium silicide nanowires were grown by depositing 0.6 nm yttrium at 1070 K sample temperature. Due to the crystal structure of the Si(110) substrate the silicide nanowires are aligned along one direction

which is vertically in the SEM image shown in Fig. 2. The silicide nanowires have a height of 5 – 30 nm, a width between 30 – 50 nm and length of several micrometers. The four tips of the STM are positioned in a line in order to contact one nanowire as shown in Fig.2.

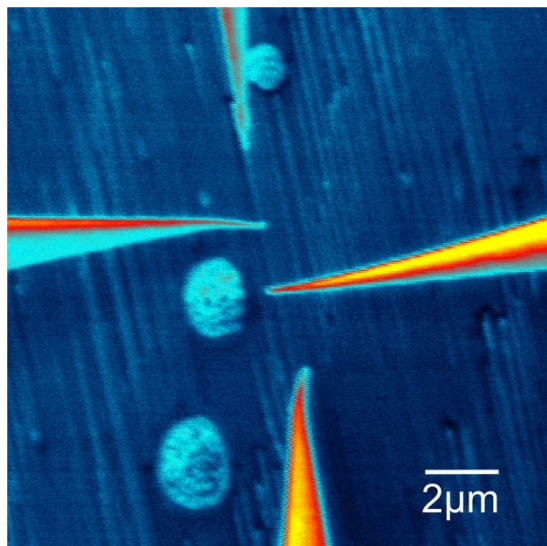


FIG. 2: SEM image of Y-silicide nanowires grown on Si(110). Due to the crystal symmetry of the Si(110) substrate the silicide nanowires are aligned in the vertical direction. The four STM tips are positioned in a line in order to contact one nanowire.

In principle the current injected by one of the outer probes can run not only through the nanowire as desired, but can also leak to the silicon substrate. In this context it is important to keep in mind that the interface between silicide nanowire to the silicon substrate forms a Schottky barrier. If this Schottky barrier is reverse biased, no current will flow to the substrate. We confirmed this by measuring the current to the substrate by a fifth current preamplifier Fig.1 (b). If the Schottky barrier was reverse biased, only a negligible current was detected proving that the current runs almost only through the silicide nanowire.

After establishing a current through the nanowire by the outer probes, the potential of the inner probes was determined. A voltage difference of 167 mV was measured between the inner tips while a current of 200 μ A was injected by the outer tips. This results in a resistance of in a resistance of 935 Ω . Taking into account the distance between the inner tips (2.4 μ m), as well as the height (~15 nm) and the average width (~50 nm) of the nano wire, results in a resistivity of 26 μ Ω cm. This value can be compared to a resistivity of about 50 μ Ω cm measured on thin yttrium silicide thin films [3,4]. This value is also comparable to the resistivity measured before on cobalt silicide nanowires using multi tip scanning tunneling microscopes [5].

We have shown that the development of a new type of piezoelectric motor serves as the basis for ultra-compact scanning probe microscopes. The KoalaDrive[®] can tap its full potential for the miniaturization in the case of multi tip scanning probe instruments. We constructed an ultra-compact multi-tip STM with an outer diameter of 50 mm with a drift of less than 0.2 nm/min at ambient conditions, which is now also commercially available [6]. This instrument can be combined with an optical microscope or a SEM in order to navigate the positioning of the tips. We demonstrate the capabilities of the instrument by four point measurements at an yttrium silicide nanowire. Here, concerted measurement processes starting and ending with the tips in tunneling conditions are essential in order to perform nondestructive electrical measurements at the nanoscale.

-
- [1] V. Cherepanov, P. Coenen, and B. Voigtländer, Rev. Sci. Instr. 83, 023703 (2012).
 - [2] V. Cherepanov, E. Zubkov, H. Junker, S. Korte, M. Blab, P. Coenen, and B. Voigtländer, Rev. Sci. Instrum. 83, 033707 (2012).
 - [3] M. Gurvitch, A. F. J. Levi, R. T. Tung, and S. Nakahara, Appl. Phys. Lett. 51, 311 (1987).
 - [4] M. P. Siegal, F. H. Kaatz, W. R. Graham, J. J. Santiago, and J. Van der Spiegel, J. Appl. Phys. 66, 2999 (1989).
 - [5] S. Yoshimoto, Y. Murata, K. Kubo, K. Tomita, K. Motoyoshi, T. Kimura, H. Okino, R. Hobara, I. Matsuda, S. Honda, M. Katayama, and S. Hasegawa, Nano Lett. 7, 956 (2007).
 - [6] www.mprobes.com

Investigations of EUV conversion efficiency of luminophores

S. Herbert¹, A. Bartelt¹, S. Danylyuk¹, P. Loosen¹, L. Juschkin²

¹ Chair for Technology of Optical Systems, RWTH Aachen University, Germany

² Chair for the Experimental Physics of EUV, RWTH Aachen University, Germany

The efficiency of luminophores to convert impinging short wavelength radiation into visible (VIS) light and their self-absorption of the converted light has been investigated. Five scintillator crystals and seven phosphors were illuminated with extreme ultraviolet (EUV) radiation of 13.5 nm wavelength and the converted light measured with a photo diode. Parallel measurements of the EUV radiation with a dose monitor enabled the calculation of the conversion efficiency. Furthermore, the self-absorption of the samples has been investigated with a broadband VIS spectrometer. This has allowed estimating the change of the conversion efficiency with the sample thickness.

Imaging in the extreme ultraviolet wavelength regime is challenging, due to the light's short penetration depth of a few hundred nanometers for solid materials [1]. Consequently, front side illuminated cameras cannot be used, as the uppermost layers thickness of silicon and silicon oxide is around 500 nm [2]. One imaging solution in the EUV is the use of a luminophore linked with a VIS camera [3]. The efficiency of this approach depends on conversion efficiency of luminophores, the degree of self-absorption of the reemitted light and their long term stability. In literature the properties of luminophores are widely studied, but mostly with particle or x-ray excitation [4]. Furthermore, a comparison between reported literature values is difficult, because the properties of luminophores are strongly dependent on their doping, which mostly is not documented [3]. For the choice of a proper luminophore for a certain application in the EUV, investigations of luminophore properties are mandatory.

In this work conversion efficiency and self-absorption of 12 luminophores (5 scintillators manufactured by Korth Kristalle GmbH and 7 phosphors from PhosphorTech Corporation) have been investigated. The conversion efficiency η_{conv} is defined as the ratio between the measured η_{meas} and the ideal photon yield η_{ideal} . Here the photon yield is the number of reemitted photons per impinging EUV photon. The reemitted light is radiated into 4π sr solid angle, but can only be detected in 2π sr with a plane detector. The ideal photon yield is therefore determined by the half of the energy ratio of the incident and the reemitted photon (Table 1).

Sample	LiF	CsI:TI	BaF ₂ ¹	CaF ₂ :Eu	YAG:Ce	Y550
λ [nm]	410	560	310 220	435	550	550
n^2	1.4	1.8	1.5 1.5	1.4	1.8	1.7
η_{ideal}	15.2	20.7	11.5 8.2	16.1	20.4	20.4

Sample	Y560	G540	R620	R650	P1	P43
λ [nm]	560	545	620	650	528	545
n^b	1.7	1.5	1.5	1.5	2.2	2.3
η_{ideal}	20.7	20.2	23.0	24.1	19.4	20.2

Table 1: Properties of the investigated samples

¹ BaF₂ emits in two wavelengths

² refraction index at the emission wavelength

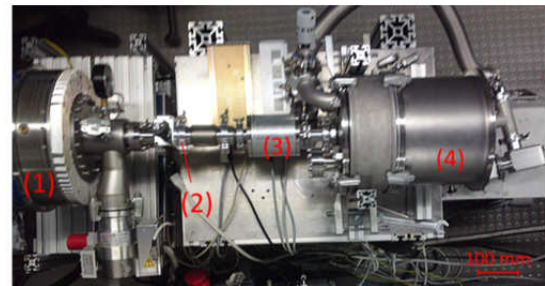


FIG. 1: Photograph of the experimental setup. (1) EUV source, (2) aperture, (3) multilayer mirror spectral band-pass filter and (4) sample chamber with dose monitor, sample and photo diode (not shown: oscilloscope for detection of dose monitor- and photodiode signals)

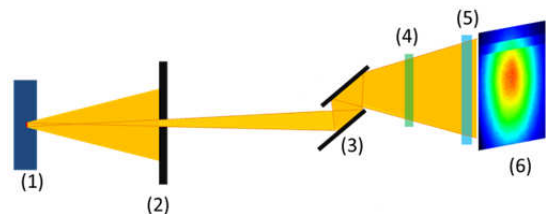


FIG. 2: Scheme of the light propagation through the experimental setup. (1) EUV source, (2) aperture, (3) multilayer mirror spectral band-pass filter, (4) dose monitor, (5) sample and (6) photodiode

The scintillator samples had a diameter of 10 mm and a thickness of 3 mm, the 10 μm thick phosphor layers had been deposited on fused silica substrates of 12.5 mm diameter and 3 mm thickness. All samples had been measured in the experimental setup shown in FIG. 1 and FIG. 2.

The experimental setup consists of a EUV source, which emits light into 4π sr solid angle. The light cone is tailored to the required size by an aperture in the beam path. The light which passed the aperture is spectrally filtered by a band-pass EUV filter. This filter consists of two multilayer mirrors, which have their peak reflectivity at 13.5 nm. The band-width of the band-pass filter is 4% around 13.5 nm. After the band-pass filter, the light passes through the dose monitor. This consists of a 200 nm thin Zr-foil and measures the amount of photoelectrons excited in the foil by the partially absorbed EUV radiation. The dose monitor is calibrated to provide an absolute number of EUV photons transmitted through the foil. The transmitted EUV light is then hitting the sample, where it is converted into VIS light. The reemitted VIS light is detected by a photodiode within a certain solid angle Ω , which is determined by the distance to the diode, the size of the diode and a refractive index of a luminophore (see Table 2). The signals of the photodiode and the dose monitor are recorded by an oscilloscope.

The measured photon yield η_{meas} is then calculated as the ratio of the amount of EUV photons hitting the sample and the amount of VIS photons, measured by the photodiode. The amount of EUV photons is calculated from the signal of the dose monitor and the amount of VIS photons is extracted from the measured photodiode current. With η_{meas} and the ideal photon yield η_{ideal} (Table 1), the conversion efficiency in the corresponding solid angle Ω is calculated (Table 2).

Sample	LiF	CsI:TI	BaF ₂	CaF ₂ :Eu	YAG:Ce	Y550
η_{conv} [%]	0.11	0.04	0.28 *	0.67	1.54	5.00
α [1/mm]	0.012	0.041	0.016 0.012	0.014	0.305	-
Ω [sr]	1.793	1.135	1.592	1.793	1.135	1.214
Sample	Y560	G540	R620	R650	P1	P43
η_{conv} [%]	4.42	1.31	2.83	1.36	3.60	15.59
α [1/mm]	42.85	41.13	79.90	71.39	22.33	69.42
Ω [sr]	1.214	1.576	1.576	1.576	0.718	0.656

Table 2: conversion efficiencies η_{conv} , absorption coefficients α and detectable solid angles Ω of the investigated samples

* Sum of the weighted efficiencies for both emitted wavelengths

To determine a degree of self-absorption of the VIS radiation, the samples were illuminated at their emission wavelengths in a Lambda1050 broadband spectrometer. The transmitted light was measured by a photodiode inside an integration sphere. Taking into account reflection

losses and known sample thickness, the absorption coefficient α had been calculated, using the Beer-Lambert law (Table 2). With the known absorption coefficient α , the conversion efficiency as a function of sample thickness is calculated (FIG. 3 and FIG. 4).

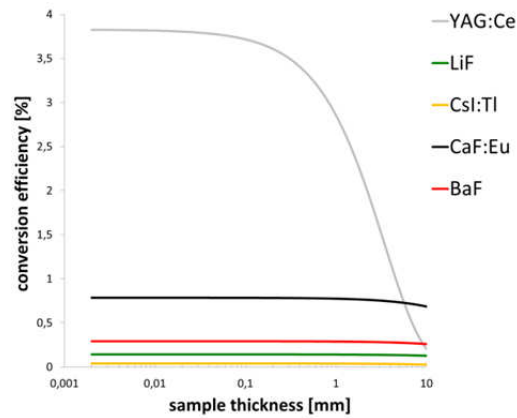


FIG. 3: Conversion efficiencies of the scintillator samples as a function of sample thickness

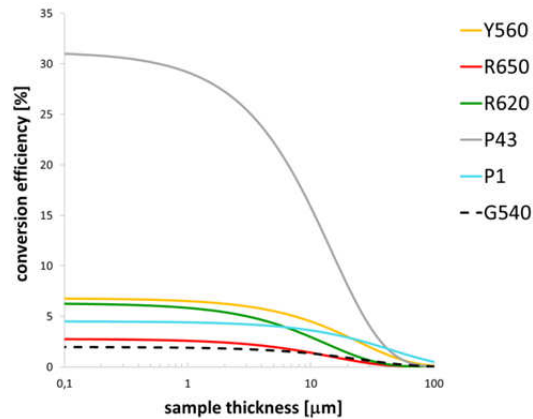


FIG. 4: Conversion efficiencies of the phosphor samples as a function of sample thickness

Generally, the investigated phosphors show higher conversion efficiencies in comparison with the scintillators. On the other hand, the scintillators show significantly lower self-absorption, which allows the fabrication of thick (and therewith solid) screens or windows. Among the investigated samples best efficiencies have been obtained with P43 phosphor and YAG:Ce scintillator crystal.

This work was supported by Ali Benmoussa from the Royal Observatory of Belgium, who supplied the phosphor coated samples.

- [1] M. Banyay et al, Meas. Sci. Technol., 20 105201 (2009)
- [2] R. P. Kraft et al, The Astrophysical Journal, 466:L51-L54 (1996)
- [3] M. Booth et al, Proc. of SPIE 5751 (2005)
- [4] <http://scintillator.lbl.gov/>

Publications

- Aabdin Z., Peranio N., Eibl O., Tollner W., Nielsch K., Bessas D., Hermann R., Winkler M., König J., Bottner H., Pacheco V., Schmidt J., Hashibon A., and Elsasser C.
Nanostucture, Excitations, and Thermoelectric Properties of Bi₂Te₃-Based Nanomaterials
Journal of Electronic Materials **41**, 1792 (2012)
- Aabdin Z., Peranio N., Winkler M., Bessas D., König J., Hermann R. P., Bottner H., and Eibl O.
Sb₂Te₃ and Bi₂Te₃ Thin Films Grown by Room-Temperature MBE
Journal of Electronic Materials **41**, 1493 (2012)
- Afanasenkau D. and Offenhäusser A.
Positively Charged Supported Lipid Bilayers as a Biomimetic Platform for Neuronal Cell Culture
Langmuir **28**, 13387 (2012)
- Ahmed M., Ganesan A., Wang F., Feyer V., Plekan O., and Prince K. C.
Photoelectron Spectra of Some Antibiotic Building Blocks: 2-Azetidinone and Thiazolidine-Carboxylic Acid
The Journal of Physical Chemistry / A **116**, 8653 (2012)
- Akola J. and Jones R. O.
Structure and dynamics in amorphous tellurium and Te_n clusters: A density functional study
Physical Review B **85**, 134103 (2012)
- Alekseev P. A., Nemkovskiy K., Mignot J.-M., Goremychkin E. A., Lazkov V. N., Shitsevalova N. Y., and Dukhnenko A. V.
Influence of an electron doping on spin dynamics of YbB₁₂
Solid State Sciences **14**, 1584 (2012)
- Ali S. R., Ghadimi M. R., Fecioru-Morariu M., Beschoten B., and Guntherodt G.
Training effect of the exchange bias in Co/CoO bilayers originates from the irreversible thermoremanent magnetization of the magnetically diluted antiferromagnet
Physical Review B **85**, 012404 (2012)
- Anbarasu M., Wimmer M., Bruns G., Salinga M., and Wuttig M.
Nanosecond threshold switching of GeTe₆ cells and their potential as selector devices
Applied Physics Letters **100**, 143505 (2012)
- Angst M., Brückel T., Richter D., and Zorn R. (eds.)
Scattering Methods for Condensed Matter: Towards Novel Applications at Future Sources,
Lecture notes of the 43rd IFF Spring School 2012
Series: Key Technologies, Vol. 33, Verlag des Forschungszentrum Jülich (2012),
ISBN: 978-3-89336-759
- Antonova E., Nather C., Kogerler P., and Bensch W.
Expansion of Antimonato Polyoxovanadates with Transition Metal Complexes: (Co(N₃C₅H₁₅)₂)₂ {Co(N₃C₅H₁₅)₂}V₁₅Sb₆O₄₂(H₂O)•5H₂O and (Ni(N₃C₅H₁₅)₂)₂ {Ni(N₃C₅H₁₅)₂}V₁₅Sb₆O₄₂(H₂O)•8H₂O
Inorganic Chemistry **51**, 2311 (2012)
- Antonova E., Nather C., Kogerler P., and Bensch W.
A C-2-symmetric antimonato polyoxovanadate cluster V₁₆Sb₄O₄₂(H₂O)⁸⁻ derived from the {V₁₈O₄₂} archetype
Dalton Transactions **41**, 6957 (2012)
- Atodiressei N., Caciuc V., Blügel S., and Callsen M.
Semiempirical van der Waals interactions versus ab initio nonlocal correlation effects in the thiophene-Cu(111) system
Physical Review B **86**, 085439 (2012)
- Baldasseroni C., Bordel C., Gray A. X., Kaiser A. M., Kronast F., Herrero-Albillos J., Schneider C. M., Fadley C. S., and Hellman F.
Temperature-driven nucleation of ferromagnetic domains in FeRh thin films
Applied Physics Letters **100**, 262401 (2012)
- Bannani F., Floquet S., Leclerc-Laronze N., Haouas M., Taulelle F., Marrot J., Kogerler P., and Cadot E.
Cubic Box versus Spheroidal Capsule Built from Defect and Intact Pentagonal Units
Journal of the American Chemical Society **134**, 19342 (2012)
- Banyay M., Juschkin L., Bersch E., Franca D., Liehr M., and Diebold A.
Cross characterization of ultrathin interlayers in HfO₂ high-k stacks by angle resolved x-ray photoelectron spectroscopy, medium energy ion scattering, and grazing incidence extreme ultraviolet reflectometry
Journal of Vacuum Science & Technology A **30**, 041506 (2012)
- Bar-Sadan M., Barthel J., Shtrikman H., and Houben L.
Direct imaging of single Au atoms in GaAs nanowires
Nano Letters **12**, 2352 (2012)

- Barthel C., Medford J., Bluhm H., Yacoby A., Marcus C. M., Hanson M. P., and Gossard A. C.
Relaxation and readout visibility of a singlet-triplet qubit in an Overhauser field gradient
Physical Review B **85**, 035306 (2012)
- Barthel J., Braun M., Ganter C., and Janiak C.
Weakly-coordinated stable platinum nanocrystals
Crystal Engineering **14**, 7607 (2012)
- Bauer O., Mercurio G., Willenbockel M., Reckien W., Heinrich Schmitz C., Fiedler B., Soubatch S., Bredow T., Tautz F. S., and Sokolowski M.
Role of functional groups in surface bonding of planar π -conjugated molecules
Physical Review B **86**, 235431 (2012)
- Bayersdorfer P., Stadtmüller B., Kleimann C., Mercurio G., Reinert F., Kumpf C., and Kröger I.
Submonolayer growth of H₂-phthalocyanine on Ag(111)
Physical Review B **86**, 195412 (2012)
- Bessas D., Sergueev I., Wille H.-C., Perßon J., Ebling D., and Hermann R.
Lattice dynamics in Bi₂Te₃ and Sb₂Te₃: Te and Sb density of phonon states
Physical Review B **86**, 224301 (2012)
- Besson C., Frielinghaus R., Saelhoff A.-K., Flötotto H., Houben L., Kögerler P., Schneider C. M., and Meyer G.
Covalent functionalization of carbon nanotubes with tetramanganese complexes
Physica Status Solidi / B **249**, 2412 (2012)
- Besson C., Schmitz S., Capella K. M., Kopilevich S., Weinstock I. A., and Kogerler P.
A regioselective Huisgen reaction inside a Keplerate polyoxomolybdate nanoreactor
Dalton Transactions **41**, 9852 (2012)
- Betzinger M., Friedrich C., Görling A., and Blügel S.
Precise response functions in all-electron methods: Application to the optimized-effective-potential approach
Physical Review B **85**, 245124 (2012)
- Bihlmayer G., Luysberg M., Blügel S., and Rahmanizadeh K.
First-principles study of intermixing and polarization at the DyScO₃/SrTiO₃ interface
Physical Review B **85**, 075314 (2012)
- Bisson R., Themlin J.-M., Layet J.-M., Angot T., and Bocquet F. C.
Reversible hydrogenation of deuterium-intercalated quasi-free-standing graphene on SiC(0001)
Physical Review B **85**, 201401 (2012)
- Blizak S., Bihlmayer G., and Blügel S.
Ab initio investigations of magnetic properties of FeCo monolayer alloy films on Rh(001)
Physical Review B **86**, 094436 (2012)
- Blomers C., Grap T., Lepsa M. I., Moers J., Trellenkamp S., Grutzmacher D., Luth H., and Schapers T.
Hall effect measurements on InAs nanowires
Applied Physics Letters **101**, 152106 (2012)
- Blomers C., Lu J. G., Huang L., Witte C., Grutzmacher D., Luth H., and Schapers T.
Electronic Transport with Dielectric Confinement in Degenerate InN Nanowires
Nano Letters **12**, 2768 (2012)
- Bolten M., Thiess A., Yavneh I., and Zeller R.
Preconditioning systems arising from the KKR Green function method using block-circulant matrices
Linear Algebra and its Applications **436**, 436 (2012)
- Bonesteel N. E. and DiVincenzo D.
Quantum Circuits for Measuring Levin-Wen Operators
Physical Review B **86**, 165113 (2012)
- Bonnes L., Hazzard K. R. A., Manmana S. R., Rey A. M., and Wessel S.
Adiabatic Loading of One-Dimensional SU(N) Alkaline-Earth-Atom Fermions in Optical Lattices
Physical Review Letters **109**, 205305 (2012)
- Bonnes L. and Wessel S.
Half-vortex unbinding and Ising transition in constrained superfluids
Physical Review B **85**, 094513 (2012)

- Borgelt C., Picado D., Berger D., Gerstein G., and Grün S.
Cell assembly detection with frequent item set mining
BMC Neuroscience **13**, 126 (2012)
- Botar B., Ellern A., and Kogerler P.
Mapping the formation areas of giant molybdenum blue clusters: a spectroscopic study
Dalton Transactions **41**, 8951 (2012)
- Breznay N. P., Volker H., Palevski A., Mazzarello R., Kapitulnik A., and Wuttig M.
Weak antilocalization and disorder-enhanced electron interactions in annealed films of the phase-change compound GeSb_2Te_4
Physical Review B **86**, 205302 (2012)
- Brontvein, Stroppa D., Popovitz-Biro R., Albu-Yaron A., Levy M., Feuerman D., Houben L., Tenne R., and Gordon J. M.
New high-temperature Pb-catalyzed synthesis of nanotubes
Journal of the American Chemical Society **134**, 39 (2012)
- Brooks C. M., Misra R., Mundy J. A., Zhang L. A., Holinworth B. S., O'Neal K. R., Heeg T., Zander W., Schubert J., Musfeldt J. L., Liu Z. K., Müller D. A., Schiffer P., and Schlom D. G.
The adsorption-controlled growth of LuFe_2O_4 by molecular-beam epitaxy
Applied Physics Letters **101**, 132907 (2012)
- Brose S., Danylyuk S., Juschkin L., Dittberner C., Bergmann K., Moers J., Panaitov G., Trellenkamp S., Loosen P., and Grutzmacher D.
Broadband transmission masks, gratings and filters for extreme ultraviolet and soft X-ray lithography
Thin Solid Films **520**, 5080 (2012)
- Brüggemann D., Michael K. E., Wolfrum B., and Offenhäusser A.
Adhesion and survival of electrogenic cells on gold nanopillar array electrodes
International Journal of Nano and Biomaterials **4**, 108 (2012)
- Brussing F., Toperverg B., Zhernenkov K., Devishvili A., Zabel H., Wolff M., Theis-Brohl K., Wiemann C., Kaiser A., and Schneider C. M.
Magnetization and magnetization reversal in epitaxial Fe/Cr/Co asymmetric spin-valve systems
Physical Review B **85**, 174409 (2012)
- Buca D., Holländer B., Hartmann J. M., Bourdelle K. K., Mantl S., and Minamisawa R. A.
p-Type Ion Implantation in Tensile $\text{Si}_{0.5}\text{Ge}_{0.5}$ /Tensile Strained Si Heterostructures
Journal of the Electrochemical Society **159**, H44 (2012)
- Buller S., Koch C., Bensch W., Zalden P., Sittner R., Kremers S., Wuttig M., Schurmann U., Kienle L., Leichtweiss T., Janek J., and Schonborn B.
Influence of Partial Substitution of Te by Se and Ge by Sn on the Properties of the Blu-ray Phase-Change Material $\text{Ge}_8\text{Sb}_2\text{Te}_{11}$
Chemistry of Materials **24**, 3582 (2012)
- Butler W., Richter M., Koepernik K., Şaşıoğlu E., Friedrich C., Blügel S., and Sims H.
Theoretical investigation into the possibility of very large moments in Fe_{16}N_2
Physical Review B **86**, 174422 (2012)
- Caciuc V., Atodiresei N., Blügel S., and Tsukamoto S.
Tuning the electron transport of molecular junctions by chemically functionalizing anchoring groups: First-principles study
Physical Review B **85**, 245435 (2012)
- Caciuc V., Atodiresei N., Callsen M., Lazic P., and Blügel S.
Ab initio and semi-empirical van der Waals study of graphene-boron nitride interaction from a molecular point of view
Journal of Physics / Condensed Matter **24**, 424214 (2012)
- Calvo H., Classen L., Splettstoesser J., and Wegewijs M. R.
Interaction-induced charge and spinpumping through a quantum dot at finite bias
Physical Review B **86**, 245308 (2012)
- Cavalca F., Laursen A. B., Kardynal B. E., Dunin-Borkowski R., and Hansen T. W.
In situ transmission electron microscopy of light-induced photocatalytic reactions
Nanotechnology **23**, 075705 (2012)
- Chen T., Huang Y., Dasgupta A., Luysberg M., Houben L., Yang D., Carius R., and Finger F.
Microcrystalline silicon carbide window layers in thin film silicon solar cells
Solar Energy Materials & Solar Cells **98**, 370 (2012)

- Cherepanov V., Coenen P., and Voigtländer B.
A nanopositioner for scanning probe microscopy: The KoalaDrive
Review of Scientific Instruments **83**, 023703 (2012)
- Cherepanov V., Zubkov E., Junker H., Korte S., Blab M., Coenen P., and Voigtlander B.
Ultra compact multipoint scanning tunneling microscope with a diameter of 50 nm
Review of Scientific Instruments **83**, 033707 (2012)
- Cho D. Y., Jung H. S., Yu I. H., Park W. G., Cho S., Kim U., Oh S. J., Park B. G., Chang F. H., Lin H. J., and Hwang C. S.
Nondestructive investigation of interface states in high-k oxide films on Ge substrate using X-ray absorption spectroscopy
Physica Status Solidi-Rapid Research Letters **6**, 181 (2012)
- Cho D. Y., Jung H. S., Yu I. H., Yoon J. H., Kim H. K., Lee S. Y., Jeon S. H., Han S., Kim J. H., Park T. J., Park B. G., and Hwang C. S.
Stabilization of Tetragonal HfO₂ under Low Active Oxygen Source Environment in Atomic Layer Deposition
Chemistry of Materials **24**, 3534 (2012)
- Cho D. Y., Valov I., van den Hurk J., Tappertzhofen S., and Waser R.
Direct Observation of Charge Transfer in Solid Electrolyte for Electrochemical Metallization Memory
Advanced Materials **24**, 4552 (2012)
- Cho J.-H., Sanyal B., Bihlmayer G., and Choi Y.-K.
Weak antiferromagnetic superexchange interaction in fcc C₆₀H_n
Physical Review B **86**, 081415(R) (2012)
- Choi Y. J., Won S. J., Jung H. S., Park S., Cho D. Y., Hwang C. S., Park T. J., and Kim H. J.
Effects of Oxygen Source on Film Properties of Atomic-Layer-Deposited La-Silicate Film Using La[N(SiMe₃)₂]₃
Ecs Solid State Letters **1**, N4 (2012)
- Chuntonov L., Bar-Sadan M., Houben L., and Haran G.
Correlating Electron Tomography and Plasmon Spectroscopy of Single Noble Metal Core-Shell Nanoparticles
Nano Letters **12**, 145 (2012)
- Cleven N. J., Muntjes J. A., Fassbender H., Urban U., Gortz M., Vogt H., Grafe M., Gottsche T., Penzkofer T., Schmitz-Rode T., and Mokwa W.
A Novel Fully Implantable Wireless Sensor System for Monitoring Hypertension Patients
IEEE Transactions on Biomedical Engineering **59**, 3124 (2012)
- Conde J. C., Benedetti A., Serra C., Werner J., Oehme M., Schulze J., Buca D. M., Holländer B., Mantl S., Chiussi S., and Stefanov S.
Silicon germanium tin alloys formed by pulsed laser induced epitaxy
Applied Physics Letters **100**, 204102 (2012)
- Contreras-Pulido L. D., Splettstoesser J., Governale M., König J., and Buttiker M.
Time scales in the dynamics of an interacting quantum dot
Physical Review B **85**, 075301 (2012)
- Costi T. A. and Merker L.
Numerical renormalization group calculation of impurity internal energy and specific heat of quantum impurity models
Physical Review B **86**, 075150 (2012)
- Costi T. A. and Zlatić V.
Charge Kondo Anomalies in PbTe Doped with Tl Impurities
Physical Review Letters **108**, 036402 (2012)
- Cui C. H., Gan L., Li H. H., Yu S. H., Heggen M., and Strasser P.
Octahedral PtNi Nanoparticle Catalysts: Exceptional Oxygen Reduction Activity by Tuning the Alloy Particle Surface Composition
Nano Letters **12**, 5885 (2012)
- Dadda J., Müller E., Klobes B., Pereira P. B., and Hermann R.
Electronic Properties as a Function of Ag/Sb Ratio in Ag_{1-y}Pb₁₈Sb_{1+z}Te₂₀ Compounds
Journal of Electronic Materials **41**, 2065 (2012)
- Danylyuk S., Juschkin L., Dittberner C., Bergmann K., Moers J., Panaitov G., Trellenkamp S., Loosen P., Grützmacher D., and Brose S.
Broadband transmission masks, gratings and filters for extreme ultraviolet and soft X-ray lithography
Thin Solid Films **520**, 5080 (2012)

- Dauber J., Terres B., Trellenkamp S., and Stampfer C.
Encapsulating graphene by ultra-thin alumina for reducing process contaminations
Physica Status Solidi B-Basic Solid State Physics **249**, 2526 (2012)
- de Groot J., Marty K., Lumsden M. D., Christianson A. D., Nagler S. E., Adiga S., Borghols W. J. H., Schmalzl K., Yamani Z., Bland S. R., de Souza R., Staub U., Schweika W., Su Y., and Angst M.
Competing Ferri- and Antiferromagnetic Phases in Geometrically Frustrated LuFe_2O_4
Physical Review Letters **108**, 037206 (2012)
- de Groot J., Müller T., Rosenberg R. A., Keavney D. J., Islam Z., Kim J.-W., and Angst M.
Charge Order in LuFe_2O_4 : An Unlikely Route to Ferroelectricity
Physical Review Letters **108**, 187601 (2012)
- Deringer V. L., Goerens C., Esters M., Dronskowski R., and Fokwa B. P. T.
Chemical Modeling of Mixed Occupations and Site Preferences in Anisotropic Crystal Structures: Case of Complex Intermetallic Borides
Inorganic Chemistry **51**, 5677 (2012)
- Deringer V. L., Hoepfner V., and Dronskowski R.
Accurate Hydrogen Positions in Organic Crystals: Assessing a Quantum-Chemical Aide
Crystal Growth & Design **12**, 1014 (2012)
- Deringer V. L., Lumeij M., and Dronskowski R.
Ab Initio Modeling of $\alpha\text{-GeTe}(111)$ Surfaces
Journal of Physical Chemistry C **116**, 15801 (2012)
- De Souza R.A., Martin M.
Secondary Ion Mass Spectrometry – a powerful tool for studying elemental distributions over various length scales
in *Methods in Physical Chemistry*, Eds. R. Schäfer and P.C. Schmidt (Wiley-VCH), pp. 548-574 (2012)
- Di Napoli S., Thiess A., Blügel S., and Mokrousov Y.
Modelling impurity-assisted chain creation in noble-metal break junctions
Journal of Physics / Condensed Matter **24**, 135501 (2012)
- Di Vece M., Laursen A. B., Bech L., Maden C. N., Duchamp M., Mateiu R. V., Dahl S., and Chorkendorff I. B.
Quenching of TiO_2 photo catalysis by silver nanoparticles
Journal of Photochemistry and Photobiology / A **230**, 10 (2012)
- Ding L., Schulz P., Farahzadi A., Shportko K. V., and Wuttig M.
Investigation of intermolecular interactions in perylene films on $\text{Au}(111)$ by infrared spectroscopy
Journal of Chemical Physics **136**, 054503 (2012)
- Disch S., Wetterskog E., Hermann R., Wiedenmann A., Vainio U., Salazar-Alvarez G., Bergström L., and Brückel T.
Quantitative spatial magnetization distribution in iron oxide nanocubes and nanospheres by polarized small-angle neutron scattering
New Journal of Physics **14**, 013025 (2012)
- Dittmann R., Muenstermann R., Krug I., Park D., Menke T., Mayer J., Besmehn A., Kronast F., Schneider C. M., and Waser R.
Scaling Potential of Local Redox Processes in Memristive SrTiO_3 Thin-Film Devices
Proceedings of the IEEE **100**, 1979 (2012)
- Divin Y., Lyatti M., Poppe U., and Urban K.
Identification of Liquids by High-Tc Josephson THz Detectors
Physics Procedia **36**, 29 (2012)
- Divin Y., Lyatti M., Poppe U., Urban K., and Pavlovskiy V. V.
Josephson Spectroscopy for Identification of Liquids
IEEE Transactions on Applied Superconductivity **21**, 311 (2012)
- DiVincenzo D.
Roadmap for the Large-Scale Quantum Computer
Physical Review / Special topics / Accelerators and beams **2**, 030001 (2012)
- Dominguez F., Hassler F., and Platero G.
Dynamical detection of Majorana fermions in current-biased nanowires
Physical Review B **86**, 140503 (2012)
- Dong H., Zhang G., Wang Y., Zhang Y., Xie X., Krause H.-J., Braginski A., and Offenhäusser A.
Effect of voltage source internal resistance on the SQUID bootstrap circuit
Superconductor Science and Technology **25**, 015012 (2012)

- Droscher S., Roulleau P., Molitor F., Studerus P., Stampfer C., Ensslin K., and Ihn T.
Quantum capacitance and density of states of graphene
Physica Scripta **T146**, 014009 (2012)
- Droste S., Andergassen S., and Splettstoesser J.
Josephson current through interacting double quantum dots with spin-orbit coupling
Journal of Physics-Condensed Matter **24**, 415301 (2012)
- Ducroquet F., Engström O., Gottlob H. D. B., Lopes J. M. J., and Schubert J.
Admittance Spectroscopy of Si/LaLuO₃ and Si/GdSiO MOS Structures
ECS Transactions **45**, 103 (2012)
- Dulcevscaia G. M., Filippova I. G., Speldrich M., van Leusen J., Kravtsov V. C., Baca S. G., Kogerer P., Liu S. X., and Decurtins S.
Cluster-Based Networks: 1D and 2D Coordination Polymers Based on {MnFe₂(μ₃-O)}-Type Clusters
Inorganic Chemistry **51**, 5110 (2012)
- Ebert P., Landrock S., Chiu Y. P., Breuer U., and Dunin-Borkowski R.
Dopant mapping of Be δ-doped layers in GaAs tailored by counterdoping using scanning tunneling microscopy
Applied Physics Letters **101**, 192103 (2012)
- Ebert P., Landrock S., Jiang Y., Wu K. H., Wang E. G., and Dunin-Borkowski R.
Electronically nonalloyed state of a statistical single atomic layer semiconductor alloy
Nano Letters **12**, 5845 (2012)
- Effertz C., Lahme S., Schulz P., Segger I., Wuttig M., Classen A., and Bolm C.
Design of Novel Dielectric Surface Modifications for Perylene Thin-Film Transistors
Advanced Functional Materials **22**, 415 (2012)
- Eisele H. and Ebert P.
Non-polar group-III nitride semiconductor surfaces
Physica Status Solidi / Rapid Research Letters **6**, 359 (2012)
- Eisele H., Ebert P., Liu N., and Holmes A. L.
Reverse mass transport during capping of In_{0.5}Ga_{0.5}As/GaAs quantum dots
Applied Physics Letters **101**, 233107 (2012)
- Ellern A. and Kogerler P.
[Co^{II}Mo^{V12}O₂₈(OH)₁₂(H₂O)₁₂]•12H₂O: facilitating single-crystal growth by deuteration
Acta Crystallographica Section C-Crystal Structure Communications **68**, I17 (2012)
- Eom T., Choi S., Choi B. J., Lee M. H., Gwon T., Rha S. H., Lee W., Kim M. S., Xiao M. C., Buchanan I., Cho D. Y., and Hwang C. S.
Conformal Formation of (GeTe₂)_{1-x}(Sb₂Te₃)_x Layers by Atomic Layer Deposition for Nanoscale Phase Change Memories
Chemistry of Materials **24**, 2099 (2012)
- Fang X. K., Kogerler P., Speldrich M., Schilder H., and Luban M.
A polyoxometalate-based single-molecule magnet with an S=21/2 ground state
Chemical Communications **48**, 1218 (2012)
- Faribault A. and Schuricht D.
On the determinant representations of Gaudin models' scalar products and form factors
Journal of Physics a-Mathematical and Theoretical **45**, 485202 (2012)
- Faley M. I., Poppe U., Dunin-Borkowski R. E., Schiek M., Boers F., Chocholacs H., Dammers J., Eich E., Shah N., Ermakov A., Slobodchikov V., Maslennikov Y., and Koshelets V.
High- T c DC SQUIDS for Magnetoencephalography
in *IEEE Transactions on Applied Superconductivity* Vol. 23, p. 1600705 (2012).
- Faure B., Wetterskog E., Gunnarsson K., Josten E., Hermann R. P., Brückel T., Andreassen J. W., Meneau F., Meyer M., Lyubartsev A., Bergström L., Salazar-Alvarez G., and Svedlindh P.
2D to 3D crossover of the magnetic properties in ordered arrays of iron oxide nanocrystals
Nanoscale **5**, 953 – 960 (2012)
- Feenstra R. M., Ebert P., Dunin-Borkowski R. E., Walker J., Towe E., and Gaan S.
Structure and electronic spectroscopy of steps on GaAs(110) surfaces
Surface Science **606**, 28 (2012)
- Fernandez-Gonzalez C., Schuch N., Wolf M. M., Cirac J. I., and Perez-Garcia D.
Gapless Hamiltonians for the Toric Code Using the Projected Entangled Pair State Formalism
Physical Review Letters **109**, 260401 (2012)

- Feyer V., Plekan O., Ptasinska S., Iakhnenko M., Tsud N., and Prince K. C.
Adsorption of Histidine and a Histidine Tripeptide on Au(111) and Au(110) from Acidic Solution
The Journal of Physical Chemistry / C **116**, 22960 (2012)
- Fielden J., Long D. L., Speldrich M., Kogerler P., and Cronin L.
[Co_xCu_{1-x}](DDOP)(OH₂)(NO₃)](NO₃): hydrogen bond-driven distortion of cobalt(II) by solid solution 'network mismatch'
Dalton Transactions **41**, 4927 (2012)
- Fielden J., Quasdorf K., Cronin L., and Kogerler P.
A fluorophosphate-based inverse Keggin structure
Dalton Transactions **41**, 9876 (2012)
- Fielden J., Speldrich M., Besson C., and Kogerler P.
Chiral Hexanuclear Ferric Wheels
Inorganic Chemistry **51**, 2734 (2012)
- Finger F., Holländer B., Rath J. K., Schropp R. E. I., and Lambert A.
Boron-doped hydrogenated microcrystalline silicon oxide (μc-SiO_x:H) for application in thin-film silicon solar cells
Journal of Non-Crystalline Solids **358**, 1962 (2012)
- Flesch A., Zhang G., Koch E., and Pavarini E.
Orbital-order melting in rare-earth manganites: Role of superexchange
Physical Review B **85**, 035124 (2012)
- Flohr K., Sladek K., Gunel H. Y., Lepsa M. I., Hardtdegen H., Liebmann M., Schapers T., and Morgenstern M.
Scanning tunneling microscopy with InAs nanowire tips
Applied Physics Letters **101**, 243101 (2012)
- Flohr K., Sladek K., Weirich T. E., Trellenkamp S., Hardtdegen H., Schäpers T., Schneider C. M., Meyer C., and Frielinghaus R.
Monitoring structural influences on quantum transport in InAs nanowires
Applied Physics Letters **101**, 062104 (2012)
- Franchini C., Kováčik R., Marsman M., Sathyanarayana Murthy S., He J., Ederer C., and Kresse G.
Maximally localized Wannier functions in LaMnO₃ within PBE + U, hybrid functionals and partially self-consistent GW: an efficient route to construct ab initio tight-binding parameters for e_g perovskites
Journal of Physics - Condensed Matter **24**, 235602 (2012)
- Frick B., Nair H., and Chatterji T.
Magnetic ordering in double perovskites R₂CoMnO₆ (R = Y, Tb) investigated by high resolution neutron spectroscopy.
Journal of Physics / Condensed Matter **24**, 266005 (2012)
- Friedrich C., Betzinger M., Schlipf M., Blügel S., and Schindlmayr A.
Hybrid functionals and GW approximation in the FLAPW method
Journal of Physics / Condensed Matter **24**, 293201 (2012)
- Friedrich C., Reiss G., Blügel S., and Meinert M.
GW study of the half-metallic Heusler compounds Co₂MnSi and Co₂FeSi
Physical Review B **86**, 245115 (2012)
- Frielinghaus R., Flohr K., Sladek K., Weirich T. E., Trellenkamp S., Hardtdegen H., Schapers T., Schneider C. M., and Meyer C.
Monitoring structural influences on quantum transport in In As nanowires
Applied Physics Letters **101**, 062104 (2012)
- Fringes S., Volk C., Terres B., Dauber J., Engels S., Trellenkamp S., and Stampfer C.
Tunable capacitive inter-dot coupling in a bilayer graphene double quantum dot
in *Physica Status Solidi C: Current Topics in Solid State Physics*, Vol 9, No 2, ed. Walther M., Vol. 9, p. 169-174 (2012)
- Früh S. M., Steuerwald D., Simon U., and Vogel V.
Covalent Cargo Loading to Molecular Shuttles via Copper-free "Click Chemistry"
Biomacromolecules, 121105162203000 (2012)
- Fulga I. C., Hassler F., and Akhmerov A. R.
Scattering theory of topological insulators and superconductors
Physical Review B **85**, 165409 (2012)
- Galanakis I., Özdoğan K., and Sasioglu E.
Half-metallic antiferromagnetism in Cr_{2+x}Se (0 ≤ x ≤ 1): A first-principles study
Physical Review B **86**, 134427 (2012)

- Galanakis I. and Sasioglu E.
Ab-initio calculation of effective exchange interactions, spin waves, and Curie temperature in L2₁- and L1₂-type local moment ferromagnets
Journal of Materials Science **47**, 7678 (2012)
- Gan L., Heggen M., Rudi S., and Strasser P.
Core-shell Compositional Fine Structures of Dealloyed Pt_xNi_{1-x} Nanoparticles and their Impact on Oxygen Reduction Catalysis
Nano Letters **12**, 5423 (2012)
- Ganahl M., Rabel E., Essler F., and Evertz H.
Observation of Complex Bound States in the Spin-1/2 Heisenberg XXZ Chain Using Local Quantum Quenches
Physical Review Letters **108**, 077206 (2012)
- Gareev R. R., Schmid M., Vancea J., Back C. H., Schreiber R., Burgler D., Schneider C. M., Stromberg F., and Wende H.
Antiferromagnetic coupling across silicon regulated by tunneling currents
Applied Physics Letters **100**, 022406 (2012)
- Gerstl C., Brodeck M., Schneider G. J., Su Y., Allgaier J., Arbe A., Colmenero J., and Richter D.
Short and Intermediate Range Order in Poly(alkylene oxide)s. A Neutron Diffraction and Molecular Dynamics Simulation Study
Macromolecules **45**, 7293 (2012)
- Gilbert M., Mertins H. C., Tesch M., Berges O., Feilbach H., and Schneider C. M.
TetraMag: A compact magnetizing device based on eight rotating permanent magnets
Review of Scientific Instruments **83**, 025109 (2012)
- Gilles S., Winter S., Michael K. E., Meffert S. H., Li P. G., Greben K., Simon U., Offenhausser A., and Mayer D.
Control of Cell Adhesion and Neurite Outgrowth by Patterned Gold Nanoparticles with Tunable Attractive or Repulsive Surface Properties
Small **8**, 3357 (2012)
- Gillessen M., Lumeij M., George J., Stoffel R., Motohashi T., Kikkawa S., and Dronskowski R.
Oxygen-Storage Materials BaYMn₂O_{5+δ} from the Quantum-Chemical Point of View
Chemistry of Materials **24**, 1910 (2012)
- Gottel S., Andergassen S., Honerkamp C., Schuricht D., and Wessel S.
Critical scales in anisotropic spin systems from functional renormalization
Physical Review B **85**, 214406 (2012)
- Gottschlich M., Gourdon O., Perßon J., da la Cruz C., Petricek V., and Brückel T.
Study of the antiferromagnetism of Mn₅Si₃: an inverse magnetocaloric effect material
Journal of Materials chemistry **22**, 15275 (2012)
- Grap S., Meden V., and Andergassen S.
Interplay of Coulomb interaction and spin-orbit effects in multilevel quantum dots
Physical Review B **86**, 035143 (2012)
- Grap T., Lepsa M. I., Moers J., Trellenkamp S., Grützmacher D., Lüth H., Schäpers T., and Blömers C.
Hall effect measurements on InAs nanowires
Applied Physics Letters **101**, 152106 (2012)
- Gray A. X., Cooke D. W., Kruger P., Bordel C., Kaiser A. M., Moyerman S., Fullerton E. E., Ueda S., Yamashita Y., Gloskovskii A., Schneider C. M., Drube W., Kobayashi K., Hellman F., and Fadley C. S.
Electronic Structure Changes across the Metamagnetic Transition in FeRh via Hard X-Ray Photoemission
Physical Review Letters **108**, 257208 (2012)
- Gray A. X., Minar J., Ueda S., Stone P. R., Yamashita Y., Fujii J., Braun J., Plucinski L., Schneider C. M., Panaccione G., Ebert H., Dubon O. D., Kobayashi K., and Fadley C. S.
Bulk electronic structure of the dilute magnetic semiconductor Ga_{1-x}Mn_xAs through hard X-ray angle-resolved photoemission
Nature Materials **11**, 957 (2012)
- Greer A. A., Gray A. X., Kanai S., Kaiser A. M., Ueda S., Yamashita Y., Bordel C., Palsson G., Maejima N., Yang S. H., Conti G., Kobayashi K., Ikeda S., Matsukura F., Ohno H., Schneider C. M., Kortright J. B., Hellman F., and Fadley C. S.
Observation of boron diffusion in an annealed Ta/CoFeB/MgO magnetic tunnel junction with standing-wave hard x-ray photoemission
Applied Physics Letters **101**, 202402 (2012)
- Grob M., Pratzner M., Morgenstern M., and Lezaic M.
Catalytic growth of N-doped MgO on Mo(001)
Physical Review B **86**, 075455 (2012)

Gröbel S., Krumbe C., Wagner T., Selmer T., Yoshinobu T., Baumann M. E. M., Keusgen M., Schöning M. J., and Werner C. F.
Nutrient concentration-sensitive microorganism-based biosensor
Physica Status Solidi / A **209**, 900 (2012)

Grope B. O. H., Zacherle T., Nakayama M., and Martin M.
Oxygen ion conductivity of doped ceria: A Kinetic Monte Carlo study
Solid State Ionics **225**, 476 (2012)

Grove-Rasmussen K., Grap S., Paaske J., Flensburg K., Andergassen S., Meden V., Jorgensen H. I., Muraki K., and Fujisawa T.
Magnetic-Field Dependence of Tunnel Couplings in Carbon Nanotube Quantum Dots
Physical Review Letters **108**, 176802 (2012)

Grzechnik A. and Fries K.
Crystal structures and stability of NaLnF_4 (Ln = La, Ce, Pr, Nd, Sm and Gd) studied with synchrotron single-crystal and powder diffraction
Dalton Transactions **41**, 10258 (2012)

Grzechnik A., Khaidukov N., and Fries K.
Crystal structures and stability of trigonal KLnF_4 fluorides (Ln = Y, Ho, Er, Tm, Yb)
Dalton Transactions **42**, 441 (2012)

Gundareva I., Volkov O. Y., Lyatti M., Divin Y., Gubankov V. N., and Pavlovskiy V. V.
Evolution of Eletronical and Electrodynamic Properties of $\text{YBa}_2\text{Cu}_3\text{O}_{7-x}$ Bicrystal Josephson Junctions with Oxygen Loading
IEEE Transactions on Applied Superconductivity **21**, 147 (2012)

Gundareva I. I., Gubankov V. N., Divin Y., Lyatti M., Pavlovskiy V. V., and Volkov O. Y.
Trimming of high-Tc bicrystal Josephson junctions by ozone and vacuum annealing
Physics Procedia **36**, 217 (2012)

Günel H. Y., Batov I. E., Hardtdegen H., Sladek K., Winden A., Weis K., Panaitov G., Grützmacher D., and Schäpers T.
Supercurrent in Nb/InAs-nanowire/Nb Josephson junctions
Journal of Applied Physics **112**, 034316 (2012)

Gunkel F., Brinks P., Hoffmann-Eifert S., Dittmann R., Huijben M., Kleibeuker J. E., Koster G., Rijnders G., and Waser R.
Influence of charge compensation mechanisms on the sheet electron density at conducting $\text{LaAlO}_3/\text{SrTiO}_3$ -interfaces
Applied Physics Letters **100**, 052103 (2012)

Guenther B., Maier M., Koeble J., Bettac A., Matthes F., Schneider C. M., and Feltz A.
High Precision Local Electrical Probing: Potential and Limitations for the Analysis of Nanocontacts and Nanointerconnects
in *Atomic Scale Interconnection Machines*, Springer Series Advances in Atom and Single Molecule Machines, Ed. Ch. Joachim, p.1-8, Springer, Berlin (2012)

Gutrah B. S., Beckmann M. F., Buchkremer A., Eckert T., Timper J., Leifert A., Richtering W., Schmitz G., and Simon U.
Size-dependent multispectral photoacoustic response of solid and hollow gold nanoparticles
Nanotechnology **23**, 225707 (2012)

Guttinger J., Molitor F., Stampfer C., Schnez S., Jacobsen A., Droscher S., Ihn T., and Ensslin K.
Transport through graphene quantum dots
Reports on Progress in Physics **75**, 126502 (2012)

Haab A., Mikulics M., Winden A., Voigt S., von der Ahe M., Moers J., Wirtz K., Stoica T., Grützmacher D., and Hardtdegen H.
Self-assembled GaN nanostructures by dry etching and their optical properties
Physica Status Solidi A **209**, 443 (2012)

Habicht S., Feste S., Zhao Q. T., Buca D., and Mantl S.
Electrical characterization of O-gated uniaxial tensile strained Si nanowire-array metal-oxide-semiconductor field effect transistors with $\langle 100 \rangle$ and $\langle 110 \rangle$ channel orientations
Thin Solid Films **520**, 3332 (2012)

Haegeman J., Perez-Garcia D., Cirac I., and Schuch N.
Order Parameter for Symmetry-Protected Phases in One Dimension
Physical Review Letters **109**, 050402 (2012)

Hafner J., Betz W., Gortz M., and Mokwa W.
Thinned CMOS Pressure Sensors for Tactile Sensing in Prosthetics
Biomedical Engineering-Biomedizinische Technik **57**, 874 (2012)

- Hahn H., Achenbach J., Ketteniss N., Noculak A., Kalisch H., and Vescan A.
Oxygen addition to fluorine based SiN etch process: Impact on the electrical properties of AlGaIn/GaN 2DEG and transistor characteristics
Solid-State Electronics **67**, 90 (2012)
- Hahn H., Alam A., Heuken M., Kalisch H., and Vescan A.
Investigation of plasma-oxidized aluminium as a gate dielectric for AlGaIn/GaN MISHFETs
Semiconductor Science and Technology **27**, 062001 (2012)
- Hahn H., Gruis J. B., Ketteniss N., Urbain F., Kalisch H., and Vescan A.
Influence of mask material and process parameters on etch angle in a chlorine-based GaN dry etch
Journal of Vacuum Science & Technology A **30**, 051302 (2012)
- Hall S., Sedghi N., Simutis G., Dhanak V. R., Bailey P., Noakes T. C. Q., Alexandrou I., Engstrom O., Lopes J. M. J., Schubert J., and Mitrovic I. Z.
On the nature of the interfacial layer in ultra-thin TiN/LaLuO₃ gate stacks
Journal of Applied Physics **112**, 044102 (2012)
- Hardrat B., Freimuth F., Heinze S., and Mokrousov Y.
Conductance fingerprints of noncollinear magnetic states in single-atom contacts: A first-principles Wannier-functions study
Physical Review B **86**, 165449 (2012)
- Hardrat B., Wang N., Freimuth F., Mokrousov Y., and Heinze S.
One-dimensional ballistic transport with FLAPW Wannier functions
Physical Review B **85**, 245412 (2012)
- Hardtdegen H., Winden A., Fox A., Marso M., Sofer Z., Lüth H., Grützmacher D., Kordos P., and Mikulics M.
Residual strain in recessed AlGaIn/GaN heterostructure field-effect transistors evaluated by micro photoluminescence measurements
Physica Status Solidi C **9**, 911 (2012)
- Harvey S. P., De Souza R. A., and Martin M.
Diffusion of La and Mn in Ba_{0.5}Sr_{0.5}Co_{0.8}Fe_{0.2}O_{3-δ} polycrystalline ceramics
Energy & Environmental Science **5**, 5803 (2012)
- Hashimoto K., Champel T., Florens S., Sohrmann C., Wiebe J., Hirayama Y., Romer R. A., Wiesendanger R., and Morgenstern M.
Robust Nodal Structure of Landau Level Wave Functions Revealed by Fourier Transform Scanning Tunneling Spectroscopy
Physical Review Letters **109**, 116805 (2012)
- Hassler F. and Schuricht D.
Strongly interacting Majorana modes in an array of Josephson junctions
New Journal of Physics **14**, 125018 (2012)
- Hauer B., Engelhardt A. P., and Taubner T.
Quasi-analytical model for scattering infrared near-field microscopy on layered systems
Optics Express **20**, 13173 (2012)
- Heber J., Schlom D., Tokura Y., Waser R., and Wuttig M. (eds.)
Frontiers of Electronic Materials: Correlation Effects, Spintronics, and Memristive Phenomena - Fundamentals and Application
Wiley (2012)
ISBN: 978-3-527-41191-7
- Heedt S., Morgan C., Weis K., Bürgler D. E., Calarco R., Hardtdegen H., Grützmacher D., and Schäpers T.
Electrical Spin Injection into InN Semiconductor Nanowires
Nano Letters **12**, 4437 (2012)
- Heers S., Mavropoulos P., Lounis S., Zeller R., and Blügel S.
Lifetime reduction of surface states at Cu, Ag, and Au(111) caused by impurity scattering
Physical Review B **86**, 125444 (2012)
- Heggen M., Oezaslan M., Houben L., and Strasser P.
Formation and impact of core-shell fine structures in Pt bimetallic nanoparticle fuel cell electrocatalysts
The Journal of Physical Chemistry / C **116**, 19073 (2012)
- Herbert S., Banyay M., Maryasov A. P., Hochschulz F., Paschen U., Vogt H., and Juschkin L.
Quantum Efficiency Determination of a Novel CMOS Design for Fast Imaging Applications in the Extreme Ultraviolet
IEEE Transactions on Electron Devices **59**, 846 (2012)

- Hirseman D., Shylesh S., De Souza R. A., Diar-Bakerly B., Biersack B., Mueller D. N., Martin M., Schobert R., and Breu J.
Large-Scale, Low-Cost Fabrication of Janus-Type Emulsifiers by Selective Decoration of Natural Kaolinite Platelets
Angewandte Chemie-International Edition **51**, 1348 (2012)
- Hoepfner V., Deringer V. L., and Dronskowski R.
Hydrogen-Bonding Networks from First-Principles: Exploring the Guanidine Crystal
Journal of Physical Chemistry A **116**, 4551 (2012)
- Hoffmann J. M., Hauer B., and Taubner T.
Antenna-enhanced infrared near-field nanospectroscopy of a polymer
Applied Physics Letters **101**, 193105 (2012)
- Hoffmann-Eifert S., Reiners M., and Waser R.
ALD grown functional oxide layers for nonvolatile resistive switching memory applications
ECS Transactions **50**, 9 (2012)
- Hohenadler M., Meng Z. Y., Lang T. C., Wessel S., Muramatsu A., and Assaad F. F.
Quantum phase transitions in the Kane-Mele-Hubbard model
Physical Review B **85**, 115132 (2012)
- Hohenadler M., Wessel S., Daghofer M., and Assaad F. F.
Interaction-range effects for fermions in one dimension
Physical Review B **85**, 195115 (2012)
- Homberger M., Schmid S., Timper J., and Simon U.
Solid Phase Supported "Click"-Chemistry Approach for the Preparation of Water Soluble Gold Nanoparticle Dimers
Journal of Cluster Science **23**, 1049 (2012)
- Honerkamp C.
Functional Renormalization Group for Interacting Many-Fermion Systems on Two-Dimensional Lattices
in *Strongly Correlated Systems: Theoretical Methods*, ed. Avella A. and Mancini F. (Springer Series in Solid-State Sciences), Vol. 171, p. 373-408 (2012)
- Honerkamp C.
Effective interactions in multiband systems from constrained summations
Physical Review B **85**, 195129 (2012)
- Hong H. B., Krause H.-J., Song K., and Choi C.-J.
In situ analysis of free radicals from the photodecomposition of hydrogen peroxide using a frequency-mixing magnetic detector
Applied Physics Letters **101**, 054105 (2012)
- Horig C. B. M. and Schuricht D.
Transport properties of a multichannel Kondo dot in a magnetic field
Physical Review B **85**, 134413 (2012)
- Horig C. B. M., Schuricht D., and Andergassen S.
Renormalization group analysis of a spin-1 Kondo dot: Nonequilibrium transport and relaxation dynamics
Physical Review B **85**, 054418 (2012)
- Houben A., Schweika W., Bruckel T., and Dronskowski R.
New neutron-guide concepts and simulation results for the POWTEX instrument
Nuclear Instruments & Methods in Physics Research Section a-Accelerators Spectrometers Detectors and Associated Equipment **680**, 124 (2012)
- Houben L., Enyashin A. N., Feldman Y., Rosentsveig R., Stroppa D., and Bar-Sadan M.
Diffraction from disordered stacking sequences in MoS₂ and WS₂ fullerenes and nanotubes
The Journal of Physical Chemistry / C **116**, 24350 (2012)
- Houben L., Heidelmann M., and Gunkel F.
Spatial resolution and radiation damage in quantitative high-resolution STEM-EEL spectroscopy in oxides
Micron **43**, 532 (2012)
- Hovmöller S., Zou X. D., Hovmöller Zou L., and Grushko B.
Structures of pseudo-decagonal approximants in Al-Co-Ni
Philosophical Transactions of the Royal Society of London / A **370**, 2949 (2012)
- Hüske M., Yakushenko A., Brüggemann D., Mayer D., Offenhäusser A., Wolfrum B., and Wesche M.
A nanoporous alumina microelectrode array for functional cell-chip coupling
Nanotechnology **23**, 495303 (2012)

- Ibach H., Schneider C. M., Costa A. T., Santos D. L. R., Mills D. L., and Jayaraman R.
Surface spin waves of fcc cobalt films on Cu(100): High-resolution spectra and comparison to theory
Physical Review B **86**, 165436 (2012)
- Ihn T., Droscher S., Schnetz S., Knowles H., Guttinger J., Huefner M., Stampfer C., Meir Y., and Ensslin K.
Electronic transport in graphene nanostructures on SiO₂
Solid State Communications **152**, 1306 (2012)
- Ishida H. and Liebsch A.
Coulomb blockade and Kondo effect in the electronic structure of Hubbard molecules connected to metallic leads: A finite-temperature exact-diagonalization study
Physical Review B **86**, 205115 (2012)
- Ishida H. and Liebsch A.
First-order metal-to-metal phase transition and non-Fermi-liquid behavior in a two-dimensional Mott insulating layer adsorbed on a metal surface
Physical Review B **85**, 045112 (2012)
- Jacob J., Lehmann H., Merkt U., Mehl S., and Hankiewicz E. M.
Direct current-biased InAs spin-filter cascades
Journal of Applied Physics **112**, 013706 (2012)
- Jagannathan A., Doucot B., Szallas A., and Wessel S.
Geometric fluctuations in a two-dimensional quantum antiferromagnet
Physical Review B **85**, 094434 (2012)
- Jones R. O. and Akola J.
Amorphous structures of Ge/Sb/Te alloys: Density functional simulations
Physica Status Solidi / B **249**, 1851 (2012)
- Kaiser A. M., Cramm S., Schneider C. M., and Wiemann C.
Deflection gating for time-resolved x-ray magnetic circular dichroism–photoemission electron microscopy using synchrotron radiation
Review of Scientific Instruments **83**, 063706 (2012)
- Kalikka J., Akola J., Jones R. O., Kohara S., and Usuki T.
Amorphous Ge₁₅Te₈₅: density functional, high-energy x-ray and neutron diffraction study
Journal of Physics / Condensed Matter **24**, 015802 (2012)
- Kalikka J., Akola J., Larrucea J., and Jones R. O.
Nucleus-driven crystallization of amorphous Ge₂Sb₂Te₅: A density functional study
Physical Review B **86**, 441113 (2012)
- Kamba S., Goian V., Orlita M., Nuzhnyy D., Lee J. H., Schlom D. G., Rushchanskii K. Z., Lezaic M., Birol T., Fennie C. J., Gemeiner P., Dkhil B., Bovtun V., Kempa M., Hlinka J., and Petzelt J.
Magnetodielectric effect and phonon properties of compressively strained EuTiO₃ thin films deposited on (001)(LaAlO₃)_{0.29}-(SrAl_{1/2}Ta_{1/2}O₃)_{0.71}
Physical Review B **85**, 094435 (2012)
- Karrasch C., Rentrop J., Schuricht D., and Meden V.
Luttinger-liquid universality in the time evolution after an interaction quench
Physical Review Letters **109**, 126406 (2012)
- Kashuba O., Schoeller H., and Splettstoesser J.
Nonlinear adiabatic response of interacting quantum dots
Europhysics Letters **98**, 57003 (2012)
- Kätelhön E. and Wolfrum B.
Simulation-based investigations on noise characteristics of redox-cycling sensors
Physica Status Solidi a - Applications and Materials Science **209**, 881 (2012)
- Kätelhön E. and Wolfrum B.
On-chip redox cycling techniques for electrochemical detection
Reviews in Analytical Chemistry **31**, 7 (2012)
- Kennes D. M., Jakobs S. G., Karrasch C., and Meden V.
Renormalization group approach to time-dependent transport through correlated quantum dots
Physical Review B **85**, 085113 (2012)

- Kennes D. M. and Meden V.
Quench dynamics of correlated quantum dots
Physical Review B **85**, 245101 (2012)
- Ketteniss N., Askar A., Reuters B., Noculak A., Hollander B., Kalisch H., and Vescan A.
Polarization-reduced quaternary InAlGaN/GaN HFET and MISHFET devices
Semiconductor Science and Technology **27**, 055012 (2012)
- Ketteniss N., Behmenburg H., Hahn H., Noculak A., Hollander B., Kalisch H., Heuken M., and Vescan A.
Quaternary Enhancement-Mode HFET With In Situ SiN Passivation
Ieee Electron Device Letters **33**, 519 (2012)
- Ketteniss N., Behmenburg H., Lecourt F., Defrance N., Hoel V., De Jaeger J. C., Heuken M., Kalisch H., and Vescan A.
The effect of gate length variation on InAlGaN/GaN HFET device characteristics
Semiconductor Science and Technology **27**, 035009 (2012)
- Khajetoorians A. A., Wiebe J., Chilian B., Lounis S., Blügel S., and Wiesendanger R.
Atom-by-atom engineering and magnetometry of tailored nanomagnets
Nature Physics **8**, 497 (2012)
- Khodjasteh K., Bluhm H., and Viola L.
Automated synthesis of dynamically corrected quantum gates
Physical Review A **86**, 042329 (2012)
- Kichin G., Temirov R., Wagner C., and Tautz F. S.
Mit atomaren Sensoren Moleküle erkennen
Nachrichten aus der Chemie **60**, 52 (2012)
- Kichin G., Weiss C., Wagner C., Tautz F. S., and Temirov R.
Single Molecule and Single Atom Sensors for Atomic Resolution Imaging of Chemically Complex Surfaces
Journal of the American Chemical Society **133**, 16847 (2012)
- Kieschnick M., Kallis K. T., Schubert J., Kunze U., Doll T., and Zimmer C. M.
Nano photoelectron ioniser chip using LaB₆ for ambient pressure trace gas detection
Microelectronic Engineering **98**, 472 (2012)
- Kirsanov D., Legin A., Osterrath T., Schubert J., Zander W., Schöning M. J., and Spelthahn H.
Development of a thin-film sensor array for analytical monitoring of heavy metals in aqueous solutions
Physica Status Solidi / A **209**, 885 (2012)
- Kiselev D. A., Rushchanskii K., Bdikin I. K., Malinkovich M. D., Parkhomenko Y. N., and Vysochanskii Y. M.
Theoretical Prediction and Direct Observation of Metastable Non-Polar Regions in Domain Structure of Sn₂P₂S₆ Ferroelectrics with Triple-Well Potential
Ferroelectrics **438**, 55 (2012)
- Kisner A., Heggen M., Fischer W., Tillmann K., Offenhäusser A., Kubota, and Mourzina Y.
In situ fabrication of ultrathin porous alumina and its application for nanopatterning Au nanocrystals on the surface of ion-sensitive field-effect transistors
Nanotechnology **23**, 485301 (2012)
- Knoch J., Chen Z. H., and Appenzeller J.
Properties of Metal-Graphene Contacts
Ieee Transactions on Nanotechnology **11**, 513 (2012)
- Knoll L., Gámiz F., Zhao Q. T., Godoy A., Mantl S., and Padilla J. L.
Simulation of Fabricated 20-nm Schottky Barrier MOSFETs on SOI: Impact of barrier Lowering
IEEE Transactions on Electron Devices **59**, 1320 (2012)
- Knoll L., Zhao Q. T., Lupták R., Trellenkamp S., Bourdelle K. K., and Mantl S.
20 nm Gate length Schottky MOSFETs with ultra-thin NiSi/epitaxial NiSi₂ source/drain
Solid State Electronics **71**, 88 (2012)
- Koch S., Joshi R. K., Noyong M., Timper J., Schneider J. J., and Simon U.
Hierarchical Structures of Carbon Nanotubes and Arrays of Chromium-Capped Silicon Nanopillars: Formation and Electrical Properties
Chemistry **18**, 11614 (2012)
- Kohl D., Natarajan G., and Wuttig M.
Structure control of sputtered zinc oxide films by utilizing zinc oxide seed layers tailored by ion beam assisted sputtering
Journal of Physics D-Applied Physics **45**, 245302 (2012)

- Köhler F., Schicho S., Wolfrum B., Gordijn A., Pust S. E., and Carius R.
Gradient etching of silicon-based thin films for depth-resolved measurements: The example of Raman crystallinity
Thin Solid Films **520**, 2605 (2012)
- Kontis C., Mueller M. R., Kuechenmeister C., Kallis K. T., and Knoch J.
Optimizing the identification of mono- and bilayer graphene on multilayer substrates
Applied Optics **51**, 385 (2012)
- Kordos P., Kúdela R., Stoklas R., Cico K., Mikulics M., Gregusová D., and Novák J.
Aluminum oxide as passivation and gate insulator in GaAs-based field-effect transistors prepared in situ by metal-organic vapor deposition
Applied Physics Letters **100**, 142113 (2012)
- Korolkov D., Busch P., Willner L., Kentzinger E., Rücker U., Paul A., Frielinghaus H., and Brückel T.
Analysis of randomly oriented structures by grazing-incidence small-angle neutron scattering
Journal of Applied Crystallography **45**, 245 (2012)
- Korte S., Romanyuk K., Schnitzler B., Cherepanov V., Voigtländer B., and Filimonov S. N.
Selective Adsorption of C₆₀ on Ge/Si Nanostructures
Physical Review Letters **108**, 116101 (2012)
- Kováčik R., Werner P., Dymkowski K., and Ederer C.
Rubidium superoxide: A p-electron Mott insulator
Physical Review B **86**, 075130 (2012)
- Kowalczyk P., Atodiressei N., Gingras M., Caciuc V., Schnaebele N., Raimundo J.-M., Blügel S., Waser R., and Karthäuser S.
Arylthio-substituted coronenes as tailored building blocks for molecular electronics
Physical Chemistry Chemical Physics **14**, 1635 (2012)
- Kowalczyk P., Rathgeber S., Karthäuser S., Waser R., Schnaebele N., and Gingras M.
Columnar self-assembly of a 3D-persulfurated coronene asterisk. The dominant role of Aryl-Sulfur bonds
New Journal of Chemistry **36**, 477 (2012)
- Krebs D., Schmidt R. M., Klomfass J., Luckas J., Bruns G., Schlockermann C., Salinga M., Carius R., and Wuttig M.
Impact of DoS changes on resistance drift and threshold switching in amorphous phase change materials
Journal of Non-Crystalline Solids **358**, 2412 (2012)
- Kroger I., Bayersdorfer P., Stadtmüller B., Kleimann C., Mercurio G., Reinert F., and Kumpf C.
Submonolayer growth of H₂-phthalocyanine on Ag(111)
Physical Review B **86**, 195412 (2012)
- Kubacki J., Molak A., Rogala M., Rodenbucher C., and Szot K.
Metal-insulator transition induced by non-stoichiometry of surface layer and molecular reactions on single crystal KTaO₃
Surface Science **606**, 1252 (2012)
- Kubart T., Schmidt R. M., Austgen M., Nyberg T., Pflug A., Siemers M., Wuttig M., and Berg S.
Modelling of sputtering yield amplification in serial reactive magnetron co-sputtering
Surface & Coatings Technology **206**, 5055 (2012)
- Kuhlen S., Schmalbuch K., Hagedorn M., Schlamme P., Patt M., Lepsa M., Guntherodt G., and Beschoten B.
Electric Field-Driven Coherent Spin Reorientation of Optically Generated Electron Spin Packets in InGaAs
Physical Review Letters **109**, 146603 (2012)
- Kupriyanov M. Y., Khapaev M. M., Divin Y. Y., and Gubankov V. N.
Anisotropic distributions of electrical currents in high-Tc grain-boundary junctions
JETP Letters **95**, 289 (2012)
- Lang T. C., Meng Z. Y., Scherer M. M., Uebelacker S., Assaad F. F., Muramatsu A., Honerkamp C., and Wessel S.
Antiferromagnetism in the Hubbard Model on the Bernal-Stacked Honeycomb Bilayer
Physical Review Letters **109**, 126402 (2012)
- La-O-Vorakiat C., Turgut E., Teale C. A., Kapteyn H. C., Murnane M. M., Mathias S., Aeschlimann M., Schneider C. M., Shaw J. M., Nembach H. T., and Silva T. J.
Ultrafast Demagnetization Measurements Using Extreme Ultraviolet Light: Comparison of Electronic and Magnetic Contributions
Phys Rev X **2**, 011005 (2012)

- Lazic P., Atodiresei N., Caciuc V., Brako R., Gumhalter B., and Blügel S.
Rationale for switching to nonlocal functionals in density functional theory
Journal of Physics / Condensed Matter **24**, 424215 (2012)
- Li H., Li D., Liu J., Qin J. R., Xu S., Liu Y., Mayer D., and Wang E.
Electrochemical current rectifier as a highly sensitive and selective cytosensor for cancer cell detection
Chemical Communications **48**, 2594 (2012)
- Li H. F., Xiao Y. G., Schmitz B., Persson J., Schmidt W., Meuffels P., Roth G., and Bruckel T.
Possible magnetic-polaron-switched positive and negative magnetoresistance in the GdSi single crystals
Scientific Reports **2**, 750 (2012)
- Li P. N. and Taubner T.
Multi-wavelength superlensing with layered phonon-resonant dielectrics
Optics Express **20**, 11787 (2012)
- Li P. N. and Taubner T.
Broadband Subwavelength Imaging Using a Tunable Graphene-Lens
Acs Nano **6**, 10107 (2012)
- Li Y. and Mazzarello R.
Magnetic Contrast in Phase-Change Materials Doped with Fe Impurities
Advanced Materials **24**, 1429 (2012)
- Liebsch A. and Ishida H.
Temperature and bath size in exact diagonalization dynamical mean field theory
Journal of Physics / Condensed Matter **24**, 053201 (2012)
- Liedel C., Hund M., Olszowka V., and Boker A.
On the alignment of a cylindrical block copolymer: a time-resolved and 3-dimensional SFM study
Soft Matter **8**, 995 (2012)
- Liedel C., Pester C. W., Ruppel M., Urban V. S., and Boker A.
Beyond Orientation: The Impact of Electric Fields on Block Copolymers
Macromolecular Chemistry and Physics **213**, 259 (2012)
- Limbach F., Caterino R., Gotschke T., Stoica T., Calarco R., Geelhaar L., and Riechert H.
The influence of Mg doping on the nucleation of self-induced GaN nanowires
AIP Advances **2**, 012157 (2012)
- Liu B., Zhang Y., Mayer D., Krause H.-J., Jin Q., Zhao J., Offenhäusser A., and Xu Y.
Determination of heavy metal ions by microchip capillary electrophoresis coupled with contactless conductivity detection
Electrophoresis **33**, 1247 (2012)
- Liu C., Zhang Y., Qiu L., Dong H., Krause H.-J., Xie X., and Offenhäusser A.
Low-field MRI measurements using a tuned HTS SQUID as detector and permanent magnet pre-polarization field
Superconductor Science and Technology **25**, 075013 (2012)
- Long N. H., Ogura M., and Akai H.
Spin-wave excitations in half-metallic materials
Physical Review B **85**, 224437 (2012)
- Longeaud C., Luckas J., Krebs D., Carius R., Klomfass J., and Wuttig M.
On the density of states of germanium telluride
Journal of Applied Physics **112**, 113714 (2012)
- Lounis S., Bringer A., and Blügel S.
Magnetic Adatom Induced Skyrmion-Like Spin Texture in Surface Electron Waves
Physical Review Letters **108**, 07202 (2012)
- Lu W., Jeong D. S., Kozicki M., and Waser R.
Electrochemical metallization cells - blending nanoionics into nanoelectronics?
Materials Research Bulletin **37**, 124 (2012)
- Luitz D. J., Assaad F. F., Novotny T., Karrasch C., and Meden V.
Understanding the Josephson Current through a Kondo-Correlated Quantum Dot
Physical Review Letters **108**, 227001 (2012)

- Lumeij M., Koettgen J., Gillessen M., Itoh T., and Dronskowski R.
Detailed insights into the structural properties and oxygen-pathways in orthorhombic $\text{Ba}_{0.5}\text{Sr}_{0.5}\text{Co}_{0.8}\text{Fe}_{0.2}\text{O}_{3-\delta}$ by electronic-structure theory
Solid State Ionics **222**, 53 (2012)
- Lustfeld H. and Hirschfeld J. A.
Finding stable minima using a nudged-elastic-band-based optimization scheme
Physical Review / E **85**, 056709 (2012)
- Lustfeld H., Pithan C., and Reißel M.
Metallic electrolyte composites in the framework of the brick-layer model
Journal of the European Ceramic Society **32**, 859 (2012)
- Lyatti M., Poppe U., and Divin Y.
Josephson spectrometer with waveguide coupling for liquid identification
Physics Procedia **36**, 193 (2012)
- Lyatti M., Poppe U., and Divin Y.
Hilbert spectral analysis of THz radiation sources by high-Tc Josephson detectors
Physics Procedia **36**, 166 (2012)
- Maier S. A. and Honerkamp C.
Renormalization group flow for fermions into antiferromagnetically ordered phases: Method and mean-field models
Physical Review B **86**, 134404 (2012)
- Maier S. A. and Honerkamp C.
Effective three-particle interactions in low-energy models for multiband systems
Physical Review B **85**, 064520 (2012)
- S. Maintz, B. Eck, R. Dronskowski
cuVASP: A GPU-Accelerated Plane-Wave Electronic-Structure Code
in *High Performance Computing in Science and Engineering '11*, Eds. W. E. Nagel, D. B. Kröner, M. M. Resch, pp. 201–205, Springer (2012)
- Malaestean I. L., Ellern A., Baca S., and Kogerler P.
Cerium oxide nanoclusters: commensurate with concepts of polyoxometalate chemistry?
Chemical Communications **48**, 1499 (2012)
- Malaestean I. L., Kutluca M., Speldrich M., Ellern A., and Kogerler P.
Macrocycles based on magnetically functionalized zirconium oxide clusters
Inorganica Chimica Acta **380**, 72 (2012)
- Malaestean I. L., Kutluca-Alici M., Ellern A., van Leusen J., Schilder H., Speldrich M., Baca S. G., and Kogerler P.
Linear, Zigzag, and Helical Cerium(III) Coordination Polymers
Crystal Growth & Design **12**, 1593 (2012)
- Manheller M., Karthäuser S., Waser R., Blech K., and Simon U.
Electrical Transport through Single Nanoparticles and Nanoparticle Arrays
The Journal of Physical Chemistry / C **116**, 20657 (2012)
- Manheller M., Trellenkamp S., Waser R., and Karthäuser S.
Reliable fabrication of 3 nm gaps between nanoelectrodes by electron-beam lithography
Nanotechnology **23**, 125302 (2012)
- Marchenko D., Varykhalov A., Scholz M. R., Bihlmayer G., Rashba E. I., Rybkin A., Shikin A. M., and Rader O.
Giant Rashba splitting in graphene due to hybridization with gold
Nature Communications **3**, 1232 (2012)
- Maris A., Melandri S., Evangelisti L., Caminati W., Giuliano B. M., Plekan O., Feyer V., Richter R., Coreno M., and Prince K. C.
Soft X-ray photoemission spectroscopy of selected neurotransmitters in the gas phase
Journal of Electron Spectroscopy and related Phenomena **185**, S244 (2012)
- Martin M.
Oxygen Potential Gradient Induced Degradation of Oxides
Journal of the Korean Ceramic Society **49**, 29-36 (2012)
- Marques M. A. L., Oliveira M. J. T., and Burnus T.
Libxc: A library of exchange and correlation functionals for density functional theory
Computer Physics Communications **183**, 2272 (2012)

- Mathias S., La-O-Vorakiat C., Grychtol P., Granitzka P., Turgut E., Shaw J. M., Adam R., Nembach H. T., Siemens M. E., Eich S., Schneider C. M., Silva T. J., Aeschlimann M., Murnane M. M., and Kapteyn H. C.
Probing the timescale of the exchange interaction in a ferromagnetic alloy
P Natl Acad Sci USA **109**, 4792 (2012)
- Mauder C., Tuna O., Gutrath B., Balmes V., Behmenburg H., Rzhetskii M. V., Lutsenko E. V., Yablonskii G. P., Noyong M., Simon U., Heuken M., Kalisch H., and Vescan A.
Highly n-type doped InGaN films for efficient direct solar hydrogen generation
in *Physica Status Solidi C: Current Topics in Solid State Physics, Vol 9, No 3-4*, eds. Parbrook P. J. et al., 964-967 (2012)
- Mazumder P., Kang S. M., and Waser R.
Memristors: Devices, Models, and Applications
Proceedings of the IEEE **100**, 1911 (2012)
- Melcher, Ch.
Global Solvability of the Cauchy Problem for the Landau-Lifshitz-Gilbert Equation in Higher Dimensions
Indiana University Mathematics Journal **61** (3) 1175-1200 (2012)
- Melville A., Mairoser T., Schmehl A., Shai D. E., Monkman E. J., Harter J. W., Heeg T., Holländer B., Schubert J., Shen K. M., Mannhart J., and Schlom D. G.
Lutetium-doped EuO films grown by molecular-beam epitaxy
Applied Physics Letters **100**, 222101 (2012)
- Meng Z. Y., Lang T., Wessel S., Assaad F., and Muramatsu A.
A quantum spin-liquid in correlated relativistic electrons
Ann. Phys.-Berlin **524**, 118 (2012)
- Mennig J., Matthes F., Bürgler D. E., and Schneider C. M.
Observation and implications of magnetic domains in lateral spin valves
Journal of Applied Physics **111**, 07C504 (2012)
- Menzel M., Mokrousov Y., Wieser R., Bickel J. E., Vedmedenko E., Blügel S., Heinze S., von Bergmann K., Kubetzka A., and Wiesendanger R.
Information Transfer by Vector Spin Chirality in Finite Magnetic Chains
Physical Review Letters **108**, 197204 (2012)
- Menzel S., Böttger U., and Waser R.
Simulation of multilevel switching in electrochemical metallization memory cells
Journal of Applied Physics **111**, 014501 (2012)
- Menzel-Severing J., Laube T., Brockmann C., Bornfeld N., Mokwa W., Mazinani B., Walter P., and Roessler G.
Implantation and explantation of an active epiretinal visual prosthesis: 2-year follow-up data from the EPIRET3 prospective clinical trial
Eye **26**, 502 (2012)
- Merker L. and Costi T. A.
Numerical renormalization group calculation of impurity internal energy and specific heat of quantum impurity models
Physical Review B **86**, 075150 (2012)
- Merker L., Weichselbaum A., and Costi T. A.
Full density-matrix numerical renormalization group calculation of impurity susceptibility and specific heat of the Anderson impurity model
Physical Review B **86**, 075153 (2012)
- Metzen M. G., Biswas S., Bousack H., Gottwald M. G., Mayekar K., and Emde G. v. d.
A biomimetic active electrolocation sensor for detection of atherosclerotic lesions in blood vessels
IEEE Sensors Journal **12**, 325 (2012)
- Metzner W., Salmhofer M., Honerkamp C., Meden V., and Schonhammer K.
Functional renormalization group approach to correlated fermion systems
Reviews of Modern Physics **84**, 299 (2012)
- Meyer C., Besson C., Frielinghaus R., Saelhoff A. K., Flototto H., Houben L., Kogerler P., and Schneider C. M.
Covalent functionalization of carbon nanotubes with tetramanganese complexes
Physica Status Solidi B-Basic Solid State Physics **249**, 2412 (2012)
- Michael E. A. and Mikulics M.
Losses from long-living photoelectrons in terahertz-generating continuous-wave photomixers
Applied Physics Letters **100**, 191112 (2012)

- Mignot J.-M., Nemkovski K. S., Rybina A. V., Lazukov V. N., Ivanov A. S., Iga F., Takabatake T., and Alekseev P. A.
Interplay of low-energy phonons and magnetiv excitations in the Kondo insulator YbB_{12}
Journal of Physics / Condensed Matter **24**, 205601 (2012)
- Mikulics M., Fox A., Marso M., Grützmacher D., Donoval D., and Kordos P.
Electrical and structural characterization of AlGaIn/GaN field-effect transistors with recessed gate
Vacuum **86**, 754 (2012)
- Mikulics M., Hardtdegen H., Gregusová D., Sofer Z., Simek P., Trellenkamp S., Grützmacher D., Lüth H., Kordos P., and Marso M.
Non-uniform distribution of induced strain in a gate recessed AlGaIn/GaN structure evaluated by micro-PL measurements
Semiconductor science and technology **27**, 105008 (2012)
- Mikulics M., Zhang J., Serafini J., Adam R., Grützmacher D., and Sobolewski R.
Subpicosecond electronhole recombination time and terahertz-bandwidth photoresponse in freestanding GaAs epitaxial mesoscopic structures
Applied Physics Letters **101**, 031111 (2012)
- Minamisawa R. A., Buca D., Hollander B., Hartmann J. M., Bourdelle K. K., and Mantl S.
p-Type Ion Implantation in Tensile Si/Compressive $\text{Si}_{0.5}\text{Ge}_{0.5}$ /Tensile Strained Si Heterostructures
Journal of the Electrochemical Society **159**, H44 (2012)
- Minamisawa R. A., Schmidt M., Knoll L., Buca D., Zhao Q. T., Hartmann J.-M., Bourdelle K. K., and Mantl S.
Hole Transport in Strained $\text{Si}_{0.5}\text{Ge}_{0.5}$ QW-MOSFETs with $\langle 110 \rangle$ and $\langle 100 \rangle$ Channel Orientations
IEEE Electron Device Letters **33**, 1105 (2012)
- Misiorny M., Weymann I., and Barnas J.
Temperature dependence of electronic transport through molecular magnets in the Kondo regime
Physical Review B **86**, 035417 (2012)
- Misiorny M., Weymann I., and Barnas J.
Underscreened Kondo effect in $S=1$ magnetic quantum dots: Exchange, anisotropy, and temperature effects
Physical Review B **86**, 245415 (2012)
- Misra R., Mundy J. A., Zhang L. A., Holinsworth B. S., O'Neal K. R., Heeg T., Zander W., Schubert J., Musfeldt J. L., Liu Z.-K., Muller D. A., Schiffer P., Schlom D. G., and Brooks C. M.
The adsorption-controlled growth of LuFe_2O_4 by molecular-beam epitaxy
Applied Physics Letters **101**, 132907 (2012)
- Moers J., Trellenkamp S., Grutzmacher D., Offenhausser A., and Rienks B.
Optimized marker definition for high overlay accuracy e-beam lithography
Microelectronic Engineering **97**, 68 (2012)
- Moftakharzadeh A., Kokabi A., Banzet M., Schubert J., and Fardmanesh M.
Detectivity Analysis and Optimization of Large-Area Freestanding-Type HTS Bolometers
IEEE Transactions on applied superconductivity **22**, 2100107 (2012)
- Moras P., Sheverdyeva P. M., Carbone C., Topwal D., Ferrari L., Bihlmayer G., Ouazi S., Rusponi S., Lehnert A., and Brune H.
Electronic states of moiré modulated Cu films
Journal of Physics / Condensed Matter **24**, 335502 (2012)
- Morgan C., Schneider C. M., and Meyer C.
Permalloy and $\text{Co}_{50}\text{Pd}_{50}$ as ferromagnetic contacts for magnetoresistance measurements in carbon nanotube-based transport structures
Journal of Applied Physics **111**, 07B309 (2012)
- Morgenstern M., Georgi A., Strasser C., Ast C. R., Becker S., and Liebmann M.
Scanning tunneling microscopy of two-dimensional semiconductors: Spin properties and disorder
Physica E-Low-Dimensional Systems & Nanostructures **44**, 1795 (2012)
- Mueller D. N., De Souza R. A., Yoo H. I., and Martin M.
Phase Stability and Oxygen Nonstoichiometry of Highly Oxygen-Deficient Perovskite-Type Oxides: A Case Study of $(\text{Ba,Sr})(\text{Co,Fe})\text{O}_{3-\delta}$
Chemistry of Materials **24**, 269 (2012)
- Müller E., Klobes B., Bauer Pereira P., Hermann R., and Dadda J.
Electronic properties as a function of Ag/Sb ratio in $\text{Ag}_{1-y}\text{Pb}_{18}\text{Sb}_{1+z}\text{Te}_{20}$ compounds
Journal of Electronic Materials **41**, 2065 (2012)

- Nair H., Sankaranarayanan V., Sethupat K., and Pradheesh R.
Large Magnetoresistance and Jahn Teller effect in $\text{Sr}_2\text{FeCoO}_6$
The European Physical Journal / B **85**, 260 (2012)
- Nair H., Swain D., Hariharan N., Adiga S., Narayana C., and Elizabeth S.
Griffiths phase-like behavior and spin-phonon coupling in double perovskite $\text{Tb}_2\text{NiMnO}_6$
Journal of Applied Physics **110**, 123919 (2012)
- Nakayama M., Ohshima H., Nogami M., and Martin M.
A concerted migration mechanism of mixed oxide ion and electron conduction in reduced ceria studied by first-principles density functional theory
Physical Chemistry Chemical Physics **14**, 6079 (2012)
- Nemkovski K. S., Mignot J.-M., Lazukov V. N., Nikolov A. A., Menushenkov A. P., Yaroslavlsev A. A., Bewley R. I., Stewart J. R., Gribov A. V., and Alekseev P. A.
Magnetic Excitations in $\text{EuCu}_2(\text{Si}_x\text{Ge}_{1-x})_2$: from mixed valence towards magnetism
Journal of Physics / Condensed Matter **24**, 375601 (2012)
- Neyman A., Wang Y. F., Sharef S., Varsano N., Botar B., Kogerler P., Meshi L., and Weinstock I. A.
Polyoxometalate-directed assembly of water-soluble AgCl nanocubes
Chemical Communications **48**, 2207 (2012)
- Nichau A., Ozben E. D., Schnee M., Lopes J. M. J., Besmehn A., Luysberg M., Knoll L., Habicht S., Musmann V., Luptak R., Lenk S., Rubio-Zuazo J., Castro G. R., Buca D., Zhao Q. T., Schubert J., and Mantl S.
 LaLuO_3 higher-kappa dielectric integration in SOI MOSFETs with a gate-first process
Solid-State Electronics **71**, 19 (2012)
- Niermann D., Waschkowski F., de Groot J., Angst M., and Hemberger J.
Dielectric Properties of Charge-Ordered LuFe_2O_4 Revisited: The Apparent Influence of Contacts
Physical Review Letters **109**, 016405 (2012)
- Oezaslan M., Heggen M., and Strasser P.
Size-dependent morphology of dealloyed bimetallic catalysts: Links the nano to the macro scale
Journal of the American Chemical Society **134**, 514 (2012)
- O'Halloran K. P., Zhao C. C., Ando N. S., Schultz A. J., Koetzle T. F., Piccoli P. M. B., Hedman B., Hodgson K. O., Bobyr E., Kirk M. L., Knottenbelt S., Depperman E. C., Stein B., Anderson T. M., Cao R., Geletii Y. V., Hardcastle K. I., Musaev D. G., Neiwert W. A., Fang X. K., Morokuma K., Wu S. X., Kogerler P., and Hill C. L.
Revisiting the Polyoxometalate-Based Late-Transition-Metal-Oxo Complexes: The "Oxo Wall" Stands
Inorganic Chemistry **51**, 7025 (2012)
- Ohkoshi T., Fujiwara H., Kotsugi M., Tsukamoto A., Arai K., Isogami S., Sekiyama A., Yamaguchi J., Fukushima K., Adam R., Schneider C. M., Nakamura T., Kodama K., Tsunoda M., Kinoshita T., and Suga S.
Microscopic and Spectroscopic Studies of Light-Induced Magnetization Switching of GdFeCo Facilitated by Photoemission Electron Microscopy
Jpn J Appl Phys **51**, 073001 (2012)
- Ohm C., Stampfer C., Splettstoesser J., and Wegewijs M. R.
Readout of carbon nanotube vibrations based on spin-phonon coupling
Applied Physics Letters **100**, 143103 (2012)
- Ondrejko P., Kempa M., Vysochanskii Y., Saint-Grégoire P., Bourges P., Rushchanskii K., and Hlinka J.
Neutron scattering study of ferroelectric $\text{Sn}_2\text{P}_2\text{S}_6$ under pressure
Physical Review B **86**, 224106 (2012)
- Ono T., Fujimoto Y., and Tsukamoto S.
First-Principles Calculation Methods for Obtaining Scattering Waves to Investigate Transport Properties of Nanostructures
Quantum Matter **1**, 4 (2012)
- Onoda S., Su Y., Kao Y.-J., Tsuei K.-D., Yasui Y., Kakurai K., Lees M. R., and Chang L.-J.
Higgs transition from a magnetic Coulomb liquid to a ferromagnet in $\text{Yb}_2\text{Ti}_2\text{O}_7$
Nature Communications **3**, 992 (2012)
- Oshima Y., Nojiri H., Schnack J., Kogerler P., and Luban M.
Determination of exchange energies in the sawtooth spin ring $\{\text{Mo}_{75}\text{V}_{20}\}$ by ESR
Physical Review B **85**, 024413 (2012)
- Ozdogan K., Sasioglu E., and Galanakis I.
Robustness and stability of half-metallic ferromagnetism in alkaline-earth metal mononitrides against doping and deformation
Journal of Applied Physics **111**, 113918 (2012)

- Padurariu C., Hassler F., and Nazarov Y. V.
Statistics of radiation at Josephson parametric resonance
Physical Review B **86**, 054514 (2012)
- Patra M., Majumdar S., Giri S., Xiao Y., and Chatterji T.
Magnetocaloric effect in RAl_2 (R = Nd, Sm, and Tm): Promising for cryogenic refrigeration close to liquid helium temperature
Journal of Alloys and Compounds **531**, 55 (2012)
- Pauly C., Bihlmayer G., Liebmann M., Grob M., Georgi A., Subramaniam D., Scholz M. R., Sanchez-Barriga J., Varykhalov A., Blugel S., Rader O., and Morgenstern M.
Probing two topological surface bands of Sb_2Te_3 by spin-polarized photoemission spectroscopy
Physical Review B **86**, 235106 (2012)
- Pavarini, E.; Koch, E.; Anders, F.; Jarrell, M. (eds.)
Correlated Electrons: From Models to Materials
Series: Modeling and Simulation, Vol. 2, Verlag des Forschungszentrum Jülich (2012)
ISBN: 978-3-89336-796-2
- Pazienti A., Flores F. J., Nawrot M. P., Maldonado P. E., Grün S., and Berger D.
Viewing strategy of Cebus monkeys during free exploration of natural images
Brain Research **1434**, 34 (2012)
- Peranio N., Eibl O., Töllner W., Nielsch K., Bessas D., Hermann R., Winkler M., König J., Böttner H., Pacheco V., Schmidt J., Hashibon A., Elsässer C., and Aabdin Z.
Nanostructure, excitations, and thermoelectric properties of Bi_2Te_3 -based nanomaterials
Journal of Electronic Materials **41**, 1792 (2012)
- Peranio N., Winkler M., Bessas D., Aabdin Z., König J., Böttner H., Hermann R., and Eibl O.
Room-temperature MBE deposition, thermoelectric properties, and advanced structural characterization of binary Bi_2Te_3 and Sb_2Te_3 thin films
Journal of Alloys and Compounds **521**, 163 (2012)
- Peranio N., Winkler M., Bessas D., König J., Hermann R., Böttner H., Eibl O., and Aabdin Z.
 Sb_2Te_3 and Bi_2Te_3 Thin Films Grown by Room-Temperature MBE
Journal of Electronic Materials **41**, 1493 (2012)
- Perlt S., Höche T., Dadda J., Müller E., Bauer Pereira P., Hermann R., Sarahan M., Pippel E., and Brydson R.
Microstructure analyses and thermoelectric properties of $\text{Ag}_{1-x}\text{Pb}_{18}\text{Sb}_{1+y}\text{Te}_{20}$
Journal of Solid State Chemistry **193**, 58 (2012)
- Peter D., Muller S., Wessel S., and Buchler H. P.
Anomalous Behavior of Spin Systems with Dipolar Interactions
Physical Review Letters **109**, 025303 (2012)
- Pietrowski M. J., De Souza R. A., Kim S., Munir Z. A., and Martin M.
Dehydration kinetics of nano-YSZ ceramics monitored by in-situ infrared spectroscopy
Solid State Ionics **225**, 241 (2012)
- Pin S., Newton M. A., D'Acapito F., Zema M., Tarantino S. C., Spinolo G., De Souza R. A., Martin M., and Ghigna P.
Mechanisms of Reactions in the Solid State: (110) Al_2O_3 + (001) ZnO Interfacial Reaction
Journal of Physical Chemistry C **116**, 980 (2012)
- Platt C., Thomale R., Honerkamp C., Zhang S. C., and Hanke W.
Mechanism for a pairing state with time-reversal symmetry breaking in iron-based superconductors
Physical Review B **85**, 180502 (2012)
- Pletyukhov M. and Schoeller H.
Nonequilibrium Kondo model: Crossover from weak to strong coupling
Physical Review Letters **108**, 260601 (2012)
- Poghossian A., Cherstvy A. G., Pedraza A. M., Ingebrandt S., Schöning M. J., and Abouzar M. H.
Label-free electrical detection of DNA by means of field-effect nanoplate capacitors: Experiments and modeling
Physica Status Solidi / A **209**, 925 (2012)
- Poilblanc D., Schuch N., Perez-Garcia D., and Cirac J. I.
Topological and entanglement properties of resonating valence bond wave functions
Physical Review B **86**, 014404 (2012)

- Popova D., Bringer A., and Blügel S.
Theoretical investigation of the inverse Faraday effect via a stimulated Raman scattering process
Physical Review B **85**, 094419 (2012)
- Poppe U. and Weber D.
Non-volatile gated variable resistor based on doped $\text{La}_2\text{CuO}_{4+\delta}$ and SrTiO_3 heterostructures
Journal of Applied Physics **111**, 056101 (2012)
- Porte L., Abel M., Amsalem P., Bocquet F., Bocquet F. C., Chevallier V., Clair S., Delafosse G., Desbief S., Gadenne V., Giovanelli L., Koudia M., Ksari Y., Loppacher C., Merlen A., Nony L., Ourdjini O., Patrone L., Pawlak R., Romann J., Valmalette J. C., and Themlin J. M.
Self-organised growth of molecular arrays at surfaces
International Journal of Nanotechnology **9**, 325 (2012)
- Pradheesh R., Nair H., Kumar C. M. N., Lamsal J., Nirmala R., Santhosh P. N., Yelon W. B., Malik S. K., Sankaranarayanan V., and Sethupathi K.
Observation of spin glass state in weakly ferromagnetic $\text{Sr}_2\text{FeCoO}_6$ double perovskite
Journal of Applied Physics **111**, 053905 (2012)
- Pradheesh R., Sankaranarayanan V., Sethupathi K., and Nair H.
Exchange bias and memory effect in double perovskite $\text{Sr}_2\text{FeCoO}_6$
Applied Physics Letters **101**, 142401 (2012)
- Pud S., Kisner A., Heggen M., Belaine D., Temirov R., Simon U., Offenhäusser A., Mourzina Y., and Vitusevich S.
Features of Transport in Ultrathin Gold Nanowire Structures
Small **9**, 846 (2012)
- Qiu L., Liu C., Dong H., Xu L., Zhang Y., Krause H.-J., Xie X., and Offenhäusser A.
Time-Domain Frequency Correction Method for Averaging Low-Field NMR Signals Acquired in Urban Laboratory Environment
Chinese physics Letters **29**, 107601 (2012)
- Radev I., Topalov G., Lefterova E., Ganske G., Schnakenberg U., Tsotridis G., and Slavcheva E.
Optimization of platinum/iridium ratio in thin sputtered films for PEMFC cathodes
International Journal of Hydrogen Energy **37**, 7730 (2012)
- Rahmanizadeh K., Bihlmayer G., Luysberg M., and Blügel S.
First-principles study of intermixing and polarization at the $\text{DyScO}_3/\text{SrTiO}_3$ interface
Physical Review B **85**, 075314 (2012)
- Rajeswari J., Ibach H., Schneider C. M., Costa A. T., Santos D. L. R., and Mills D. L.
Surface spin waves of fcc cobalt films on Cu(100): High-resolution spectra and comparison to theory
Physical Review B **86**, 165436 (2012)
- Raoux S., Ielmini D., Wuttig M., and Karpov I.
Phase change materials
Mrs Bulletin **37**, 118 (2012)
- Raoux S., König A. K., Cheng H. Y., Garbin D., Cheek R. W., Jordan-Sweet J. L., and Wuttig M.
Phase transitions in Ga-Sb phase change alloys
Physica Status Solidi B-Basic Solid State Physics **249**, 1999 (2012)
- Raty J. Y., Bichara C., Mazzarello R., Rausch P., Zalden P., and Wuttig M.
Comment on "New Structural Picture of the $\text{Ge}_2\text{Sb}_2\text{Te}_5$ Phase-Change Alloy"
Physical Review Letters **108**, 239601 (2012)
- Reininghaus M., Wortmann D., Finger J., Faley O., Poprawe R., and Stampfer C.
Laser induced non-thermal deposition of ultrathin graphite
Applied Physics Letters **100**, 151606 (2012)
- Rentrop J., Schuricht D., and Meden V.
Quench dynamics of the Tomonaga-Luttinger model with momentum-dependent interaction
New Journal of Physics **14**, 075001 (2012)
- Reuters B., Finken M., Wille A., Hollander B., Heuken M., Kalisch H., and Vescan A.
Relaxation and critical strain for maximum In incorporation in AlInGaN on GaN grown by metal organic vapour phase epitaxy
Journal of Applied Physics **112**, 093524 (2012)
- Reuters B., Wille A., Hollander B., Sakalauskas E., Ketteniss N., Mauder C., Goldhahn R., Heuken M., Kalisch H., and Vescan A.
Growth Studies on Quaternary AlInGaN Layers for HEMT Application
Journal of Electronic Materials **41**, 905 (2012)

- Richter S., Sandow C., Nichau A., Trellenkamp S., Schmidt M., Luptak R., Bourdelle K. K., Zhao Q. T., and Mantl S.
Omega-Gated Silicon and Strained Silicon Nanowire Array Tunneling FETs
IEEE Electron Device Letters **33**, 1535 (2012)
- Rieger T., Heiderich S., Lenk S., Lepsa M. I., and Grützmacher D.
Ga-assisted MBE growth of GaAs nanowires using thin HSQ layer
Journal of Crystal Growth **353**, 39 (2012)
- Rinklin P., Krause H.-J., and Wolfrum B.
On-chip control of magnetic particles
Physica Status Solidi / A **209**, 871 (2012)
- Rinklin P., Krause H.-J., and Wolfrum B.
Actuation and tracking of a single magnetic particle on a chip
Applied Physics Letters **100**, 014107 (2012)
- Rodriguez-Llamazares S., Jara P., Yutronic N., Fischler M., Simon U., and Noyong M.
Preferential Adhesion of Silver Nanoparticles Onto Crystal Faces of α -Cyclodextrin/Carboxylic Acids Inclusion Compounds
Journal of Nanoscience and Nanotechnology **12**, 8929 (2012)
- Roleder K., Bussmann-Holder A., Gorny M., Szot K., and Glazer A. M.
Precursor dynamics to the structural instability in SrTiO₃
Phase Transitions **85**, 939 (2012)
- Rudolf D., La-O-Vorakiat C., Battiato M., Adam R., Shaw J. M., Turgut E., Maldonado P., Mathias S., Grychtol P., Nembach H. T., Silva T. J., Aeschlimann M., Kapteyn H. C., Murnane M. M., Schneider C. M., and Oppeneer P. M.
Ultrafast magnetization enhancement in metallic multilayers driven by superdiffusive spin current
Nature Communications **3**, 1037 (2012)
- Rushchanskii K. Z. and Lezaic M.
Ab initio phonon structure of h-YMnO₃ in low-symmetry ferroelectric phase
Ferroelectrics **426**, 90 (2012)
- Rushchanskii K. Z., Spaldin N. A., and Lezaic M.
First-principles prediction of oxygen octahedral rotations in perovskite-structure EuTiO₃
Physical Review B **85**, 104109 (2012)
- Sachenko A. V., Belyaev A. E., Boltovets N. S., Konakova R. V., Kudryk Y. Y., Novitskii S. V., Sheremet V. N., Li J., and Vitusevich S. A.
Mechanism of contact resistance formation in ohmic contacts with high dislocation density
Journal of Applied Physics **111**, 083701 (2012)
- Sachenko A. V., Belyaev A. E., Boltovets N. S., Vinogradov A. O., Kladko V. P., Konakova R. V., Kudryk Y. Y., Kuchuk A. V., Sheremet V. N., and Vitusevich S. A.
Features of temperature dependence of contact resistivity in ohmic contacts on lapped n-Si
Journal of Applied Physics **112**, 063703 (2012)
- Sadowski J., Domagala J., Mathieu R., Kovacs A., Kasama T., Dunin-Borkowski R., and Dietl T.
Formation process and superparamagnetic properties of (Mn,Ga)As nanocrystals in GaAs fabricated by annealing of (Ga,Mn)As layers with low Mn content
Physical Review B **245306**, 84 (2012)
- Sandraskii L. M. and Mavropoulos P.
Magnetic excitations and ferromagnetism of FeRh: A first-principles study
Physical Review B **83**, 174408 (2012)
- Sanetra N., Karipidou Z., Wirtz R., Knorr N., Rosselli S., Nelles G., Offenhäusser A., and Mayer D.
Printing of Highly Integrated Crossbar Junctions
Advanced Functional Materials **22**, 1129 (2012)
- Sapezanskaia I., Nayak A., Tsuruoka T., Bredow T., Hasegawa T., Staikov G., Aono M., Waser R., and Valov I.
Atomically controlled electrochemical nucleation at superionic solid electrolyte surfaces
Nature Materials **11**, 530 (2012)
- Saptsov R. B. and Wegewijs M. R.
Fermionic superoperators for zero-temperature nonlinear transport: Real-time perturbation theory and renormalization group for Anderson quantum dots
Physical Review B **86**, 235432 (2012)

- Sasioglu E., Friedrich C., and Blügel S.
Strength of the Effective Coulomb Interaction at Metal and Insulator Surfaces
Physical Review Letters **109**, 146401 (2012)
- Sawinski P. K. and Dronskowski R.
Solvothermal Synthesis, Crystal Growth, and Structure Determination of Sodium and Potassium Guanidinate
Inorganic Chemistry **51**, 7425 (2012)
- Schaal P. A., Besmehn A., Maynicke E., Noyong M., Beschoten B., and Simon U.
Electrically Conducting Nanopatterns Formed by Chemical e-Beam Lithography via Gold Nanoparticle Seeds
Langmuir **28**, 2448 (2012)
- Scherer M. M., Uebelacker S., and Honerkamp C.
Instabilities of interacting electrons on the honeycomb bilayer
Physical Review B **85**, 235408 (2012)
- Scherer M. M., Uebelacker S., Scherer D. D., and Honerkamp C.
Interacting electrons on trilayer honeycomb lattices
Physical Review B **86**, 155415 (2012)
- Schmidt M., Minamisawa R. A., Richter S., Lupták R., Hartmann J.-M., Buca D., Zhao Q. T., and Manti S.
Impact of strain and Ge concentration on the performance of planar SiGe band-to-band-tunneling transistors
Solid State Electronics **71**, 42 (2012)
- Schmidt M., Minamisawa R. A., Richter S., Schafer A., Buca D., Hartmann J. M., Zhao Q. T., and Manti S.
Unipolar behavior of asymmetrically doped strained $\text{Si}_{0.5}\text{Ge}_{0.5}$ tunneling field-effect transistors
Applied Physics Letters **101**, 123501 (2012)
- Schmidt M. J.
Strong correlations at topological insulator surfaces and the breakdown of the bulk-boundary correspondence
Physical Review B **86**, 161110 (2012)
- Schmidt M. J.
Bosonic field theory of tunable edge magnetism in graphene
Physical Review B **86**, 075458 (2012)
- Schmidt M. J., Rainis D., and Loss D.
Decoherence of Majorana qubits by noisy gates
Physical Review B **86**, 085414 (2012)
- Schmitz H., Soltner H., and Bousack H.
Biomimetic Infrared Sensors Based on Photomechanical Infrared Receptors in Pyrophilous (fire-loving) Insects
IEEE Sensors Journal **12**, 281 (2012)
- Schneider C. M., Wiemann C., Patt M., Feyer V., Plucinski L., Krug I. P., Escher M., Weber N., Merkel M., Renault O., and Barrett N.
Expanding the view into complex material systems: From micro-ARPES to nanoscale HAXPES
Journal of Electron Spectroscopy and related Phenomena **185**, 330 (2012)
- Schnitker J., Wolfrum B., and Yakushenko A.
Printed Carbon Microelectrodes for Electrochemical Detection of Single Vesicle Release from PC12 Cells
Analytical chemistry **84**, 4613 (2012)
- Schober H. R.
Modeling aging rates in a simple glass and its melt
Physical Review B **85**, 024204 (2012)
- Schottdorf M., Hofmann B., Kätelhöhn E., Offenhausser A., and Wolfrum B.
Frequency-dependent signal transfer at the interface between electrogenic cells and nanocavity electrodes
Physical Review / E **85**, 031917 (2012)
- Schroper F., Baumann A., Offenhausser A., and Mayer D.
Direct electrochemistry of novel affinity-tag immobilized recombinant horse heart cytochrome c
Biosensors & Bioelectronics **34**, 171 (2012)
- Schuch N., Poilblanc D., Cirac J. I., and Perez-Garcia D.
Resonating valence bond states in the PEPS formalism
Physical Review B **86**, 115108 (2012)

- Schuricht D.
Spectral properties of one-dimensional spiral spin density wave states
Physical Review B **85**, 121101 (2012)
- Schuricht D. and Essler F. H. L.
Dynamics in the Ising field theory after a quantum quench
Journal of Statistical Mechanics-Theory and Experiment, 04017 (2012)
- Seemann K. M., Garcia-Sanchez F., Kronast F., Miguel J., Kakay A., Schneider C. M., Hertel R., Freimuth F., Mokrousov Y., and Blugel S.
Disentangling the Physical Contributions to the Electrical Resistance in Magnetic Domain Walls: A Multiscale Study
Physical Review Letters **108**, 077201 (2012)
- Shirazi R., Kopylov O., Kovacs A., and Kardynal B. E.
Temperature dependent recombination dynamics in InP/ZnS colloidal nanocrystals
Applied Physics Letters **101**, 091910 (2012)
- Shulman M. D., Dial O. E., Harvey S. P., Bluhm H., Umansky V., and Yacoby A.
Demonstration of Entanglement of Electrostatically Coupled Singlet-Triplet Qubits
Science **336**, 202 (2012)
- Sickinger H., Lipman A., Weides M., Mints R. G., Kohlstedt H., Koelle D., Kleiner R., and Goldobin E.
Experimental evidence of a ϕ -Josephson Junction
Physical Review Letters **109**, 107002 (2012)
- Siegrist T., Merkelbach P., and Wuttig M.
Phase Change Materials: Challenges on the Path to a Universal Storage Device
in *Annual Review of Condensed Matter Physics, Vol 3*, ed. Langer J. S., Vol. 3, p. 215-237 (2012)
- Simons T. and Simon U.
Zeolites as nanoporous, gas-sensitive materials for in situ monitoring of DeNO_x-SCR
Beilstein Journal of Nanotechnology **3**, 667 (2012)
- Singh P. S., Kätelhön E., Mathwig K., Wolfrum B., and Lemay S. G.
Stochasticity in Single-Molecule Nanoelectrochemistry: Origins, Consequences, and Solutions
ACS Nano **6**, 9662 (2012)
- Singh T. B., Chen X., Wong W. W. H., Ehlig T., Kemppinen P., Chen M., Watkins S. E., Winzenberg K. N., Holdcroft S., Jones D. J., and Holmes A. B.
Correlation of charge extraction properties and short circuit current in various organic binary and ternary blend photovoltaic devices
Applied physics / A **108**, 515 (2012)
- Sladek K., Winden A., Wirths S., Weis K., Blömers C., Gül Ö., Grap T., Lenk S., von der Ahe M., Weirich T. E., Hardtdegen H., Lepsa M. I., Lysov A., Li Z. A., Prost W., Tegude F. J., Lüth H., Schäpers T., and Grützmacher D.
Comparison of InAs nanowire conductivity: influence of growth method and structure
Physica Status Solidi / C **9**, 230 (2012)
- Slipukhina I., Mavropoulos P., Blügel S., and Lezaic M.
Ferromagnetic Spin Coupling of 2p Impurities in Band Insulators Stabilized by an Intersite Coulomb Interaction: Nitrogen-Doped MgO
Physical Review Letters **107**, 137203 (2012)
- Sluka V., Kakay A., Deac A. M., Burgler D. E., Hertel R., and Schneider C. M.
Quenched Slonczewski windmill in spin-torque vortex oscillators
Physical Review B **86**, 214422 (2012)
- Sofer Z., Sedmidubský D., Jankovsky O., Hejtmanek J., Marysko M., Vaclavu M., Mikulics M., and Simek P.
Mn doping of GaN layers grown by MOVPE
Ceramics Silikáty **56**, 122 (2012)
- Sofer Z., Sedmidubský D., Jankovsky O., Mikulics M., and Nadherny L.
ZnO thin films prepared by spray-pyrolysis technique from organo-metallic precursor
Ceramics Silikáty **56**, 117 (2012)

- Splettstoesser J., Governale M., and König J.
Tunneling-induced renormalization in interacting quantum dots
Physical Review B **86**, 035432 (2012)
- Stadtmüller B., Sueyoshi T., Kichin G., Kröger I., Soubatch S., Temirov R., Tautz F. S., and Kumpf C.
Commensurate registry and chemisorptions at a hetero-organic interface
Physical Review Letters **108**, 106103 (2012)
- Stadtmüller B., Willenbockel M., Reinisch E. M., Ules T., Bocquet F. C., Soubatch S., Puschnig P., Koller G., Ramsey M. G., Tautz F. S., and Kumpf C.
Orbital tomography for highly symmetric adsorbate systems
Europhysics Letters **100**, 26008 (2012)
- Stampfer C.
Chips 2020
Physik Journal **11**, 61 (2012).
- Standop S., Morgenstern M., Michely T., and Busse C.
H₂O on Pt(111): structure and stability of the first wetting layer
Journal of Physics-Condensed Matter **24**, 124103 (2012)
- Stefanov S., Conde J. C., Benedetti A., Serra C., Werner J., Oehme M., Schulze J., Buca D., Holländer B., Mantl S., and Chiussi S.
Silicon germanium tin alloys formed by pulsed laser induced epitaxy
Applied Physics Letters **100**, 204102 (2012)
- Stefanov S., Conde J. C., Benedetti A., Serra C., Werner J., Oehme M., Schulze J., Buca D., Holländer B., Mantl S., and Chiussi S.
Laser synthesis of germanium tin alloys on virtual germanium
Applied Physics Letters **100**, 104101 (2012)
- Stemme F., Geßwein H., Drahus M. D., Holländer B., Azucena C., Binder J. R., Eichel R.-A., Haußelt J., and Bruns M.
Characterization of non-stoichiometric co-sputtered Ba_{0.6}Sr_{0.4}(Ti_{1-x}Fe_x)_{1+x} O_{3-δ} thin films for tunable passive microwave applications
Analytical and Bioanalytical Chemistry **403**, 643 (2012)
- Stille S., Lenser C., Dittmann R., Koehl A., Krug I., Muenstermann R., Perlich J., Schneider C. M., Klemradt U., and Waser R.
Detection of filament formation in forming-free resistive switching SrTiO₃ devices with Ti top electrodes
Applied Physics Letters **100**, 223503 (2012)
- Stockmann R., Jansen M., Yegin U., Offenhäusser A., Kubota L. T., Mourzina Y., and Kisner A.
Sensing small neurotransmitter enzyme interaction with nanoporous gated ion-sensitive field effect transistors
Biosensors and Bioelectronics **31**, 157 (2012)
- Stoffel R. P. and Dronskowski R.
Barium Peroxide: a Simple Test Case for First-Principles Investigations on the Temperature Dependence of Solid-State Vibrational Frequencies
Zeitschrift für anorganische und allgemeine Chemie **638**, 1403 (2012)
- Subramaniam D., Libisch F., Li Y., Pauly C., Geringer V., Reiter R., Mashoff T., Liebmann M., Burgdorfer J., Busse C., Michely T., Mazzeo R., Pratzner M., and Morgenstern M.
Wave-Function Mapping of Graphene Quantum Dots with Soft Confinement
Physical Review Letters **108**, 046801 (2012)
- Sydoruk V. A., Xiang D., Vitusevich S. A., Petrychuk M. V., Vladyka A., Zhang Y., Offenhäusser A., Kochelap V. A., Belyaev A. E., and Mayer D.
Noise and transport characterization of single molecular break junctions with individual molecule
Journal of Applied Physics **112**, 014908 (2012)
- Takahashi T., Burghaus J., Music D., Dronskowski R., and Schneider J. M.
Elastic properties of gamma '-Fe₄N probed by nanoindentation and ab initio calculation
Acta Materialia **60**, 2054 (2012)
- Tang X. J., Speldrich M., Tchougreeff A. L., and Dronskowski R.
Syntheses, Crystal Structures and Magnetic Properties of Cr(NCNH₂)₄Cl₂ and Mn(NCNH₂)₄Cl₂
Zeitschrift für Naturforschung Section B-a Journal of Chemical Sciences **67**, 1205 (2012)
- Tappertzhofen S., Mündelein H., Valov I., and Waser R.
Nanoionic transport and electrochemical reactions in resistively switching silicon dioxide
Nanoscale **4**, 3040 (2012)

- Tappertzhofen S., Valov I., and Waser R.
Quantum conductance and switching kinetics of AgI based microcrossbar cells
Nanotechnology **23**, 5703 (2012)
- Tchougreeff A. L., Liu X. H., Muller P., van Beek W., Ruschewitz U., and Dronskowski R.
Structural Study of CuNCN and Its Theoretical Implications: A Case of a Resonating-Valence-Bond State?
Journal of Physical Chemistry Letters **3**, 3360 (2012)
- Teliban I., Chemnitz S., Thede C., Bechtold C., Mozooni B., Krause H.-J., and Quandt E.
M(H) shape reconstruction using magnetic spectroscopy
Journal of Magnetism and Magnetic Materials **324**, 895 (2012)
- Tennant D. A., Lake B., James A. J. A., Essler F. H. L., Notbohm S., Mikeska H. J., Fielden J., Kogerler P., Canfield P. C., and Telling M. T. F.
Anomalous dynamical line shapes in a quantum magnet at finite temperature
Physical Review B **85**, 014402 (2012)
- Terhal B. M., Hassler F., and DiVincenzo D.
From Majorana Fermions to Topological Order
Physical Review Letters **108**, 260504 (2012)
- Terhal, B.M.
The Fragility of Quantum Information?
in *Lecture Notes in Computer Science*, Eds: D. Hutchison et al., Vol. **7505**, pp. 47-56 (2012)
- Thiess A., Dederichs P. H., Zeller R., Blügel S., and Lambrecht W. R. L.
Superparamagnetism in Gd-doped GaN induced by Ga-vacancy clustering
Physical Review B **86**, 180401 (2012)
- Timper J., Gutmiedl K., Wirges C., Broda J., Noyong M., Carell T., Simon U., and Mayer J.
Surface "Click" Reaction of DNA followed by Directed Metalization for the Construction of Contactable Conducting Nanostructures
Angewandte Chemie / International edition **51**, 7586 (2012)
- Topwal D., Manju U., Pacilé D., Papagno M., Wortmann D., Bihlmayer G., Blügel S., and Carbone C.
Quantum electron confinement in closely matched metals: Au films on Ag(111)
Physical Review B **86**, 085419 (2012)
- Torricelli G., van Zwol P. J., Shpak O., Palasantzas G., Svetovoy V. B., Binns C., Kooi B. J., Jost P., and Wuttig M.
Casimir Force Contrast Between Amorphous and Crystalline Phases of AlSi
Advanced Functional Materials **22**, 3729 (2012)
- Trellenkamp S., Grützmacher D., Offenhausser A., Rienks B., and Moers J.
Optimized marker definition for high overlay accuracy e-beam lithography
Microelectronic Engineering **97**, 68 (2012)
- Trinkaus H., Buca D., Minamisawa R. A., Holländer B., Luysberg M., and Mantl S.
Anisotropy of strain relaxation in (100) and (110) Si/SiGe heterostructures
Journal of Applied Physics **111**, 014904 (2012)
- Trotzky S., Chen Y.-A., Flesch A., McCulloch I. P., Schollwöck U., Eisert J., and Bloch I.
Probing the relaxation towards equilibrium in an isolated strongly correlated one-dimensional Bose gas
Nature physics **8**, 325 (2012)
- Tsuruoka T., Terabe K., Hasegawa T., Valov I., Waser R., and Aono M.
Effects of Moisture on the Switching Characteristics of Oxide-Based, Gapless-Type Atomic Switches
Advanced Functional Materials **22**, 70 (2012)
- Uebelacker S. and Honerkamp C.
Self-energy feedback and frequency-dependent interactions in the functional renormalization group flow for the two-dimensional Hubbard model
Physical Review B **86**, 235140 (2012)
- Uebelacker S. and Honerkamp C.
Multiband effects on superconducting instabilities driven by electron-electron interactions
Physical Review B **85**, 155122 (2012)
- Valov I., Sapezanskaia I., Nayak A., Tsuruoka T., Bredow T., Hasegawa T., Staikov G., Aono M., and Waser R.
Atomically controlled electrochemical nucleation at superionic solid electrolyte surfaces
Nature Materials **11**, 530 (2012)

- van Aken B. B., Duchamp M., Boothroyd C. B., Dunin-Borkowski R., and Soppe W.
EELS measurements of boron concentration profiles in p-a-Si and n-p a-Si solar cells
Journal of Non-Crystalline Solids **358**, 2179 (2012)
- van Heck B., Akhmerov A. R., Hassler F., Burrello M., and Beenakker C. W. J.
Coulomb-assisted braiding of Majorana fermions in a Josephson junction array
New Journal of Physics **14**, 035019 (2012)
- Varykhalov A., Marchenko D., Scholz M. R., Rienks E. D. L., Kim T. K., Bihlmayer G., Sánchez-Barriga J., and Rader O.
Ir(111) Surface State with Giant Rashba Splitting Persists under Graphene in Air
Physical Review Letters **108**, 066804 (2012)
- Vestgård J. I., Yurchenko V. V., Wördenweber R., and Johansen T. H.
Mechanism for flux guidance by micrometric antidot arrays in superconducting films
Physical Review B **85**, 014516 (2012)
- Voleská I., Akola J., Jovari P., Gutwirth J., Wágner T., Vasileiadis T., Yannopoulos S. N., and Jones R. O.
Structure, electronic, and vibrational properties of glassy $\text{Ga}_{11}\text{Ge}_{11}\text{Te}_{78}$: Experimentally constrained density functional study
Physical Review B **86**, 094108 (2012)
- Volkov O. Y., Divin Y., and Gubankov V. N.
Terahertz Characterization of External Resonant Systems by High-Tc Josephson Junctions
IEEE Transactions on Applied Superconductivity **21**, 306 (2012)
- von Bergmann K., Bihlmayer G., and Heinze S.
Gitter aus magnetischen Wirbeln
Physik in unserer Zeit **43**, 6 (2012)
- Vuong Q. L., Van Doorslaer S., Bridot J. L., Argente C., Alejandro G., Hermann R., Disch S., Mattea C., Stapf S., and Gossuin Y.
Paramagnetic nanoparticles as potential MRI contrast agents: characterization, NMR relaxation, simulations and theory
Magnetic Resonance Materials in Physics Biology and Medicine **25**, 467 (2012)
- Wagner C., Forker R., and Fritz T.
On the Origin of the Energy Gain in Epitaxial Growth of Molecular Films
Journal of Physical Chemistry Letters **3**, 419 (2012)
- Wagner C., Fournier N., Tautz F. S., and Temirov R.
Measurement of the Binding Energies of the Organic-Metal Perylene-Tetracarboxylic-Dianhydride/Au(111) Bonds by Molecular Manipulation Using an Atomic Force Microscope
Physical Review Letters **109**, 076102 (2012)
- Wang J., Nather C., Kogerler P., and Bensch W.
 $\text{V}_{15}\text{Ge}_6\text{O}_{42}\text{S}_6(\text{H}_2\text{O})^{12-}$, a Thiogermanatopolyoxovanadate Cluster Featuring the Spin Topology of the Molecular Magnet $\text{V}_{15}\text{As}_6\text{O}_{42}(\text{H}_2\text{O})^{6-}$
European Journal of Inorganic Chemistry, 1237 (2012)
- Wang K. R., Mauder C., Wan Q., Jenichen B., Woitok J. F., Grahn H. T., Kalisch H., Heuken M., Vescan A., and Trampert A.
Formation of a Monocrystalline, M-Plane AlN Layer by the Nitridation of gamma-LiAlO₂(100)
Applied Physics Express **5**, 105501 (2012)
- Wang X., Sui Y., Tang J., Wang C., Zhang X., Lu Z., Liu Z., Su W., Wei X., and Yu R.
Amplification of magnetoresistance of magnetite in an $\text{Fe}_3\text{O}_4\text{-SiO}_2\text{-Si}$ structure
Applied Physics Letters **92** (1), 012122 (2012)
- Weher D., Wessel C., Reimann C., Schwickert C., Müller A., Ressler T., Pottgen R., Bredow T., Dronskowski R., and Lerch M.
Anosovite-Type V_3O_5 : A New Binary Oxide of Vanadium
Inorganic Chemistry **51**, 8524 (2012)
- Wei X., Su Y. T., Sui Y., Zhang Q. H., Yao Y., Jin C. Q., and Yu R. C.
Structure, electrical and magnetic property investigations on dense Fe-doped hexagonal BaTiO_3
Journal of Applied Physics **110**, 114112 (2012)
- Wei X., Yao L. D., Shen X., Yang Y., You S. J., Li F. Y., Jin C. Q., and Yu R. C.
Structural modulation and magnetic properties of hexagonal $\text{Ba}(\text{Ti}_{1-x}\text{Fe}_x)\text{O}_{3.5}$ ceramics
Physica / B **405**, 4851 (2012)
- Wei X., Zhang Q., Jin C., and Yu R.
Structural incommensurate modulation rule in hexagonal $\text{Ba}(\text{Ti}_{1-x}\text{M}_x)\text{O}_{3.5}$ (M=Mn,Fe) multiferroics
AIP Advances **2**, 042129 (2012)

- Wei X., Zhang Q., Li F., Yu R., and Jin C.
Structural evolution induced by acceptor doping into BaTiO₃ ceramics
Journal of Alloys and Compounds **508** 486 (2012)
- Wei X., Zou T., Wang F., Zhang Q. H., Sun Y., Gu L., Hirata A., Chen M. W., Yao Y., Jin C. Q., and Yu R. C.
Origin of ferromagnetism and oxygen-vacancy ordering induced cross-controlled magnetoelectric effects at room temperature
Journal of Applied Physics **111** 073904 (2012)
- Weigel S., Schulte P., Meffert S., Bräunig P., and Offenhäusser A.
Locust primary neuronal culture for the study of synaptic transmission
Journal of Molecular Histology **43**, 405 (2012)
- Weil M. H., Bäcker M., Mayer D., Schöning M. J., and Poghosian A.
Field-effect Devices Functionalised with Gold-Nanoparticle/Macromolecule Hybrids: New Opportunities for a Label-Free Biosensing
Procedia Engineering **47**, 273 (2012)
- Weingarten M., Slawinski M., Urbain F., Fahle D., Bertram D., Heuken M., Kalisch H., and Vescan A.
Characterization of charge carrier injection in organic and hybrid organic/inorganic semiconductor devices by capacitance-voltage measurements
in *Organic Light Emitting Materials and Devices XVI*, ed. So F. and Adachi C., Vol. 8476, p. 84761H (2012)
- Wesche M., Huske M., Yakushenko A., Bruggemann D., Mayer D., Offenhäusser A., and Wolfrum B.
A nanoporous alumina microelectrode array for functional cell-chip coupling
Nanotechnology **23**, 495303 (2012)
- Wessel C. and Dronskowski R.
A First-Principles Study on the Existence of Niobium and Tantalum Sesquioxide
Zeitschrift für anorganische und allgemeine Chemie **638**, 2117 (2012)
- Wessel C., Reimann C., Müller A., Weber D., Lerch M., Ressler T., Bredow T., and Dronskowski R.
Electronic structure and thermodynamics of V₂O₃ polymorphs
Journal of Computational Chemistry **33**, 2102 (2012)
- Wessel S.
Absence of valence-bond supersolidity on the checkerboard lattice
Physical Review B **86**, 140501 (2012)
- Wicklein S., Sambri A., Amoroso S., Wang X., Bruzzese R., Koehl A., and Dittmann R.
Pulsed laser ablation of complex oxides: The role of congruent ablation and preferential scattering for the film stoichiometry
Applied Physics Letters **101**, 131601 (2012)
- Wiemann C., Kaiser A. M., Cramm S., and Schneider C. M.
Deflection gating for time-resolved x-ray magnetic circular dichroism-photoemission electron microscopy using synchrotron radiation
Review of Scientific Instruments **83**, 063706 (2012)
- Wiemann C., Patt M., Cramm S., Escher M., Merkel M., Gloskovskii A., Thiess S., Drube W., and Schneider C. M.
Probing buried layers by photoelectron spectromicroscopy with hard x-ray excitation
Applied Physics A **100**, 223106 (2012)
- Wießner M., Hauschild D., Schöll A., Reinert F., Feyer V., Winkler K., and Krömker B.
Electronic and geometric structure of the PTCDA/Ag(110) interface probed by angle-resolved photoemission
Physical Review B **86**, 045417 (2012)
- Williams E. R., Diesmann M., Grün S., Trengove C., and Gerstein G. L.
Detecting synfire chains in parallel spike data
Journal of Neuroscience Methods **206**, 54 (2012)
- Windén A., Mikulics M., Haab A., Stoica T., von der Ahe M., Wirtz K., Hardtdegen H., and Grützmacher D.
Morphology evolution and optical properties of GaN nano-pyramids grown by selective area MOVPE
Physica Status Solidi / C **9**, 624 (2012)
- Winkin N. and Mokwa W.
Flexible Multi-Electrode Array with Integrated Bendable CMOS-Chip for Implantable Systems
in *2012 Annual International Conference of the IEEE Engineering in Medicine and Biology Society*, 3882-3885 (2012)
- Wirths S., Mikulics M., Heintzmann P., Windén A., Weis K., Volk C., Sladek K., Demarina N., Hardtdegen H., Grützmacher D., and Schäpers T.
Preparation of Ohmic contacts to GaAs/AlGaAs-core/shell-nanowires
Applied Physics Letters **100**, 042103 (2012)

- Witte W., Fahle D., Koch H., Heuken M., Kalisch H., and Vescan A.
Electrical properties of quasi-vertical Schottky diodes
Semiconductor Science and Technology **27**, 085015 (2012)
- Wördenweber R., Grellmann T., Greben K., Schubert J., Kutzner R., and Hollmann E.
Stress Generated Modifications of Structural and Morphologic Properties of Epitaxial SrTiO₃ Films on Sapphire
Ferroelectrics **430**, 57 (2012)
- Wördenweber R., Hollmann E., Schubert J., Kutzner R., and Panaitov G.
Flux transport in nanostructured high-T_c films at microwave frequencies
Physica / C **479**, 69 (2012)
- Wördenweber R., Hollmann E., Schubert J., Kutzner R., and Panaitov G.
Regimes of flux transport at microwave frequencies in nanostructured high-T_c films
Physical Review B **85**, 04503 (2012)
- Wuttig M.
Phase change materials: Chalcogenides with remarkable properties due to an unconventional bonding mechanism
Physica Status Solidi B-Basic Solid State Physics **249**, 1843 (2012)
- Wuttig M. and Raoux S.
The Science and Technology of Phase Change Materials
Zeitschrift für anorganische und allgemeine Chemie **638**, 2455 (2012)
- Wuttig M. and Salinga M.
PHASE-CHANGE MATERIALS Fast transformers
Nature Materials **11**, 270 (2012)
- Xiao Y., Schmitz B., Perßon J., Schmidt W., Meuffels P., Roth G., Brückel T., and Li H.
Possible magnetic-polaron-switched positive and negative magnetoresistance in the GdSi single crystals
Scientific Reports **2**, 750 (2012)
- Xiao Y., Su Y., Nandi S., Price S., Schmitz B., Kumar C. M. N., Mittal R., Chatterji T., Kumar N., Dhar S. K., Thamizhavel A., and Brückel T.
Anomalous in-plane magnetoresistance in a EuFe₂As₂ single crystal: Evidence of strong spin-charge-lattice coupling
Physical Review B **85**, 094504 (2012)
- Xie L., Li Y. L., Yu R., Cheng Z. Y., Wei X. Y., Yao X., Jia C. L., Urban K., Bokov A., Ye Z. G., and Zhu J.
Static and dynamic polar nanoregions in relaxor ferroelectric Ba(Ti_{1-x}Sn_x)O₃ system at high temperature
Physical Review B **85**, 014118 (2012)
- Yadgarov L., Stroppa D., Rosentsveig R., Ron R., Enyashin A. N., Houben L., and Tenne R.
Investigation of Rhenium-Doped MoS₂ Nanoparticles with Fullerene-Like Structure
Zeitschrift für anorganische und allgemeine Chemie **638** 2610 (2012)
- Yakushenko A., Schnitker J., and Wolfrum B.
Printed Carbon Microelectrodes for Electrochemical Detection of Single Vesicle Release from PC12 Cells
Analytical chemistry **84**, 4613 (2012)
- Yamada T., Deringer V. L., Dronskowski R., and Yamane H.
Synthesis, Crystal Structure, Chemical Bonding, and Physical Properties of the Ternary Na/Mg Stannide Na₂MgSn
Inorganic Chemistry **51**, 4810 (2012)
- Yang S., Huang S., Chen H., Zhou C., Zhou Q., Schnee M., Zhao Q. T., Schubert J., and Chen K. J.
AlGaIn/GaN MISHEMTs with High-k LaLuO₃ Gate Dielectric
IEEE Electron Device Letters **33**, 979 (2012)
- Yao H., Günel H. Y., Blömers C., Weis K., Chi J., Lu J. G., Liu J., Grützmacher D., and Schäpers T.
Phase coherent transport in InSb nanowires
Applied Physics Letters **101**, 082103 (2012)
- Yi J. X., Brendt J., Schroeder M., and Martin M.
Oxygen permeation and oxidation states of transition metals in (Fe, Nb)-doped BaCoO_{3-δ} perovskites
Journal of Membrane Science **387**, 17 (2012)
- Yu R., Lentzen M., and Zhu J.
Effective object planes for aberration-corrected transmission electron microscopy
Ultramicroscopy **112**, 15 (2012)

- Yu W., Zhang B., Zhao Q. T., Buca D., Hartmann J. M., Luptak R., Mussler G., Fox A., Bourdelle K. K., Wang X., and Mantl S.
Hole Mobilities of Si/Si_{0.5}Ge_{0.5} Quantum-Well Transistor on SOI and Strained SOI
IEEE Electron Device Letters **33**, 758 (2012)
- Zalden P., Aquilanti G., Prestipino C., Mathon O., Andre B., Wuttig M., and Coulet M. V.
Simultaneous calorimetric and quick-EXAFS measurements to study the crystallization process in phase-change materials
Journal of Synchrotron Radiation **19**, 806 (2012)
- Zanolli Z. and Charlier J.-C.
Single-Molecule Sensing Using Carbon Nanotubes Decorated with Magnetic Clusters
ACS nano **6**, 10786 (2012)
- Zarpellon J., Jaffrès H., Frougier J., Deranlot C., George J., Mosca D., Lemaître A., Freimuth F., Duong Q., Renucci P., and Marie X.
Spin injection at remanence into III-V spin light-emitting diodes using (Co/Pt) ferromagnetic injectors
Physical Review B **86**, 205314 (2012)
- Zeller, R., Thiess, A., Bolten, M., Dederichs, P.H., and Blügel, S.
KKRnano: Precise Density Functional Calculations for Thousands of Atoms
in: *NIC Symposium 2012 – Proceedings*, Eds. K. Binder, G. Münster, and M. Kremer, Verlag des Forschungszentrum Jülich, NIC Series Vol. **45**, pp. 267-274 (2012)
- Zhang B., Zhao Q. T., Buca D., Hartmann J.-M., Lupták R., Mussler G., Fox A., Bourdelle K. K., Wang X., Mantl S., and Yu W.
Hole Mobilities of Si/Si_{0.5}Ge_{0.5} Quantum-Well Transistor on SOI and Strained SOI
IEEE Electron Device Letters **33**, 758 (2012)
- Zhang G., Zhang Y., Dong H., Krause H.-J., Xie X., Braginski A. I., Offenhäusser A., and Jiang M.
Parameter tolerance of the SQUID Bootstrap Circuit
Superconductor Science and Technology **24**, 015006 (2012)
- Zhang G., Zhang Y., Zhang S., Krause H.-J., Wang Y., Liu C., Zeng J., Qiu Y., Kong X., Dong H., Xie X., Offenhäusser A., and Jiang M.
A SQUID gradiometer module with wire-wound pickup antenna and integrated voltage feedback circuit
Physica C **480**, 10 (2012)
- Zhang G. R., Gorelov E., Koch E., and Pavarini E.
Importance of exchange anisotropy and superexchange for the spin-state transitions in RCoO₃ (R = rare earth) cobaltates
Physical Review B **86**, 184413 (2012)
- Zhang H., Freimuth F., Bihlmayer G., Blügel S., and Mokrousov Y.
Topological phases of Bi(111) bilayer in an external exchange field
Physical Review B **86**, 035104 (2012)
- Zhang H., Lazo C., Blügel S., Heinze S., and Mokrousov Y.
Electrically Tunable Quantum Anomalous Hall Effect in Graphene Decorated by 5d Transition-Metal Adatoms
Physical Review Letters **108**, 056802 (2012)
- Zhang Q. H., Wang L. J., Wei X., Yu R. C., Gu L., Hirata A., Chen M. W., Jin C. Q., Yao Y., Wang Y. G., and Duan X. F.
Direct observation of interlocked domain walls in hexagonal RMnO₃ (R=Tm,Lu)
Physical Review B **85**, 4 (2012)
- Zhang W., Ronneberger I., Li Y., and Mazzarello R.
Magnetic Properties of Crystalline and Amorphous Phase-Change Materials Doped with 3d Impurities
Advanced Materials **24**, 4387 (2012)
- Zhang W., Thiess A., Zalden P., Zeller R., Dederichs P. H., Raty J. Y., Wuttig M., Blügel S., and Mazzarello R.
Role of vacancies in metal-insulator transitions of crystalline phase-change materials
Nature Materials **11**, 952 (2012)
- Zhang Y., Liu C., Schmelz M., Krause H.-J., Braginski A. I., Stolz R., Xie X., Meyer H.-G., Offenhäusser A., and Jiang M.
Planar SQUID magnetometer integrated with bootstrap circuitry under different bias modes
Superconductor Science and Technology **25**, 125007 (2012)

- Zhao Q. T., Yu W. J., Zhang B., Schmidt M., Richter S., Buca D., Hartmann J.-M., Lupták R., Fox A., Bourdelle K. K., and Mantl S.
Tunneling field-effect transistor with a strained Si channel and a $\text{Si}_{0.5}\text{Ge}_{0.5}$ source
Solid State Electronics **74**, 97 (2012)
- Zhu G. B., Geletii Y. V., Kogerler P., Schilder H., Song J., Lense S., Zhao C. C., Hardcastle K. I., Musaev D. G., and Hill C. L.
Water oxidation catalyzed by a new tetracobalt-substituted polyoxometalate complex: $\{\text{Co}^{\text{IV}}(\mu\text{-OH})(\text{H}_2\text{O})_3\}(\text{Si}_2\text{W}_{19}\text{O}_{70})^{11-}$
Dalton Transactions **41**, 2084 (2012)
- Zhukov, Volk C., Winden A., Hardtdegen H., and Schäpers T.
Negative differential conductance in InAs wire based double quantum dot induced by a charged AFM tip
Journal of Experimental and Theoretical Physics **115**, 1062 (2012)
- Zhukov A. A., Volk C., Winden A., Hardtdegen H., and Schäpers T.
Direct Observation of Standing Electron Waves in Diffusively Conducting InAs Nanowire
Journal of Experimental and Theoretical Physics **96**, 114 (2012)
- Ziegler M., Soni R., Patelczyk T., Ignatov M., Bartsch T., Meuffels P., and Kohlstedt H.
An Electronic Version of Pavlov's Dog
Advanced Functional Materials **22**, 2744 (2012)
- Zimmer C. M., Kieschnick M., Kallis K. T., Schubert J., Kunze U., and Doll T.
Nano photoelectron ioniser chip using LaB_6 for ambient pressure trace gas detection
Microelectronic Engineering **98**, 472 (2012)
- Zimmermann B., Mavropoulos P., Heers S., Long N., Blügel S., and Mokrousov Y.
Anisotropy of Spin Relaxation in Metals
Physical Review Letters **109**, 236603 (2012)
- Zimmermann F., Schwenninger C., Noltén U., Firmbach F. P., Elfring R., and Radermacher K.
A new approach to implant alignment and ligament balancing in total knee arthroplasty focussing on joint loads
Biomedical Engineering-Biomedizinische Technik **57**, 283 (2012)
- Zlatic V. and Costi T. A.
Charge Kondo anomalies in PbTe doped with Tl impurities
Physical Review Letters **108**, 036402 (2012)
- Zou Y., He D., Wei X., Yu R., Lu T., Chang X., Wang S., and Lei L.
Nanosintering mechanism of MgAl_2O_4 transparent ceramics under high pressure
Materials Chemistry and Physics **123** (2), 592 (2012)
- Zubkov E., Junker H., Korte S., Blab M., Coenen P., Voigtländer B., and Cherepanov V.
Ultra compact multitip scanning tunneling microscope with a diameter of 50 nm
Review of Scientific Instruments **83**, 033707 (2012)
- Zurbuchen M. A., Cahill D. G., Schubert J., Jia Y., and Schlom D. G.
Determination of the thermal conductivity tensor of the $n=7$ Aurivillius phase $\text{Sr}_4\text{Bi}_4\text{Ti}_7\text{O}_{24}$
Applied Physics Letters **101**, 021904 (2012)
- Zurbuchen M. A., Podraza N. J., Schubert J., Jia Y., and Schlom D. G.
Synthesis of the superlattice complex oxide $\text{Sr}_5\text{Bi}_4\text{Ti}_8\text{O}_{27}$ and its band gap behavior
Applied Physics Letters **100**, 223109 (2012)

